EXPLORING THE REACTIVITY OF IRIDIUM AND RHODIUM BIS-PHOSPHINE COMPLEXES WITH AMINE-BORANES

Amit Kumar

A thesis submitted in partial fulfilment of the requirements for the degree of

Doctor of Philosophy at the University of Oxford





Balliol College

March 2016

बड़े-बड़े नाज़ों से मैंने पाली है साकीबाला,
कलित कल्पना का ही इसने सदा उठाया है प्याला,
मान-दुलारों से ही रखना इस मेरी सुकुमारी को,
विश्व, तुम्हारे हाथों में अब सौंप रहा हूँ मधुशाला।।

Madhushala, Harivansh Rai Bachchan.

Translation:

With immense care, I have raised up my wine-maiden

She has always picked up goblets of creativity and innovation

Keep my cherished with comfort and affection

World, to your hands, I am submitting the tavern.

The work presented in this thesis was carried out between October 2012 and March 2016 under the supervision of Professor Andrew S. Weller. All of the work is my own, unless otherwise stated, and has not been submitted previously for any degree at this, or any other, university.

Amit Kumar

March 2016

Acknowledgements

Andy

Thank you for taking a chance on me

and offering me an opportunity to be one of the Wellers,

so that a young boy could travel 4500 miles from Delhi

to dehydrocouple amine-boranes and make some cool Rh-dimers.

Thank you for the inspirations and suggestions whenever I got stuck

and be a part of the evenings when we all could get drunk

Thank you for showering your experiences, intellect and wisdom

and teach an eaglet to fly high with the confidence and freedom

Thank you for not giving me food

instead training me how to hunt;

to dive deep into the sea, with the hands empty

and not just stroll on an oceanfront.

It is not just about a song

it is about the lesson-lifelong

The experiences from the past three and a half years

are much beyond this 250 pages chemistry report

and nothing could have ever been possible

without your supreme guidance and support.

Indrek, My hands owe you for teaching me glove box and Schlenk line

and these restless lips for introducing me to spirits and wine

thank you for teaching me all the coolest lab tricks

so that I build this thesis-home with colourful bricks

Tom, Thank you for sharing, from authorship to bedrooms, almost like a lab better half

and mounting many of my colourless crystals, which often came out to be sodium barf

thank you for the advices that opened up windows, the front and the back door

and directing my path, whether it is research or a zoo in Singapore.

Heather, You were no less than a 'Senapati' of an amine-borane force

thank you for teaching me all from the dehydrocoupling course

and for an excellent company to down pints of cider

and then break the dancing floors with the 'Womanizer'.

Amparo, Ahead was the parting, behind the partying; between them lay the chemistry

Gracias for the tips to solve the lab problems and resolve my life's mystery.

Thanks a lot to

Seb, for the excellent companionship and sharing the wealth of crystallography

and Mark for the advices in solving crystal structures, introducing 'cock or ball' and hosting house party

Gemma, for running GPC, and always being excited that mixed love in the air

and Peng, for a great friendship that will be valued for ever

Miguel and Rowan for getting my DPhil truck in top gear

Rosie, Mark and Becky for a great fun in the first year

Isobel for being a lovely part-II and exploring the B-phenyl amine-boranes

Nick and Amy for the ultimate night outs and being such great companions

Annie, I must thank your cheerful presence and baking that keeps everyone happy

and Alasdair for the chemdraw advices and a tough competition to swallow chilli

Joe, undoubtedly a great friendship, thank you for the epic emails from badminton club

Anna and Hannah, thanks for the awesome time whether in tea-breaks or in uni-club

Thanks to all the collaborators

Dr. A.G. Algarra, Nick Beattie and Prof. S. A. Macgregor for the DFT calculations

And Jacob Ishibashi and Prof. S.-Y. Liu for providing cyclic amine-boranes

and to all the CRL staffs in particular

Dr. Nick Rees for the NMR assistance and offering Bollywood music in the basement

Colin for the mass-spec help and Dr. Amber Thompson for the X-ray diffraction training

Other than amine-boranes

Life has been full of men-boranes and women-boranes;

thank you all for giving me infinite love and happiness:

Arnab, Vikaran, Krishna, Challenger, Anuradha, Midori,

Shiksha, Vikranth, Urmi, Richa, Moni, Harish, Jed, Shifali,

Alex, Nikita, Simin, Abhishek, Sudakshina, Aparajita, Sneha, Karishma, Madhav,

Akul, Dhruti, Anjul, Shreya, Amogh, Rituraj, Zoubeir,Toli, Natasha and Rami.

Sincere gratitude to the Rhodes Trust for offering me the funding and family in Oxford

and finally a big thanks to my parents for the unconditional love and support.

Abbreviations

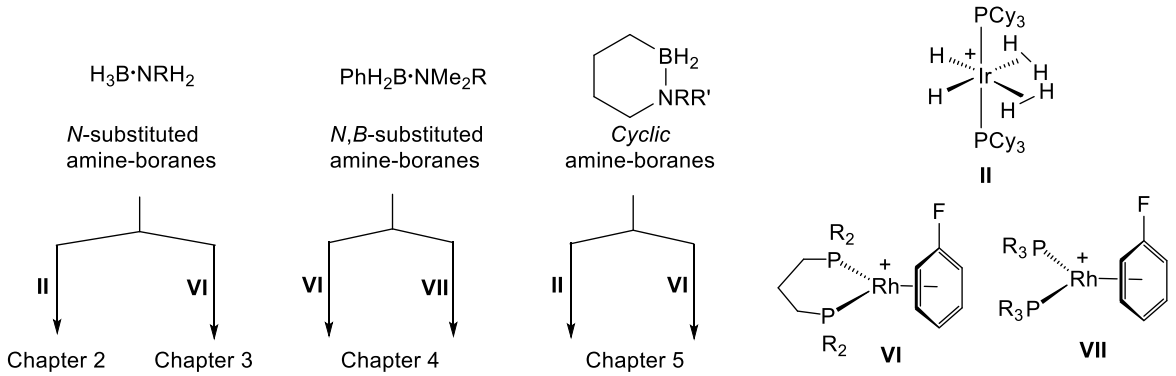
3C-2e	Three-center two-electron
atm	Atmospheres
$[BAr^F{}_4]^-$	$[B\{3,5\text{-}C_6H_3(CF_3)_2\}_4]^-$
$[BAr^{Cl}{}_4]^-$	$[B\{3,5\text{-}C_6H_3Cl_2\}_4]^-$
Bu	Butyl
COD	Cyclooctadiene
Cp	Cyclopentadienyl
Cy	Cyclohexyl
δ	Chemical shift
ΔG	Change in Gibb's free energy
ΔH	Change in enthalpy
ΔS	Change in entropy
DCM	Dichloromethane
dcype	1,2-*Bis*(dicyclohexylphosphino)ethane
Dipp	2,6-di-isopropylphenyl
ESI-MS	Electrospray Ionisation Mass Spectrometry
Et	Ethyl
HBCat	Catecholborane
Hz	Hertz
IMes	*N,N-bis*(2,4,6-trimethylphenyl)imidazol-2-ylidene
^{i}Bu	Isobutyl
^{i}Pr	Isopropyl
IR	Infrared
J	Coupling constant
K_{eq}	Equilibrium constant
LUMO	Lowest Unoccupied Molecular Orbital
M	Mol dm^{-3}
Me	Methyl
m/z	Mass to charge ratio

NBD	Norbornadiene
NHC	*N*-heterocyclic carbene
NMR	Nuclear Magnetic Resonance
OA	Oxidative addition
Ph	Phenyl
ppm	Parts per million
Pr	Propyl
$t_{½}$	Half life
TBE	3,3-Dimetyl-1-butene
THF	Tetrahydrofuran
^{t}Bu	Tertiary butyl
TOF	Turnover frequency
TON	Turnover number

Abstract

This thesis details the reactivity of amine-boranes with iridium and rhodium bis-phosphine complexes and offers mechanistic insights into the catalytic dehydrocoupling of amine-boranes to produce polyamino-boranes $[H_2BNRH]_n$ that are isoelectronic to the societally ubiquitous polyolefins $[H_2CCRH]_n$.

The 18-electron cationic complexes $[Ir(H)_2(PCy_3)(\eta^2\text{-}H_2)_2][BAr^F{}_4]$ (**II**) and $[Rh(PP)(\eta^6\text{-}C_6H_5F)][BAr^F{}_4]$ (**VI** and **VII**) have been used to study the catalytic dehydrogenation of *N*-substituted amine-boranes ($H_3B{\cdot}NRH_2$, Chapter 2 and 3), *B*,*N*-substituted amine-boranes ($PhH_2B{\cdot}NRMe_2$, Chapter 4) and cyclic amine-boranes (Chapter 5).



The stoichiometric (1 equivalent) reactions of metal-complexes (**II**, **III** and **VI**) with amine-boranes result in the formation of metal···amine-borane complexes which have either been isolated in the solid state or characterised *in situ* in the solution state by NMR spectroscopy and ESI-MS. Further addition of amine-boranes to these metal···amine-borane complexes results in the dehydrogenation/dehydrocoupling of the amine-boranes. Direct intermediates involved in the catalytic dehydrogenation/dehydrocoupling processes have either been isolated or characterised *in situ* to gain insight into the dehydrogenation mechanism. Dehydrogenation mechanisms have been postulated based upon the observed intermediates, kinetic studies, and DFT calculations performed by Prof. Stuart A Macgregor (Heriot-Watt University, Edinburgh).

Overall, a detailed investigation into the coordination chemistry of metal···amine-borane complexes and their subsequent dehydrogenation is reported.

Contents

Declaration i
Acknowledgements ii
Abbreviations v
Abstract vii
Contents viii

1 Introduction 1

1.1 Organotransition metal complexes 1

1.2 Phosphine-ligands 1

1.2.1 Introduction 1

1.2.2 Chelating phosphines 3

1.3 Weakly coordinating anions 5

1.4 Homogeneous organometallic catalysis 7

1.5 Homogeneous vs Heterogeneous catalysis 8

1.6 Rhodium: General properties and applications 10

1.7 Iridium: General properties and applications 11

1.8 Comparison of properties of rhodium and iridium (complexes) 13

1.8.1 $[RhCl(PPh_3)_3]$ vs $[IrCl(PPh_3)_3]$ towards hydrogenation 14

1.8.2 $[Rh(CO)_2(I)_2]^-$ vs $[Ir(CO)_2(I)_2]^-$ towards carbonylation of methanol 15

1.9 Sigma-complexes 17

1.9.1 Dihydrogen sigma-complexes 19

1.9.2 Borane sigma-complexes 22

1.10 Amine-boranes 24

1.11 General pathway for the dehydrocoupling of amine-boranes 25

1.12 Metal catalysed dehydrocoupling of amine-boranes 27

1.13 Heterogenous catalysts for the dehydrocoupling of amine-boranes 27

1.14 Homogeneous catalysts for the dehydrocoupling of amine-boranes 29

1.14.1 Outer sphere mechanism based on metal-ligand cooperativity 29

1.14.2 Inner sphere mechanism for the dehydrocoupling of amine-boranes 34

1.15 Main group catalysed dehydrocoupling of amine-boranes 35

1.16 Transition metal catalysed dehydrocoupling of amine-boranes 37

1.17 Sigma-complexes of amine-boranes 47

1.18 Sigma-complexes of amino-boranes 49

1.19 Summary 50

1.20 References 51

2 Dehydrocoupling of amine-boranes using an $\{Ir(PCy_3)_2\}^+$ fragment 59

2.1 Introduction 59

2.2 Reactivity of $H_3B{\cdot}NH_3$ with $[Ir(H)_2(PCy_3)_2(\eta^2\text{-}H_2)_2][BAr^F{}_4]$ (**II**): Synthesis of $[Ir(H)_2(PCy_3)_2(\eta^2\text{-}H_3B{\cdot}NH_3)][BAr^F{}_4]$ (**4**) 62

2.3 Addition of 10 equivalents of $H_3B{\cdot}NH_3$ to **II** 65

2.4 Synthesis of $[Ir(H)_2(PCy_3)_2$ $(\eta^2\text{-}H_3B{\cdot}\{NH_2BH_2\}_n{\cdot}NH_3)][BAr^F{}_4]$ (n = 1, 2) 68

2.5 Formation of $[Ir(H)_2(PCy_3)_2(\mu\text{-}BH_4)Ir(H)_2(PCy_3)_2][BAr^F{}_4]$ (**5a**) 72

2.6 Comparison of the NMR spectra of the independently synthesised Ir-bound oligomers with the spectra from the dehydrocoupling of $H_3B{\cdot}NH_3$ catalysed by **II** 74

2.7 Formation of polyaminoborane 76

2.8 Sequential addition of $H_3B{\cdot}NH_3$ to $[Ir(H)_2(PCy_3)_2(H_2)_2][BAr^F{}_4]$ 77

2.9 Further evidences of equilibrium between free and bound amine-boranes 79

2.9.1 Addition of $H_3B{\cdot}NH_3$ to $[Ir(H)_2(PCy_3)_2(H_3B{\cdot}(NH_2BH_2)_2{\cdot}NH_3)][BAr^F{}_4]$ (**4b**) 79

2.9.2 Addition of $H_3B{\cdot}NH_2BH_2{\cdot}NH_3$ to $([Ir(H)_2(PCy_3)_2(\eta^2\text{-}H_3B{\cdot}NH_3)][BAr^F{}_4]$ (**4**) 81

2.10 Addition of $H_3B{\cdot}NH_3$ and $H_3B{\cdot}NMeH_2$ to complex **II** 82

2.11 Addition of $H_3B{\cdot}NMeH_2$ to complex **4b** 83

2.12 Addition of cyclohexene to the catalytic dehydrocoupling of $H_3B{\cdot}NH_3$ 84

2.13 Effects of steric bulk on the catalytic dehydrocoupling of amine-boranes 84

2.14 DFT calculations on iridium catalysed dehydrocoupling of amine-boranes 87

2.14.1 Dehydrogenation mechanism: requirement of additional amine-boranes 88

2.14.2 Mechanism for the B−N coupling step 90

2.14.3 Effect of steric bulk on the dehydrocoupling barrier 92

2.15 Conclusions 94

2.16 References 95

3 The dehydrocoupling of amine-boranes catalysed by [Rh(chelating bis-phosphine)]$^+$ fragments 99

3.1 Introduction 99

3.2 Reactivity of **III** with THF 102

3.3 Reactivity of **III** with $H_3B{\cdot}NH_3$ 103

3.3.1 Catalytic dehydrocoupling of $H_3B{\cdot}NH_3$ in an open system 103

3.3.2 Stoichiometric reaction of **III** with $H_3B{\cdot}NH_3$ 106

3.4 Reactivity of $[Rh(P^iPr_2(CH_2)_3P^iPr_2)(C_6H_5F)][BAr^F_4]$ (**VI**) with $H_3B{\cdot}NH_3$ 110

3.5 Synthesis of $[Rh(P^iPr_2(CH_2)_3P^iPr_2)(\eta^2\text{-}H_3B{\cdot}NMe_3)][BAr^F_4]$ (**8**) 112

3.6 The mechanism of the formation of the dimers 113

3.7 Independent synthesis of the dimer **9** 115

3.8 Mechanism of the fluxional process in **9** 120

3.9 Reactivity of **9** towards $H_3B{\cdot}NMe_3$, CH_3CN, toluene and H_2 121

3.10 Structure and bonding of **9** using DFT calculations 123

3.11 Reactivity of **III** with $H_3B{\cdot}NH_2Me$ in THF and 1,2-$F_2C_6H_4$ 126

3.11.1 Reactivity of **III** with 1 - 4 equivalents of $H_3B{\cdot}NH_2Me$ 126

3.11.2 Catalytic dehydrocoupling of $H_3B{\cdot}NH_2Me$ using III and *in situ* prepared **10** 129

3.12 Reactivity of **III** with $H_3B{\cdot}NMe_2H$ 132

3.13 Reactivity of **VI** with $H_3B{\cdot}NMeHR$ (R = H, Me) 132

3.13.1 Reactivity of **VI** with $H_3B{\cdot}NMeH_2$ 132

3.13.2 Reactivity of **VI** with $H_3B{\cdot}NMe_2H$ 134

3.14 Reactivity of **9** with $H_3B{\cdot}NH_3$ 135

3.15 Reactivity of $[\{Rh(P^iPr_2(CH_2)_3P^iPr_2)\}_2(H)_2(\mu\text{-}H)_3][BAr^F_4]$ with $H_3B{\cdot}NH_3$ 135

3.16 Catalytic dehydrocoupling of $H_3B{\cdot}NH_3$ using **VI** and **9** in THF 136

3.17 Catalytic dehydrocoupling of $H_3B{\cdot}NH_3$ using 0.5 mol% $[BH_2(NH_3)(OEt_2)][BAr^F_4]$ in THF 138

3.18 Kinetic studies using initial rate methods 139

3.19 Conclusions 141

3.20 Future work 142

3.21 References 142

4 Sigma-complexes and dehydrogenation of *B*-phenyl amine-boranes 145

4.1 Introduction 145
4.2 Synthesis of $H_2PhB{\cdot}NMe_3$ and $H_2PhB{\cdot}NMe_2H$ 148
4.3 Coordination Chemistry of $H_2PhB{\cdot}NMe_3$ 148
4.3.1 Reactivity of $H_2PhB{\cdot}NMe_3$ with $[Rh(P^iPr_2(CH_2)_3P^iPr_2)(C_6H_5F)][BAr^F_4]$ (**VI**) 148
4.3.2 Reactivity of $H_2PhB{\cdot}NMe_3$ with $[Rh(P^iPr_3)_2(C_6H_5F)][BAr^F_4]$ (**VII**) 150
4.3.3 Reactivity of $H_2PhB{\cdot}NMe_3$ with $[Rh(P^iBu_3)_2(C_6H_5F)][BAr^F_4]$ (**VIII**) 152
4.3.4 Effect of bite angle on the coordination mode of $H_2PhB{\cdot}NMe_3$ 156
4.4 Catalytic dehydrogenation of $H_2PhB{\cdot}NMe_2H$ using **VI** and **VII** 160
4.5 Reactivity of $H_2PhB{\cdot}NMe_2H$ with **VI** 163
4.6 Stoichiometric reactivity of $H_2PhB{\cdot}NMe_2H$ with **VII** 165
4.7 Mechanism for the formation of **21** 170
4.8 Conclusions 173
4.9 References 174
5 The Synthesis and Dehydrogenation of Sigma-Complexes of BN−Cyclohexanes 177
5.1 Introduction 177
5.2 Synthesis of cyclic amine-boranes 180
5.3 Reactivity of cyclic amine-boranes (**A** - **C**) with $[Ir(PCy_3)_2(H_2)_2(H)_2][BAr^F_4]$ (**II**) 181
5.3.1 Formation of $[Ir(PCy_3)_2(H)_2(\eta^2\text{-}H_2BNH_2C_4H_8)][BAr^F_4]$ (**22**) 181
5.3.2 Reactivity of $[Ir(PCy_3)_2(H)_2(\eta^2\text{-}H_2BNH_2C_4H_8)][BAr^F_4]$ (**22**) with D_2 185
5.3.3 Formation of $[Ir(PCy_3)_2(H)_2(c^2\text{-}H_2BNRMeC_4H_8)][BAr^F_4]$ (R = H, Me) 189
5.4 Catalytic dehydrogenation of **A** and **B** using Ir-BN complexes 191
5.4.1 Catalytic dehydrogenation of **A** using **22** 191
5.4.2 Catalytic dehydrogenation of **B** using $[Ir(PCy_3)_2(H_2)_2(H)_2][BAr^F_4]$ (**II**) 194
5.5 Reactivity of the cyclic amine-boranes **A** - **C** with **VI** 194
5.5.1 Formation of $[Rh(^iPr_2P(CH_2)_3P^iPr_2)(\eta^2\text{-}H_2BNH_2C_4H_8)][BAr^F_4]$ (**24**) 195
5.5.2 Formation of $[Rh(^iPr_2P(CH_2)_3P^iPr_2)(\eta^2\text{-}H_2BNHMeC_4H_8)][BAr^F_4]$ (**25**) 196
5.5.3 Formation of $[Rh(^iPr_2P(CH_2)_3P^iPr_2)(\eta^2\text{-}H_2BNMe_2C_4H_8)][BAr^F_4]$ (**26**) 199
5.6 Catalytic dehydrogenation of **A** and **B** using **VI** and **III** 200
5.6.1 Catalytic dehydrocoupling of **A** using **VI** and **III** 200
5.6.2 Catalytic dehydrogenation of **B** using **III** and **VI** 203

5.7 Mechanistic investigation for the dehydrogenation of **B** catalysed by **VI** 204
5.7.1 Formation of [{Rh($P^iPr_2(CH_2)_3P^iPr_2$)}$_2$(H)$_2$(μ-H)$_3$][BAr^F_4] (**27**) 204
5.7.2 Catalytic dehydrogenation of **B** using monomeric **25** and dimeric **27** 207
5.7.3 Dimer (**27**) - monomer (**25**) equilibrium 208
5.7.4 Kinetic studies 214
5.8 Conclusions 217
5.9 References 218
6 Experimental 221
6.1 Experimental techniques 221
6.1.1 Nuclear Magnetic Resonance Spectroscopy 221
6.1.2 Mass Spectrometry 221
6.1.3 Elemental microanalysis 222
6.1.4 Gel Permeation Chromatography 222
6.1.5 X-ray crystallography 222
6.1.6 General procedure for hydrogenation 223
6.2 Synthesis and characterisation 223
6.2.1 Starting materials 223
6.2.2 Synthesis of new complexes 223
6.3 Catalytic procedures 242
6.3.1 General procedure for the dehydrocoupling of amine-boranes in an open system − hydrogen evolution experiment 242
6.3.2 General procedure for the dehydropolymerisation of $H_3B{\cdot}NMeH_2$ 243
6.3.3 General procedure for the dehydrocoupling of amine-boranes in a closed system 243
6.4 Computational details 243
6.5 References 244
7 Appendices 248
7.1 Crystallographic data 248
7.2 Publications 253

1 Introduction

1.1 Organotransition metal complexes

"Today, it is virtually impossible to find a multistep organic synthesis that does not employ organotransition metal chemistry."

Prof. Per-ola Norrby, from the review of Organotransition Metal Chemistry: From Bonding to Catalysis by John Hartwig.[1]

Transition metal organometallic chemistry is involved with the interactions between transition metal fragments and organic molecules. The presence of d-electrons in the valence shell of transition metals allows the occupancy of variable oxidation states and hence facilitates transition metal complexes to act as efficient catalysts by oxidation, reduction and ligand redistribution. Many commercial processes have been developed using transition metal complexes as catalysts, for example production of acetic acid (Cativa process or Monsanto process), production of ketones (hydroacylation process), production of polyolefins (Zieglar Natta polymerization), production of olefins (metathesis using Grubb's / Shrock catalyst) and hydrogenation of olefins (Wilkinson's catalyst or Crabtree's catalyst).[2] Thus, proper understanding of transition metal chemistry is of significant importance to develop the modern science of synthesis and the manufacture of new molecules of value.

1.2 Phosphine-ligands

1.2.1 Introduction

Phosphines are among the most commonly used ligands in homogeneous catalysis and well known for their remarkable electronic and steric tunability and innocence.[3] An additional and important advantage of phosphine ligands over other N and O – donor

ligands is the suitable nuclear properties of ^{31}P nucleus with a nuclear spin of ½ and an isotopic abundance of 100% making it a very powerful tool to monitor reactions using NMR spectroscopy. Phosphines can act as both σ-donor and π acceptor ligands. The lone pair of the phosphorus atom can donate into an empty metal d orbital forming a σ-bond while the metal can backdonate electrons into the σ* orbital of the P–R bond forming a π bond (Figure 1.1).[4]

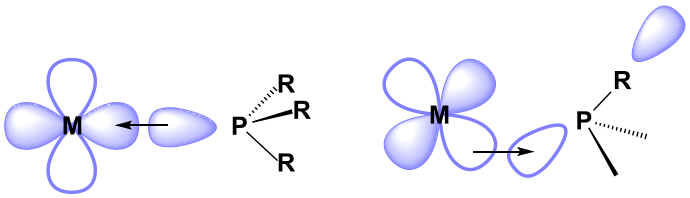


Figure 1.1 Bonding in metal-phosphine complex. Left: σ-σ interaction, right: π-σ* interaction

The electronic properties of metal-phosphine complexes can be tuned by varying the π acidity of the phosphine ligands. The effect of π acidity is small for alkyl substituents on phosphine ligand but is significant for electron withdrawing substituents like aryl, alkoxy groups, chloride and in particular fluoride substituents for example PF_3, whose π acidity is equivalent to CO (Figure 1.2).[5]

$$PMe_3 \approx P(NR_2)_3 < PAr_3 < P(OMe)_3 < PCl_3 < PF_3 \approx CO$$

Figure 1.2 Order of increasing π-acidity for phosphine ligands, with respect to carbon monoxide.

The electronic effect of phosphine ligands was quantified by Tolman at DuPont, who measured the value of highest-frequency of CO band in IR spectra of many $[Ni(CO)_3L]$ complexes (where L is a phosphine).[6] A lower CO frequency was suggestive of higher metal-CO backbonding which due to less metal-phosphine backbonding, indicative of lesser π aciditiy of phosphines. For example, the CO stretching frequency in $[Ni(CO)_3P^tBu_3]$ is 2056 cm^{-1} while in $[Ni(CO)_3PF_3]$ it is 2110 cm^{-1} suggesting that PF_3 is a stronger π accepting ligand.

Steric properties of phosphine ligands have also been explored extensively to control the kinetics and selectivity in the catalysis carried by organometallic complexes.[7-9] Tolman, again, devised a way to quantify the steric properties of phosphine ligands using a structural parameter called the 'Cone angle (θ)' which is the angle defined by the outer edge of the substituents at phosphorus and the metal centre of a space-filling model, where the metal-phosphorus distance is fixed at 2.28 Å and the metal is at the vertex, as shown in Figure 1.3. As it is clear by the definition, a phosphine with bulky substituents has a larger cone-angle, for example cone angle for PH_3 is 87° while the cone angle for P(mesityl)$_3$ group is 212°.[6]

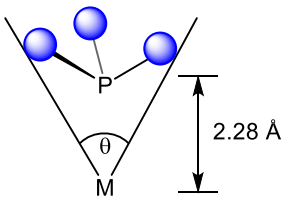


Figure 1.3 Tolman cone angle (θ)

Tolman also studied the equilibrium for the dissociation of NiL_4 complexes (L = phosphine ligands) and correlated with the cone angles of the corresponding phosphine complexes. Extent of ligand dissociation in these complexes are in the order PMe_3 < PMe_2Ph < $PMePh_2$ < PEt_3 < PPh_3 < P^iPr_3 < PCy_3 < PPh^tBu_2.[10]

1.2.2 Chelating phosphines

Phosphines can be incorporated into a chelating motif to create a ligand which can bind the metal through more than one binding sites. Such ligand architectures are often helpful in discouraging ligand dissociation by the chelate effect.[3] Casey and Whiteker have defined a term called 'Bite angle' (P–M–P angle, β) to quantify the preferred chelation angle determined by ligand backbone constraints.[11] Bite angle and the corresponding flexibility range (FR) for some of the chelating phosphines are shown in Figure 1.4.

Flexibility range has been defined as the accessible range of bite angles with strain energy within 3 kcal mol^{-1} of the calculated bite angle.[12]

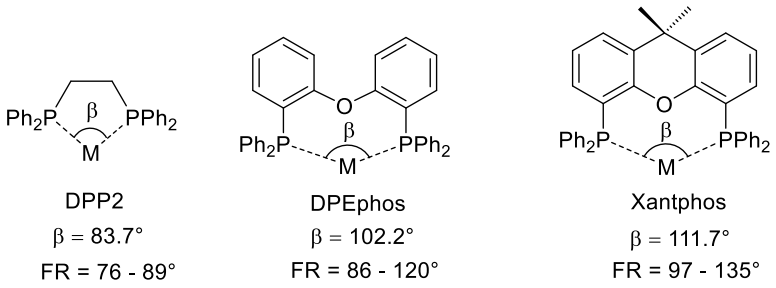
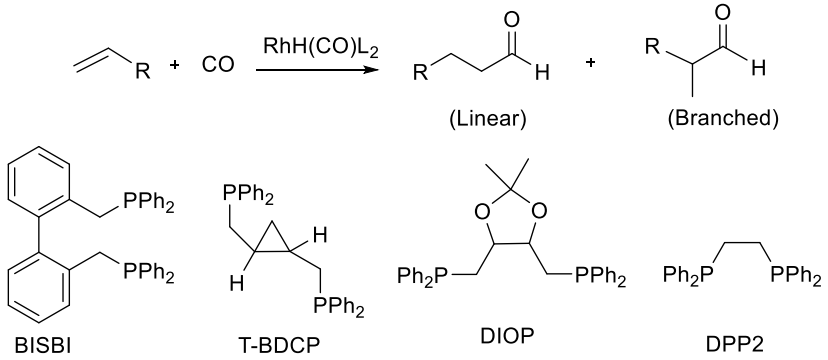


Figure 1.4 Calculated bite angles and flexibility ranges for DPP2,[13] DPEphos[12] and Xantphos.[12]

A longer ligand backbone will make a bigger P–M–P angle and hence change in the steric properties can also electronically favour or disfavour certain geometries of transition metal complexes. Effects of bite angles on C–C and C–X bond forming reactions for example hydroformylation, hydroacylation, alkene / carbon monoxide copolymerization and metal catalysed cross-coupling reactions have been extensively studied in the past two decades.[13-18] Casey has studied the effects of bite angle on the hydroformylation reaction and has shown experimentally that the larger bite angles offer better selectivity towards the linear product (Scheme 1.1).



L_2	Bite angle	Linear : Branched (ratio)
BISBI	113°	66:1
T-BDCP	107°	12:1
DIOP	102°	8.5:1
DPP2	84°	2.1:1

Scheme 1.1 Effects of bite angle on the selectivity (linear : branched) of aldehyde formation in hydroformylation reaction.

Relevant to this thesis is the recent report by the Weller group where the bite angle effects the rate of dehydrogenation of $H_3B{\cdot}NMe_2H$ and properties of the polymers formed upon dehydrocoupling of $H_3B{\cdot}NMeH_2$ catalysed by the $\{RhPPh_2(CH_2)_nPPh_2\}^+$ (n = 3 - 5) fragment. $\{RhPPh_2(CH_2)_3PPh_2\}^+$ with the smallest bite angle (93°) showed the highest TOF of 1250 h^{-1} for the dehydrogenation of $H_3B{\cdot}NMe_2H$ while $\{RhPPh_2(CH_2)_5PPh_2\}^+$ with the largest bite angle (~107°) showed the smallest TOF of 180 h^{-1}.[19]

1.3 Weakly coordinating anions

Selection of appropriate anion systems is important for the synthesis of low coordinate cationic metal complexes. Such anions should be weakly coordinating so that they do not coordinate strongly to the reactive metal centres and allow the generation of vacant or “latent” sites. In addition to this, anions should also be robust. Thus, anions like $[PF_6]^-$ and $[BF_4]^-$ although, weakly coordinating and ubiquitous, are not very commonly used to

synthesize low valent complexes due to its competitive side reactions such as hydrolysis and fluoride abstraction.[20, 21] Several alkoxy, carborane and borate-based weakly coordinating anions are known in literature.[22] Figure 1.5 shows examples of some of these anions from which $[B\{3,5\text{-}(CF_3)_2C_6H_3\}_4]^-$ ($[BAr^F{}_4]^-$) and $[B\{3,5\text{-}Cl_2C_6H_3\}_4]^-$ ($[BAr^{Cl}{}_4]^-$) are of particular significance to this thesis. $[BAr^F{}_4]^-$ is a very weakly coordinating anion, is easy to handle as a variety of salts and has been used as an anion in most of the organometallic complexes reported in this thesis. The $[BAr^{Cl}{}_4]^-$ anion has been shown to be useful in obtaining good quality crystals as discussed in Chapter Two, and also avoids rotational disorderness in the crystal structure often observed for $[BAr^F{}_4]^-$ due to the presence of CF_3 groups.[23]

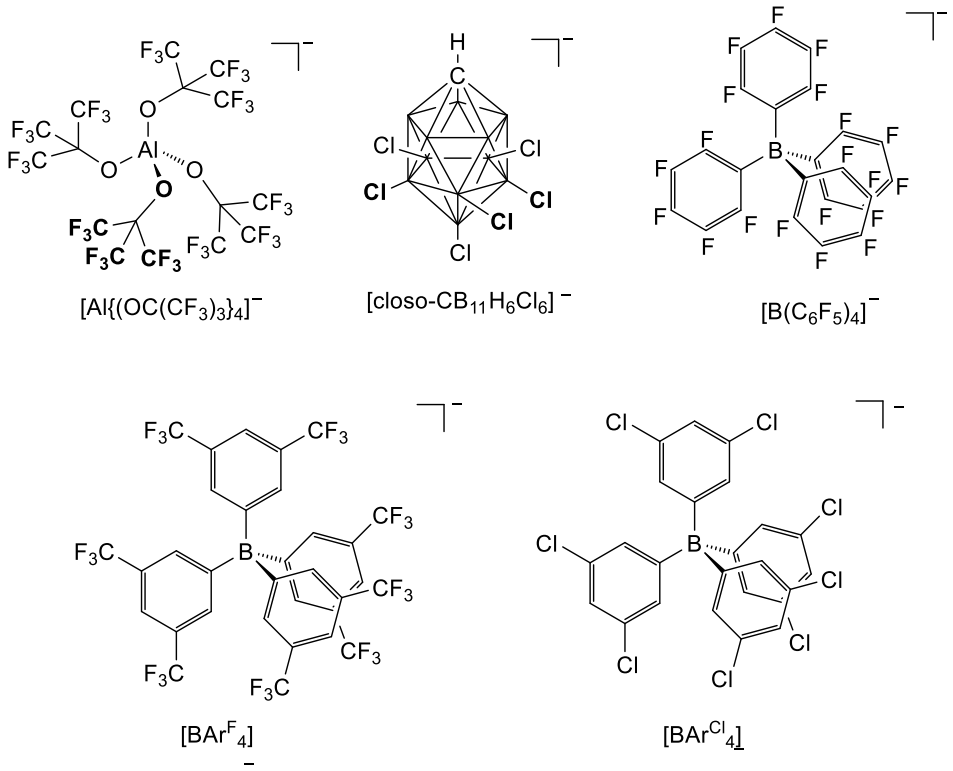


Figure 1.5 Examples of commonly used weakly coordinated anions.

1.4 Homogeneous organometallic catalysis

Homogeneous catalysis is a sequence of reactions that involves reactants and catalyst in the same phase. If a soluble organometallic complex is used as a catalyst, the process is termed as homogeneous organometallic catalysis.[24] The primary advantages of homogeneously catalysed processes are that (i) they can be studied on a molecular level and hence offer the possibility of catalyst development and optimisation and (ii) a wide range of catalysts can be designed through the variation of metals and ligands. However, the major disadvantages of this process is that purification of product from the catalyst becomes expensive and that homogeneous catalysts are often not as robust as heterogeneous catalysts. Despite the difficulties that can be associated with the separation of products from catalyst and solvent, a very high activity and selectivity of homogeneous catalytic systems has allowed this methodology to be extensively exploited in chemical industries.

To explain the fundamental course of catalytic organometallic transformation, we consider a model of substrate (**S**) converting to product (**P**) under the catalytic effect of [**M**].

$$S \xrightarrow{[M]} P$$

A typical cycle of an organometallic catalysed reactions can be explained in four elementary steps (Scheme 1.2).[24]

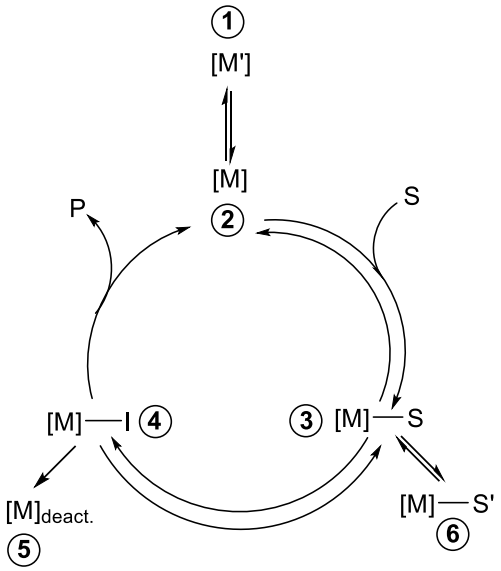
1 → **2** Formation of the catalyst [**M**] from the precatalyst [**M'**]. The catalyst thus formed is coordinatively and electronically unsaturated and is termed as a 'low-coordinate complex'.

2 → **3** Activation of a substrate by the formation of [M]–S. This activation can occur through σ bond or through π bond leading to the formation of σ-complex or π-complex respectively.

3 → 4 Transformation of [M]–S to an intermediate [M]–I. This transformation can occur through various mechanisms for example oxidative addition, migratory insertion or beta hydrogen elimination.

4 → 2 Cleavage of product from the intermediate [M]–I and regeneration of catalyst.

3 → 6 or **4 → 5** (Catalyst decomposition) The reversible formation of catalytically inactive species ([M]–S') and irreversible decomposition of intermediate ([M]–I) leads to the deactivation of the catalytically active species and decrease the productivity.



Scheme 1.2 General homogeneous organometallic catalytic cycles.

1.5 Homogeneous vs Heterogeneous catalysis

Generally, a transition metal complex added to the solution for the catalytic transformation is the *precatalyst* and not the *true catalyst*. The precatalyst in the solution can undergo organometallic transformation to form more reactive 'active species' called the *true catalyst* which can either be single active metal site making a homogeneous system or can be metal colloids or nano-particles or insoluble metal-particles making a

heterogeneous system.[24] The nature of catalytic processes i.e. homogeneous or heterogeneous can influence the catalytic properties like the catalyst's activity, selectivity, recovery and stability and therefore vary the overall cost of the catalytic process. It is, therefore, important to distinguish between both these systems and find whether the catalysis is homogeneous or heterogeneous. However, there is no single definitive experiment to distinguish between both these processes and a series of experiments are generally performed to reach at the conclusion. Widegren and Finke have reviewed various methods to distinguish between homogeneous and heterogeneous catalysis, some of which are discussed here:[25]

(a) Kinetics: It has been suggested that a homogeneous catalyst produces reproducible kinetics while the kinetics from a heterogeneous system are generally not reproducible. This is mainly because a true homogeneous catalyst acts through well-defined catalytic sites while a heterogeneous catalyst's activity arises from the decomposition of a metal complex into colloidal or nanoparticles which are not so well-defined. Although, non-reproducible kinetics accounts for the heterogeneous catalysis, a reproducible kinetics cannot completely rule out catalysis via heterogeneous process.[26] Other than reproducibility, a sigmoidal kinetics curve has been observed as an important tool to confirm the *in situ* formation of a heterogeneous catalyst.

(b) Transmission Electron Microscopy (TEM): TEM is an important technique to detect the presence of nano-clusters deposited from the reaction. However, the presence of nano-particles does not guarantee the occurrence of heterogeneous catalysis as TEM does not give evidence of the metal-particles being involved in catalysis.

(c) Catalyst poisoning: Catalyst poisoning experiments have been used as a powerful method to distinguish between homogenous and heterogeneous catalysis. Hg(0) is commonly used to poison heterogeneous catalyst. Therefore, suppression of catalytic activity upon addition of Hg(0) is suggestive of a heterogeneous process. Stronger ligands like CS_2, thiophene and PPh_3 can bind strongly with a metal centre and block the active sites. It is generally suggested that catalyst poisoning by adding << 1.0 equivalent of the

added ligand (per metal atom) is indicative of heterogeneous catalyst whereas poisoning by ≥ 1.0 equivalent of ligand, is indicative of homogeneous catalyst. This is mainly because in a heterogeneous catalyst only a fraction of metal is on the surface requiring less than one equivalent of ligand to be poisoned.

(d) Filtration test: This test compares the catalytic activity before and after filtering the active catalytic solution. If the filtration does not change the catalytic activity, this is suggestive of a homogeneous catalyst where as if the catalytic activity gets suppressed upon filtration, this is suggestive of a heterogeneous catalyst.

1.6 Rhodium: General properties and applications

Rhodium is one of the rarest elements of Earth's crust, constituting of 0.0002 parts per million which makes it expensive to use.[27, 28] Rhodium is primarily (> 80% of the world rhodium production) used in automobiles as a catalytic converter, which changes nitrogen oxide and carbon monoxide emissions to less harmful gases such as carbon dioxide and nitrogen.[29] Rhodium can exist in oxidation states –III to +VI such as $[Rh(CO)_3]^{3-}$ and RhF_6 respectively. However, the most stable oxidation states for Rh are +I and +III which allows it to be used as an effective catalyst in homogeneous systems facilitating oxidative addition and reductive elimination steps.[30] The three very successful applications of Rh-complexes as homogeneous catalysts are detailed below:

(a) Hydroformylation of alkenes using $[RhH(CO)(PPh_3)_3]$: Hydroformylation is an important homogeneously catalysed industrial process for the production of aldehydes from alkenes and CO. This process is important because the resulting product aldehyde can easily be converted to many secondary products for example alcohols which can be then converted to plasticizers or detergents. The original catalyst used for this process was $HCo(CO)_4$, but since the discovery of a highly active rhodium catalyst $RhH(CO)(PPh3)_3$ in 1960, most of the hydroformylation processes rely on rhodium.[31, 32]

(b) Carbonylation of methanol using $[Rh(CO)_2I_2]^-$: Carbonylation of methanol (*vide*

infra) is an industrial process for the catalytic production of acetic acid, the global demand for which is 6.5 Mt/a.[6] This process was developed by BASF in 1960 and improved by the Monsanto Company in 1966 and therefore the process is also called as Monsanto process.

(c) Hydrogenation: Hydrogenation of alkenes in particular catalysed by Wilkinson's catalyst [$RhCl(PPh_3)_3$] is a well-known process (*vide infra*).[33, 34] Other than alkenes, rhodium catalysts are also used to hydrogenate nitriles (e.g. by [$RhH(P^iPr_3)_3$]),[35] aldehydes (for example using [$Rh(nbd)(PEt_3)_2]ClO_4$),[36] ketones[37], epoxides[38] and arenes.[39] Rhodium bound to chiral phosphine ligands are used for the asymmetric hydrogenation of olefins, aldehydes and ketones to produce the corresponding chiral compounds. Amongst these, of significance importance is the Rh complex with DIPAMP ligand (**i-6**) which is used to hydrogenate α-amidocinnamic acid. This hydrogenation step is used in the synthesis of α-dihydroxyphenylalanine (L-DOPA) drug which is commercially used for the control of the symptoms of Parkinson's disease.[40, 41]

In addition to these, Rh-complexes are used for the catalytic dehydrogenation of alcohols, carbonylation of C–H bonds, alkyl halides and amines and decarbonylation reactions.[41] Of particular relevance to this thesis is the application of Rh-complexes for the catalytic dehydrocoupling of amine-boranes which has been discussed in detail later in this chapter (Section 1.16).

1.7 Iridium: General properties and applications

Iridium, like rhodium is also one of the least abundant metals in earth's crust (0.001 parts per million).[30] However, it is believed that the overall concentration of iridium on Earth is much higher than what is observed in earth's crust. This is because the high density and siderophilic (iron-loving) character of iridium let it descend below the crust into Earth's core when the planet was still molten.[42] Iridium is mainly used in electronics related

applications for example spark-plugs, electrodes and crucibles which are used to grow large high quality single crystals. Iridium forms compounds in oxidation states between –III to +IX, out of which the most common oxidation states are +III and +IV.[30] Iridium compounds have been exploited extensively for various catalytic processes, a selection of which are listed below:

(a) Carbonylation of methanol: $[Ir(CO)_2I_2]^-$ complex is used as a catalyst for the production of acetic acid by the carbonylationn of methanol (*vide infra*). The technology was developed by BP Chemicals and is known as Cativa process which is similar to Monsanto process mentioned in previous section.[43]

(b) Hydrogenation: Cationic iridium complexes based on $[Ir(COD)(Phosphine)_2]$ are effective hydrogenation catalysts, the most notable of which is the Crabtree's catalyst $[Ir(COD)(py)PCy_3][PF_6]$.[44] Iridium complexes with chiral phosphine ligands have been extensively used for the asymmetric hydrogenation of olefins, esters, carbocycles and heterocycles, the most common of which is the Pfaltz's catalyst (**i-5**) which is the chiral analogue of the Crabtree's catalyst (**i-3**).[45]

(c) C–H activation and dehydrogenation of alkanes: Bergman and co-workers reported that under photolytic condition, $[Ir(Cp^*)(H)_2PMe_3]$ shows the ability to activate C–H bonds in alkanes for example cyclohexane and neo-pentane.[46] Recently, Goldman and co-workers have also reported Ir-pincer complexes for the C–H bond activation and dehydrogenation of alkanes.[47-52]

Ir-complexes have also been exploited for the dehydrogenation/ dehydrocoupling of amine-boranes which will be discussed later in this chapter.

1.8 Comparison of properties of rhodium and iridium (complexes)

Some of the rhodium and iridium complexes which are extensively studied and well known for their catalytic applications are shown in Figure 1.6.

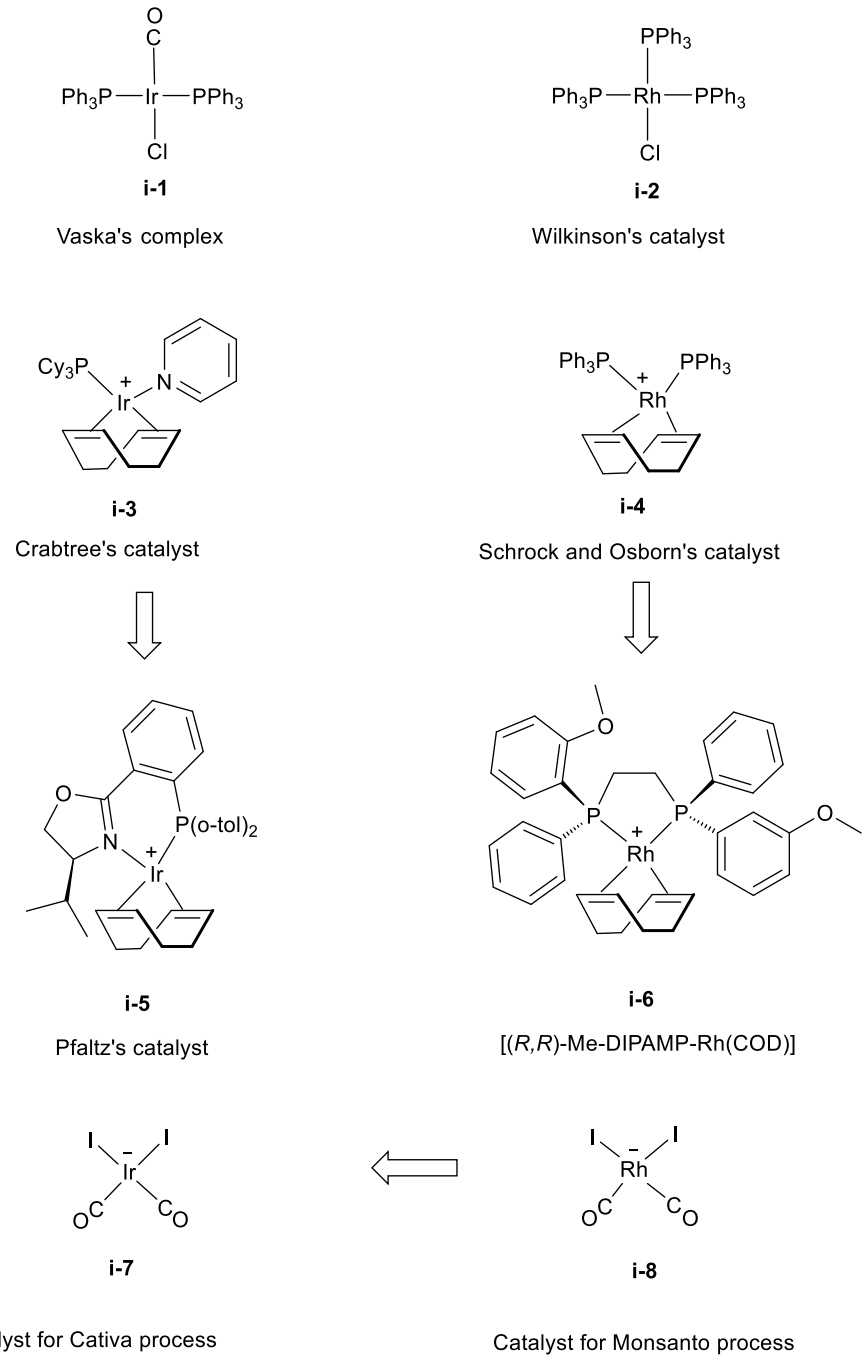
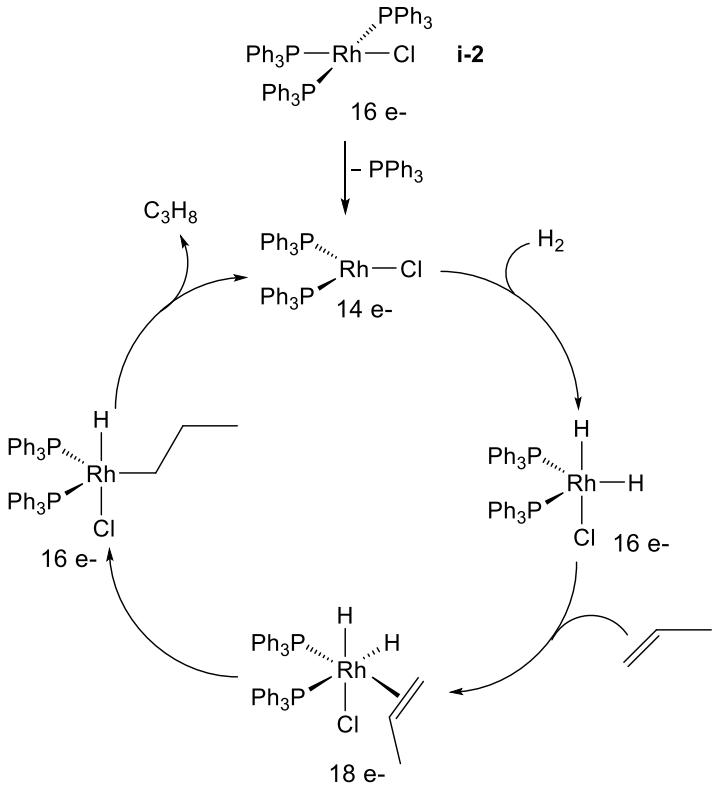


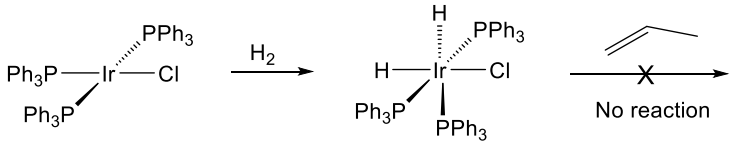
Figure 1.6 Ir and Rh complexes used in catalysis. Cations and anions are not shown.

1.8.1 $[RhCl(PPh_3)_3]$ vs $[IrCl(PPh_3)_3]$ towards hydrogenation

The catalytic activity of rhodium and iridium complexes can vary depending on the nature of binding with the substrates. A classic example for this is the catalytic hydrogenation of olefins using $[RhCl(PPh_3)_3]$ and $[IrCl(PPh_3)_3]$ complexes. $[RhCl(PPh_3)_3]$ (**i-2**) Wilkinson's catalyst is well known for the hydrogenation of olefins. $[RhCl(PPh_3)_3]$ undergoes ligand dissociation step to form the 14 e^- active species $[RhCl(PPh_3)_2]$. $[RhCl(PPh_3)_2]$, then oxidatively adds H_2 to form the 16 e^- species $[RhClH_2(PPh_3)_2]$. Subsequent coordination of alkene and migratory insertion step followed by the reductive elimination step results in the formation of alkane and regenerates the active species $[RhCl(PPh_3)_3]$ as shown in Scheme 1.3. However, its iridium analogue, $[IrCl(PPh_3)_3]$, is inactive for the hydrogenation of alkene. This is because (a) $[IrCl(PPh_3)_3]$ doesn't dissociate a phosphine as readily to offer vacant site for the coordination of olefin. (b) The Ir–H bond is stronger than Rh–H bond. Therefore, $[IrCl(PPh_3)_3]$ binds with H_2 irreversibly forming stable complex $[Ir(H)_2Cl(PPh_3)_3]$, from which hydrogen doesn't get transferred to olefin via insertion and reductive elimination steps (Scheme 1.4).[53]



Scheme 1.3 Catalytic hydrogenation of propylene using Wilkinson's catalyst.



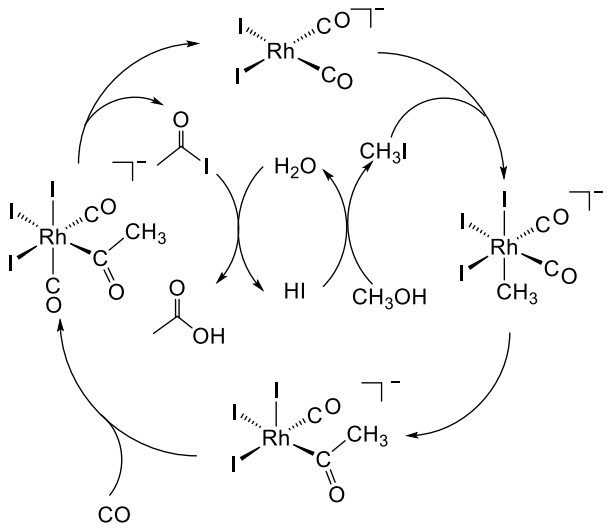
Scheme 1.4 Reactivity of $[IrCl(PPh_3)_3]$ with H_2 and alkene.

1.8.2 $[Rh(CO)_2(I)_2]^-$ vs $[Ir(CO)_2(I)_2]^-$ towards carbonylation of methanol

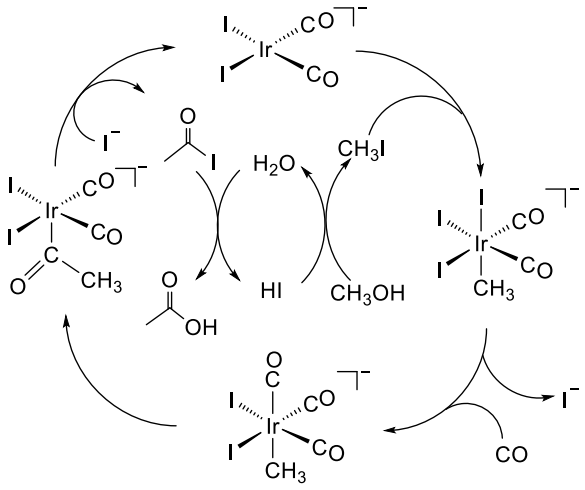
Due to very attractive price difference of iridium compared to rhodium researchers at BP Chemicals, during the early 1990s started looking at the iridium analogue of $[Rh(CO)_2(I)_2]^-$, the catalyst used in Monsanto process for the carbonylation of methanol. The iridium analogue, $[Ir(CO)_2(I)_2]^-$ was found to carry the catalytic transformation through the similar mechanism as $[Rh(CO)_2(I)_2]^-$ (Schemes 1.5 and 1.6). However, use of iridium made a significant improvement to the catalytic process because:

(i) $[Ir(CO)_2(I)_2]^-$ is stable under a wide range of conditions under which $[Rh(CO)_2(I)_2]^-$ undergoes decomposition forming inactive and irrecoverable rhodium salts.

(ii) The iridium catalyst is more soluble than its rhodium analogue, thus allowing higher catalyst concentration and increasing the rate of carbonylation. (iii) The iridium catalyst is found to be robust at low water concentration allowing the use of less water in the reaction compared to the rhodium catalyst. This change reduced the number of drying columns necessary and also reduced the CO loss by driving the water gas shift reaction equilibrium (equilibrium reaction of CO and H_2O to form CO_2 and H_2) towards the side of CO and H_2O.



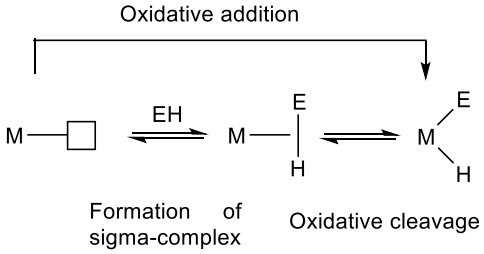
Scheme 1.5 Mechanism of the Monsanto process, rhodium catalysed carbonylation of methanol.



Scheme 1.6 Mechanism of the Cativa process, iridium catalysed carbonylation of methanol.

1.9 Sigma-complexes

Sigma-complexes refer to the side-on 3-center interaction of a bonding electron pair in an E−H bond (where E = H, Si, B, C, P, Sn, Ge) or X−Y bonds (like C−C) with metals.[4] Formation of a sigma-complex by the coordination of substrate to the transition metal centres is considered the first step in the catalytic cycle prior to the oxidative cleavage step (Scheme 1.7).



Scheme 1.7 A general oxidative addition and oxidative cleavage step.

Sigma-complexes have been proposed as the important intermediates or "true" catalysts during catalytic hydrogenolysis (**i-9**),[54] hydrogenation (**i-10**),[55] hydrosilylation (**i-11**),[56] hydroboration (**i-12**),[57] amine-borane / phosphine-borane dehydrogenation (**i-13** and **i-14**),[58-61], oxidative addition of germane (**i-15**)[62] and hydrogermylation of norbornadiene (**i-16**, Figure 1.7).[63] Characterisation and study of sigma-complexes, therefore, provides important insight into the catalysis mechanism.

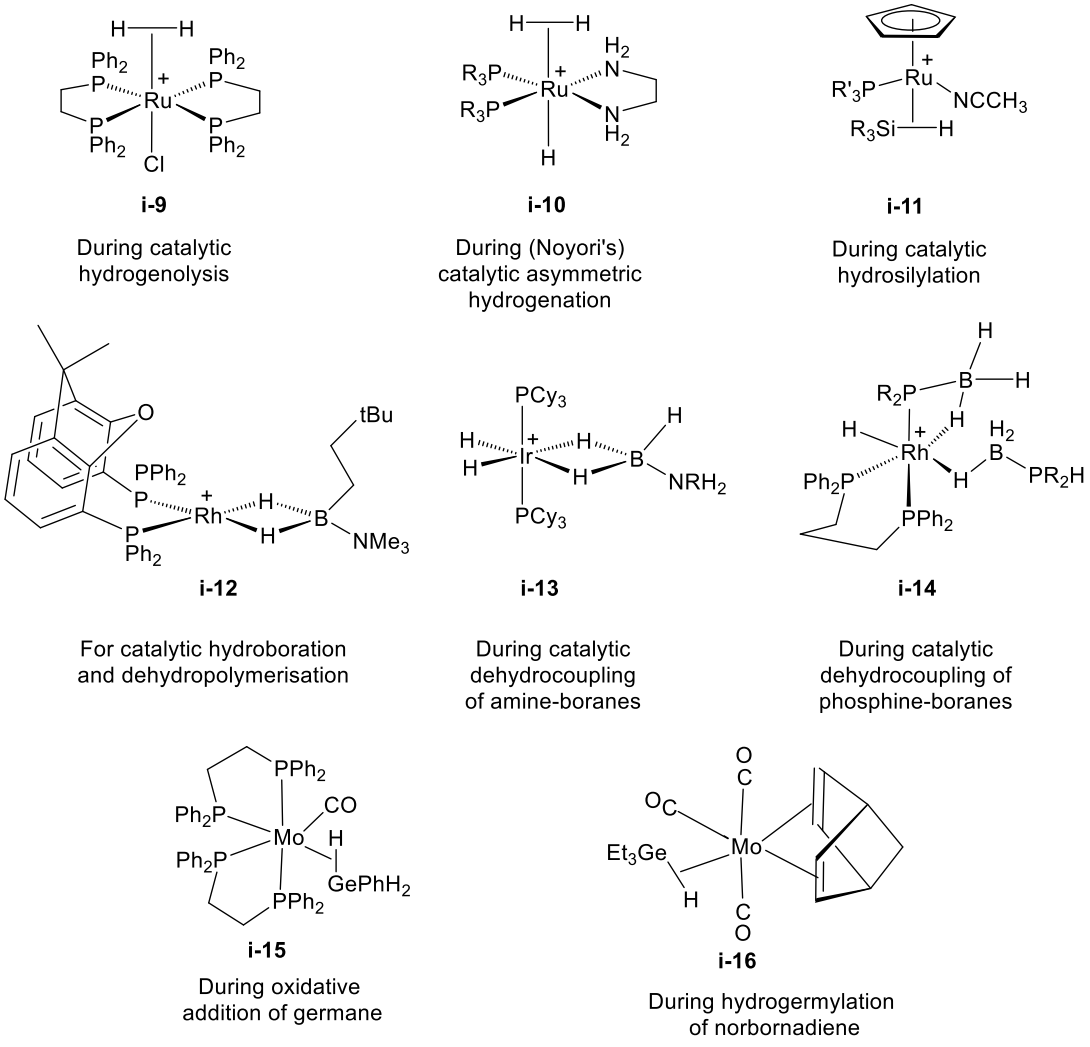


Figure 1.7 Sigma-complexes as important interemdiates in organometallic catalysis.

A sigma-interaction is different from agostic interaction which is used to represent the interaction of a transition metal with a chemical bond such as C−X (X = H, C, B) from a ligand which is already coordinated to metal (Figure 1.8).[64]

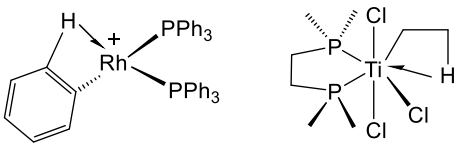
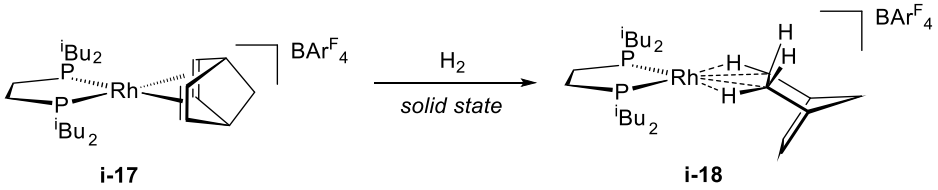


Figure 1.8 Examples of rhodium[65] and titanium[66] complexes showing agostic interactions.

Sigma-complexes feature weak E−H interaction (in particular when E = C) and are often very transient in the solution state. This makes sigma-complexes, in particular sigma-alkane complexes, difficult to be isolated. The Weller group has employed solid state hydrogenation technique for the synthesis of sigma-alkane complexes. $[Rh(^{i}Bu_2PCH_2CH_2P^{i}Bu_2)(\eta^2,\eta^2\text{-}C_7H_{12})][BAr^F{}_4]$ (**i-18**) was produced by the hydrogenation of the strained alkene precursor $[Rh(^{i}Bu_2PCH_2CH_2P^{i}Bu_2)(NBD)][BAr^F{}_4]$ (**i-17)** in solid state employing a single crystal to single crystal transformation (Scheme 1.8).[67]

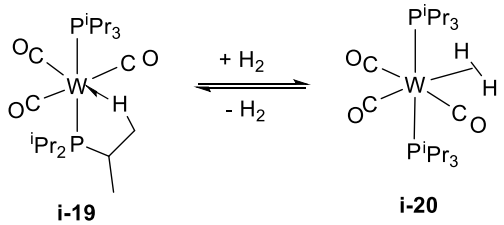


i-17 **i-18**

Scheme 1.8 Synthesis of sigma-alkane complex by the solid state hydrogenation.

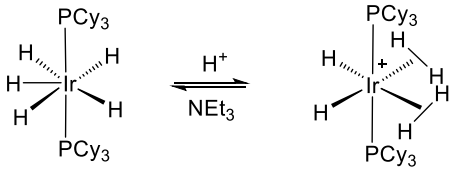
1.9.1 Dihydrogen sigma-complexes

Kubas and co-workers isolated the first stable and crystallographically characterised sigma-complex, $[W(\eta^2\text{-}H_2)(CO)_3(P^{i}Pr_3)_2]$ (**i-20**) in 1983 by the reversible addition of hydrogen to $[W(CO)_3(P^{i}Pr_3)_2]$ (**i-19**) (Scheme 1.9).[68]



i-19 **i-20**

Scheme 1.9 Formation of $[W(\eta^2\text{-}H_2)(CO)_3(P^{i}Pr_3)_2]$ (**i-20**).



i-21 **i-22**

Scheme 1.10 Formation of $[Ir(H)_2(\eta^2\text{-}H_2)_2(PCy_3)_2][PhC(SO_2CF_3)_2]$. $[PhC(SO_2CF_3)_2]^-$ anion is not shown.

Soon after, Crabtree and co-workers reported the first *bis*-dihydrogen complex, $[Ir(H)_2(\eta^2\text{-}H_2)_2(PCy_3)_2][PhC(SO_2CF_3)_2]$ (**i-22**) in 1985 by reversible protonation of $[IrH_5(PCy_3)_2]$ (**i-21**) (Scheme 1.10).[69] In the same year, Chaudret and Poiblanc reported a ruthenium polyhydride complex $[RuH_6(PCy_3)_2]$,[70] which three years later, was specified as *bis*-dihydrogen sigma-complex $[Ru(H)_2(\eta^2\text{-}H_2)_2(PCy_3)_2]$.[71] The complex was crystallographically characterised in 2000 by Sabo-Etienne and co-workers.[72] Its rhodium analogue, $[Rh(H)_2(\eta^2\text{-}H_2)_2(PCy_3)_2][BAr^F{}_4]$ was reported by Weller and co-workers in 2005 by the hydrogenation of $[Rh(PCy_3)_2(NBD)][BAr^F{}_4]$.[73] The Sabo-Etienne group has also reported the synthesis and neutron structure of $[Ru(H)_2(\eta^2\text{-}H_2)_2(PCyp_3)_2]$.[74] Many other examples of dihydrogen sigma-complexes are now known.[75-77]

Bonding in dihydrogen sigma-complexes has been studied in detail.[4, 76-78] The interaction of the H−H single bond with the metal makes a three centre-two electron bond. The H−H σ orbital donates electrons to an empty d orbital of the metal forming a σ bond and the filled d orbital of the metal backdonates to the H−H σ* orbital forming a π bond. This is analogous to the Dewar-Chatt-Duncanson model for olefin coordination (Figure 1.9).[79]

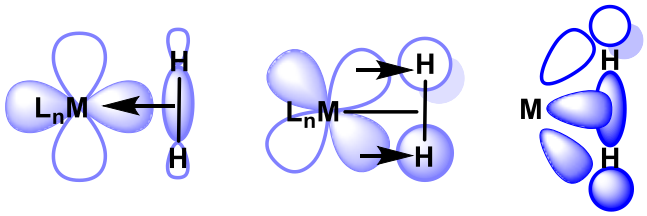


Figure 1.9 Bonding in a sigma-complex. Bonding model for dihydrogen coordination is on the right.

Backbonding to the E−H σ* orbital is crucial in the bonding of sigma-complexes. The greater the extent of backdonation the more the E−H bond is weakened and lead to the oxidative cleavage product (Figure 1.10).[80]

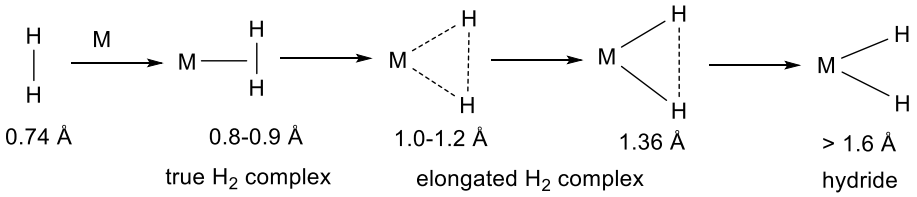


Figure 1.10 Elongation and breakage of H−H bond by increased back donation from the metal.

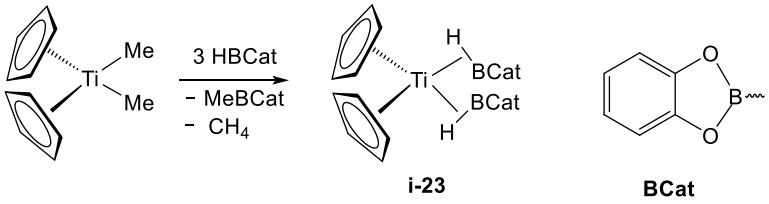
The extent of backdonation / oxidative cleavage can be dependent on nature of metals, ligands and overall charge. Dihydrogen activation or oxidative cleavage is more favoured by third row metal, strongly donating ligands and neutral charge.[80]

The characterisation of a dihydrogen sigma-complex by NMR spectroscopy or X-ray diffraction is challenging. Due to the very low electron density of the hydrogen atom, its scattering by X-rays is very weak, making the location of hydrogen unreliable by single crystal X-ray diffraction techniques. Generally, neutron diffraction techniques are used to locate the position of hydrogen atoms with more accuracy, as neutrons interact with the nuclei of atoms, unlike X-ray which interacts with the electrons. However, neutron diffraction is expensive, geographically dependent and requires large crystals. Another important technique to characterise dihydrogen sigma-complexes is based on T_1 relaxation time, using ^{1}H NMR spectroscopy. T_1 relaxation, also known as spin-lattice

relaxation, corresponds to the process of redistribution of the population of nuclear spin states in order to reach thermal equilibrium states. Shorter T_1 relaxation times mean the nuclear magnetisation can be recovered more quickly, which is dependent on the rates that nearby nuclei are relaxing. This interaction diminishes rapidly (r^{-6}) with internuclear separation 'r'.[81] The internuclear separation between hydrogen nuclei is different for a dihydrogen ligand than two hydrides, giving rise to two different range of values for T_1 relaxation times. Generally, a relaxation times of T_1 < 50 ms (at 400 MHz) are suggestive of dihydrogen ligands, whereas relaxation times of T_1 > 150 ms (at 400 MHz) are suggestive of the presence of classical hydride ligands.[69, 81]

1.9.2 Borane sigma-complexes

Borane sigma-complexes have long been considered as an intermediate during B−H oxidative cleavage of boranes, a process which can be implicated in catalytic hydroboration and dehydrogenative borylation of alkenes.[82-84] The first sigma borane-complex, $ZnCl_2{\cdot}B_2H_4{\cdot}2P(CH_3)$ was reported by Shimoi in 1984.[85] Hartwig and co-workers in 1996 reported another sigma-complex, $TiCp_2(HBcat)_2$ (**i-23**).[86] Reaction of three to five equivalents of catechol-borane (HB cat) with dimethyl titonacene at −35°C resulted in the formation of $TiCp_2(HBcat)_2$ (**i-23**) along with the evolution of methane and formation of B-(methylcatechol)-borane (Scheme 1.11). The formed sigma-complex was extremely temperature sensitive in solution and reactive towards both THF and dichloromethane at low temperature.



Scheme 1.11 Formation of $TiCp_2(HBcat)_2$.

The bonding in $TiCp_2(HBcat)_2$ shows that ligands are bound in an η^2 side-on coordination mode. Sigma-donation occurs from the sigma B−H bond to the vacant d orbital of the metal. Backdonation into the σ* B−H antibonding orbital is prevented due to its high energy and the backdonation occurs into the vacant p-orbital of boron resulting in the side-on coordination.[86] This is different from Shimoi-type borane (BH_3·L, L = amine or phosphine) complexes in which the M−H−B linkage occurs mainly due to the sigma-donation of B−H bond to the metal with negligible backdonation into the σ* B−H antibonding orbital.[87] Shimoi-type amine-borane complexes are discussed in detail in Section 1.17 of this Chapter.

Hartwig and co-workers further reported the sigma-borane complexes of Mn and Re (**i-24** - **i-28**) as shown in Figure 1.11.[88] Garcia and co-workers reported the formation of Ni(0) sigma-complex, [(dcype)Ni($HBEt_2$)] (**i-29**) by the reaction of [(dcype)NiH]$_2$ with an $LiHBEt_3/BEt_3$ mixture (Figure 1.11).[89] Further to this, Sabo-Etienne and co-workers reported ruthenium-borane complexes (**i-30** and **i-31**) by the reaction of HBpin or HBcat with $[RuH_2(\eta^2\text{-}H_2)_2(PCy_3)_2]$ (Scheme 1.12).[90]

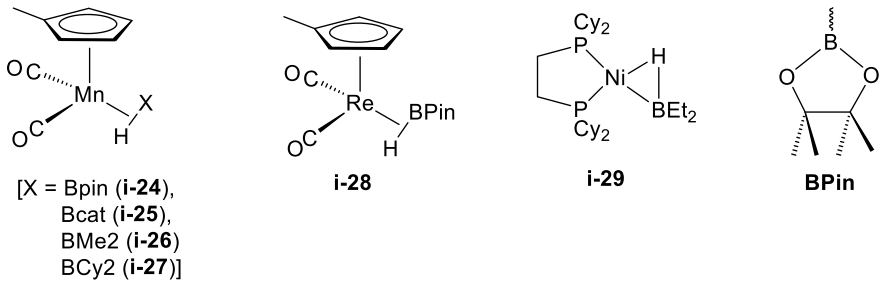
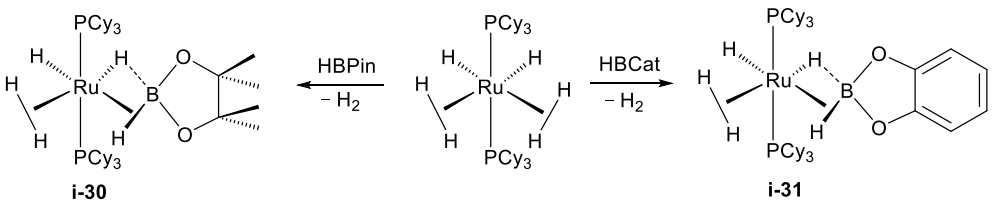


Fig 1.11 Borane sigma-complexes of transition metals.



Scheme 1.12 Reactivity of $[RuH_2(\eta^2\text{-}H_2)_2(PCy_3)_2]$ with HBPin and HBCat.

1.10 Amine-boranes

The B−N fragment is classical isostere (having same number of valence electrons) with C−C fragment (Figure 1.12). Replacement of a carbon-carbon bond with a boron-nitrogen bond has not only offered a versatile strategy to expand the structural diversity of chemical space but also developed materials of interesting properties because of the polar nature of B−N bond compared to the non-polar nature of C−C bond.[91]

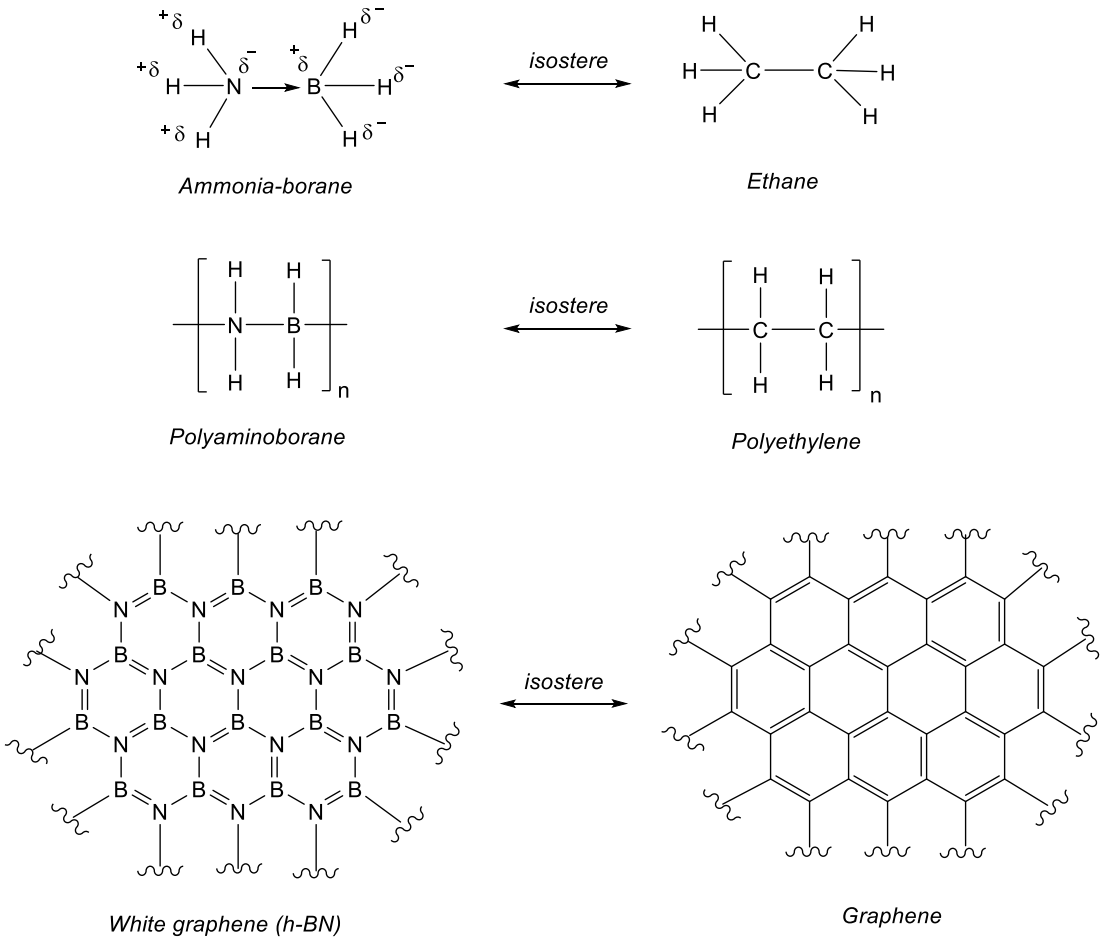


Figure 1.12 Isostere relationship between B−N compounds with the corresponding C−C compounds relevant to this thesis.

Amine-boranes (for example $H_3B{\cdot}NH_3$, ammonia borane) are Lewis acid - Lewis base adducts containing protic N−H and hydridic B−H bonds.[95] The resulting intra or inter B−H···H−N dihydrogen interaction can assist in dihydrogen loss from amine-boranes

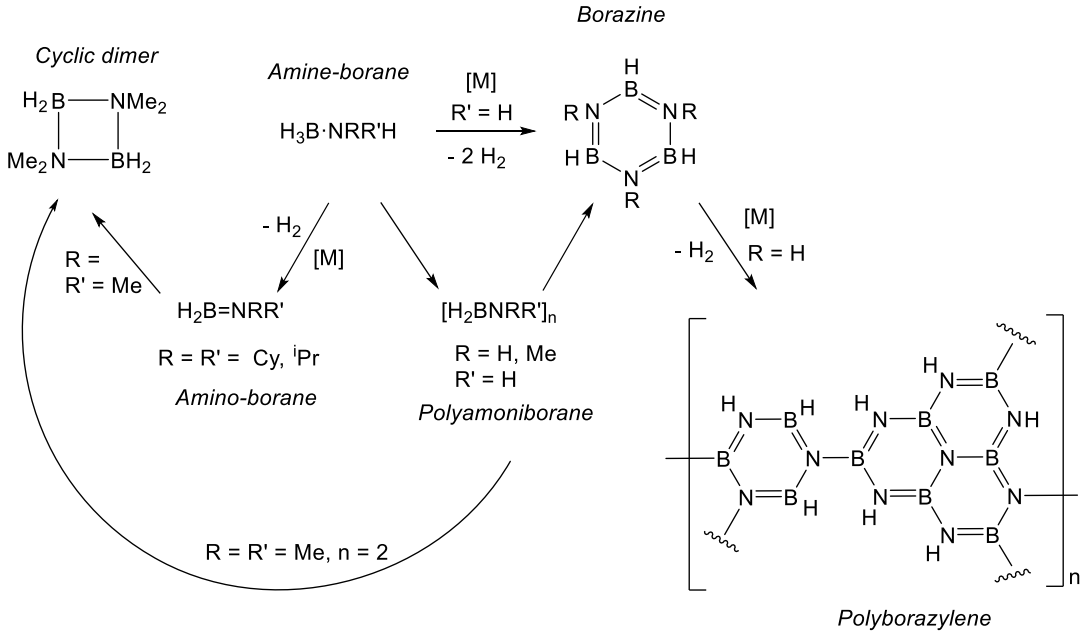
making the dehydrogenation process more feasible compared to its alkane analogues.[92] When dehydrogenation of amine-boranes is accompanied by a simultaneous formation of new B−N bond, the process is called dehydrocoupling. Dehydrocoupling of amine-boranes has attracted significant interest in past. One of the main applications that has caused this attention is its potential to be used as chemical hydrogen storage materials. The parent amine-borane, $H_3B{\cdot}NH_3$, has gravimetric hydrogen density of 19.6 wt% and has been intensively studied for chemical hydrogen storage materials.[93, 94] Dehydrocoupling of amine-boranes (for example $H_3B{\cdot}NMeH_2$) also results in the formation of new type of polymers isoelectronic with the societally ubiquitous polyolefins.[95, 96] Such polymers may have different physical properties due to polar B−N bonds or B−H···H−N dihydrogen interactions. Further to this, $H_3B{\cdot}NH_3$ has recently been used to prepare hexagonal boron nitride (hBN) films which is B−N analogue of graphene, also known as white graphene.[97] White graphene has potential applications in layered nanoscale circuits, lubricants and cosmetics.[98] $H_3B{\cdot}NH_3$ has also been used as precursor to piezoelectric materials and ceramics.[99] Thus, the dehydrocoupling of amine-boranes is of great importance to the development of new types of materials and the current hydrogen economy.

1.11 General pathway for the dehydrocoupling of amine-boranes

A general pathway for the dehydrocoupling of amine-boranes is shown in Scheme 1.13. Secondary amine-boranes of $H_3B{\cdot}NR_2H$ type can release only one equivalent of H_2 gas. $H_3B{\cdot}NR_2H$ with bulky substituents such as R = Cy or ^{i}Pr, can dehydrogenate but cannot dehydrocouple due to the steric bulk at nitrogen centre resulting in the formation of *amino-borane* ($H_2B{=}NR_2$) as the final dehydrogenation product. Less bulky amine-borane, $H_3B{\cdot}NMe_2H$ can dehydrocouple to form the cyclic dimer $[H_2BNMe_2]_2$ via the amino-borane $H_2B{=}NMe_2$ intermediate. Alcaraz and co-workers have reported that the amino-borane with the bulky substituents $H_2B{=}NR_2$, where R = Cy, ^{i}Pr are stable and can be synthesized by the thermal dehydrogenation of the corresponding amine-boranes,[100] while $H_2B{=}NRH$

having less bulky substituents (R = Me, H) are unstable and have not been isolated yet at room temperature.

The primary amine-borane, $H_3B{\cdot}NMeH_2$ can release one equivalent of H_2 and dehydrocouple to form polyamino-borane $[H_2BNMeH]_n$. $H_3B{\cdot}NRH_2$ (R = H, Me, ^nBu) can also dehydrocouple to form borazine releasing two equivalents of H_2. Dehydrocoupling of $H_3B{\cdot}NH_3$ is particularly interesting as it can release up to more than two equivalents of H_2 resulting in the formation of polyamino-borane $[H_2BNH_2]_n$ (1 equivalent H_2), borazine (2 equivalents H_2) or polyborazylene (> 2 equivalents H_2). Polyamino-borane $[H_2BNH_2]_n$, is insoluble in organic solvents which makes its characterisation difficult and only solid state techniques like IR or solid state NMR spectroscopy can be applied for its characterisation. Formation of a mixture of products, especially insoluble and poorly defined oligomers, upon dehydrocoupling makes mechanistic and kinetics study difficult for $H_3B{\cdot}NH_3$. Products / intermediates formed from the dehydrocoupling of $H_3B{\cdot}NMe_2H$ are soluble and well defined making the mechanism relatively easy to probe. Thus, $H_3B{\cdot}NMe_2H$ is used as model to study the mechanism of dehydrocoupling of amine-boranes and has been extensively studied as discussed later in this Chapter.



Scheme 1.13 General pathways for the dehydrocoupling of amine-boranes, [M] = Metal catalyst.

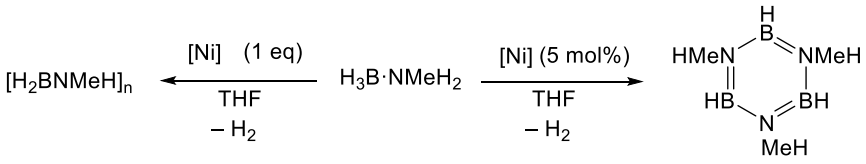
1.12 Metal catalysed dehydrocoupling of amine-boranes

Although amine-boranes can be dehydrogenated thermally and metal free dehydrogenation of amine-boranes has been reported, [100-102] the use of metal catalysts for the dehydrocoupling can allow the control of kinetics and the final product distributions.[94] The first example of metal catalysed dehydrocoupling of an amine-borane was reported by Roberts and co-workers in 1989.[103] They used a colloidal Pd catalyst to dehydrogenate $H_3B{\cdot}NH^tBuMe$ to produce amino-borane $H_2B{=}N^tBuMe$, which was a volatile liquid at room temperature, but rapidly solidified on standing at room temperature to form the mixture of two isomeric dimers.[103] Since then there have been various reports on the metal catalysed dehydrocoupling of amine-boranes, some of which have been discussed here.[104]

1.13 Heterogenous catalysts for the dehydrocoupling of amine-boranes

Heterogeneous catalysts, because of easy and relatively inexpensive methods of separation of products from the catalysts, have been employed in the dehydrocoupling of

amine-boranes. Manners and co-workers, in 2001, reported the dehydrocoupling of $H_3B{\cdot}NMe_2H$ to form the cyclic dimer $[H_2BNMe_2]_2$ using a $[Rh(COD)(\mu\text{-}Cl)_2]$ precatalyst. Three years later, in 2004, the nature of the true catalyst was reported by the same group. TEM experiments, kinetic profiling and catalyst poisoning (by adding Hg) experiments all indicated towards the heterogeneous nature of the catalyst.[105] Manners and co-workers also reported dehydrocoupling of $H_3B{\cdot}NMe_2H$ and $H_3B{\cdot}NMeH_2$ using skeletal metal catalysts of first row transition metals Ni, Cu and Fe.[106] The skeletal catalyst of Fe was found to be completely inactive towards amine-borane dehydrocoupling at temperature up to 50°C and Cu was found to be very slow (5% conversion of $H_3B{\cdot}NMe_2H$ in 16 h). However, skeletal Ni was found to be more active and at 5 mol% catalytic loading, showed complete dehydrocoupling of $H_3B{\cdot}NMe_2H$ in 6 h at 20°C. Under the same catalytic conditions (5 mol%), $H_3B{\cdot}NMeH_2$, dehydrocoupled to form cyclic triborazane, however, when stoichiometric quantity of Ni was used, $H_3B{\cdot}NMeH_2$ dehydrocoupled to form polyamino-borane, $[BH_2NMeH]_n$ (M_w = 78,000 Da, Đ = 1.52) (Scheme1.14).[106]



Scheme 1.14 Dehydrocoupling of $H_3B{\cdot}NMeH_2$ using skeletal Ni.

Morris and co-workers, in 2013 reported the first example of iron-nanoparticles catalysed dehydrocoupling of $H_3B{\cdot}NH_3$ in a non-protic solvent. The iron precatalyst based on $[Fe(NCMe)_2(PNNP)][BF_4]_2$ / KO^tBu [PNNP = $(PPh_2C_6H_4CH{=}NCH_2)_2$] dehydrogenated $H_3B{\cdot}NH_3$ with a turnover frequency (TOF) of approximately 2400 h^{-1}, yielding a mixture of products: borazine, polyborazylene, and B−N oligomers or partially cross-linked polyborazylene, as well as unreacted $H_3B{\cdot}NH_3$. The catalytic activity of iron-complexes was compared with those generated *in situ* using commercially available Fe^{2+} sources and

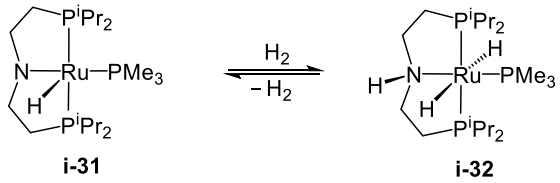
substoichiometric amounts of the PNNP ligand. They showed that catalytic activity remained the same on changing the ligand concentration suggesting that the active species is likely to be zerovalent iron nanoparticles. This experiment together with TEM images suggest that the highly active catalyst is heterogeneous in nature.[107]

1.14 Homogeneous catalysts for the dehydrocoupling of amine-boranes

Although heterogeneous catalysts can offer fast dehydrogenation of amine-boranes and easy catalyst separation, the nature of the active catalytic species is often unclear due to poorly defined catalytic sites.[25] On the other hand, active sites in homogeneous catalysts are well-defined and can be tuned by modification of metal or ligand and therefore have been extensively studied. Dehydrogenation by homogeneous catalysts operates via two mechanisms: Outer sphere or inner sphere mechanisms.

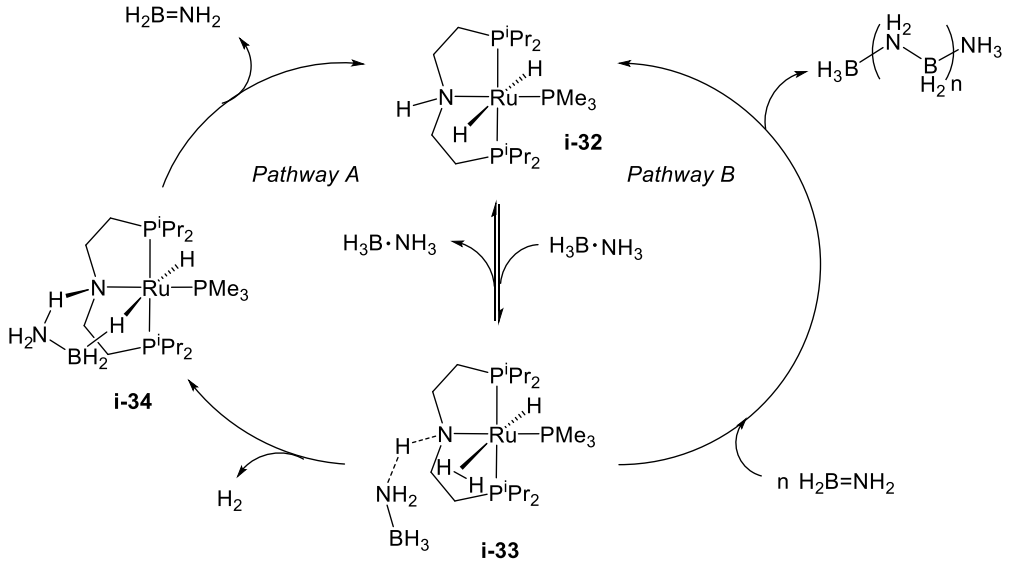
1.14.1 Outer sphere mechanism based on metal-ligand cooperativity

An outer sphere mechanism employs the involvement of ligands attached to the metal centre for the dehydrogenation process, usually via metal-ligand cooperativity. In 2009 Schneider reported a very fast ruthenium based bifunctional catalyst, [Ru(PNP)(H)(PMe_3)] (PNP = $N(CH_2CH_2P^iPr_2)_2$) (**i-31,** TOF ~12 000 h^{-1} at 0.1 mol%) for the dehydrocoupling of $H_3B{\cdot}NH_3$ to form $[H_2BNH_2]_n$.[108] Borazine was also formed in a small quantity. The KIE (Kinetic Isotopic Effect: 2.1 for $D_3B{\cdot}NH_3$, 5.2 for $H_3B{\cdot}ND_3$ and 8.1 for $D_3B{\cdot}ND_3$) studies suggested that dehydrogenation takes place via a concerted mechanism in which the N−H and B−H bond cleavages both are involved in the rate determining steps. $H_3B{\cdot}NMe_2H$ was also rapidly dehydrocoupled by **i-31** to form $[H_2BNMe_2]_2$.[109] Complex **i-31** showed reversible addition of H_2 to form *trans*-[Ru(PNP^H)$(H)_2$(PMe_3)] (PNP^H = $HN(CH_2CH_2P^iPr_2)_2$) (**i-32**) which was suggested to be the resting state during the dehydrocoupling of $H_3B{\cdot}NMe_2H$ (Scheme 1.15).



Scheme 1.15 Ruthenium bifunctional catalyst and reversible addition of H_2.

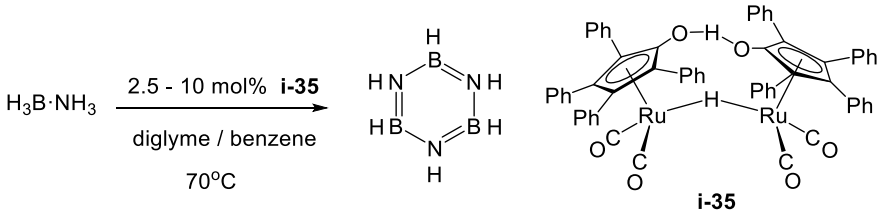
A detailed mechanistic study was reported in 2013 by the same group on the basis of DFT calculations and spectroscopic experiments.[110] Two mechanistically connected catalytic cycles have been proposed which account for both metal-mediated dehydrogenation of $H_3B{\cdot}NH_3$ to $H_2B{=}NH_2$ and catalyzed polymer chain growth by formal insertion of $H_2B{=}NH_2$ into a $H{-}NH_2{\cdot}BH_3$ bond (Scheme 1.16). The mechanism involves (i) dehydrogenation of $H_3B{\cdot}NH_3$, via initial N−H activation forming complex **i-33** and then release of $H_2B{=}NH_2$ via **i-34** (Pathway A) and (ii) oligomerisation by catalytic insertion of $H_2B{=}NH_2$ into the N–H bond of the substrate **i-33** (Pathway B).



Scheme 1.16 Dehydrogenation and dehydrocoupling pathways proposed by Schneider and co-workers.

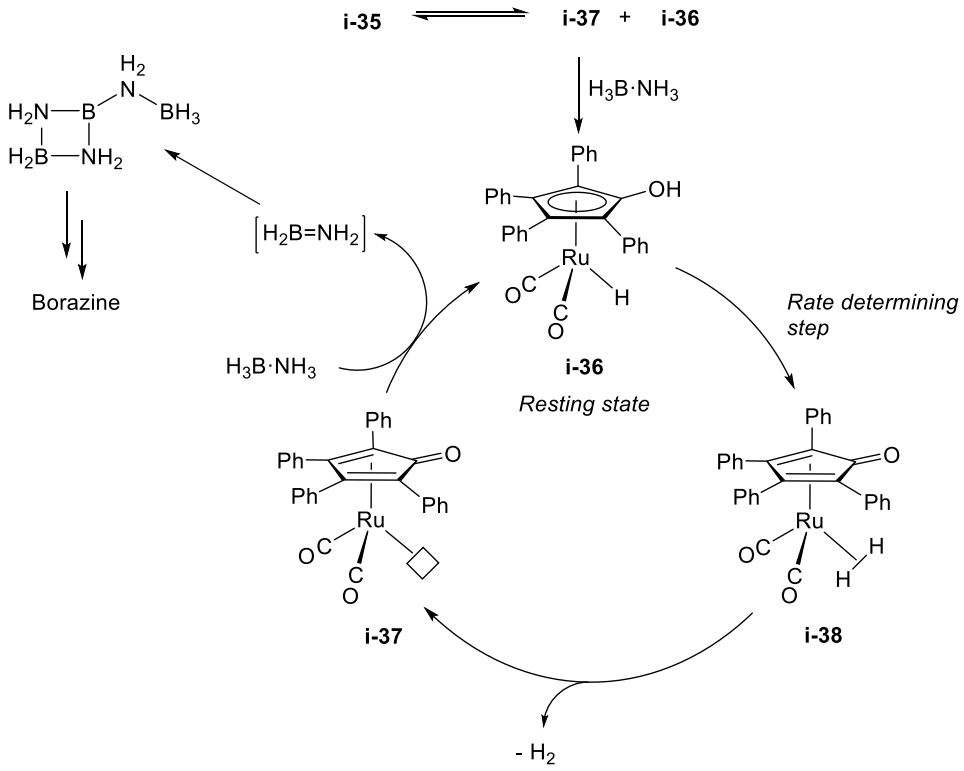
Williams and co-workers, in 2010, reported the dehydrogenation of $H_3B{\cdot}NH_3$ using Shvo's cyclopentadienone-ligated ruthenium catalyst.[111] Shvo's catalyst **i-35** was found to be an

efficient catalyst for the dehydrocoupling of $H_3B{\cdot}NH_3$ forming borazine and liberating 2 equivalents of H_2 (Scheme 1.17).



Scheme 1.17 Dehydrocoupling of $H_3B{\cdot}NH_3$ by Shvo's catalyst, **i-35**.

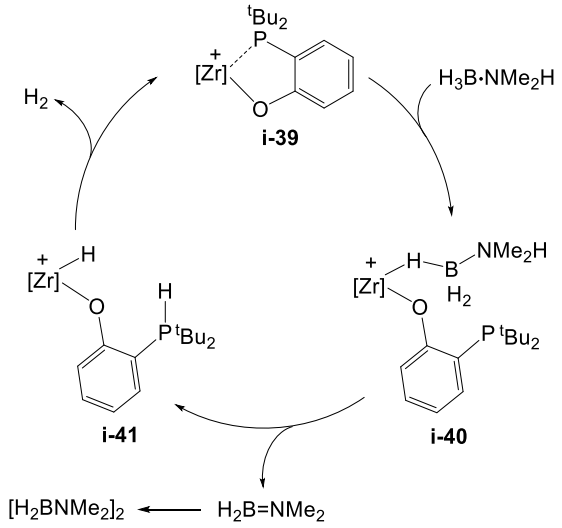
It has been suggested that the coordinative saturation of complex **i-35** forces the dehydrogenation to occur through an outer sphere mechanism and also prevents binding of $H_2B{=}NH_2$ to metal centre, thus enabling further dehydrogenation of resulting intermediates. According to the mechanism the first step is the dissociation of complex **i-35** to form complexes **i-36** and **i-37**. This step has been suggested as a possible reason for the induction period observed in the kinetic profile. Complex **i-37** gets reduced by $H_3B{\cdot}NH_3$ to form **i-36** which is proposed as the resting state of the catalysis. Dehydrogenation of $H_3B{\cdot}NH_3$ leads to the formation of a dihydrogen complex, **i-38** which is the rate determining step. Complex **i-38** eliminates dihydrogen forming **i-37** which dehydrogenates $H_3B{\cdot}NH_3$ regenerating the resting state **i-36** (Scheme 1.18).[111]



Scheme 1.18 Proposed mechanism for the catalytic dehydrocoupling of $H_3B{\cdot}NH_3$ by Shvo's catalyst.

A kinetic profile for the consumption of $H_3B{\cdot}NH_3$ was generated by plotting the concentration of $H_3B{\cdot}NH_3$ against time which reveal that the dehydrogenation takes place in three regimes: (i) Brief initiation period which shows zero order dependence on $[H_3B{\cdot}NH_3]$ and a first order dependence on **i-35**. This suggests that the dissociation of the dimer is the rate limiting in the initiation step. (ii) Fast linear regime showing zero order dependence on $[H_3B{\cdot}NH_3]$ and a first order dependence on **i-35** consistent with **i-36** being the resting state and $H_3B{\cdot}NH_3$ not being involved in the rate determination step. (iii) Slower regime showing first order decay of $H_3B{\cdot}NH_3$. A dimer-monomer equilibrium has also been observed during catalytic dehydrogenation of cyclic amine-boranes as discussed in Chapter Five.

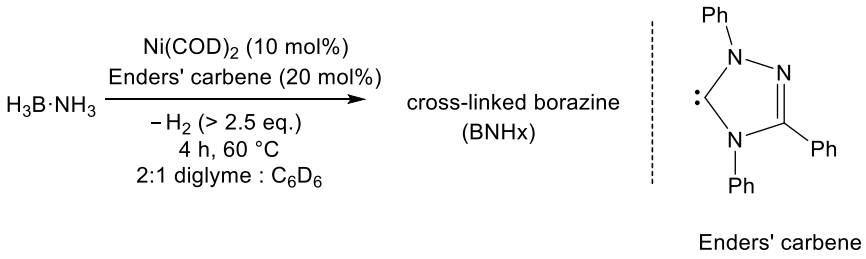
An outer sphere mechanism for the dehydrocoupling of $H_3B{\cdot}NMe_2H$ using β-diketiminato arene-substituted Ru(II) complexes has also been reported by Phillips and co-workers.[112] Wass and co-workers have extended the concept of Frustrated Lewis Pairs[113] from main group to transition metals by reporting the synthesis of $[Cp_2ZrOC_6H_4P^tBu_2][B(C_6F_5)_4]$ (**i-39**) which can activate small molecules such as H_2, CO_2, alkenes, alkynes, THF and alkyl halides.[114] Complex **i-39** has also been found to catalyse the dehydrocoupling of $H_3B{\cdot}NMe_2H$ (1 mol% **i-39**, TOF ~600 h^{-1}) to ultimately produce the cyclic dimer $[BH_2NMe_2]_2$. An outer sphere mechanism has been proposed according to which the first step is the sigma-coordination of $H_3B{\cdot}NMe_2H$ with the Zr(IV) centre (**i-39**) to form **i-40**, which then undergoes a ligand assisted dehydrogenation process via **i-41** (Scheme 1.19). The reaction using $[Cp_2ZrO^tBu][B(C_6F_5)_4]$ did not dehydrogenate $H_3B{\cdot}NMe_2H$, showing the importance of phosphine group supporting an outer sphere mechanism.[115]



Scheme 1.19 Suggested outer sphere mechanism for Zr(IV) catalysed dehydrocoupling of $H_3B{\cdot}NMe_2H$. [Zr] = Cp_2Zr.

Baker and co-workers reported $Ni(NHC)_2$ based system for the catalytic dehydrogenation of $H_3B{\cdot}NH_3$ to form B−N cross-linked borazine releasing more than 2.5 equivalents of H_2 gas. Dehydrocoupling showed a first order kinetics, the highest rate constant (64.6 x 10^{-3}

min^{-1}) was observed with Enders' carbene (1,3,4-triphenyl-4,5-dihydro-1H-1,2,4-triazol-5-ylidene) (Scheme 1.20).[116]

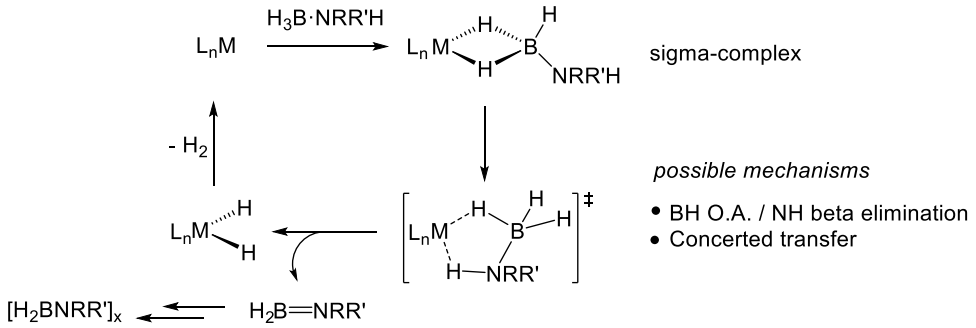


Scheme 1.20 Dehydrocoupling of $H_3B{\cdot}NH_3$ using Baker's $Ni(NHC)_2$ catalyst.

Later, Hall reported DFT calculations on this system and showed that the dehydrogenation takes place through an outer sphere mechanism which involves proton transfer from nitrogen to the carbene instead of B−H or N−H bond activations on metal centres.

1.14.2 Inner sphere mechanism for the dehydrocoupling of amine-boranes

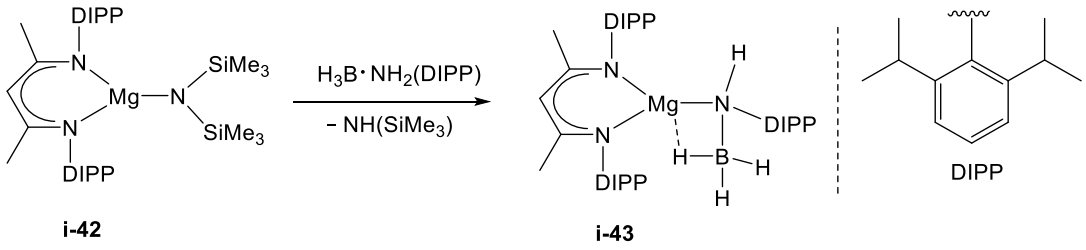
Inner sphere mechanism involves initial coordination of amine-borane to the metal centre, followed by dehydrogenation without any co-operative ligand assistance (Scheme 1.21). Various inner sphere mechanisms have been proposed for the dehydrogenation of amine-boranes which involve: (i) oxidative addition of NH then BH transfer (ii) concerted NH/BH activation at the metal center or (iii) oxidative addition of the BH bond followed by NH elimination. These have been discussed in depth later in this chapter (Section 1.15 and 1.16).



Scheme 1.21 General inner sphere mechanism for the dehydrogenation of amine-boranes.

1.15 Main group catalysed dehydrocoupling of amine-boranes

Harder and co-workers, in 2009, reported a synthetic route to the formation of a magnesium-amidoborane complex (**i-43**) and its role in the catalytic conversion of $H_3B{\cdot}NRH_2$ to $HB(NRH)_2$ (R = 2,6-diisopropylphenyl). Addition of (DIPP-nacnac)$MgN(SiMe_3)_2$ (**i-42**) to $H_3B{\cdot}NRH_2$ resulted in the immediate dehydrogenation and formation of $HB(NRH)_2$ along with the by-product B_2H_6. A magnesium-amidoborane complex (**i-43**) has been proposed to be the active catalyst (Scheme 1.22).[117]



i-42 **i-43**

Scheme 1.22 Formation of active catalyst **i-51** from (DIPP-nacnac)$MgN(SiMe_3)_2$ (**i-50**).

Hill and co-workers have recently reported group two complexes of Ca (**i-44**) and Mg (**i-45** and **i-46**, Figure 1.13) for the dehydrocoupling of $H_3B{\cdot}NMe_2H$ to produce $[H_2BNMe_2]_2$.[118] Formation of $H_2B{=}NMe_2$ and $HB(NMe_2)_2$ are also observed during dehydrocoupling. Addition of four equivalents of $H_3B{\cdot}NMe_2H$ to di-n-butyl magnesium produced a magnesium complex i**-47** in which two $[H_3BNMe_2BH_2NMe_2]^-$ anions are bound to metal through Mg···N and Mg···HB interactions. Heating this complex results in the formation of

$[H_2BNMe_2]_2$, which has been proposed to occur via δ-hydride elimination process along with the formation of a magnesium hydrido species.

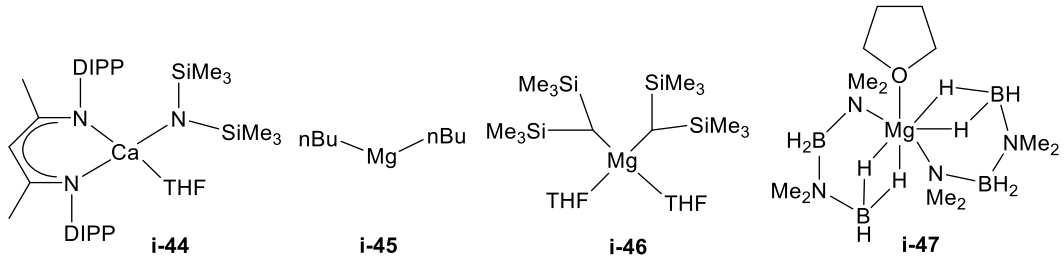
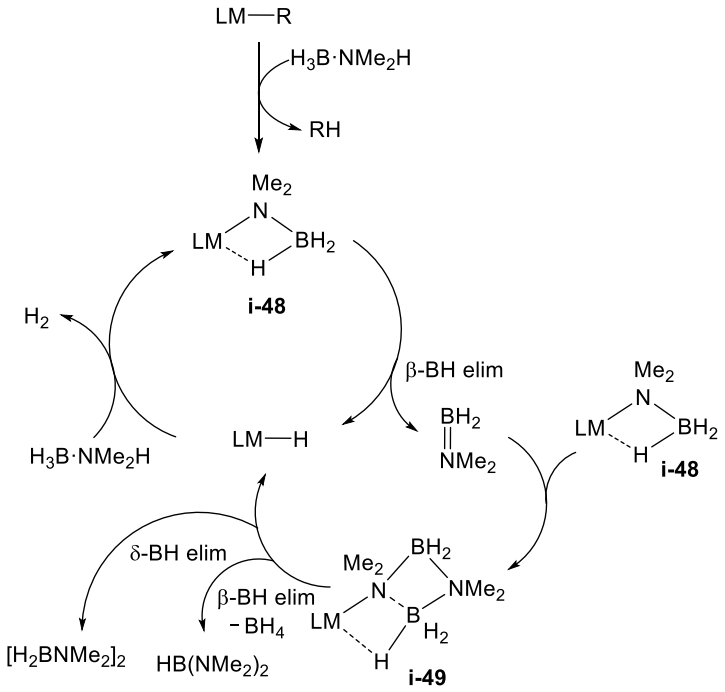


Figure 1.13 Ca and Mg complexes (**i-44** - **i-46**) used by Hill for the dehydrogenation of $H_3B{\cdot}NMe_2H$.

Based on these observations a mechanism has been proposed as outlined in Scheme 1.23. The first step involves the N−H activation and the concomitant protonation of ligand to form **i-48**. Complex **i-48** can undergo β-B−H elimination to form $H_2B{=}NMe_2$, which inserts into **i-48** to form the observed amido species **i-49**. **i-49** can undergo, either β-B−H elimination to yield the observed $HB(NMe_2)_2$, or δ-B−H elimination to form $[H_2BNMe_2]_2$.

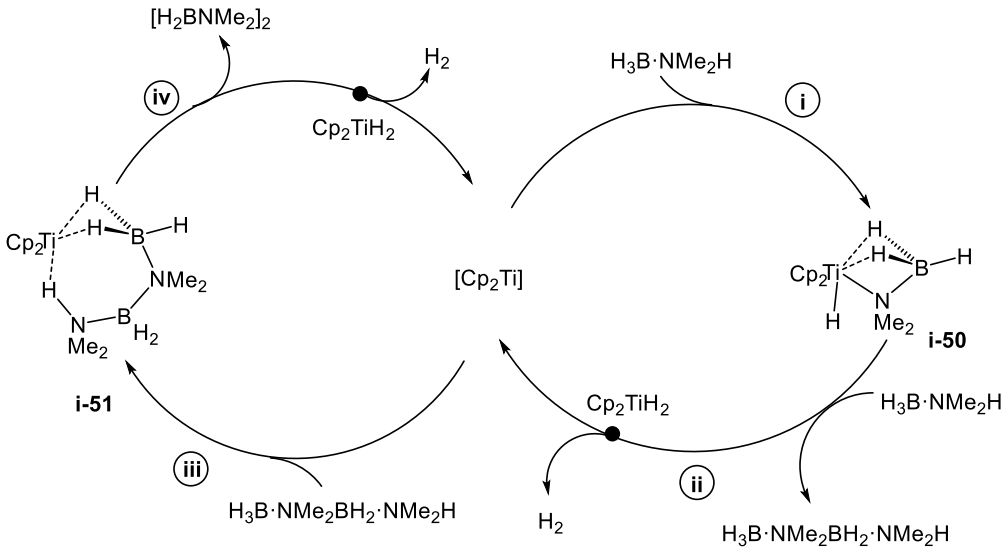


Scheme 1.23 Proposed mechanism for the dehydrocoupling of $H_3B{\cdot}NMe_2H$ by group II catalysts.

Many other main group catalysts based on Al,[119, 120] Mg[117, 121, 122] Ca,[121-123] Y,[124] Sc,[124] La[125] and Sn [126] have been reported for the dehydrogenation of amine-boranes.

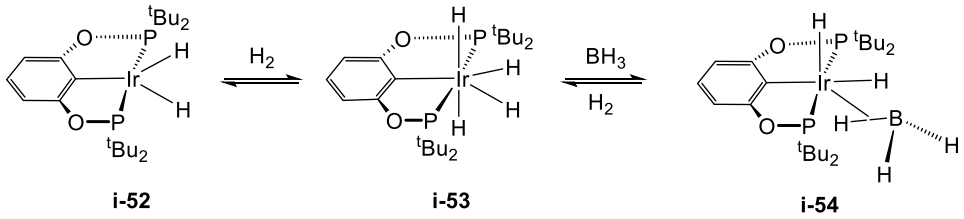
1.16 Transition metal catalysed dehydrocoupling of amine-boranes

The application of transition metals for the dehydrocoupling of amine-boranes has probably been the most attractive area in amine-borane dehydrogenation chemistry in last decade. In 2006, Manners reported the first example of well-defined homogenous catalyst, [Cp_2Ti], *in situ* generated from Cp_2TiCl_2 / ^nBuLi, for the dehydrocoupling of amine-boranes.[127] A 2 mol% catalytic loading of [Cp_2Ti] afforded complete conversion of $H_3B{\cdot}NMe_2H$ to $[H_2BNMe_2]_2$ in 4 h. A detailed kinetics and mechanism study on this system was reported by Manners, Lloyd-Jones and co-workers in 2010 where the linear dimer (diborazane), $H_3B{\cdot}NMe_2BH_2{\cdot}NMe_2H$ was identified as an intermediate in the formation of the cyclic dimer $[H_2BNMe_2]_2$.[128] A two cycle, four step mechanism as outlined in Scheme 1.24 was proposed which involves: (i) Coordination of $H_3B{\cdot}NMe_2H$ to [Cp_2Ti] followed by N−H activation to form an amidoborane complex [$Cp_2Ti(H)(NMe_2{\cdot}BH_3)$], **i-50**. (ii) Reaction of **i-50** with the second equivalent of $H_3B{\cdot}NMe_2H$ results in the formation of $H_3B{\cdot}NMe_2BH_2{\cdot}NMe_2H$ and Cp_2TiH_2, which upon reductive elimination forms Cp_2Ti. (iii) The thus formed $H_3B{\cdot}NMe_2BH_2{\cdot}NMe_2H$ reacts with Cp_2Ti to form a sigma complex **i-51**. Sigma-complexes of $H_3B{\cdot}NMe_2BH_2{\cdot}NMe_2H$ with Rh(I) and Rh(III), similar to **i-51** have also been reported by the Weller group.[129, 130] (iv) **i-51** undergoes on-metal dehydrocyclisation to form $[H_2BNMe_2]_2$ and [Cp_2Ti]. Addition of independently synthesized $H_3B{\cdot}NMe_2BH_2{\cdot}NMe_2H$ to [Cp_2Ti] resulted in the complete formation of $[H_2BNMe_2]_2$ with the negligible amount of $H_2B{=}NMe_2$ suggesting that $H_3B{\cdot}NMe_2BH_2{\cdot}NMe_2H$ and not $H_2B{=}NMe_2$ is the sole intermediate in the formation of $[H_2BNMe_2]_2$. This is contrary to the mechanism proposed by Luo and Ohno which proposed off metal dimerisation of $H_2B{=}NMe_2$ to form $[H_2BNMe_2]_2$ using DFT calculations.[131]



Scheme 1.24 Proposed mechanism for the dehydrocoupling of $H_3B{\cdot}NMe_2H$ by Manners $[Cp_2Ti]$ catalyst.

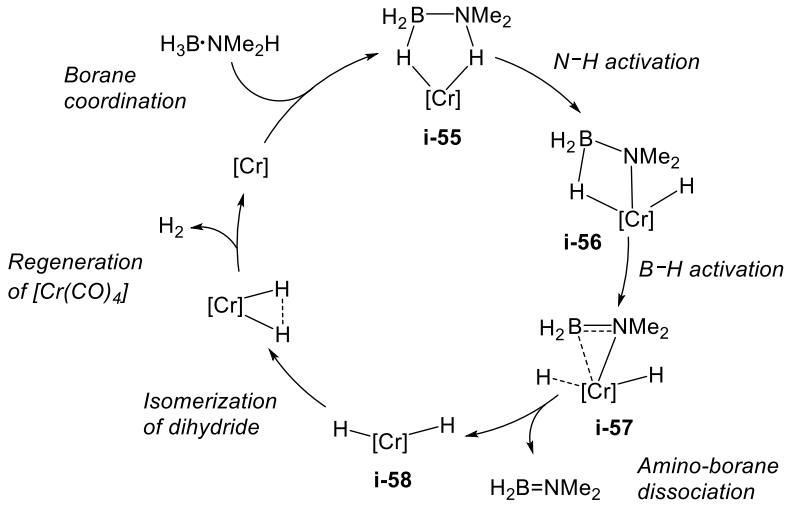
Goldberg and Heinkey in the same year of 2006 reported Ir(^{t}BuPOCOP^{t}Bu) (^{t}BuPOCOP^{t}Bu = κ^3-PCP-1,3-{OP^{t}Bu$_2$}$_2$C$_6$H$_3$) catalyst, **i-52** (Brookhart's catalyst) for the catalytic dehydrogenation of $H_3B{\cdot}NH_3$.[132] The Ir(^{t}BuPOCOP^{t}Bu) catalyst gave an unprecedented dehydrogenation rate (TOF of 1500 h^{-1}, 1 mol% **i-52**) and released one equivalent of H_2 gas. The product was proposed to be the cyclic pentamer $[H_2BNH_2]_5$ on the basis of IR spectroscopy and powder X-ray diffraction,[132] which was later reassigned by Manners and co-workers as $[H_2BNH_2]_n$ (n ~20) on the basis of the solid-state NMR spectroscopy.[133] Monitoring the catalytic dehydrogenation through *in situ* NMR spectroscopy showed the initial formation of a tetrahydride complex **i-53** which was later converted to a dormant species, Ir(^{t}BuPOCOP^{t}Bu)H_2(BH_3) **i-54**.[134] **i-54** can also be transformed back to form the catalytically active species, **i-53** on addition of H_2 (Scheme 1.25). Heinekey later, using variable temperature NMR spectroscopy and neutron diffraction data showed that **i-54** exhibits η^1 binding of BH_3 with H_2Ir(^{t}BuPOCOP^{t}Bu).[134]



i-52 **i-53** **i-54**

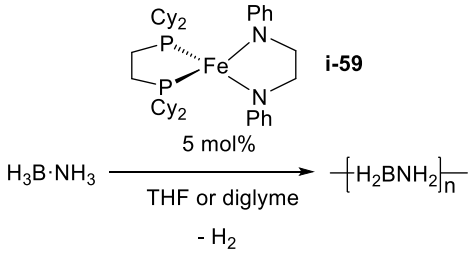
Scheme 1.25 Organometallic species involved in the dehydrocoupling of $H_3B{\cdot}NH_3$ using Brookhart's Ir(^{t}BuPOCOP^{t}Bu) catalyst.

Shimoi and co-workers, in 2009 reported $[M(CO)_6]$ (M = Cr, Mo, W) type catalysts for the dehydrocoupling of amine-boranes upon photoirradiation.[135] Photoirradiation of a solution of $H_3B{\cdot}NMe_2H$ in the presence of $[M(CO)_6]$ (M = Cr, Mo, W) afforded the formation of $[H_2BNMe_2]_2$ while bulkier amine-boranes, $H_3B{\cdot}NR_2H$ produced amino-boranes, $H_2B{=}NR_2$ (R = ^{i}Pr and Cy). Dehydrocoupling of primary amine-boranes $H_3B{\cdot}NH_2R$ (R = Me, Et and ^{t}Bu) gave borazine $[BHNR]_3$. The reaction mechanism for the dehydrocoupling of amine-boranes was investigated by DFT calculations. A mechanism as shown in Scheme 1.26 was proposed in which the active catalyst is a 14-electron $[Cr(CO)_4]$ fragment. The first step is the formation of a chelate sigma-complex **i-55** which first undergoes an N−H activation step producing an amido-borane complex **i-56** and then a B−H activation step to produce **i-57**. Loss of $H_2B{=}NMe_2$ from **i-57** resulted in the formation of $[Cr(CO)_4(H)_2]$ (**i-58**) which upon reductive elimination of dihydrogen regenerates the active catalyst $[Cr(CO)_4]$.



Scheme 1.26 Shimoi's proposed mechanism for the dehydrocoupling of $H_3B{\cdot}NMe_2H$. [Cr] = $[Cr(CO)_4]$.

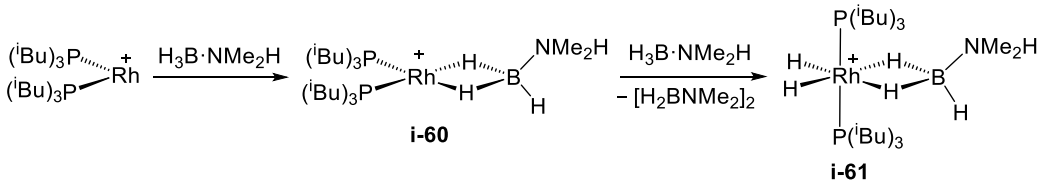
Baker and co-workers in 2012 reported on iron complex (such as **i-59**) catalysed dehydrocoupling of $H_3B{\cdot}NH_3$ to form $[H_2BNH_2]_n$ and $[NHBH]_n$, the product distribution was dependent on the ligands attached to metal centre. The most interesting result was obtained using the $[Fe(Cy_2PCH_2CH_2PCy_2)(NPhCH_2CH_2NPh)]$ (**i-59**) catalyst which selectively produced polyamino-borane $[H_2BNH_2]_n$ at 5 mol% loading (TOF ~80 h^{-1}) (Scheme 1.27).[136]



Scheme 1.27 Dehydrocoupling of $H_3B{\cdot}NH_3$ using Baker's iron catalyst.

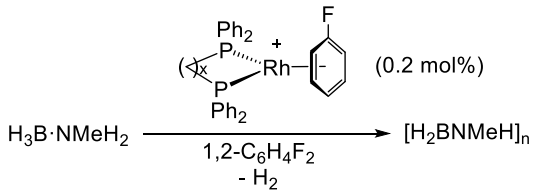
Various other transition metal catalysts based on Re,[137] Fe,[138, 139] Pd,[140] Os,[141] Pt,[142] and Ru[112, 143] including a review written by Weller *et al.*[104] have been reported for the dehydrogenation of amine-boranes. To particular significance of this thesis are the

dehydrocoupling of amine-boranes catalysed by rhodium and iridium complexes. The Weller group in 2008 reported the first homogeneous rhodium catalyst, $[Rh(P^iBu_3)_2][BAr^F_4]$ (5 mol%, TOF 34 h^{-1}) for the dehydrocoupling of $H_3B{\cdot}NMe_2H$ to form $[H_2BNMe_2]_2$ and also reported the sigma-complexes relevant to the catalytic dehydrogenation cycle.[144] Addition of $H_3B{\cdot}NMe_2H$ to $[Rh(P^iBu_3)_2][BAr^F_4]$ results in the immediate formation of the sigma complex $[Rh(P^iBu_3)_2(\eta^2\text{-}H_3B{\cdot}NMe_2H)][BAr^F_4]$ (**i-60**). This was short-lived in the presence of excess $H_3B{\cdot}NMe_2H$ and rapidly formed $[Rh(P^iBu_3)_2(H)_2(\eta^2\text{-}H_3B{\cdot}NMe_2H)][BAr^F_4]$ (**i-61**) and $[H_2BNMe_2]_2$ (Scheme 1.28).



Scheme 1.28 Sigma-complex and dehydrogenation of $H_3B{\cdot}NMe_2H$. $[BAr^F_4]^-$ anions are not shown.

Weller and Manners in 2011 reported rhodium complexes based on $[Rh(Ph_2P(CH_2)_xPPh_2)(\eta^6\text{-}C_6H_5F)][BAr^F_4]$ (x = 3 - 5) as very efficient catalysts for the dehydrocoupling of $H_3B{\cdot}NMe_2H$ forming $[H_2BNMe_2]_2$ (fastest TOF ~1250 h^{-1} when x = 3) and the dehydropolymerization of $H_3B{\cdot}NMeH_2$ to form high molecular weight polymer $[H_2BNMeH]_n$ (when x = 4, M_n = 144 000 g mol^{-1}, Đ = 1.3, Scheme 1.29). A comparison of catalytic activity towards dehydrogenation of $H_3B{\cdot}NMe_2H$ on the basis of bite angle was also reported. $[Rh(Ph_2P(CH_2)_3PPh_2)(\eta^2\text{-}H_3B{\cdot}NMe_3)][BAr^F_4]$, having the smallest bite angle showed the weakest Rh···H_3B interaction and the highest activity towards the dehydrocoupling of $H_3B{\cdot}NMe_2H$.[19]



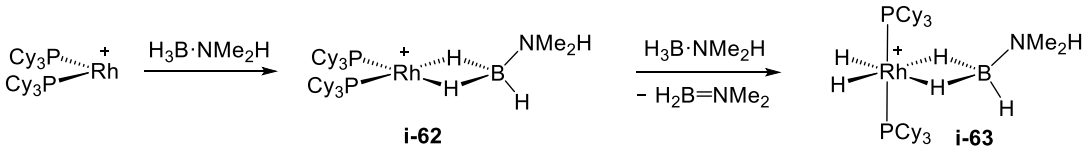
Scheme 1.29 Dehydrocoupling of $H_3B{\cdot}NMeH_2$ catalysed by a rhodium chelating bis-phosphine fragment; x = 3 - 5. $BAr^F{}_4]^-$ anion is not shown.

Kinetics experiments showed the occurrence of an induction period which increased on increasing catalyst loading. Formation of a dimer $[Rh(Ph_2P(CH_2)_xPPh_2)_2(H)(H_2BNMe_2)][BAr^F{}_4]$ (x = 3 - 5) was also observed during catalytic dehydrogenation experiment through ESI-MS. The issues of the induction period and the dimer formation have been discussed in detail in Chapter 4.

In 2012, Weller and Lloyd-Jones reported a detailed kinetic and mechanistic investigation on the dehydrocoupling of $H_3B{\cdot}NMe_2H$ catalysed by $\{Rh(PCy_3)_2L_n\}^+$ (L_n = solvent or agostic interaction) fragment.[145] Various stoichiometric and catalytic experiments were carried out which included the following:

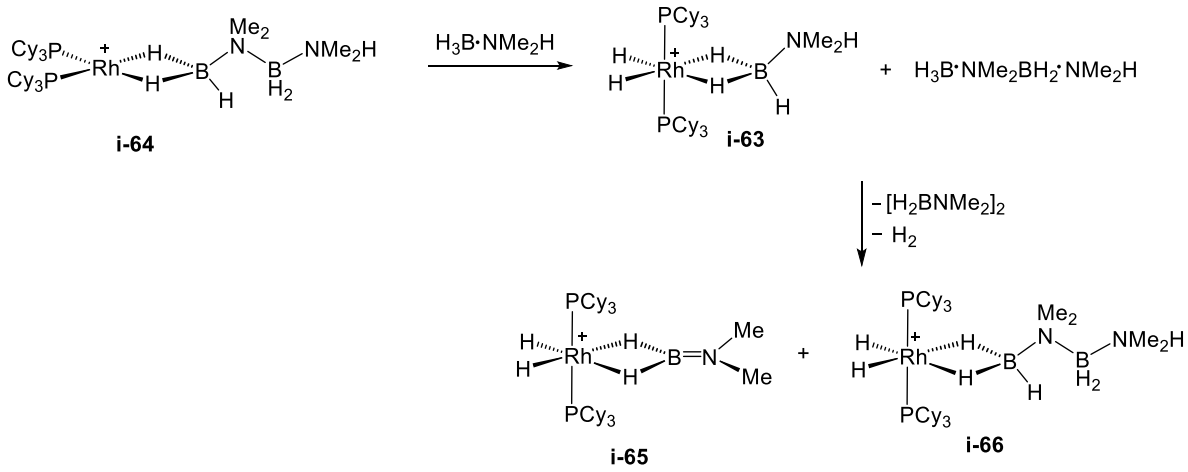
(i) Investigation of the actual catalyst: Addition of two equivalents of $H_3B{\cdot}NMe_2H$ to $\{Rh(PCy_3)_2L_n\}^+$ resulted in the formation of a Rh(I) sigma complex $[Rh(PCy_3)_2(\eta^2\text{-}H_3B{\cdot}NMe_2H)][BAr^F{}_4]$ (**i-62**), which rapidly converted to a Rh(III) species $[Rh(PCy_3)_2(H)_2(\eta^2\text{-}H_3B{\cdot}NMe_2H)][BAr^F{}_4]$ (**i-53**). $H_2B{=}NMe_2$ was observed as intermediate which proceeded to form $[H_2BNMe_2]_2$ (Scheme 1.30). **i-63** did not lose hydrogen in vacuum and was relatively stable in the absence of excess $H_3B{\cdot}NMe_2H$. However, addition of 5 equivalents of $H_3B{\cdot}NMe_2H$ resulted in the complete conversion of $H_3B{\cdot}NMe_2H$ to $[H_2BNMe_2]_2$ via free $H_2B{=}NMe_2$ in one hour. **i-63** was the only organometallic species observed during this transformation which after 24 h showed 50% conversion to $[Rh(PCy_3)_2(H)_2(\eta^2\text{-}H_2B{=}NMe_2)][BAr^F{}_4]$ (**i-65**). This experiment suggested that Rh(I) is a fast catalyst while

Rh(III) is a slow catalyst and is also the resting state in catalysis. This also suggested that additional equivalents of amine-boranes are required for the dehydrogenation, possibly via outer-sphere B−H···H−N intermolecular interactions.[92, 146]



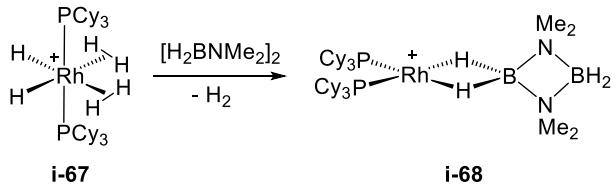
Scheme 1.30 Stoichiometric reactivity of $\{Rh(PCy_3)_2L_n\}^+$ with $H_3B{\cdot}NMe_2H$. $[BAr^F{}_4]^-$ anions are not shown.

(ii) Involvement of $H_3B{\cdot}NMe_2BH_2{\cdot}NMe_2H$ in dehydrogenation: Addition of one equivalent of $H_3B{\cdot}NMe_2BH_2{\cdot}NMe_2H$ to $\{Rh(PCy_3)_2L_n\}^+$ resulted in the immediate formation of $[Rh(PCy_3)_2(\eta^2\text{-}H_3B{\cdot}NMe_2BH_2{\cdot}NMe_2H)][BAr^F{}_4]$ (**i-64**) which slowly converted to a mixture of Rh(III) complexes **i-63**, $[Rh(PCy_3)_2(H)_2(\eta^2\text{-}H_2B{=}NMe_2)][BAr^F{}_4]$ **(i-65**) and $[Rh(PCy_3)_2(H)_2(\eta^2\text{-}H_3B{\cdot}NMe_2BH_2{\cdot}NMe_2H)][BAr^F{}_4]$ (**i-66**) (90% consumption of **i-64** in 3h). Consumption of **i-64** was accelerated by the addition of one more equivalent of $H_3B{\cdot}NMe_2H$ (Scheme 1.31). Addition of $H_3B{\cdot}NMe_2H$ to **i-64** resulted in the immediate formation of **i-63** by the displacement of $H_3B{\cdot}NMe_2BH_2{\cdot}NMe_2H$ which proceeds to give $[H_2BNMe_2]_2$ via $H_2B{=}NMe_2$ intermediate. A mixture of **i-63** and **i-65** was observed at the end of catalysis. Overall, these studies suggested that at the beginning of catalysis sigma-complex of $H_3B{\cdot}NMe_2H$ will dominate, rather than the sigma-complex of $H_3B{\cdot}NMe_2BH_2{\cdot}NMe_2H$. However, when sigma-complexes of $H_3B{\cdot}NMe_2BH_2{\cdot}NMe_2H$ do form at lower $H_3B{\cdot}NMe_2H$ concentration, they undergo either B−N bond cleavage or dehydrocyclisation to form $[H_2BNMe_2]_2$.



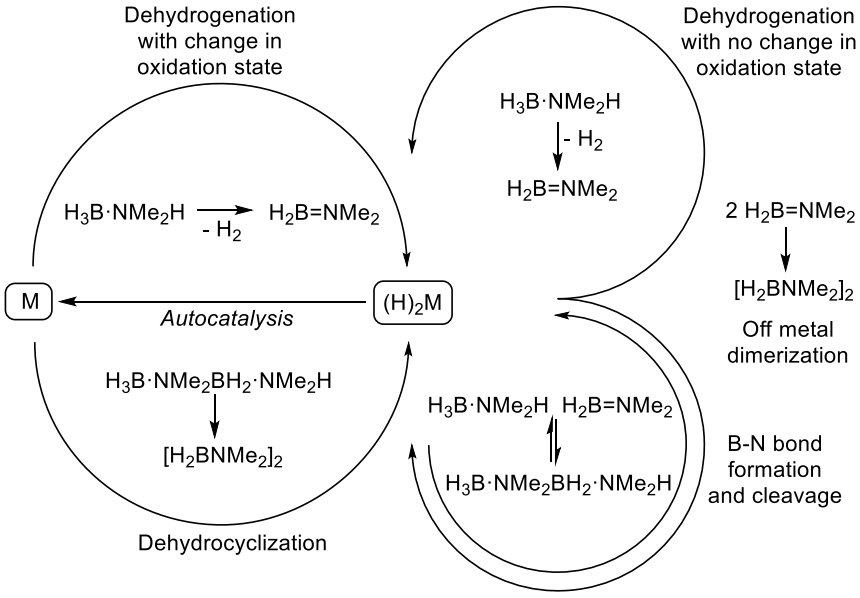
Scheme 1.31 Reactivity of **i-64** with $H_3B{\cdot}NMe_2H$. $[BAr^F{}_4]^-$ anions are not shown.

(iii) **Role of $[H_2BNMe_2]_2$ in the dehydrogenation**: Addition of $[H_2BNMe_2]_2$ to the Rh(III) species $[Rh(PCy_3)_2(H)_2(\eta^2\text{-}H_2)_2][BAr^F{}_4]$ (**i-67**) resulted in the immediate formation of a Rh(I) complex $[Rh(PCy_3)_2(\eta^2\text{-}[H_2BNMe_2]_2)][BAr^F{}_4]$ (**i-68**) in 70% yield. Formation of **i-68** was increased on adding more $[H_2BNMe_2]_2$, indicating that $[H_2BNMe_2]_2$ can drive the reductive elimination of H_2 and establishes an equilibrium between **i-67** and **i-68** (Scheme 1.32). Under catalytic conditions, $[H_2BNMe_2]_2$ was found to have an autocatalytic role in the dehydrocoupling catalysis and produced kinetically significant amounts of a catalytically active Rh(I) species alongside the Rh(III) species. This suggests that $[H_2BNMe_2]_2$ acts as a modifier and acts in an autocatalytic role which allows the catalysis to run in both a Rh(III)/Rh(III) cycle (slow), and a Rh(I)/Rh(III) cycle (faster).



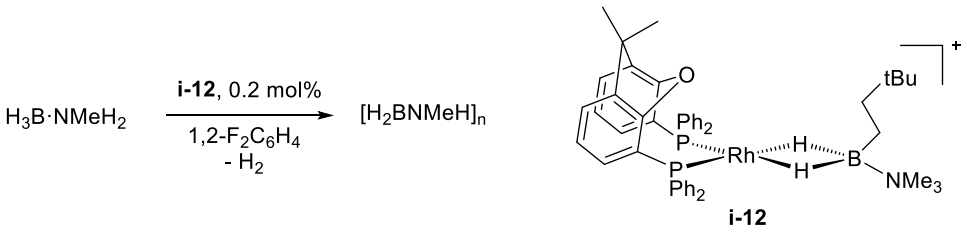
Scheme 1.32 Reduction from Rh(III) to Rh(I) by addition of $[H_2BNMe_2]_2$. $[BAr^F{}_4]^-$ anions are not shown.

These and other observations led to a generalised mechanism (Scheme 1.33) for the dehydrocoupling of $H_3B{\cdot}NMe_2H$ which involves: (a) dehydrogenation of $H_3B{\cdot}NMe_2H$ under a constant oxidation state [Rh(III)/Rh(III)] or a change in oxidation state [Rh(I)/Rh(III)]; (b) formation, cleavage and dehydrocyclization of $H_3B{\cdot}NMe_2BH_2{\cdot}NMe_2H$; (c) the off-metal dimerisation of $H_2B{=}NMe_2$ to give $[H_2BNMe_2]_2$. This general mechanism is applicable to many transition metal or main group catalysed dehydrocoupling of amine-boranes.



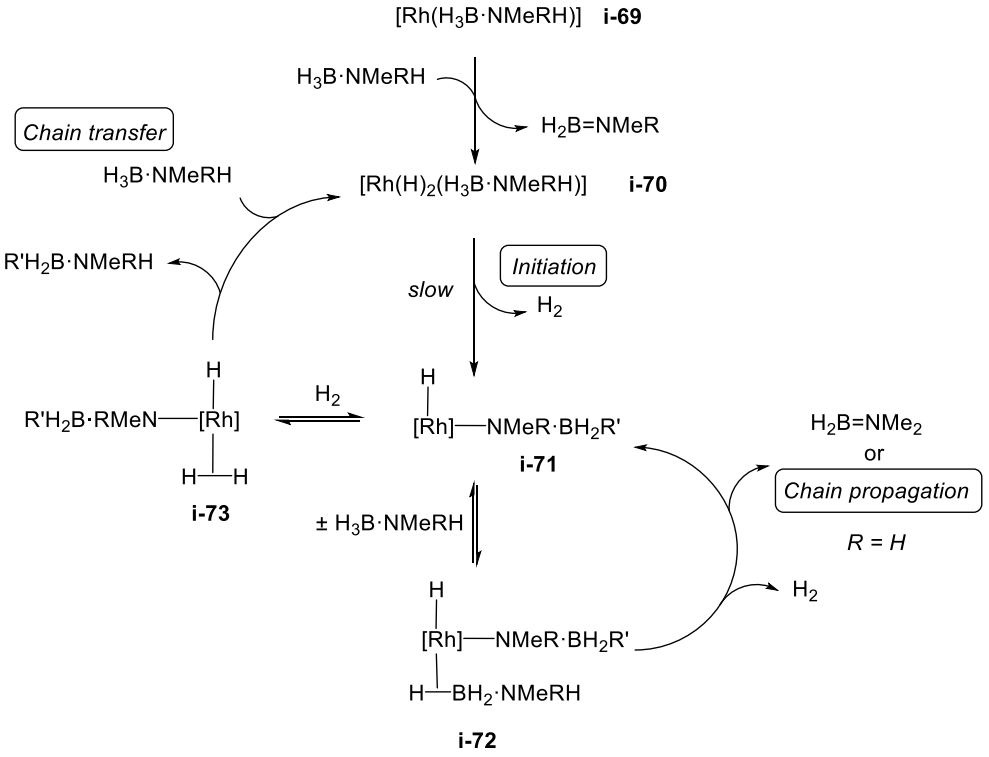
Scheme 1.33 Weller and Lloyd-Jones' general mechanistic cycle for the dehydrocoupling of $H_3B{\cdot}NMe_2H$. M = rhodium catalyst.

The Weller group in 2014 reported a detailed mechanism on $[Rh(Xantphos)]^+$ (**i-12**) catalysed dehydrocoupling of $H_3B{\cdot}NMe_2H$ and $H_3B{\cdot}NMeH_2$ to form the $[H_2BNMe_2]_2$ and polyaminoborane $[H_2BNMeH]_n$ respectively (M_n = 22, 700 and Đ = 2.1 Scheme 1.34).[58]



Scheme 1.34 Dehydrocoupling of $H_3B{\cdot}NMeH_2$ using $[Rh(Xantphos)]^+$. $[BAr^F{}_4]^-$ anion is not shown.

A dehydrocoupling mechanism as shown in Scheme 1.35 has been proposed. Addition of $H_3B{\cdot}NMeRH$ to **i-12** results in the rapid dehydrogenation to form a Rh(III) species **i-70** presumably via the Rh(I) sigma-complex **i-69**. The stoichiometric and kinetics experiments indicated an induction period which is suggested to be due to the formation of a tentative Rh-amido-borane species, **i-71** proposed to be the actual catalyst. **i-71** can rapidly and reversibly coordinate with amine-borane to give **i-72**. **i-72** can undergo BH/NH transfer to produce amino-borane $H_2B{=}NRH$ (R = Me, H) and regenerates the actual catalyst **i-71**. $H_2B{=}NMe_2$ can dimerize to produce the cyclic dimer $[H_2BNMe_2]_2$, while $H_2B{=}NMeH$ can involve in chain propagating B−N bond formation steps to produce the polyaminoborane. Chain termination step can occur by the heterolytic cleavage of the coordinated dihydrogen in **i-73** resulting in the formation of a $Rh(III)H_2$ fragment (**i-70**) and free polymer.



Scheme 1.35 Overall proposed mechanism for the dehydrocoupling of $H_3B{\cdot}NMe_2H$ (R' = H, R = Me) and dehydropolymerisation of $H_3B{\cdot}NMeH_2$ (R' = H or growing polymer chain, R = H). [Rh] = $\{Rh(Xantphos)\}^+$.

1.17 Sigma-complexes of amine-boranes

As discussed above, sigma-complexes are important intermediates during catalytic dehydrocoupling of amine-boranes and precede the oxidative addition step. The synthesis and characterisation of sigma-complexes of amine-boranes are therefore important from mechanistic point of view. Shimoi and co-workers in 1999 reported the first sigma-complexes of amine-boranes by the photolysis of $[M(CO)_6]$ in the presence of $H_3B{\cdot}NMe_3$ to form $[M(CO)_5(\eta^1\text{-}BH_3.NMe_3)]$ (**i-74**; M = Cr, W and Mo).[147] The Weller group has reported extensively on sigma-complexes of amine-boranes with Rh (**i-75** - **i-78**)[19, 59, 148, 149] and Ir (**i-79**)[59] and in 2015, Crimmin has reported sigma-complex of $H_3B{\cdot}NMe_3$ with Cu (**i-80** Figure 1.14).[150]

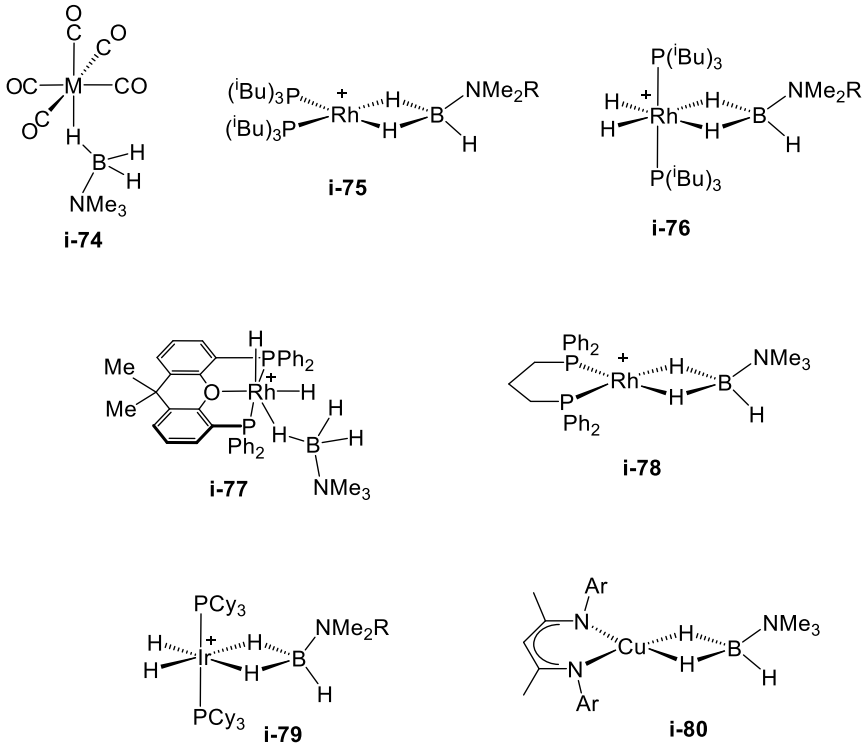
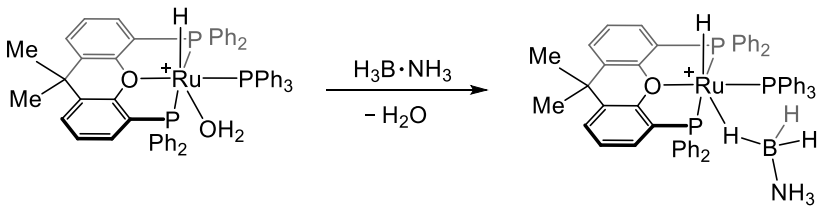


Figure 1.14 Sigma-complexes of $H_3B{\cdot}NMe_2R$ (R = Me, H); M = Cr, W, Mo. $[BAr^F{}_4]^-$ anions are not shown.

As shown in Figure 1.13, there are several examples of sigma-complexes of amine-boranes with alkyl substitution, $H_3B{\cdot}NRR'R''$($NRR'R''$ = NMe_3, $NHMe_2$, NH_2Me) but none of $H_3B{\cdot}NH_3$ untill 2011 when the Whittlesey group uncovered the reactivity of $\{Ru(Xantphos)(PPh_3)(H)\}^+$ fragment towards $H_3B{\cdot}NHR'R$ ($NHRR'$ = NH_2tBu, $NHMe_2$ and NH_3) and reported the first sigma-complex of $H_3B{\cdot}NH_3$ (Scheme 1.36).[143] Chapter Two of this thesis presents the second example of sigma-complex of $H_3B{\cdot}NH_3$.



Scheme 1.36 Sigma-complex of $H_3B{\cdot}NH_3$. $[BAr^F{}_4]^-$ anions are not shown.

Other than the sigma-complexes of amine-boranes of $H_3B{\cdot}NRR'R''$ type, sigma-complexes of linear dimers for example $H_3B{\cdot}NMe_2BH_2{\cdot}NMe_2H$ (**i-81**)[148] and $H_3B{\cdot}NMeHBH_2{\cdot}NMeH_2$ (**i-82**)[151] and cyclic dimers $[H_2BNMe_2]_2$ (**i-83**)[152] and cyclic trimers $[H_2BNMeH]_3$ (**i-84**)[130] have also been reported. The Weller group has also reported bis(σ-amine-borane) complexes showing different binding modes (η^1 and η^2) of both the bound amine-boranes on the same metal centre (**i-85,** Figure 1.15).[153]

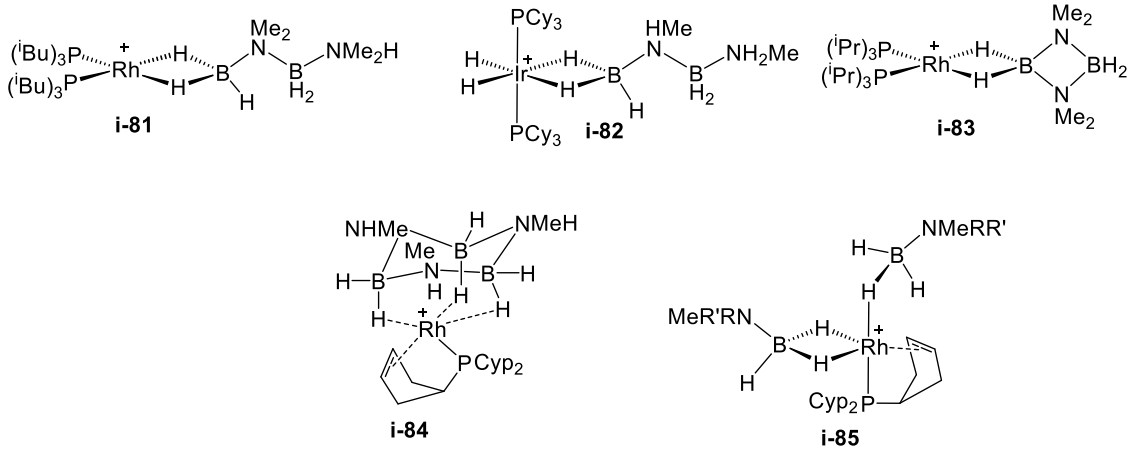


Figure 1.15 Examples of sigma-complexes of amine-boranes and their oligomers, R, R' = H, Me. $[BAr^F_4]^-$ anions are not shown.

1.18 Sigma-complexes of amino-boranes

Amino-boranes result from the release of one equivalent of hydrogen gas from amine-boranes and are the simplest dehydrogenation products. Metal complexes of amino-boranes have previously been proposed as important intermediates during the dehydrogenation process.[135] Aldridge and co-workers reported the sigma-complexes of amino-boranes ($H_2B{=}NR_2$, R = ^{i}Pr and Cy) with the group 9 metals and showed for the first time that these systems bind in an end-on fashion through two M−H−B bridges in contrast to the related alkene donors which bind in a side-on fashion.[154] $[M(IMeS)_2(H)_2(H_2BNR_2)][BAr^F_4]$ (IMes = N,N-bis(2,4,6-trimethylphenyl)imidazol-2-yli-dene; M = Rh, Ir; R = ^{i}Pr, Cy; e.g. **i-88**) were isolated as the end product from the catalytic dehydrogenation of $H_3B{\cdot}NRH_2$ using $[M(IMeS)_2(H)_2Cl(Na)][BAr^F_4]$. Several other examples

of sigma-complexes of amino-boranes with rhodium,[145, 154-156] iridium[59, 156-158] and ruthenium,[156, 159-161] are reported, some of which are shown in Figure 1.16. Bonding in transition metal sigma-complexes of amino-boranes can be described as σ-donation from the B−H bond to the metal and π-backdonation from an occupied nonbonding d orbital on the metal into the π* B-N orbital of the aminoborane.[156] Alcaraz, Weller and Sabo-Etienne reported the sigma-complexes of ruthenium (Ru), rhodium (Rh) and iridium (Ir) with diisopropylamino-borane (**i-86**).[156] DFT calculations showed that the backdonation varies according to the order: [Ru] > $[Ir]^+$ > $[Rh]^+$, however σ-donation is similar for [Ru] and $[Ir]^+$. This is consistent with the calculated M−B bond distance in **i-86**: Ru−B = 2.003, Ir−B = 2.088 Å, and Rh−B = 2.159 Å.

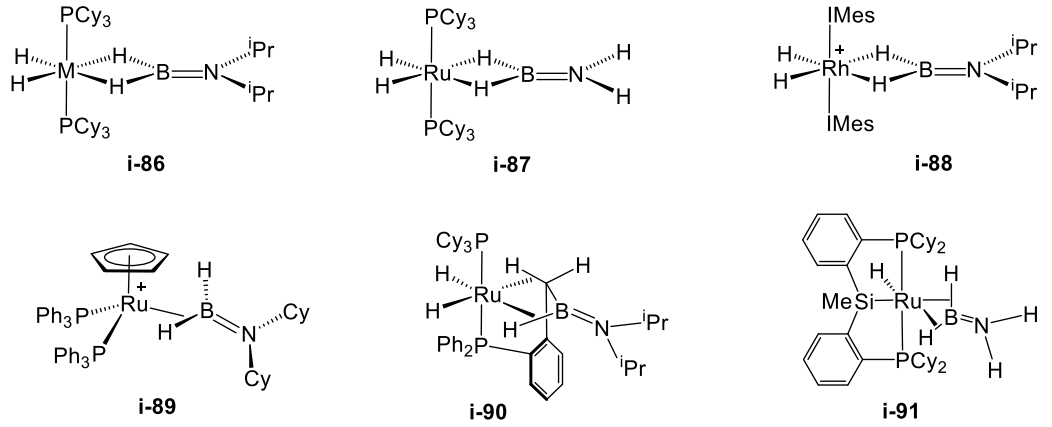


Figure 1.16 Selected sigma-complexes of aminoborane. M = Ru, Rh^+, Ir^+; $[BAr^F{}_4]^-$ anions are not shown.

1.19 Summary

This chapter starts with an introduction to the fundamentals of organometallic catalysis, in particular, transformations carried out by rhodium and iridium-phosphine complexes and description of relevant intermediates like sigma-complexes during catalysis. Previous mechanistic investigations reported on the metal catalysed dehydrocoupling of amine-boranes have been discussed in great detail. Literature survey reveals that much of such work has been centred on $H_3B{\cdot}NMe_2H$ and $H_3B{\cdot}NMeH_2$ and very less on $H_3B{\cdot}NH_3$ and

other substituted amine-boranes such as $RH_2B{\cdot}NMe_2R'$ or cyclic amine-boranes. This motivated an investigation on the reactivity of these less explored amine-boranes with iridium and rhodium-phosphine complexes.

This thesis reports the synthesis and characterisation of iridium and rhodium sigma-complexes of amine-boranes and their subsequent dehydrogenation. Metal-bisphosphine systems, $\{Ir(H)_2(PCy_3)_2\}^+$ and $\{Rh(PR_2(CH_2)PR_2\}^+$ (R = ^{i}Pr and Ph) fragments have been used to study the coordination chemistry and dehydrogenation of amine-boranes. Catalytic dehydrogenation experiments have been followed by NMR spectroscopy and intermediates (organometallic complexes and B−N containing dehydrocoupling products) have been either characterised *in situ* (by NMR spectroscopy or ESI-MS) or isolated or independently synthesized. Mechanisms of catalytic dehydrogenation have been proposed by the direct observation of these intermediates, kinetic studies and the DFT calculations performed in collaboration by Prof. Stuart Macgregor (Heriot-Watt University).

Chapter Two and Three presents the detailed mechanistic investigation on the catalytic dehydrocoupling of $H_3B{\cdot}NH_3$ using $\{Ir(H)_2(PCy_3)_2\}^+$ and $\{Rh(PR_2(CH_2)PR_2\}^+$ (R = ^{i}Pr and Ph) fragments. Chapter Four presents coordination chemistry and dehydrogenation of a *B*-phenyl amine-borane. Chapter five involves cyclic amine-boranes based on BN-cyclohexanes, whose coordination chemistry and catalytic dehydrogenation mechanism with iridium and rhodium complexes have been reported.

1.20 References

1. P.-O. Norrby, *ChemCatChem*, 2010, **2**, 872.
2. P. M. Maitlis, *Metal-catalysis in Industrial Organic Processes*, 2006.
3. *Phosphorus (III) Ligands in Homogeneous Catalysis: Design and Synthesis*, 2012.
4. R. H. Crabtree, *Organometallic Chemistry of the Transition Metals, 4th Edition*, 2005.
5. J. D. Atwood, *Inorganic and Organometallic Reaction Mechanisms*, Wiley-VCH, 2nd Edition edn., 1997.

6. J. F. Hartwig, *Organotransition Metal Chemistry: From Bonding to Catalysis*, 2010.

7. C. Oconnor and Wilkinso.G, *Tetrahedron Letters*, 1969, 1375-1377.

8. C. A. Tolman, *Chem. Rev.*, 1977, **77**, 313-348.

9. R. D. W. Kemmitt, D. I. Nichols and R. D. Peacock, *J. Chem.Soc. A*, 1968, 1898-&.

10. C. A. Tolman, *J. Am. Chem. Soc.*, 1970, **92**, 2956-2965.

11. C. P. Casey and G. T. Whiteker, *Isr. J. Chem.*, 1990, **30**, 299-304.

12. M. Kranenburg, Y. E. M. Vanderburgt, P. C. J. Kamer, P. Vanleeuwen, K. Goubitz and J. Fraanje, *Organometallics*, 1995, **14**, 3081-3089.

13. P. D. Achord, P. Kiprof and B. Barker, *J. Mol. Struct.-Theochem*, 2008, **849**, 103-111.

14. M.-N. Birkholz, Z. Freixa and P. W. N. M. van Leeuwen, *Chem. Soc. Rev.*, 2009, **38**, 1099-1118.

15. A. Prades, M. Fernandez, S. D. Pike, M. C. Willis and A. S. Weller, *Angew. Chem. Int. Ed.*, 2015, **54**, 8520-8524.

16. I. Pernik, J. F. Hooper, A. B. Chaplin, A. S. Weller and M. C. Willis, *ACS Catal.*, 2012, **2**, 2779-2786.

17. M. Kranenburg, P. C. J. Kamer, P. Vanleeuwen, D. Vogt and W. Keim, *J. Chem. Soc., Chem. Commun.*, 1995, 2177-2178.

18. F. Liron, C. Fosse, A. Pernolet and E. Roulland, *J. Org. Chem.*, 2007, **72**, 2220-2223.

19. R. Dallanegra, A. P. M. Robertson, A. B. Chaplin, I. Manners and A. S. Weller, *Chem. Commun.*, 2011, **47**, 3763-3765.

20. R. L. Paul, A. J. Amoroso, P. L. Jones, S. M. Couchman, Z. R. Reeves, L. H. Rees, J. C. Jeffery, J. A. McCleverty and M. D. Ward, *J. Chem. Soc. Dalton Trans.*, 1999, 1563-1568.

21. S. Kannan, M. A. Moody, C. L. Barnes and P. B. Duval, *Inorg. Chem.*, 2006, **45**, 9206-9212.

22. I. Krossing and I. Raabe, *Angew. Chem. Int. Ed.*, 2004, **43**, 2066-2090.

23. A. B. Chaplin and A. S. Weller, *Eur. J. Inorg. Chem.*, 2010, 5124-5128.

24. A. H. Dirk Steinborn, 2011.

25. J. A. Widegren and R. G. Finke, *J. Mol. Cat. A*, 2003, **198**, 317-341.

26. Y. Lin and R. G. Finke, *Inorg. Chem.*, 1994, **33**, 4891-4910.

27. www.kitco.com.

28. K. Barbalace, *Table of Elements*, Environmental Chemistry.com.

29. P. J. Loferski, *United States Geological Survey*, 2013.

30. A. E. N.N. Greenwood, *Chemistry of the elements*, Elsevier, 1997.

31. B. Cornils, W. A. Herrmann and M. Rasch, *Angew. Chem. Int. Ed.*, 1994, **33**, 2144-2163.

32. D. Evans, J. A. Osborn and Wilkinso.G, *J. Chem.Soc. A*, 1968, 3133-&.

33. F. H. Jardine, *Polyhedron*, 1982, **1**, 569-605.

34. R. R. Schrock and J. A. Osborn, *J. Am. Chem. Soc.*, 1976, **98**, 2134-2143.

35. T. Yoshida, T. Okano and S. Otsuka, *J. Chem. Soc., Chem. Commun.*, 1979, 870-871.

36. H. Fujitsu, E. Matsumura, K. Takeshita and I. Mochida, *J. Org. Chem.*, 1981, **46**, 5353-5357.

37. R. R. Schrock and J. A. Osborn, *J. Chem. Soc. D*, 1970, 567-568.

38. H. Fujitsu, S. Shirahama, E. Matsumura, K. Takeshita and I. Mochida, *J. Org. Chem.*, 1981, **46**, 2287-2290.

39. M. J. Russell, C. White and P. M. Maitlis, *J. Chem. Soc., Chem. Commun.*, 1977, 427-428.

40. J. M. Brown, *Angew. Chem. Int. Ed.*, 1987, **26**, 190-203.

41. M. C. Simpson and D. J. ColeHamilton, *Coord. Chem. Rev.*, 1996, **155**, 163-207.

42. H. S. Renner, G.; Kleinwächter, I.; Drost, E.; Lüschow, H. M.; Tews, P.; Panster, P.; Diehl, M.; et al., *Platinum group metals and compounds*, Wiley, 2002.

43. G. J. Sunley and D. J. Watson, *Catal. Today*, 2000, **58**, 293-307.

44. R. Crabtree, *Acc. Chem. Res.*, 1979, **12**, 331-338.

45. A. Cadu and P. G. Andersson, *Dalton Trans.*, 2013, **42**, 14345-14356.

46. A. H. Janowicz and R. G. Bergman, *J. Am. Chem. Soc.*, 1982, **104**, 352-354.

47. S. Kundu, Y. Choliy, G. Zhuo, R. Ahuja, T. J. Emge, R. Warmuth, M. Brookhart, K. Krogh-Jespersen and A. S. Goldman, *Organometallics*, 2009, **28**, 5432-5444.

48. Z. Huang, M. Brookhart, A. S. Goldman, S. Kundu, A. Ray, S. L. Scott and B. C. Vicente, *Adv. Synth. Catal.*, 2009, **351**, 188-206.

49. B. Punji, T. J. Emge and A. S. Goldman, *Organometallics*, 2010, **29**, 2702-2709.

50. R. Ahuja, B. Punji, M. Findlater, C. Supplee, W. Schinski, M. Brookhart and A. S. Goldman, *Nat. Chem.*, 2011, **3**, 167-171.

51. D. A. Laviska, C. Guan, T. J. Emge, M. Wilklow-Marnell, W. W. Brennessel, W. D. Jones, K. Krogh-Jespersen and A. S. Goldman, *Dalton Trans.*, 2014, **43**, 16354-16365.

52. C. M. Jensen, *Chem. Commun.*, 1999, 2443-2449.

53. M. A. Bennett and D. L. Milner, *J. Am. Chem. Soc.*, 1969, **91**, 6983-6994.

54. Y. Nishibayashi, I. Takei and M. Hidai, *Angew. Chem. Int. Ed.*, 1999, **38**, 3047-3050.

55. R. Noyori, M. Koizumi, D. Ishii and T. Ohkuma, *Pure Appl. Chem.*, 2001, **73**, 227-232.

56. D. V. Gutsulyak, S. F. Vyboishchikov and G. I. Nikonov, *J. Am. Chem. Soc.*, 2010, **132**, 5950-5951.

57. H. C. Johnson, R. Torry-Harris, L. Ortega, R. Theron, J. S. McIndoe and A. S. Weller, *Catal. Sci. Tech.*, 2014, **4**, 3486-3494.

58. H. C. Johnson, E. M. Leitao, G. R. Whitten, I. Manners, G. C. Lloyd-Jones and A. S. Weller, *J. Am. Chem. Soc.*, 2014, **136**, 9078-9093.

59. C. J. Stevens, R. Dallanegra, A. B. Chaplin, A. S. Weller, S. A. Macgregor, B. Ward, D. McKay, G. Alcaraz and S. Sabo-Etienne, *Chem. Eur. J.*, 2011, **17**, 3011-3020.

60. A. Kumar, H. C. Johnson, T. N. Hooper, A. S. Weller, A. G. Algarra and S. A. Macgregor, *Chem. Sci.*, 2014, **5**, 2546-2553.

61. T. N. Hooper, M. A. Huertos, T. Jurca, S. D. Pike, A. S. Weller and I. Manners, *Inorg. Chem.*, 2014, **53**, 3716-3729.

62. J. L. Vincent, S. Luo, B. L. Scott, R. Butcher, C. J. Unkefer, C. J. Burns, G. J. Kubas, A. Lledos, F. Maseras and J. Tomas, *Organometallics*, 2003, **22**, 5307-5323.

63. M. Zyder and T. Szymanska-Buzar, *J. Organomet. Chem.*, 2009, **694**, 2110-2113.

64. M. Brookhart, M. L. H. Green and G. Parkin, *Proc. Natl. Acad. Sci. U.S.A.*, 2007, **104**, 6908-6914.

65. Y. W. Yared, S. L. Miles, R. Bau and C. A. Reed, *J. Am. Chem. Soc.*, 1977, **99**, 7076-7078.

66. Z. Dawoodi, M. L. H. Green, V. S. B. Mtetwa, K. Prout, A. J. Schultz, J. M. Williams and T. F. Koetzle, *J. Chem. Soc. Dalton Trans.*, 1986, 1629-1637.

67. S. D. Pike, A. L. Thompson, A. G. Algarra, D. C. Apperley, S. A. Macgregor and A. S. Weller, *Science*, 2012, **337**, 1648-1651.

68. G. J. Kubas, R. R. Ryan, B. I. Swanson, P. J. Vergamini and H. J. Wasserman, *J. Am. Chem. Soc.*, 1984, **106**, 451-452.

69. R. H. Crabtree and M. Lavin, *J. Chem. Soc., Chem. Commun.*, 1985, 1661-1662.

70. B. Chaudret and R. Poilblanc, *Organometallics*, 1985, **4**, 1722-1726.

71. T. Arliguie, B. Chaudret, R. H. Morris and A. Sella, *Inorg. Chem.*, 1988, **27**, 598-599.

72. A. F. Borowski, B. Donnadieu, J. C. Daran, S. Sabo-Etienne and B. Chaudret, *Chem. Commun.*, 2000, 543-544.

73. M. J. Ingleson, S. K. Brayshaw, M. F. Mahon, G. D. Ruggiero and A. S. Weller, *Inorg. Chem.*, 2005, **44**, 3162-3171.

74. M. Grellier, L. Vendier, B. Chaudret, A. Albinati, S. Rizzato, S. Mason and S. Sabo-Etienne, *J. Am. Chem. Soc.*, 2005, **127**, 17592-17593.

75. G. J. Kubas, *Metal Dihydrogen and Sigma Bond Complexes*, Kleuwer Academic / Plenum Publishers NY, 2001.

76. G. J. Kubas, *Chem. Rev.*, 2007, **107**, 4152-4205.

77. R. H. Crabtree, *Angew. Chem. Int. Ed.*, 1993, **32**, 789-805.

78. R. Gelabert, M. Moreno, J. M. Lluch, A. Lledos, V. Pons and D. M. Heinekey, *J. Am. Chem. Soc.*, 2004, **126**, 8813-8822.

79. J. Chatt and L. A. Duncanson, *J. Chem. Soc.*, 1953, 2939-2947.

80. G. J. Kubas, *Catal. Lett.*, 2005, **104**, 79-101.

81. J. A. Iggo, *NMR Spectroscopy in Inorganic Chemistry*, Oxford University Press, Oxford, 1999.

82. C. M. Crudden and D. Edwards, *Eur. J. Org. Chem.*, 2003, 4695-4712.

83. R. B. Coapes, F. E. S. Souza, R. L. Thomas, J. J. Hall and T. B. Marder, *Chem. Commun.*, 2003, DOI: 10.1039/b211789d, 614-615.

84. K. K. Pandey, *Coord. Chem. Rev.*, 2009, **253**, 37-55.

85. S. A. Snow, M. Shimoi, C. D. Ostler, B. K. Thompson, G. Kodama and R. W. Parry, *Inorg. Chem.*, 1984, **23**, 511-512.

86. J. F. Hartwig, G. N. Muhoro, X. M. He, O. Eisenstein, R. Bosque and F. Maseras, *J. Am. Chem. Soc.*, 1996, **118**, 10936-10937.

87. G. Alcaraz and S. Sabo-Etienne, *Angew. Chem. Int. Ed.*, 2010, **49**, 7170-7179.

88. S. Schlecht and J. F. Hartwig, *J. Am. Chem. Soc.*, 2000, **122**, 9435-9443.

89. M. G. Crestani, M. Munoz-Hernandez, A. Arevalo, A. Acosta-Ramirez and J. J. Garcia, *J. Am. Chem. Soc.*, 2005, **127**, 18066-18073.

90. S. Lachaize, W. Essalah, V. Montiel-Palma, L. Vendier, B. Chaudret, J. C. Barthelat and S. Sabo-Etienne, *Organometallics*, 2005, **24**, 2935-2943.

91. Z. Liu and T. B. Marder, *Angew. Chem. Int. Ed.*, 2008, **47**, 242-244.

92. S. Aldridge, A. J. Downs, C. Y. Tang, S. Parsons, M. C. Clarke, R. D. L. Johnstone, H. E. Robertson, D. W. H. Rankin and D. A. Wann, *J. Am. Chem. Soc.*, 2009, **131**, 2231-2243.

93. F. H. Stephens, V. Pons and R. T. Baker, *Dalton Trans.*, 2007, 2613-2626.

94. A. Staubitz, A. P. M. Robertson and I. Manners, *Chem. Rev.*, 2010, **110**, 4079-4124.

95. E. M. Leitao, T. Jurca and I. Manners, *Nat. Chem.*, 2013, **5**, 817-829.

96. A. Staubitz, A. P. M. Robertson, M. E. Sloan and I. Manners, *Chem. Rev.*, 2010, **110**, 4023-4078.

97. K. Sung-Kwan, C. Hyunjin, K. Myung Jong, L. Hee-Jun, P. Jin-hyung, L. Young-Boo, K. Hwan Chul, Y. Chang Won, N. Suk Woo and K. Sang Ook, *J. Mat. Chem. A*, 2013, **1**, 1976-1981.

98. N. Sakhavand and R. Shahsavari, *Acs Appl. Mater. Interfaces*, 2015, **7**, 18312-18319.

99. Z. Liu, L. Song, S. Zhao, J. Huang, L. Ma, J. Zhang, J. Lou and P. M. Ajayan, *Nano Lett.*, 2011, **11**, 2032-2037.

100. L. Euzenat, D. Horhant, Y. Ribourdouille, C. Duriez, G. Alcaraz and M. Vaultier, *Chem. Commun.*, 2003, 2280-2281.

101. K. J. Sabourin, A. C. Malcolm, R. McDonald, M. J. Ferguson and E. Rivard, *Dalton Trans.*, 2013, **42**, 4625-4632.

102. N. E. Stubbs, A. Schaeger, A. P. M. Robertson, E. M. Leitao, T. Jurca, H. A. Sparkes, C. H. Woodall, M. F. Haddow and I. Manners, *Inorg. Chem.*, 2015, **54**, 10878-10889.

103. I. G. Green, K. M. Johnson and B. P. Roberts, *J. Chem. Soc.-Perkin Trans. 2*, 1989,1963-1972.

104. H. C. Johnson, T. N. Hooper and A. S. Weller, in *Synthesis and Application of Organoboron Compounds*, eds. E. Fernandez and A. Whiting, 2015, vol. 49, pp. 153-220.

105. C. A. Jaska and I. Manners, *J. Am. Chem. Soc.*, 2004, **126**, 9776-9785.

106. A. P. M. Robertson, R. Suter, L. Chabanne, G. R. Whittell and I. Manners, *Inorg. Chem.*, 2011, **50**, 12680-12691.

107. J. F. Sonnenberg and R. H. Morris, *ACS Catal.*, 2013, **3**, 1092-1102.

108. M. Kaess, A. Friedrich, M. Drees and S. Schneider, *Angew. Chem. Int. Ed.*, 2009, **48**, 905-907.

109. A. Friedrich, M. Drees and S. Schneider, *Chem. Eur. J.*, 2009, **15**, 10339-10342.

110. A. N. Marziale, A. Friedrich, I. Klopsch, M. Drees, V. R. Celinski, J. S. A. D. Guenne and S. Schneider, *J. Am. Chem. Soc.*, 2013, **135**, 13342-13355.

111. B. L. Conley and T. J. Williams, *Chem. Commun.*, 2010, **46**, 4815-4817.

112. D. F. Schreiber, C. O'Connor, C. Grave, Y. Ortin, H. Mueller-Bunz and A. D. Phillips, *Acs Catalysis*, 2012, **2**, 2505-2511.

113. D. W. Stephan, *Org. Biomol. Chem.*, 2008, **6**, 1535-1539.

114. A. M. Chapman, M. F. Haddow and D. F. Wass, *J. Am. Chem. Soc.*, 2011, **133**, 18463-18478.

115. A. M. Chapman, M. F. Haddow and D. F. Wass, *J. Am. Chem. Soc.*, 2011, **133**, 8826-8829.

116. R. J. Keaton, J. M. Blacquiere and R. T. Baker, *J. Am. Chem. Soc.*, 2007, **129**, 1844-1845.

117. J. Spielmann, M. Bolte and S. Harder, *Chem. Commun.*, 2009, DOI: 10.1039/b914979a, 6934-6936.

118. D. J. Liptrot, M. S. Hill, M. F. Mahon and D. J. MacDougall, *Chem. Eur. J.*, 2010, **16**, 8508-8515.

119. H. J. Cowley, M. S. Holt, R. L. Melen, J. M. Rawson and D. S. Wright, *Chem. Commun.*, 2011, **47**, 2682-2684.

120. M. M. Hansmann, R. L. Melen and D. S. Wright, *Chem. Sci.*, 2011, **2**, 1554-1559.

121. D. J. Liptrot, M. S. Hill, M. F. Mahon and D. J. MacDougall, *Chem. Eur. J.*, 2010, **16**, 8508-8515.

122. P. Bellham, M. S. Hill, G. Kociok-Kohn and D. J. Liptrot, *Chem. Commun.*, 2013, **49**, 1960-1962.

123. P. Bellham, M. S. Hill and G. Kociok-Köhn, *Organometallics*, 2014, **33**, 5716-5721.

124. M. S. Hill, G. Kociok-Kohn and T. P. Robinson, *Chem. Commun.*, 2010, **46**, 7587-7589.

125. P. Cui, T. P. Spaniol, L. Maron and J. Okuda, *Chem. Eur. J.*, 2013, **19**, 13437-13444.

126. K. A. Erickson, D. S. Wright and R. Waterman, *J. Organomet. Chem.*, 2014, **751**, 541-545.

127. T. J. Clark, C. A. Russell and I. Manners, *J. Am. Chem. Soc.*, 2006, **128**, 9582-9583.

128. M. E. Sloan, A. Staubitz, T. J. Clark, C. A. Russell, G. C. Lloyd-Jones and I. Manners, *J. Am. Chem. Soc.*, 2010, **132**, 3831-3841.

129. A. B. Chaplin and A. S. Weller, *Acta Crystallogr. Sect. C-Cryst. Struct. Commun.*, 2011, **67**, M355-M358.

130. R. Dallanegra, A. B. Chaplin, J. Tsim and A. S. Weller, *Chem. Commun.*, 2010, **46**, 3092-3094.

131. Y. Luo and K. Ohno, *Organometallics*, 2007, **26**, 3597-3600.

132. M. C. Denney, V. Pons, T. J. Hebden, D. M. Heinekey and K. I. Goldberg, *J. Am. Chem. Soc.*, 2006, **128**, 12048-12049.

133. A. Staubitz, M. E. Sloan, A. P. M. Robertson, A. Friedrich, S. Schneider, P. J. Gates, J. Gunne and I. Manners, *J. Am. Chem. Soc.*, 2010, **132**, 13332-13345.

134. T. J. Hebden, M. C. Denney, V. Pons, P. M. B. Piccoli, T. F. Koetzle, A. J. Schultz, W. Kaminsky, K. I. Goldberg and D. M. Heinekey, *J. Am. Chem. Soc.*, 2008, **130**, 10812-10820.

135. Y. Kawano, M. Uruichi, M. Shimoi, S. Taki, T. Kawaguchi, T. Kakizawa and H. Ogino, *J. Am. Chem. Soc.*, 2009, **131**, 14946-14957.

136. R. T. Baker, J. C. Gordon, C. W. Hamilton, N. J. Henson, P. H. Lin, S. Maguire, M. Murugesu, B. L. Scott and N. C. Smythe, *J. Am. Chem. Soc.*, 2012, **134**, 5598-5609.

137. Y. F. Jiang, O. Blacque, T. Fox, C. M. Frech and H. Berke, *Organometallics*, 2009, **28**, 5493-5504.

138. C. Lichtenberg, L. Viciu, M. Adelhardt, J. Sutter, K. Meyer, B. de Bruin and H. Gruetzmacher, *Angew. Chem. Int. Ed.*, 2015, **54**, 5766-5771.

139. J. R. Vance, A. Schaefer, A. P. M. Robertson, K. Lee, J. Turner, G. R. Whittell and I. Manners, *J. Am. Chem. Soc.*, 2014, **136**, 3048-3064.

140. A. Rossin, G. Bottari, A. M. Lozano-Vila, M. Paneque, M. Peruzzini, A. Rossi and F. Zanobini, *Dalton Trans.*, 2013, **42**, 3533-3541.

141. M. A. Esteruelas, I. Fernandez, A. M. Lopez, M. Mora and E. Onate, *Organometallics*, 2014, **33**, 1104-1107.

142. M. Rosello-Merino, J. Lopez-Serrano and S. Conejero, *J. Am. Chem. Soc.*, 2013, **135**, 10910-10913.

143. A. E. W. Ledger, C. E. Ellul, M. F. Mahon, J. M. J. Williams and M. K. Whittlesey, *Chem. Eur. J.*, 2011, **17**, 8704-8713.

144. T. M. Douglas, A. B. Chaplin and A. S. Weller, *J. Am. Chem. Soc.*, 2008, **130**, 14432-14433.

145. L. J. Sewell, G. C. Lloyd-Jones and A. S. Weller, *J. Am. Chem. Soc.*, 2012, **134**, 3598-3610.

146. W. T. Klooster, T. F. Koetzle, P. E. M. Siegbahn, T. B. Richardson and R. H. Crabtree, *J. Am. Chem. Soc.*, 1999, **121**, 6337-6343.

147. M. Shimoi, S. Nagai, M. Ichikawa, Y. Kawano, K. Katoh, M. Uruichi and H. Ogino, *J. Am. Chem. Soc.*, 1999, **121**, 11704-11712.

148. T. M. Douglas, A. B. Chaplin, A. S. Weller, X. Yang and M. B. Hall, *J. Am. Chem. Soc.*, 2009, **131**, 15440-15456.

149. H. C. Johnson and A. S. Weller, *Angew. Chem. Int. Ed.*, 2015, **54**, 10173-10177.

150. A. E. Nako, A. J. P. White and M. R. Crimmin, *Dalton Trans.*, 2015, **44**, 12530-12534.

151. H. C. Johnson, A. P. M. Robertson, A. B. Chaplin, L. J. Sewell, A. L. Thompson, M. F. Haddow, I. Manners and A. S. Weller, *J. Am. Chem. Soc.*, 2011, **133**, 11076-11079.

152. A. B. Chaplin and A. S. Weller, *Inorg. Chem.*, 2010, **49**, 1111-1121.

153. R. Dallanegra, A. B. Chaplin and A. S. Weller, *Angew. Chem. Int. Ed.*, 2009, **48**, 6875-6878.

154. C. Y. Tang, A. L. Thompson and S. Aldridge, *Angew. Chem. Int. Ed.*, 2010, **49**, 921-925.

155. T. M. Douglas, A. B. Chaplin, A. S. Weller, X. Yang and M. B. Hall, *J. Am. Chem. Soc.*, 2009, **131**, 15440-15456.

156. G. Alcaraz, A. B. Chaplin, C. J. Stevens, E. Clot, L. Vendier, A. S. Weller and S. Sabo-Etienne, *Organometallics*, 2010, **29**, 5591-5595.

157. C. Y. Tang, N. Phillips, J. I. Bates, A. L. Thompson, M. J. Gutmann and S. Aldridge, *Chem. Commun.*, 2012, **48**, 8096-8098.

158. H. C. Johnson and A. S. Weller, *J. Organomet. Chem.*, 2012, **721**, 17-22.

159. D. Vidovic, D. A. Addy, T. Kramer, J. McGrady and S. Aldridge, *J. Am. Chem. Soc.*, 2011, **133**, 8494-8497.

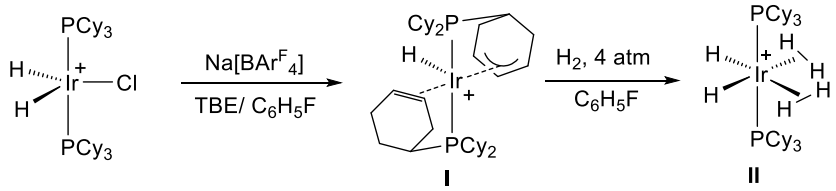
160. G. Alcaraz, L. Vendier, E. Clot and S. Sabo-Etienne, *Angew. Chem. Int. Ed.*, 2010, **49**, 918-920.

161. M. C. MacInnis, R. McDonald, M. J. Ferguson, S. Tobisch and L. Turculet, *J. Am. Chem. Soc.*, 2011, **133**, 13622-13633.

2 Dehydrocoupling of amine-boranes using an $\{Ir(PCy_3)_2\}^+$ fragment

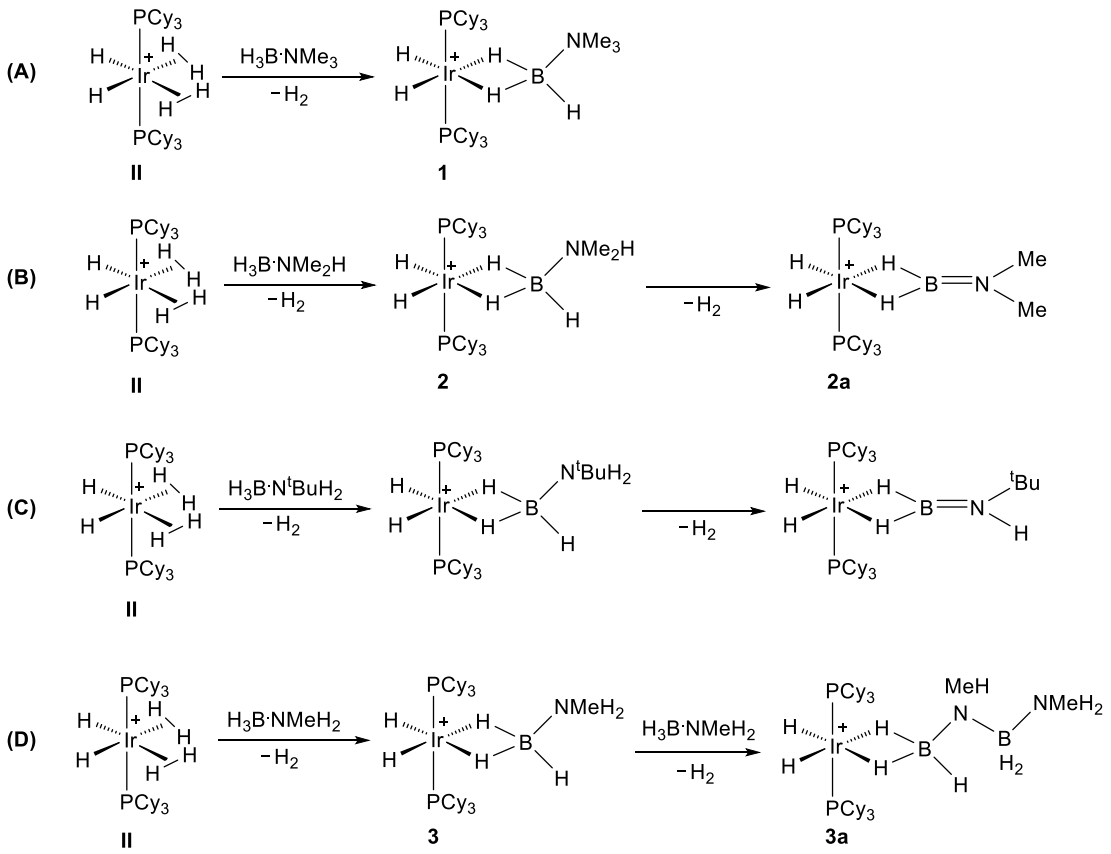
2.1 Introduction

The transition metal catalysed dehydrocoupling of amine-boranes, in particular the parent $H_3B{\cdot}NH_3$, which results in the formation of borazine, polyborazylene and polyaminoborane or any combination of these three, has attracted significant interest in the past decade as discussed in Chapter 1. Various mechanisms, mostly based on DFT calculations and kinetic studies have been proposed for the transition metal catalysed dehydrocoupling of $H_3B{\cdot}NH_3$. To particular significance of this thesis is the use of the $\{Ir(H)_2(PCy_3)_2\}^+$ fragment for the dehydrogenation of amine-boranes. The latent source of the $\{Ir(H)_2(PCy_3)_2\}^+$ fragment is an 18 electron species, $[Ir(H)_2(PCy_3)_2(\eta^2\text{-}H_2)_2][BAr^F{}_4]$ (**II**), which is generated *in situ* from the hydrogenation of $[IrHPCy_2(\eta^2\text{-}C_6H_9)PCy_2(\eta^3\text{-}C_6H_8)][BAr^F{}_4]$ (**I**) (Scheme 2.1). The $\{IrHPCy_2(\eta^2\text{-}C_6H_9)PCy_2(\eta^3\text{-}C_6H_8)\}^+$ fragment was first reported with the $[PhC(SO_2CF_3)_2]^-$ anion by Crabtree in 1986 by the addition of $PhCH(SO_2CF_3)_2$ to $[IrH_5(PCy_3)_2]$.[1] In 2010, the $\{IrHPCy_2(\eta^2\text{-}C_6H_9)PCy_2(\eta^3\text{-}C_6H_8)\}^+$ cation was reported with weakly coordinating $[BAr^F{}_4]^-$ anion by the Weller group (Scheme 2.1).[2]



Scheme 2.1 Formation of **I** and *in situ* hydrogenation to form the precatalyst **II**. $[BAr^F{}_4]^-$ anions are not shown.

The Weller group has also reported extensively on the coordination chemistry and the dehydrocoupling of $H_3B{\cdot}NMeRR'$ (R, R' = Me, H) using the $\{Ir(H)_2(PCy_3)_2\}^+$ fragment. Addition of $H_3B{\cdot}NMe_3$ to the C_6H_5F solution of $[Ir(H)_2(PCy_3)_2(\eta^2\text{-}H_2)_2][BAr^F{}_4]$ (**II**) results in the immediate loss of hydrogen and the formation of the sigma-complex $[Ir(H)_2(PCy_3)_2(\eta^2\text{-}H_3B{\cdot}NMe_3)][BAr^F{}_4]$ (**1**, Scheme 2.2A).[3] Complex **1** remains stable in solution and does not undergo any dehydrogenation process due to the absence of an N−H proton although exchange between the terminal and bridging B–H hydrides in the presence of D_2 have been reported.[3, 4] The analogous sigma-complex $[Ir(H)_2(PCy_3)_2(\eta^2\text{-}H_3B{\cdot}NMe_2H)][BAr^F{}_4]$ (**2**) formed from the reaction of $H_3B{\cdot}NMe_2H$ with $[Ir(H)_2(PCy_3)_2(\eta^2\text{-}H_2)_2][BAr^F{}_4]$ (**II**) dehydrogenates over time ($t_{1/2}$ = 24 h) to give the bound amino-borane complex $[Ir(H)_2(PCy_3)_2(\eta^2\text{-}H_2B{=}NMe_2)][BAr^F{}_4]$ (**2a**, Scheme 2.2B).[3] Consistent with this observation, $[Ir(H)_2(PCy_3)_2(\eta^2\text{-}H_3B{\cdot}N^tBuH_2)][BAr^F{}_4]$ also dehydrogenates to give the bound amino-borane complex $[Ir(H)_2(PCy_3)_2(\eta^2\text{-}H_2B{=}N^tBuH)][BAr^F{}_4]$ (Scheme 2.2C).[5] Further to this series, the reactivity of $H_3B{\cdot}NMeH_2$ towards the $\{Ir(H)_2(PCy_3)_2\}^+$ fragment is also interesting. When prepared pure, sigma-complex $[Ir(H)_2(PCy_3)_2(\eta^2\text{-}H_3B{\cdot}NMeH_2)][BAr^F{}_4]$ (**3**) remains stable in solution (for 48 h at 298 K) and does not undergo dehydrogenation to give an amino-borane ($H_2B{=}NMeH$)-bound complex, $[Ir(H)_2(PCy_3)_2(\eta^2\text{-}H_2B{=}NMeH)][BAr^F{}_4]$. However, addition of a further one equivalent of $H_3B{\cdot}NMeH_2$ to **3** results in the dehydrocoupling of $H_3B{\cdot}NMeH_2$ and the formation of the bound dimer $[Ir(H)_2(PCy_3)_2(\eta^2\text{-}H_3B{\cdot}NMeHBH_2{\cdot}NMeH_2)][BAr^F{}_4]$ (**3a**, Scheme 2.2D).[6]



Scheme 2.2 Reactivity of $H_3B{\cdot}NMeRR'$ (R, R' = Me, H) and $H_3B{\cdot}N^tBuH_2$ with $[Ir(H)_2(PCy_3)_2(\eta^2\text{-}H_2)_2][BAr^F{}_4]$ (**II**). $[BAr^F{}_4]^-$ anions are not shown.

Reactions of $[Ir(H)_2(PCy_3)_2(\eta^2\text{-}H_2)_2][BAr^F{}_4]$ with $H_3B{\cdot}NHRR'$ (RR' = Me_2, HMe, H^tBu) show a trend which can be correlated with the steric bulk on nitrogen of amine-boranes:

$H_3B{\cdot}NMe_2H$: Dehydrogenation but no dehydrocoupling.

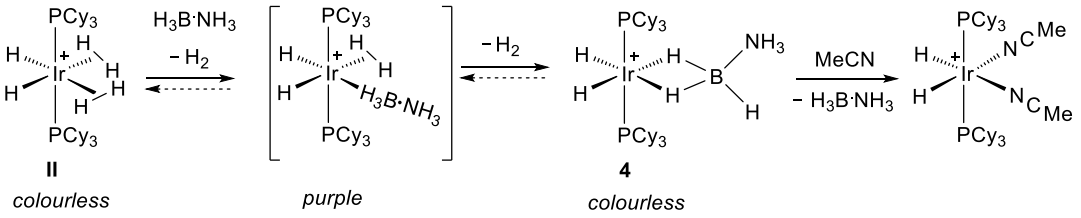
$H_3B{\cdot}N^tBuH_2$: Dehydrogenation but no dehydrocoupling.

$H_3B{\cdot}NMeH_2$: Dehydrocoupling and formation of diborazane $H_3B{\cdot}NMeHBH_2{\cdot}NMeH_2$.

To probe further into the role of steric bulk on the dehydrogenation of amine-boranes, the reactivity of the least bulky amine-borane, $H_3B{\cdot}NH_3$ is explored with complex **II**, in order to investigate both fundamental coordination chemistry and B–N bond forming events.

2.2 Reactivity of $H_3B{\cdot}NH_3$ with $[Ir(H)_2(PCy_3)_2(\eta^2\text{-}H_2)_2][BAr^F{}_4]$ (II): Synthesis of $[Ir(H)_2(PCy_3)_2(\eta^2\text{-}H_3B{\cdot}NH_3)][BAr^F{}_4]$ (4)

Addition of 1.2 equivalents of $H_3B{\cdot}NH_3$ to a colourless C_6H_5F solution of $[Ir(H)_2(PCy_3)_2(\eta^2\text{-}H_2)_2][BAr^F{}_4]$ (**II**) resulted in the immediate formation of a purple solution. Upon degassing, (freeze-pump-thaw), the purple solution turned back to a colourless solution which was characterised to be $[Ir(H)_2(PCy_3)_2(\eta^2\text{-}H_3B{\cdot}NH_3)][BAr^F{}_4]$ (**4**) (Scheme 2.3). Due to the instability of the purple species in a non-hydrogen environment, we were unable to isolate it or employ ESI-MS technique for its characterisation. However, the hydride region of the ^{1}H NMR spectrum of the purple solution showed resonances corresponding to both **II** (δ −8.22, br)[2] and **4** (*vide infra*) in addition to an unidentified broad resonance at δ −12.02. We speculate that the purple species is $[Ir(H)_2(PCy_3)_2(\eta^1\text{-}H_3B{\cdot}NH_3)(\eta^2\text{-}H_2)][BAr^F{}_4]$, which upon degassing, proceeds to form **4** suggesting the possibility of an equilibrium between **II** and **4** affected by the competitive ligands $H_3B{\cdot}NH_3$ and H_2 as shown in Scheme 2.3. Reaction time for the formation of **4** (1 h) is relatively longer than compared to the formation of sigma-complexes **1**, **2** and **3**. This may be due to the poor solubility of $H_3B{\cdot}NH_3$ in C_6H_5F solvent which causes slow displacement of the sigma-bound H_2 by $H_3B{\cdot}NH_3$. Addition of 10 equivalents of CH_3CN to the C_6H_5F solution of **4** resulted in the displacement of the bound $H_3B{\cdot}NH_3$ and the formation of the known complex $[Ir(H)_2(PCy_3)_2(NCMe)_2][BAr^F{}_4]$[3, 7] (Scheme 2.3) and the free $H_3B{\cdot}NH_3$ (^{11}B NMR: δ 21.7, q, $^1J_{HB}$ = 97 Hz).[8]



Scheme 2.3 Synthesis of **4** and displacement of bound $H_3B{\cdot}NH_3$ by CH_3CN. $[BAr^F{}_4]^-$ anions are not shown.

Complex **4** was characterised by NMR spectroscopy and ESI-MS. Attempts to isolate crystals of **4** by layering with pentane or hexane were not successful, and resulted in unidentified non-crystalline decomposition products. However, analytically pure, crystalline material of $[Ir(H)_2(PCy_3)_2(\eta^2\text{-}H_3B{\cdot}NH_3)][BAr^{Cl}{}_4]$ (**4'**) was obtained by the addition of $H_3B{\cdot}NH_3$ to $[Ir(H)_2(PCy_3)_2(\eta^2\text{-}H_2)_2][Bar^{Cl}{}_4]$[6] in 1,2-$F_2C_6H_4$. Complex **4'** was characterised by NMR spectroscopy, ESI-MS, microanalysis and single crystal X-ray diffraction. The solid state structure of complex **4'** is shown in Figure 2.1 and shows the formulation.

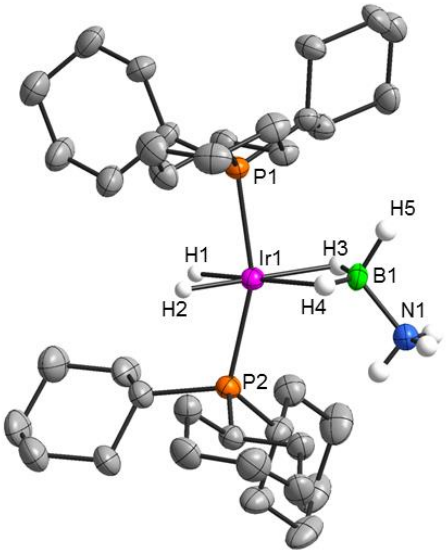


Figure 2.1 Solid state structure of **4'** with displacement ellipsoids at the 50% probability level. $[BAr^{Cl}{}_4]^-$ anion and all cyclohexyl hydrogen atoms omitted for clarity. Selected bond lengths (Å) and angles (°): Ir1−B1, 2.209(5); Ir1−P1, 2.3206(12); Ir1−P2, 2.3319(12); B1−N1, 1.595(7). P1−Ir1−P2, 159.52(4).

The B−*H* hydrides were located in the final difference map, while Ir−*H* hydrides were not located with any reliability and placed in calculated positions geometrically trans to the appropriate B−*H* hydride, and set at a sensible bond length of 1.55 Å consistent with the Ir−H bond lengths in complexes **1** and **3**.[3, 6] The Ir1−B1, Ir1−P1, Ir1−P2 and B1−N1 distances are all the same within error with the previously reported sigma-complexes **1** and **3** (Table 2.1).

Table 2.1: Selective bond lengths (Å) for the sigma-complexes of amine-boranes with $\{Ir(H)_2(PCy_3)_2\}^+$ fragment.

Bond	Complex **1**[3]	Complex **3**[6]	Complex **4'**
Ir−B	2.207(7)	2.210(7)	2.209(5)
Ir−P1	2.3245(13)	2.3281(8)	2.3206(12)
Ir−P2	2.3287(14)	2.3347(8)	2.3319(12)
B−N	1.593(8)	1.580(8)	1.595(7)

In solution (1,2-$F_2C_6H_4$, 298 K), the ^{1}H NMR spectrum of complex **4'** shows a singlet at δ 4.22 (s, 3H) corresponding to the N*H*$_3$ protons and a triplet assigned to the iridium hydrides at δ −20.33 (broad t, $^2J_{HP}$ = 15 Hz, 2H). A quadrupolar broadened signal of integral 2H at δ −5.91, corresponding to the iridium bound B−*H* hydrides, is also observed. The remaining B−*H* signal is not observed at room temperature as presumably it is too broad, but appears at δ 6.13 on cooling to 250 K. The $^{31}P\{^1H\}$ NMR spectrum of **4'** at 298 K shows two broad signals which resolve to two tightly coupled AB roofed doublets at 250 K: δ 38.5 (d, $^2J_{PP}$ = 273 Hz, 1P) and 31.9 (d, $^2J_{PP}$ = 273 Hz, 1P), the centre of signals essentially unchanged from that at 298 K (Figure 2.2). This is suggestive of a slow fluxional process in which the bridging and the terminal B−H bonds of **4'** slowly exchange in solution at room temperature.[4] An exchange mechanism that involves the change of amine-borane coordination mode from η^2 to η^1 followed by the rotation around Ir−H bond has been proposed for the bridging and the terminal B−H exchange in $[Ir(H)_2(PCy_3)_2(\eta^2\text{-}H_3B{\cdot}NMe_3)][BAr^F{}_4]$.[4]

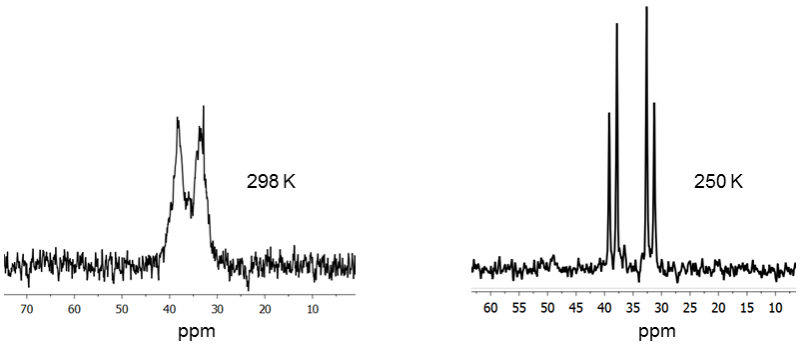


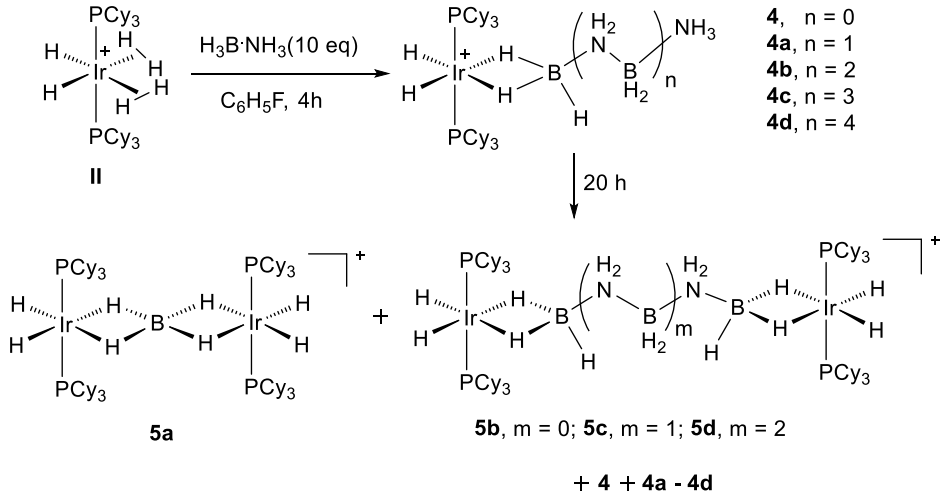
Figure 2.2 $^{31}P\{^{1}H\}$ NMR spectra of **4'** at 298 K (left) and 250 K (right).

The ^{11}B NMR spectrum of **4'** shows a broad resonance at δ 10.2 corresponding to the bound BH_3 group, shifted downfield by 31.9 ppm compared with that of free $H_3B{\cdot}NH_3$ (δ −21.7, q, $^{1}J_{BH}$ = 97.7 Hz). All the spectral data for complexes **4'** and **4** are consistent with the spectral data of complexes **1**, **2** and **3**.[3, 9]

2.3 Addition of 10 equivalents of $H_3B{\cdot}NH_3$ to II

In order to explore the catalytic dehydrocoupling, 10 equivalents of $H_3B{\cdot}NH_3$ were added to a C_6H_5F solution of $[Ir(H)_2(PCy_3)_2(\eta^2\text{-}H_2)_2][BAr^F{}_4]$ (**II**). An ESI-Mass Spectrum (Figure 2.3) after 4 h showed the formation of multiple metal-bound oligomers, $[Ir(H)_2(PCy_3)_2(\eta^2\text{-}H_3B{\cdot}\{NH_2BH_2\}_n{\cdot}NH_3)][BAr^F{}_4]$ (**4**, n = 0; **4a**, n = 1; **4b**, n = 2; **4c** n = 3 and **4d**, n = 4) (Scheme 2.4). Isotopic patterns of the observed ESI-MS match well with the calculated isotopic patterns of **4** and **4a** - **4d**. The formation of bound oligomeric fragments was also observed by NMR spectroscopy. However, due to overlapping signals proper characterisation of these complexes was problematic from this mixture and was achieved by the independent synthesis of **4a** and **4b** as discussed later in Sections 2.4 and 2.6. The ^{1}H NMR spectrum of the mixture (Figure 2.4) showed distinct broad signals at δ −20.29, −19.87 and −19.60 corresponding to the IrH_2 hydrides of bound oligomers **4**, **4a** and **4b** in a 1:10:10 ratio respectively. The higher order bound oligomers **4c** and **4d** observed in ESI-MS are not observed by NMR spectroscopy presumably due to their low concentrations. A broad overlapping signal corresponding to bound BH_2 hydrides was also

observed at δ −6.3. The ^{11}B NMR spectrum (Figure 2.5) showed peaks at δ 14.2 corresponding to Ir···H_3B, and at δ −11.8 corresponding to the BH_2 and BH_3 fragments present on the bound oligomers. Formation of borazine in ~ 10% yield was also observed by the ^{11}B NMR spectroscopy. The ^{31}P{^{1}H} NMR spectrum showed overlapping AB doublets at δ 37.2 and 32.2 [$^2J_{PP}$ ~ 280 Hz]. All the above discussed spectral features suggest the formation of multiple metal-bound oligomers during Ir-catalysed dehydrocoupling of $H_3B{\cdot}NH_3$ (Scheme 2.4) similar to those observed by ESI-MS for olefin polymerisation.[10, 11] To the best of our knowledge this is the first observation of multiple metal bound insertion products during metal-catalysed dehydrocoupling of amine-boranes. The sigma-complexes **4** and **4a**-**4d** can be represented as the model complexes for the growing polymer chain on a metal centre.



Scheme 2.4 Reactivity of 10 equivalents of $H_3B{\cdot}NH_3$ with $[Ir(H)_2(PCy_3)_2(\eta^2\text{-}H_2)_2][BAr^F{}_4]$ **(II)**. $[BAr^F{}_4]^-$ anions are not shown.

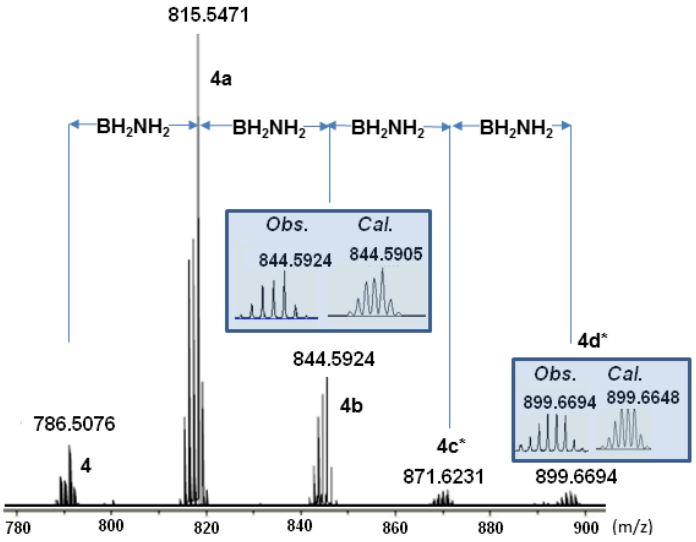


Figure 2.3 ESI-MS after 4 h of adding 10 equivalents of $H_3B{\cdot}NH_3$ to complex **II**. * corresponds to $[M\text{-}H_2]^+$.

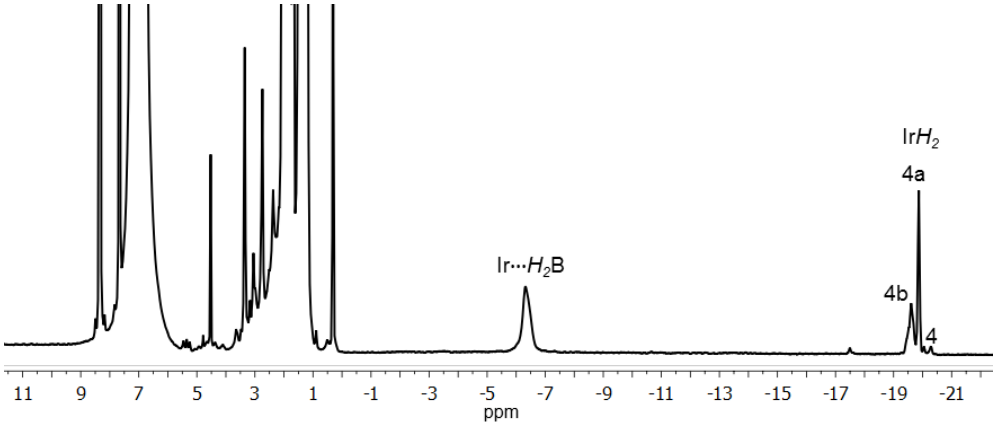


Figure 2.4 ^{1}H NMR spectrum after 4 h of adding 10 equivalents of $H_3B{\cdot}NH_3$ to complex **II**.

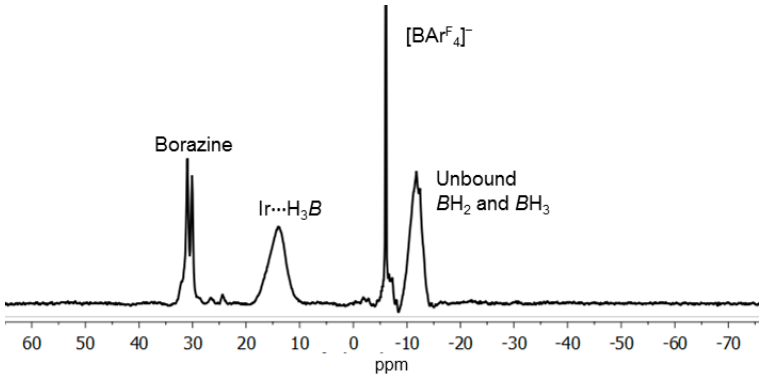


Figure 2.5 ^{11}B NMR spectrum after 4 h of adding 10 equivalents of $H_3B{\cdot}NH_3$ to complex **II**.

Proposed sigma-complexes **4** and **4a−4d** showed decomposition over time in solution. An ESI-MS after 24 h showed the formation of multiple iridium-dimers bound to either $[BH_4]^-$ or $[BH_3{\cdot}(NH_2BH_2)_mNH_2{\cdot}BH_3]^-$ (m = 0 - 2) fragments (Scheme 2.4, Figure 2.6). Structural characterisation of one of the decomposition products, $[Ir(H)_2(PCy_3)_2(\mu\text{-}H_4B)Ir(H)_2(PCy_3)_2][BAr^F{}_4]$ (**5a**), is discussed in Section 2.5 which shows that the $[BH_4]^-$ fragment is bridged between two iridium centres, giving the overall complex a monocationic charge. On the basis of the structure of **5a**, the formulation of other decomposition products was speculated to be $[Ir(H)_2(PCy_3)_2\mu\text{-}(\eta^2\text{-}BH_3{\cdot}\{NH_2BH_2\}_mNH_2{\cdot}\eta^2\text{-}BH_3)Ir(H)_2(PCy_3)_2][BAr^F{}_4]$ (**5b**, m = 0; **5c**, m = 1; **5d**, m = 2) in which the $[BH_3{\cdot}\{NH_2BH_2\}_mNH_2{\cdot}BH_3]^-$ fragments are bridged between two metal centres (Scheme 2.4). The observed ESI-MS isotopic patterns match well with the calculated isotopic patterns for **5a**-**5d**.

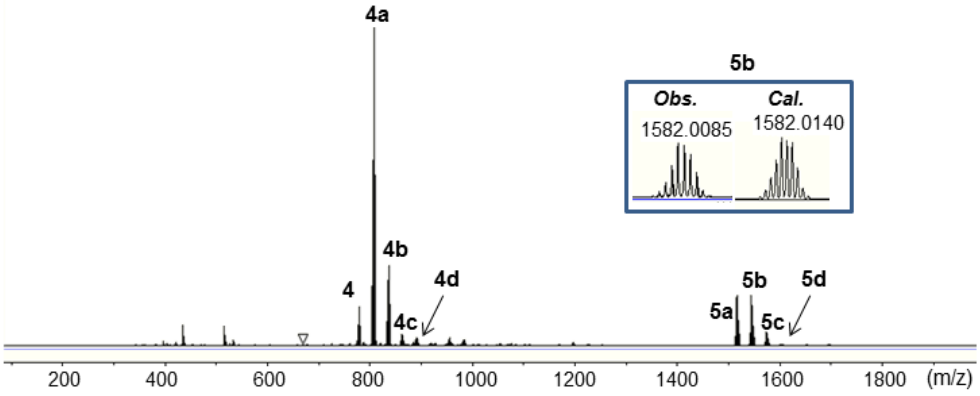
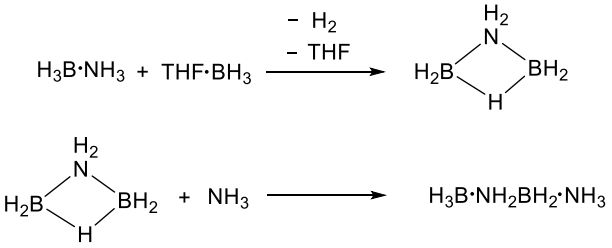


Figure 2.6 ESI-MS after 24 h of adding 10 equivalents of $H_3B{\cdot}NH_3$ to complex **II**.

2.4 Synthesis of $[Ir(H)_2(PCy_3)_2\ (\eta^2\text{-}H_3B{\cdot}\{NH_2BH_2\}_n{\cdot}NH_3)][BAr^F{}_4]$ (n = 1, 2)

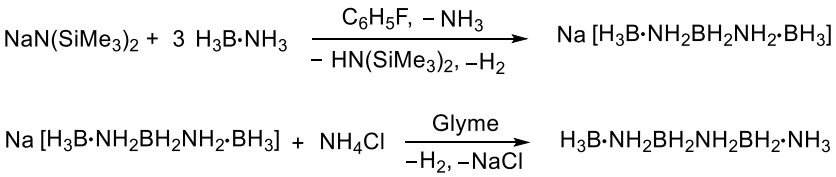
To elucidate the mixtures of organometallic species observed during catalytic dehydrocoupling of $H_3B{\cdot}NH_3$ as discussed in Section 2.3, we synthesised the major observed complexes, **4a** and **4b**. In order to synthesise **4a** and **4b**, we prepared $H_3B{\cdot}NH_2BH_2{\cdot}NH_3$ (dimer) and $H_3B{\cdot}NH_2BH_2NH_2BH_2{\cdot}NH_3$ (trimer). $H_3B{\cdot}NH_2BH_2{\cdot}NH_3$ was

synthesised as per the recent method reported by Shore *et al*.[12] in which $H_3B{\cdot}NH_3$ was first reacted with $BH_3{\cdot}THF$ to produce amino-diborane to which ammonia gas was added to produce $H_3B{\cdot}NH_2BH_2{\cdot}NH_3$ (Scheme 2.5).



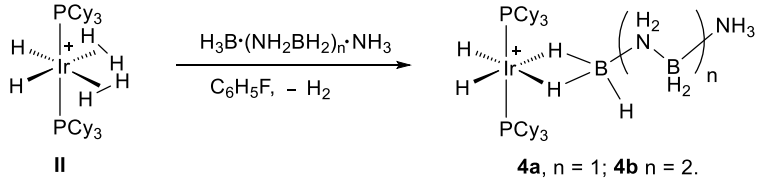
Scheme 2.5 Synthesis of $H_3B{\cdot}NH_2BH_2{\cdot}NH_3$

$H_3B{\cdot}NH_2BH_2NH_2BH_2{\cdot}NH_3$ was synthesised using the method reported by Sneddon *et al.* by reacting the linear anionic borazane $Na[H_3B{\cdot}NH_2BH_2NH_2{\cdot}BH_3]$ with NH_4Cl in glyme (Scheme 2.6).[13] $Na[H_3B{\cdot}NH_2BH_2NH_2{\cdot}BH_3]$ was prepared by the reaction of sodium bis(trimethylsilyl) amide (NaHMDS) with $H_3B{\cdot}NH_3$ in C_6H_5F.



Scheme 2.6 Synthesis of $H_3B{\cdot}NH_2BH_2NH_2BH_2{\cdot}NH_3$.

The sigma-complexes $[Ir(H)_2(PCy_3)_2(\eta^2\text{-}H_3B{\cdot}\{NH_2BH_2\}n{\cdot}NH_3)][BAr^F{}_4]$ (**4a**, n = 1; **4b**, n = 2) were then prepared by the reaction of $[Ir(H)_2(PCy_3)_2(\eta^2\text{-}H_2)_2][BAr^F{}_4]$ (**II**) with the corresponding amine-boranes ($H_3B{\cdot}\{NH_2BH_2\}_n{\cdot}NH_3$, n = 1, 2) in quantitative yields measured by ^1H NMR spectroscopy (Scheme 2.7).



Scheme 2.7 Synthesis of complexes **4a** and **4b**. $[BAr^F{}_4]^-$ anions are not shown.

Complexes **4a** and **4b** were initially characterised by NMR spectroscopy and ESI-MS. $^{31}P\{^{1}H\}$ NMR spectra for the both **4a** and **4b** show two tightly coupled AB roof doublets [**4a**: δ 37.4 (d, $^{2}J_{PP}$ = 284 Hz, 1P), 32.2 (d, $^{2}J_{PP}$ = 284 Hz, 1P); **4b**: δ 37.1 (d, $^{2}J_{PP}$ = 284 Hz, 1P), 32.2 (d, $^{2}J_{PP}$ = 284 Hz, 1P)] consistent with the previously reported complex $[Ir(H)_2(PCy_3)_2(\eta^2\text{-}H_3B{\cdot}NMeHBH_2{\cdot}NH_2Me)][BAr^F{}_4]$.[9] ^{1}H NMR signals, in particular those for Ir*H*$_2$ [**4a**: δ −19.87 (apparent triplet, $^{2}J_{HP}$ = 15, 2H, IrH_2); **4b**: δ −19.61 (apparent triplet, $^{2}J_{HP}$ = 15, 2H, IrH_2)] and IrB*H*$_2$ [**4a**: δ – 6.32 (br, 2H); **4b**: δ −6.48 (br, 2H] are consistent with those observed for the amine-borane sigma-complexes with the same metal fragments (**1** - **4**) as discussed in Sections 2.2 and 2.3. The ^{11}B NMR spectrum of complex **4a** shows signals at δ 13.8 (br) and −11.5 (br) corresponding to the bound *B*H_3 and the unbound *B*H_2 fragments, similar to those reported for the analogous dimer $[Ir(H)_2(PCy_3)_2(\eta^2\text{-}H_3B{\cdot}NMeHBH_2{\cdot}NH_2Me)][BAr^F{}_4]$ **3a**.[9] The ^{11}B NMR spectrum of complex **4b** shows signals at δ 15.6 (br, 1B) and −11.7 (br, 2B) corresponding to the bound *B*H_3 and the two unbound *B*H_2 fragments. Attempts to isolate crystals of **4a** and **4b** by layering with C_6H_5F/pentane or hexane were not successful. However, changing the anion from $[BAr^F{}_4]^-$ to $[BAr^{Cl}{}_4]^-$, in a similar way as described above for the isolation of **4'**, allowed for the isolation of $[Ir(H)_2(PCy_3)_2(\eta^2\text{-}H_3B{\cdot}NH_2BH_2NH_2BH_2{\cdot}NH_3)][BAr^{Cl}{}_4]$ (**4b'**) in approximately 50% yield. Complex **4b'** was characterised by NMR spectroscopy, ESI-MS, single crystal X-ray diffraction and elemental analysis. NMR spectral details of **4b'** are similar to that of **4b** (See Chapter 6 for the spectral details) and are consistent with the η^2 binding of $H_3B{\cdot}NH_2BH_2NH_2BH_2{\cdot}NH_3$ with the $\{Ir(H)_2(PCy_3)_2\}^+$ fragment.

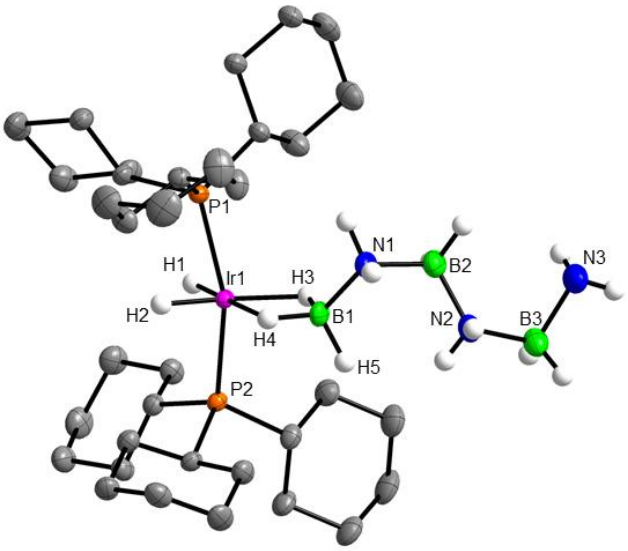


Figure 2.7 Structure of the cationic portion of **4b'** with displacement ellipsoids at the 50% probability level. All cyclohexyl hydrogen atoms omitted for clarity. Selected bond lengths (Å) and bond angles (˚): Ir1−B1, 2.198(3); Ir1−P1, 2.3182(8); Ir1−P2, 2.3188(7); P1−Ir1−P2, 160.64(3).

The solid state structure of complex **4b'** further confirms the formulation as the product of two insertion events in the dehydrocoupling of $H_3B{\cdot}NH_3$ (Figure 2.7). The phosphorus atoms occupy trans geometry around the iridium centre, as also confirmed by its solution state $^{31}P\{^1H\}$ NMR spectrum which shows inequivalent phosphorus environments with a trans phosphorus coupling ($^2J_{PP}$ = 286 Hz). In the X-ray structure, all the hydrogen atoms were located on the Fourier map. Bond lengths Ir1···B1 2.198(3) Å and B1−N1 1.556(4) Å are consistent with the previously reported η^2 sigma amine-borane complexes with the same metal fragment $\{IrH_2(PCy_3)_2\}^+$, as compared to the corresponding bond lengths in complexes **1**, **3** and **4** (Table 2.1).

Intermolecular dihydrogen interactions between hydridic $BH^{\delta-}$ and protic $NH^{\delta+}$ in amine-boranes has previously been reported in the literature[14-19] and has been suggested to be important in the dehydrogenation process.[6] In the solid state, these dihydrogen interactions are usually characterised as B−H···H−N bond distances of ~1.7-2.2 Å, B−H−H angles of 95-120˚ and slightly larger H−H−N angles of 117-171˚.[20-23] Aldridge and co-workers have reported the intermolecular B−H···H−N dihydrogen bonds with short

H···H contacts measuring about 2.0 Å for $H_3B{\cdot}NMe_xH_{3-x}$ (x = 0 - 2).[17] Figure 2.8 shows the dihydrogen interactions in the extended structure of the unit cell of $[Ir(H)_2(PCy_3)_2H_3B{\cdot}(NH_2BH_2)_2{\cdot}NH_3][BAr^{Cl}{}_4]$ (**4b'**). H13 and H14 attached to B3 and N3 respectively show a contact distance of 2.106 Å exhibiting a dihydrogen bond between H13 and H14. Bond angles N3−H14···H13, 160.9˚ and H14···H13−B3, 102.2˚ are also consistent with a $B{-}H^{\delta-}\cdots{}^{\delta+}H{-}N$ interaction. This is similar to the B−H···H−N contact distances 2.06(2) and 2.20(2) Å found in $H_3B[(CH_3)NHBH_2]_2N(CH_3)H_2$ for which N−H···H bond angles [151.7(11)° and 150.5(11)°] and H···H−B bond angles [97.7(7)° and 90.9(8)°] also fall in the range indicated above.[13]

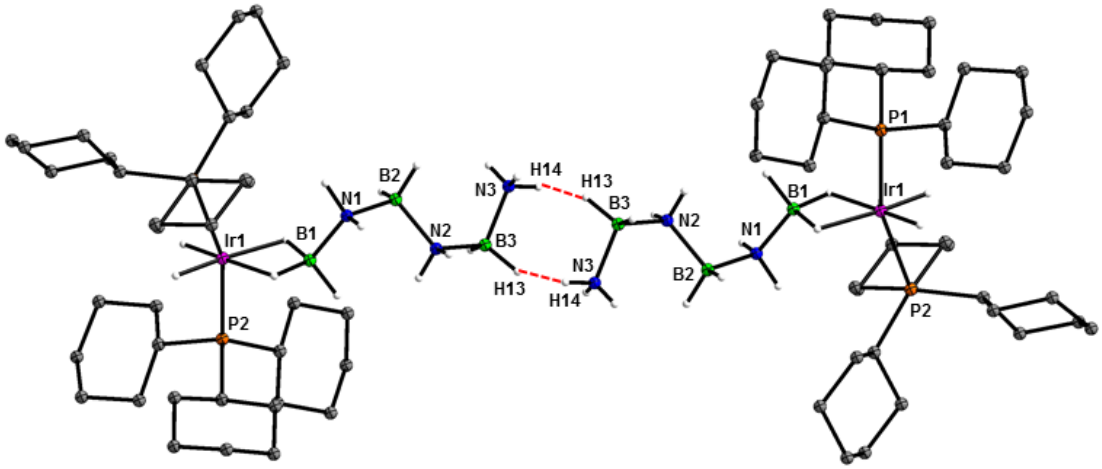


Figure 2.8 Dihydrogen interactions in **4b'**. Displacement ellipsoids are shown at the 50% probability level. $[BAr^F{}_4]^-$ anion and all cyclohexyl hydrogen atoms omitted for clarity. Selected bond lengths (Å) and bond angles (˚): H13−H14, 2.106; N3−H14−H13, 160.9; H14−H13−B3, 102.2.

2.5 Formation of $[Ir(H)_2(PCy_3)_2(\mu\text{-}BH_4)Ir(H)_2(PCy_3)_2][BAr^F{}_4]$ (5a)

As discussed above, $[Ir(H)_2(PCy_3)_2(\mu\text{-}BH_4)Ir(H)_2(PCy_3)_2][BAr^F{}_4]$ is observed as a decomposition product during the catalytic dehydrocoupling of $H_3B{\cdot}NH_3$. In order to properly characterise it, its isolation was attempted. Three equivalents of $H_3B{\cdot}NH_3$ was added to a C_6H_5F solution of complex **II**, degassed after 1 h and then stirred overnight at the room temperature. Layering the resulting mixture with pentane for one week at 298 K

resulted in the formation of a yellow-brown oil and several yellow crystals. Yellow crystals were characterised to be **5a** using single crystal X-ray diffraction method. Due to the very low yield, NMR spectra of **5a** could not be obtained.

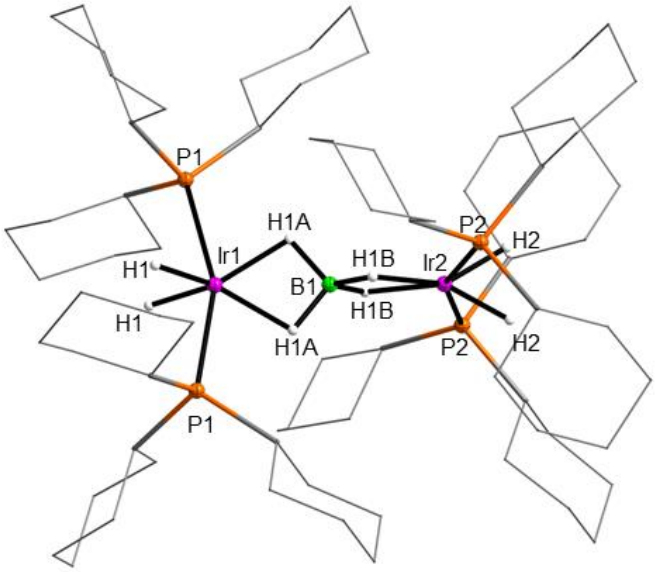


Figure 2.9 Structure of the cationic portion of **5a**. Displacement ellipsoids are drawn at the 50% probability level. For clarity, cyclohexyl groups are depicted as a wire frame and all cyclohexyl hydrogen atoms are omitted. Selected bond lengths (Å): Ir1–B1, 2.170(5); Ir2–B1, 2.159(5); Ir1–P1, 2.3357(11); Ir2–P2, 2.3327(11). Selected bond angles (˚): P1–Ir1–P1, 157.98(5); P2–Ir2–P2, 154.77(6); ∠plane(Ir1H1AB1H1A)/plane(Ir2H1BB1H1B), 78.4; ∠plane(P1Ir1P1)/plane(P2Ir2P2), 79.9.

Figure 2.9 represents the solid state structure of **5a** which shows its formulation. The $[BH_4]^-$ fragment is linked with the two distorted octahedral iridium centres via two η^2 three-centre-two electron B−H bonds. Both the phosphine groups occupy trans positions with bond angles of 157.98(5)˚, P1–Ir1–P1 and 154.77(6)˚, P2–Ir2–P2. Each iridium-phosphine plane (P/Ir/P) is twisted with respect to one another by 79.9˚. Ir1···B1, 2.170(5) Å and Ir2···B1, 2.159(5) Å are consistent with a sigma B−H interaction with iridium.[3] Both $IrBH_2$ fragments lie at 78.4˚ relative to one another. Monometallic borohydride complexes have been previously reported as the end product of the dehydrocoupling of amine-boranes catalysed by zirconium and iridium complexes.[24, 25] The coordination chemistry of the tetrahydroborate ion in **5a** is similar to that observed in $[Cu(PPh_3)_2(\mu$-

BH_4)Cu(PPh_3)$_2$][ClO_4][26] and [(tripod)HRu(μ-BH_4)RuH(tripod)][BPh_4][27] [tripod = MeC(CH_2PPh_2)$_3$] in which a tetrahedral $[BH_4]^-$ group bridges the two tetrahedral Cu(I) centres or two octahedral Ru(II) centres.

2.6 Comparison of the NMR spectra of the independently synthesised Ir-bound oligomers with the spectra from the dehydrocoupling of $H_3B{\cdot}NH_3$ catalysed by II

The ^1H, $^{31}P\{^1H\}$ and ^{11}B NMR spectra of the mixture of sigma-complexes observed during catalytic dehydrocoupling (10 mol% **II**, Section 2.3) of $H_3B{\cdot}NH_3$ match well with the independently synthesised sigma-complexes **4**, **4a** and **4b** (Figure 2.10 - 2.12).

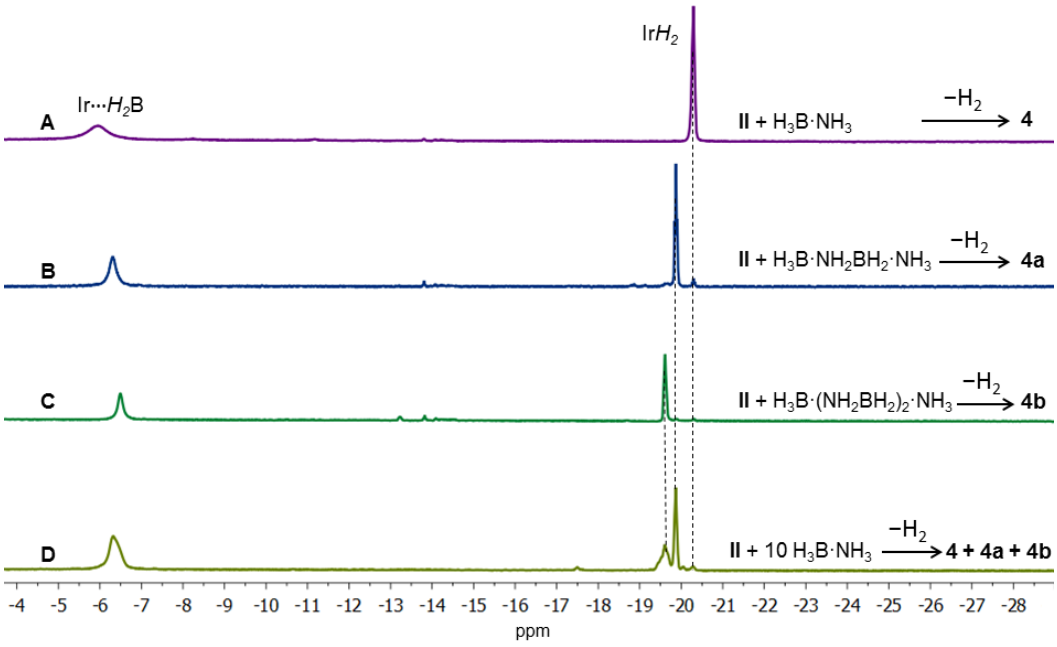


Figure 2.10 ^1H NMR spectra of the hydride region, **A**: **4**; **B**: **4a**; **C**: **4b**; **D**: after 4 h of the addition of 10 equivalents of $H_3B{\cdot}NH_3$ to complex **II**.

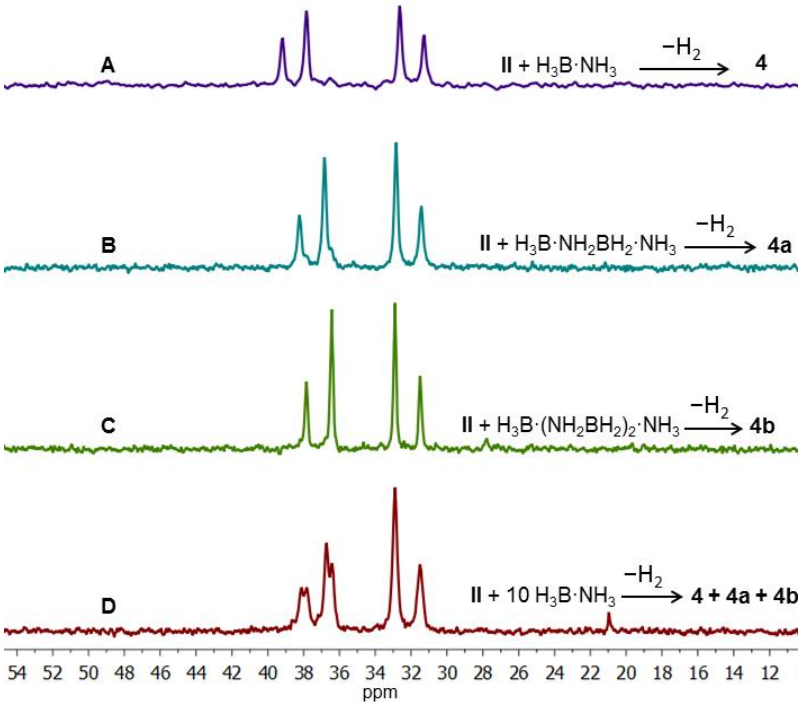


Figure 2.11 $^{31}P\{^{1}H\}$ NMR spectra, **A**: **4** (at 250 K); **B**: **4a**; **C**: **4b**; **D**: after 4 h of the addition of 10 equivalents of $H_3B{\cdot}NH_3$ to complex **II**.

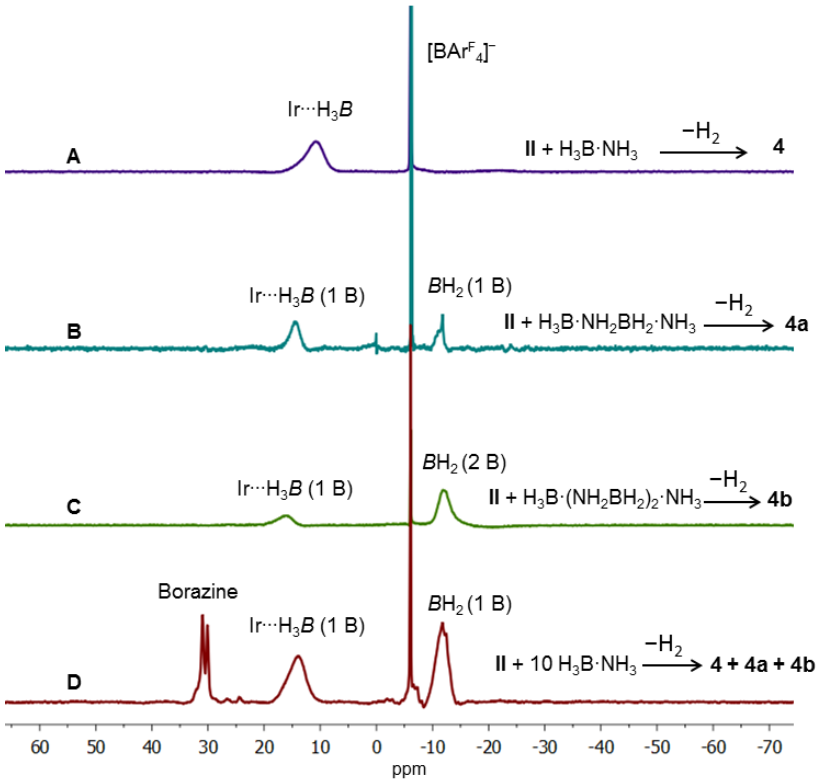


Figure 2.12 ^{11}B NMR spectra, **A**: **4**; **B**: **4a**; **C**: **4b**; **D**: after 4 h of the addition of 10 equivalents of $H_3B{\cdot}NH_3$ to complex **II**. Numbers in parentheses are relative integrals with respect to $[BAr^F{}_4]^-$.

2.7 Formation of polyaminoborane

During the course of $H_3B{\cdot}NH_3$ dehydrocoupling (10 mol% **II**, C_6H_5F, closed system), a white precipitate was obtained which was purified by filtration and then subsequent washing with pentane and THF. The white solid was found to be insoluble in benzene, pentane, hexane, toluene, chloroform, water and THF. The insolubility of polyaminoborane has long been known in literature[28] and therefore we employed solid state IR-spectroscopic techniques for its characterisation. The IR spectrum of the isolated white solid showed characteristic features corresponding to polyaminoborane. A broad band at 3245 cm^{-1} was observed which was assigned to N−H stretches. A similar broad peak at 2324 cm^{-1} was assigned to B−H stretches. A narrower band at 1570 cm^{-1} was assigned to NH_2 deformation and a sharp band at 1354 cm^{-1} was assigned to B−N stretches (Figure 2.13). The IR spectrum of polyaminoborane, reported by Manners and co-workers using Brookhart's IrH_2POCOP catalyst, has relatively sharp bands corresponding to N−H (3299 and 3248 cm^{-1}) and B−H (2356 cm^{-1}) stretches.[29] The IR-spectral features of polyaminoborane reported here also differ with the polyaminoborane reported by Shore *et al.*, synthesised by the reaction of lithium amide and diborane, in which case the IR spectrum showed relatively broader bands corresponding to N−H (3320-3220 cm^{-1}) and B−H (2380-2280 cm^{-1}) stretches although bands corresponding to NH_2 deformation (1575 cm^{-1}) and B−N stretches (1405 cm^{-1}) match with the corresponding bands of polyaminoborane shown in Figure 2.13.[30] The polyaminoborane reported here also differs from other samples reported to be polyaminoborane; $[BH_2NH_2]_n$ prepared by thermal decomposition of $H_3B{\cdot}NH_3$ (by Baumann *et al.*) [31] and by subjecting borazine to a radio frequency discharge (by McGee Jr. and co-workers).[32] The IR spectrum of the polyaminoborane isolated here match most accurately with that reported by Kim and co-workers using the reaction of $NaBH_4$ and $(NH_4)_2SO_4$ which showed N−H and B−H stretches at 3300 cm^{-1} and 2350 cm^{-1} respectively and NH_2 deformation at 1560 cm^{-1}.[33] The properties of polyaminoborane vary slightly depending on the method by which it is

produced. The IR spectrum of the material isolated here matches broadly with the polyaminoborane reported in the literature as discussed above. However, the complete structural characterisation of polyaminoborane is beyond the scope of this thesis.

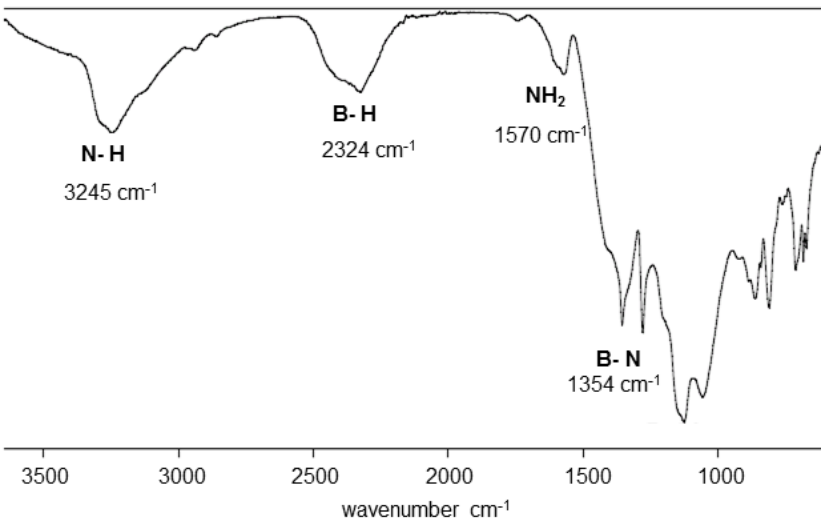
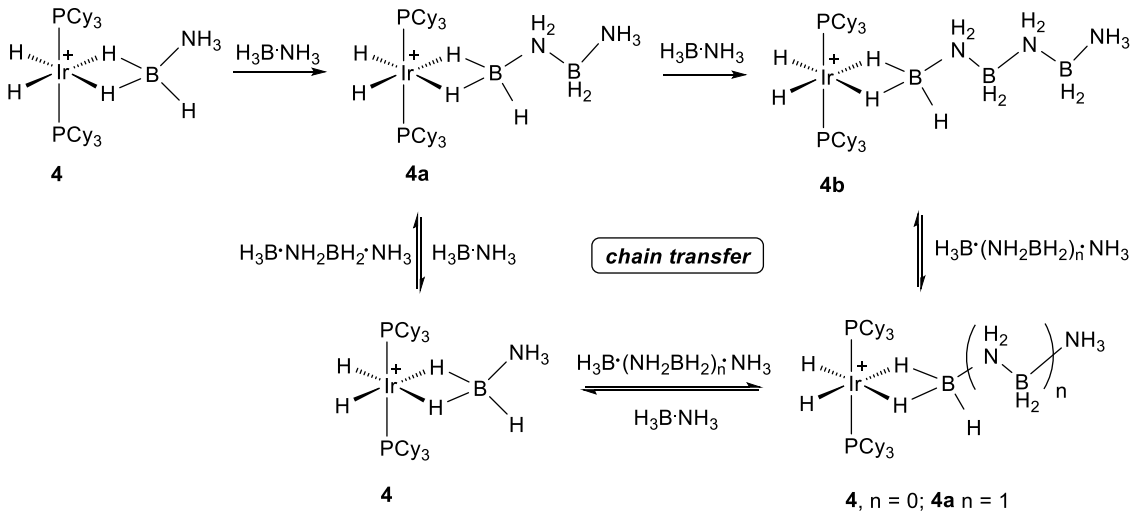


Figure 2.13 IR spectrum of the white insoluble product obtained from the dehydrocoupling of $H_3B{\cdot}NH_3$ catalysed by **II**.

2.8 Sequential addition of $H_3B{\cdot}NH_3$ to $[Ir(H)_2(PCy_3)_2(H_2)_2][BAr^F{}_4]$

In order to further probe the events that produce a growing polymer chain on the $\{Ir(PCy_3)_2\}^+$ fragment, sequential addition of $H_3B{\cdot}NH_3$ to **II** was performed. ESI-MS was used to monitor the dehydrocoupling process as it allows the clear observation of mixtures of oligomeric products formed under inert conditions,[34, 35] unlike NMR spectroscopy which exhibits overlapping spectra. Addition of 1.1 equivalents of $H_3B{\cdot}NH_3$ to the *in situ* produced C_6H_5F solution of $[Ir(H)_2(PCy_3)_2(\eta^2\text{-}H_2)_2][BAr^F{}_4]$ (**II**) in a sealed NMR tube resulted in the formation of $[Ir(H)_2(PCy_3)_2(\eta^2\text{-}H_3B{\cdot}NH_3)][BAr^F{}_4]$ (**4**). No dehydrogenation was observed when the reaction mixture was kept at room temperature for another 4 h. The requirement of additional amine-boranes for the dehydrogenation process has been previously noted by the Weller group[6] and also discussed later in Section 2.14.1. Addition of another 1.1 equivalents of $H_3B{\cdot}NH_3$ to the same solution resulted in the dehydrocoupling and formation of a mixture of complexes, **4** and **4a**, in 4 h which

persisted for the next 50 h as observed by NMR spectroscopy and ESI-MS. Further to this, when another 1.1 equivalents of $H_3B{\cdot}NH_3$ was added to the same solution, the formation of **4, 4a** and **4b** was observed in 4h as indicated by NMR spectroscopy and ESI-MS (Figure 2.14). Formation of an insoluble white solid, likely to be the polyaminoborane, was also observed during the course of sequential addition of $H_3B{\cdot}NH_3$. As shown in Figure 2.14 the mixture (**4, 4a** and **4b**) is biased towards **4** and **4a**, presumably because the sigma-bound oligomers, e.g. **4a** and **4b**, are only weakly bound and can be displaced by excess $H_3B{\cdot}NH_3$. This has the consequence that the sequential addition of $H_3B{\cdot}NH_3$ does not lead to the selective formation of higher order bound oligomeric complexes but instead gives the mixture of complexes e.g. addition of $H_3B{\cdot}NH_3$ to **4** does not give only **4a** but gives mixture of **4** and **4a**. This is suggestive of the equilibrium between the free and bound amine-boranes implying that a reversible chain transfer mechanism can occur (Scheme 2.8)[36] which is different from a chain growth mechanism proposed for the dehydropolymerisation of $H_3B{\cdot}NMeH_2$ catalysed by $[Rh(Xantphos)]^+$ fragment.[37]



Scheme 2.8 Sequential addition of $H_3B{\cdot}NH_3$ to **4** and equilibrium between the free and bound amine-boranes. $[BAr^F{}_4]^-$ anions are not shown.

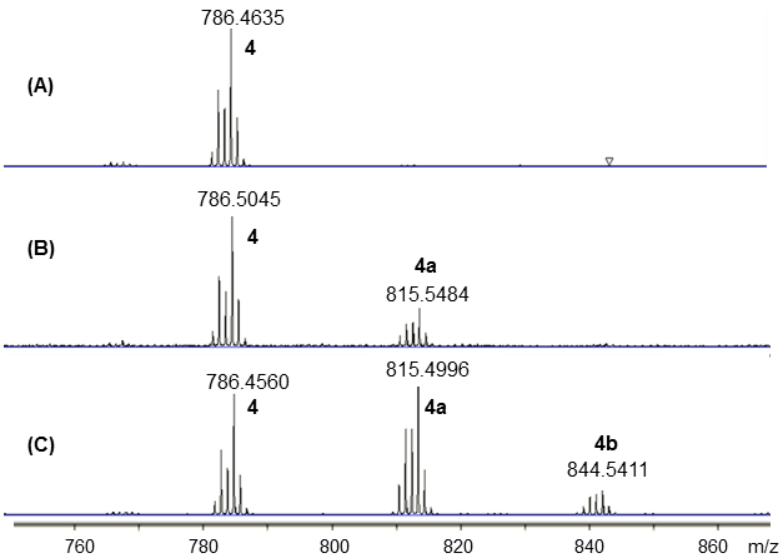


Figure 2.14 ESI-MS for the sequential addition of $H_3B{\cdot}NH_3$ to **II**. (**A**) after 4 h of the addition of 1.1 equivalents of $H_3B{\cdot}NH_3$ to the complex **II** resulting in the formation of **4**. (**b**) after 4 h of the addition of a further 1.1 equivalents of $H_3B{\cdot}NH_3$ to **4** (total 2.2 equivalents to **II**) resulting in the formation of a mixture of **4** and **4a.** (**c**) after 4 h of the addition of further 1.1 equivalents of $H_3B{\cdot}NH_3$ to the mixture of **4** and **4a** (total 3.3 equivalents to **1**) resulting in the formation of a mixture of **4, 4a** and **4b.**

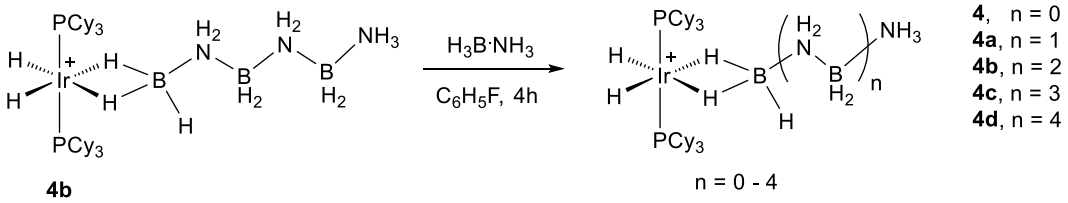
2.9 Further evidences of equilibrium between free and bound amine-boranes

As discussed in section 2.8, sequential addition of $H_3B{\cdot}NH_3$ to $[Ir(H)_2(PCy_3)_2(\eta^2\text{-}H_2)_2][BAr^F{}_4]$ (**II**) leads to the formation of a mixture of bound oligomers suggesting an equilibrium between bound and free amine-boranes implying a reversible chain transfer. This was further verified by adding $H_3B{\cdot}NH_3$ to **4b** and by adding $H_3B{\cdot}NH_2BH_2NH_2BH_2{\cdot}NH_3$ to **4a** as discussed below.

2.9.1 Addition of $H_3B{\cdot}NH_3$ to $[Ir(H)_2(PCy_3)_2(H_3B{\cdot}(NH_2BH_2)_2{\cdot}NH_3)][BAr^F{}_4]$ (4b)

1.3 equivalents of $H_3B{\cdot}NH_3$ were added to a C_6H_5F solution of $[Ir(H)_2(PCy_3)_2(H_3B{\cdot}NH_2BH_2NH_2BH_2{\cdot}NH_3)][BAr^F{}_4]$ (**4b**) in a sealed NMR tube. An ESI-MS after 4 h showed the presence of a mixture of species containing **4** and **4a**-**4d** which persisted for the next 20 h (Scheme 2.9, Figure 2.15). The presence of the mixture of complexes **4** and **4a**-**4d** gives an insight into the dehydrocoupling mechanism. Formation

of **4** occurs by the initial displacement of the bound trimer ($H_3B{\cdot}NH_2BH_2NH_2BH_2{\cdot}NH_3$) by $H_3B{\cdot}NH_3$ which suggests that an equilibrium between free and bound amine-boranes, as shown in Scheme 2.8, is possible in solution. At this stage, **4a** forms presumably due to the dehydrocoupling of two equivalents of $H_3B{\cdot}NH_3$ which could occur through either a metal-mediated or an off-metal process.[38-41] Formation of **4b** could either be a result of the partial displacement of the bound trimer by $H_3B{\cdot}NH_3$ resulting in the formation of **4** and unreacted **4b** or due to the direct dehydrocoupling of $H_3B{\cdot}NH_3$ and dimer ($H_3B{\cdot}NH_2BH_2{\cdot}NH_3$) leading to the formation of $H_3B{\cdot}NH_2BH_2NH_2BH_2{\cdot}NH_3$ that binds to the metal centre to form **4b**. Formation of **4c** and **4d** results from the further dehydrocoupling events to form the higher oligomers, tetramer and pentamer, bound to metal centre. The observation that **4b** does not exclusively form **4c** upon the addition of $H_3B{\cdot}NH_3$ but instead gives a mixture of **4** and **4a**-**4d** further confirms the reversible chain transfer mechanism of the free and bound oligomers $H_3B{\cdot}(NH_2BH_2)_n{\cdot}NH_3$ (n = 0-4).



Scheme 2.9 Addition of $H_3B{\cdot}NH_3$ to **4b**. $[BAr^F{}_4]^-$ anions are not shown.

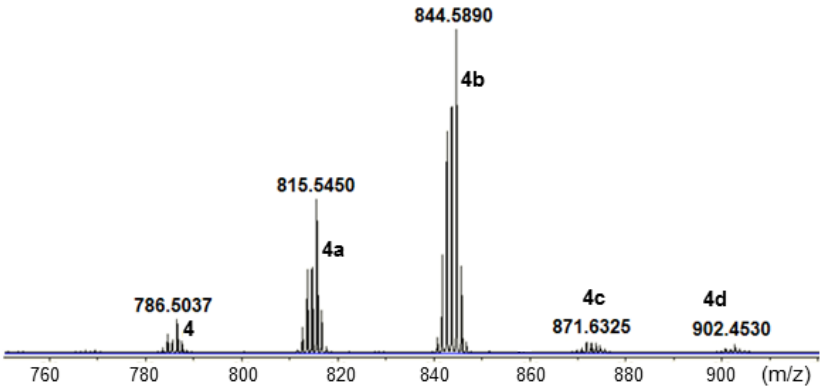
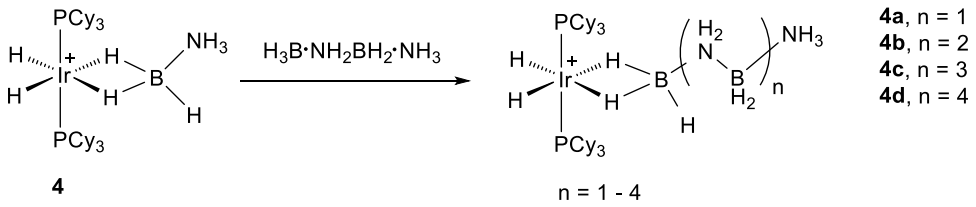


Figure 2.15 ESI-MS after 4 h of addition of $H_3B{\cdot}NH_3$ to $[Ir(H)_2(PCy_3)_2(\eta^2\text{-}H_3B{\cdot}NH_2BH_2NH_2BH_2{\cdot}NH_3)][BAr^F{}_4]$ (**4b**).

2.9.2 Addition of $H_3B{\cdot}NH_2BH_2{\cdot}NH_3$ to $([Ir(H)_2(PCy_3)_2(\eta^2\text{-}H_3B{\cdot}NH_3)][BAr^F{}_4]$ (4)

Two equivalents of $H_3B{\cdot}NH_2BH_2{\cdot}NH_3$ were added to the C_6H_5F solution of $[Ir(H)_2(PCy_3)_2(\eta^2\text{-}H_3B{\cdot}NH_3)][BAr^F{}_4]$ (**4**) in a sealed NMR tube. ESI-MS after 4 h showed the formation of **4a-4d** with **4a** being the major species (Scheme 2.10, Figure 2.16). The formation of **4a** suggests that the dimer, $H_3B{\cdot}NH_2BH_2{\cdot}NH_3$ can displace $H_3B{\cdot}NH_3$ from $[Ir(H)_2(PCy_3)_2(\eta^2\text{-}H_3B{\cdot}NH_3)][BAr^F{}_4]$ (**4**) to form $[Ir(H)_2(PCy_3)_2(\eta^2\text{-}H_3B{\cdot}NH_2BH_2{\cdot}NH_3)][BAr^F{}_4]$ (**4a**). The free $H_3B{\cdot}NH_3$, can then coordinate back to the metal centre forming **4** and then undergo dehydrocoupling to produce higher oligomers bound to metal centres (**4b** - **4d**). In this experiment also, **4c** is not formed exclusively which further confirms the reversible chain transfer mechanism.



Scheme 2.10 Addition of $H_3B{\cdot}NH_2BH_2{\cdot}NH_3$ to **4a**. $[BAr^F{}_4]^-$ anions are not shown.

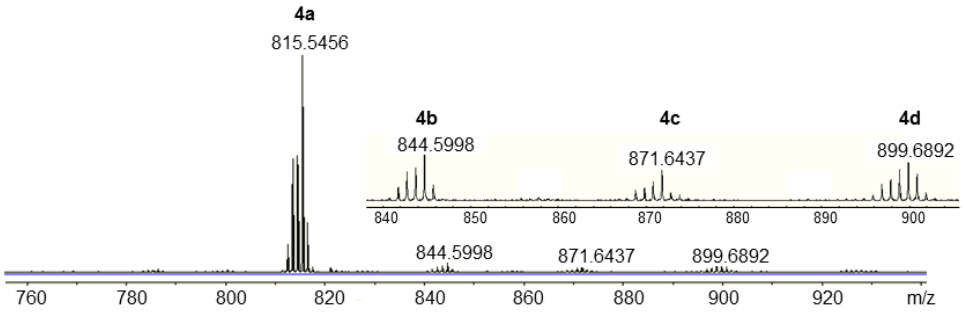
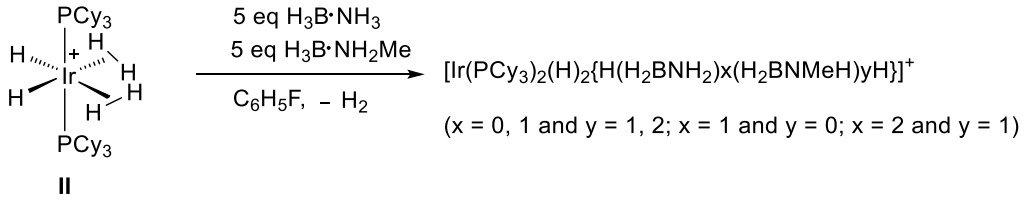


Figure 2.16 ESI-MS after 4 h of addition of 2 equivalents of $H_3B{\cdot}NH_2BH_2{\cdot}NH_3$ to $[Ir(H)_2(PCy_3)_2(\eta^2\text{-}H_3B{\cdot}NH_3)][BAr^F{}_4]$ (**4**).

Both the experiments discussed above in Section 2.9 show that during the dehydropolymerisation process, metal-bound oligomers can be displaced by free amine-boranes present in the solution and hence are suggestive of equilibrium between free and bound amine-boranes, implying a reversible chain transfer mechanism.

2.10 Addition of $H_3B{\cdot}NH_3$ and $H_3B{\cdot}NMeH_2$ to complex II

To probe further into the observation of multiple insertion events on the $\{Ir(H)_2(PCy_3)_2\}^+$ fragment, $H_3B{\cdot}NH_3$ (5 equivalents) and $H_3B{\cdot}NMeH_2$ (5 equivalents) were added to a C_6H_5F solution of $[Ir(H)_2(PCy_3)_2(\eta^2\text{-}H_2)_2][BAr^F{}_4]$ (**II**) in an NMR tube. An ESI-MS spectrum after 4 h showed the formation of metal bound co-oligomers $[Ir(PCy_3)_2(H)_2\{H(H_2BNH_2)_x(H_2BNMeH)_yH\}][BAr^F{}_4]$ (x = 0, 1 and y = 1, 2; x = 1 and y = 0; x = 2 and y = 1) (Figure 2.17, Scheme 2.11).



II

Scheme 2.11 Reaction of **II** with a mixture of $H_3B{\cdot}NH_3$ (5 eq) and $H_3B{\cdot}NMeH_2$ (5 eq). $[BAr^F{}_4]^-$ anions are not shown.

The observation of multiple complexes and not exclusively $[Ir(H)_2(PCy_3)_2(\eta^2\text{-}H_3B{\cdot}NMeH_2)][BAr^F{}_4]$ (**3**) or $[Ir(H)_2(PCy_3)_2(\eta^2\text{-}H_3B{\cdot}NH_3)][BAr^F{}_4]$ (**4**) or $[Ir(PCy_3)_2(H)_2(H_3BNH_2BH_2NMeH_2)][BAr^F{}_4]$ is consistent with an equilibrium between the free and bound amine-boranes. Formation of random copolymers of $H_3B{\cdot}NH_3$ /$H_3B{\cdot}NMeH_2$ and $H_3B{\cdot}N\textit{n}BuH_2$/$H_3B{\cdot}NMeH_2$ have been previously reported by Manners and co-workers using Brookhart's IrH_2POCOP catalyst.[29, 42] However, there has not been any report on the direct evidence of the role of metal-complex in the copolymerisation process. The ESI-MS shown in Figure 2.17 shows the sigma-complexes of copolymers bound to the metal centre which can be considered as the model complexes involved in a metal-catalysed copolymerisation process.

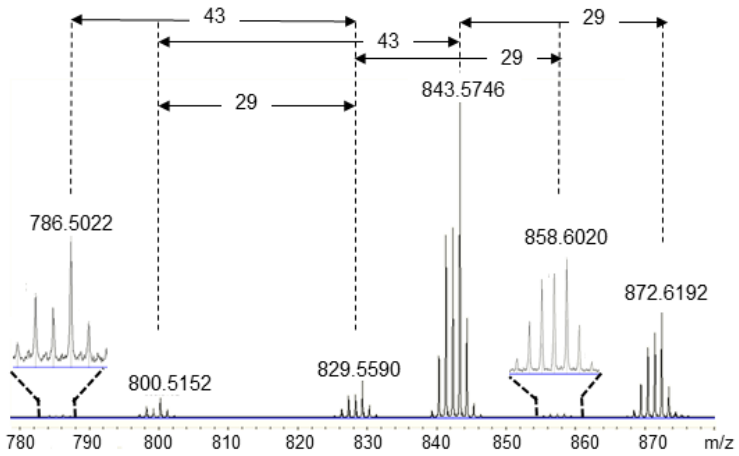


Figure 2.17 ESI-MS after 4 h of addition of 5 equivalents of $H_3B{\cdot}NH_3$ and $H_3B{\cdot}NMeH_2$ to $[Ir(H)_2(PCy_3)_2(H_2)_2][BAr^F{}_4]$ (**II**). m/z values of 43 and 29 are equivalent to $H_2B{=}NMeH$ and $H_2B{=}NH_2$ respectively.

2.11 Addition of $H_3B{\cdot}NMeH_2$ to complex 4b

1.5 equivalents of $H_3B{\cdot}NMeH_2$ were added to the C_6H_5F solution of $[Ir(H)_2(PCy_3)_2(\eta^2\text{-}H_3B{\cdot}NH_2BH_2NH_2BH_2{\cdot}NH_3)][BAr^F{}_4]$ (**4b**) in order to observe the insertion events and the formation of the bound copolymers. ESI-MS after 4 h showed the presence of the mixture of metal bound copolymers $[Ir(PCy_3)_2(H)_2\{H(H_2BNH_2)_x(H_2BNMeH)_yH][BAr^F{}_4]$ (x = 0, 1 and y = 1, 2; x = 1, 2 and y = 0; x = 2 and y = 1) (Figure 2.18). This experimental observation reveals that: (i) $H_3B{\cdot}NMeH_2$ can displace the bound trimer from **4b** and form $[Ir(H)_2(PCy_3)_2(\eta^2\text{-}H_3B{\cdot}NMeH_2)][BAr^F{}_4]$ (**3**; i.e. x = 0, y = 1) which in the presence of slight excess of free $H_3B{\cdot}NMeH_2$ can undergo dehydrocoupling to form $[Ir(H)_2(PCy_3)_2(\eta^2\text{-}H_3B{\cdot}NMeHBH_2{\cdot}NMeH_2)][BAr^F{}_4]$ (**3a**; i.e. x = 0, y = 2). (ii) B−N bond cleavage occurs during dehydrocoupling as the formation of **4a** can only occur from the B−N bond cleavage of **4b** or the related sigma-complexes. B−N bond cleavage leading to the formation of decomposition products **5a**-**5d** during $\{Ir(H_2)(PCy_3)_2\}^+$ catalysed dehydrocoupling of $H_3B{\cdot}NH_3$ has been reported earlier in Sections 2.3 and 2.5.

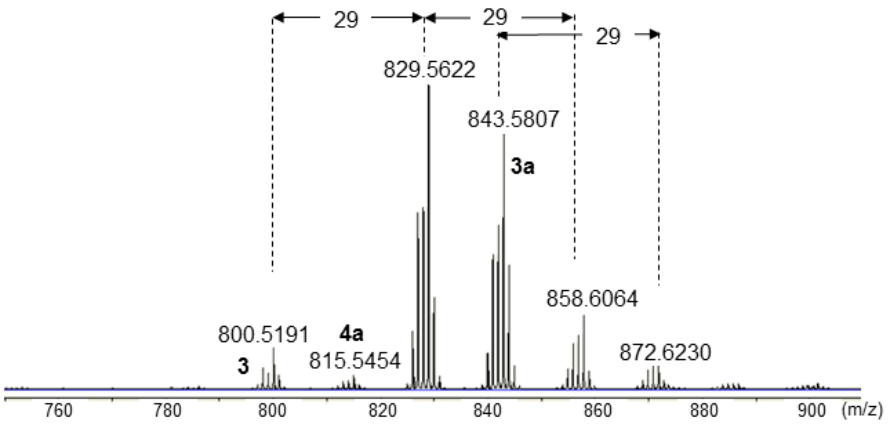


Figure 2.18 ESI-MS after 4 h of addition of 1.5 equivalents of $H_3B{\cdot}NMeH_2$ to **4b**. m/z value of 29 corresponds to H_2BNH_2.

2.12 Addition of cyclohexene to the catalytic dehydrocoupling of $H_3B{\cdot}NH_3$

Baker and co-workers have demonstrated that the addition of cyclohexene can be considered as a tool to detect the presence of free amino-borane ($H_2B{=}NH_2$) during transition metal catalysed dehydrocoupling of $H_3B{\cdot}NH_3$ via hydroboration of cyclohexene to form $Cy_2B{=}NH_2$.[43] However, the addition of 20 equivalents of cyclohexene to the iridium catalysed dehydrocoupling of $H_3B{\cdot}NH_3$ (10 mol% $[Ir(H)_2(PCy_3)_2(H_2)_2][BAr^F{}_4]$) did not result in the hydroboration of cyclohexene and the formation of $Cy_2B{=}NH_2$ was not observed (after 24 h). The dehydrocoupling products were the same as discussed in section 2.3. We suggest this is due to the hydroboration step being slower than the oligomerisation steps as also reported recently by Schneider *et al.*, or that the free amino-borane is not formed.[44]

2.13 Effects of steric bulk on the catalytic dehydrocoupling of amine-boranes

The effects of ligand steric bulk on metal-complex catalysed olefin polymerisation has been previously reported.[45-48] For example, Li and co-workers have studied ligand steric effects on β-ketiminato neutral nickel(II) olefin polymerisation catalysts and found that

complexes with bulky ligands show greater catalytic activities and also produce more branched polyethylene.[46] Pellecchia and co-workers have reported the effects of olefin sterics on polymerisation using ethylene and propylene and metal complexes of the general formula ($^{-}$NNN^{-})M(NMe_2)$_2$ [M = Ti(IV), Zr(IV) and Hf(IV); $^{-}$NNN^{-} = pyrrolylpyridylanilido ligands]. It was reported that all the metal complexes (Ti, Zr and Hf) resulted in the efficient polymerisation of ethylene and formed highly linear polyethylenes with ultrahigh molecular weights (M_w up to 2.7 MDa); whereas polymerisation of propylene was found to be dependent on the metal catalyst. For example, Zr and Hf complexes produced isotactic polymers of high-molecular-weight polypropylenes (M_w up to 1.8 MDa for Hf) while the Ti-based catalysts were found to be less stereospecific, affording polypropylenes of very high molecular weights but very broad molecular weight distributions.[49]

In this context, the use of $\{Ir(H)_2(PCy_3)_2\}^+$ fragment and amine-boranes $H_3B{\cdot}NRR'R''$ (NRR'R'' = Me_3, Me_2H, MeH_2, H_3) of varying substituents offer us an opportunity to understand the effect of sterics on the catalytic dehydrocoupling of amine-boranes. The reactivity of $H_3B{\cdot}NRR'R''$ (NRR'R'' = Me_3, Me_2H, MeH_2, H_3) with $[Ir(H)_2(PCy_3)_2(\eta^2\text{-}H_2)_2][BAr^F{}_4]$ (**II**) under the catalytic conditions is studied using the ESI-MS and the results obtained are summarised below:

(A) Ten equivalents of $H_3B{\cdot}NMe_3$ were added to the C_6H_5F solution of $[Ir(H)_2(PCy_3)_2(\eta^2\text{-}H_2)_2][BAr^F{}_4]$ (**II**) in an NMR tube. An ESI-MS was recorded after 4 h which showed the formation of $[Ir(H)_2(PCy_3)_2(\eta^2\text{-}H_3B{\cdot}NMe_3)][BAr^F{}_4]$ (**1**) as the only organometallic species. No onward dehydrogenation of complex **1** was observed due to the absence of N−H protons in $H_3B{\cdot}NMe_3$. This result is as reported previously by the Weller group.[3]

(B) $H_3B{\cdot}NMe_2H$ showed slow dehydrogenation under identical conditions (10 mol% of **II**), as demonstrated by an ESI-MS after 10 days that showed the mixture of bound amine-borane $[Ir(H)_2(PCy_3)_2(\eta^2\text{-}H_3B{\cdot}NMe_2H)][BAr^F{}_4]$ (**2**) and the bound amino–borane $[Ir(H)_2(PCy_3)_2(\eta^2\text{-}H_2B{=}NMe_2)][BAr^F{}_4]$ (**2a**). When 3 equivalents of $H_3B{\cdot}NMe_2H$ were added

to complex **II**, complete dehydrogenation of **2** to **2a** was observed in 4 days by ESI-MS. However, formation of any bound oligomer $[Ir(H)_2(PCy_3)_2(\eta^2\text{-}H_3B{\cdot}NMe_2BH_2NMe_2H)][BAr^F{}_4]$ was not observed.

(C) Addition of 10 equivalents of $H_3B{\cdot}NMeH_2$ to a C_6H_5F solution of $[Ir(H)_2(PCy_3)_2(\eta^2\text{-}H_2)_2][BAr^F{}_4]$ (**II**) resulted in the dehydrocoupling of $H_3B{\cdot}NMeH_2$. An ESI-MS after 4 h showed the formation of $[Ir(H)_2(PCy_3)_2(\eta^2\text{-}H_3B{\cdot}NMeH_2)][BAr^F{}_4]$ (**3**) and $[Ir(H)_2(PCy_3)_2(H_3B{\cdot}NMeHBH_2{\cdot}NMeH_2)]\ [BAr^F{}_4]$ (**3a**), as reported previously.[6]

(D) Monitoring the catalytic dehydrocoupling of $H_3B{\cdot}NH_3$ under the same conditions (10 mol% complex **II**) revealed the formation of bound dimer (**4a**), trimer (**4b**), tetramer (**4c**) and pentamer (**4d**) (**4c** and **4d** showed relatively smaller intensity) along with the formation of bound $H_3B{\cdot}NH_3$ (**4**, Figure 2.19).

In summary, $H_3B{\cdot}NMe_2H$ dehydrogenates but does not form any bound dimer; $H_3B{\cdot}NMeH_2$ dehydrocouples and forms bound dimer whereas $H_3B{\cdot}NH_3$ on dehydrocoupling forms the metal-bound higher oligomers (dimer-pentamer). This outlines a trend that decrease in the steric bulk of amine-boranes results in the increased degree of dehydrocoupling of amine-boranes. These experimental observations have been further corroborated by the DFT calculations discussed later in Section 2.14.

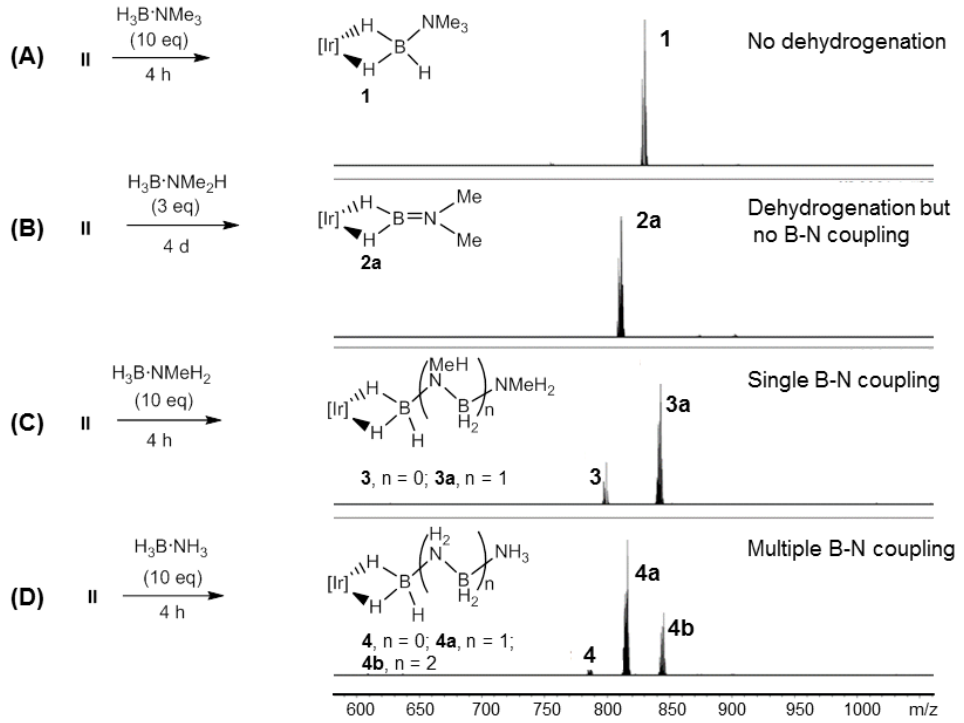
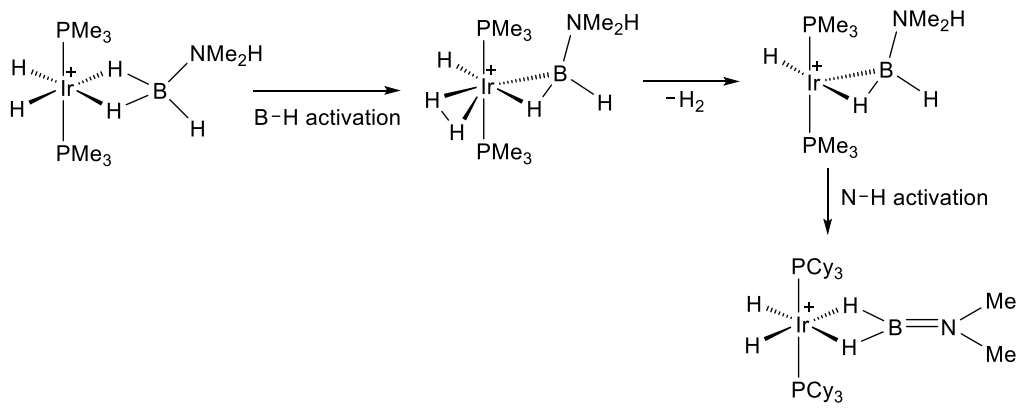


Figure 2.19 ESI-MS for the reactivity of amine-boranes with $[Ir(H)_2(PCy_3)_2(H_2)_2][BAr^F{}_4]$ (**II**), [Ir] = $\{Ir(H)_2(PCy_3)_2\}^+$, $[BAr^F{}_4]^-$ anions are not shown.

2.14 DFT calculations on iridium catalysed dehydrocoupling of amine-boranes

DFT calculations were performed by Dr. Andrés G. Algarra and Prof. Stuart A. Macgregor (Heriot-Watt University, Edinburgh) to study the mechanism of catalytic dehydrocoupling of $H_3B{\cdot}NMe_xH_{3-x}$ (x = 0 - 2). These calculations employed PMe_3 ligands with $[Ir(PMe_3)_2(H)_2(\eta^2\text{-}H_3B{\cdot}NMe_xH_{3-x})]^+$ (x = 0 - 2). Weller and Macgregor have previously reported the mechanism for the dehydrogenation of $[Ir(PMe_3)_2(H)_2(\eta^2\text{-}H_3B{\cdot}NMe_2H)][BAr^F{}_4]$ in which the dehydrogenation proceeds via B−H activation, H_2 loss and a rate-limiting N−H activation step (Scheme 2.12).



Scheme 2.12 DFT calculated mechanism for the dehydrogenation of $[Ir(PMe_3)_2(H)_2(\eta^2\text{-}H_3B{\cdot}NMe_2H)][BAr^F{}_4]$. $[BAr^F{}_4]^-$ anions are not shown.

Applying similar strategies to study the dehydrocoupling of $[Ir(PMe_3)_2(H)_2(\eta^2\text{-}H_3B{\cdot}NMe_xH_{3-x})]^+$ (x = 0 - 2) offered new mechanistic insights which have been discussed here.

2.14.1 Dehydrogenation mechanism: requirement of additional amine-boranes

$[Ir(H)_2(PCy_3)_2(H_3B{\cdot}NH_3)][BAr^F{}_4]$ (**4**), if pure, is found to be stable in solution (C_6H_5F or 1,2-$F_2C_6H_4$) and no onward dehydrogenation is observed for next 4 h. Addition of another equivalent of $H_3B{\cdot}NH_3$ induces dehydrogenation allowing the observation of the bound oligomeric species as also discussed in Section 2.8. DFT calculations have revealed that the presence of an additional equivalent of $H_3B{\cdot}NH_3$ lowers the dehydrogenation barrier from 33.8 kcal mol^{-1} to 26.7 kcal mol^{-1}. Figure 2.20 shows the optimised transition state structures for the rate limiting N−H activation steps. The presence of an additional $H_3B{\cdot}NH_3$ ligand (Figure 2.20 B) allows the formation of a $BH(\delta^-)\cdots H(\delta^+)N$ dihydrogen bond (1.8 Å), offering extra stabilisation to the transition state, and thus lowering the dehydrogenation barrier. The role of the $BH(\delta^-)\cdots H(\delta^+)N$ dihydrogen interaction has also been previously noted for the dehydrogenation of amine-boranes.[50, 51]

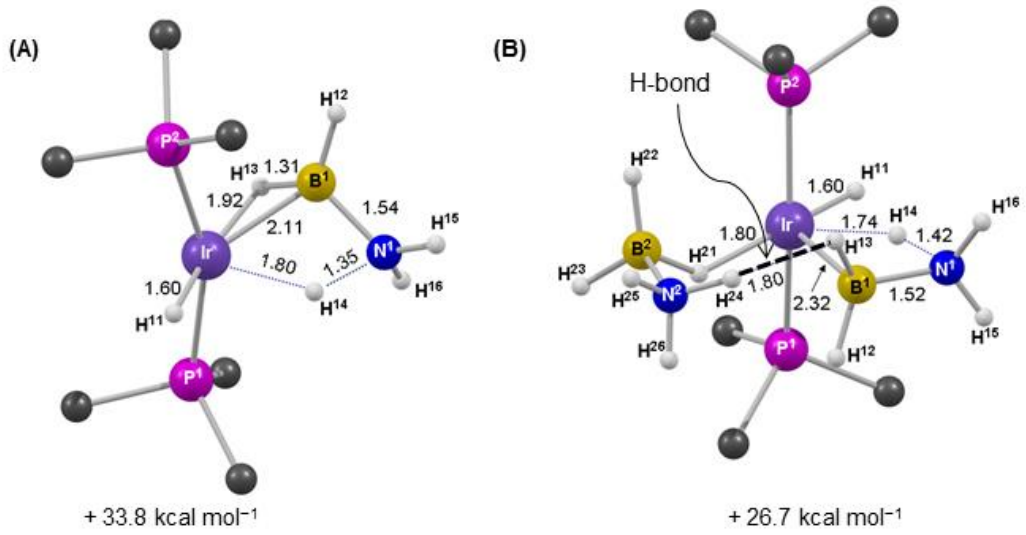
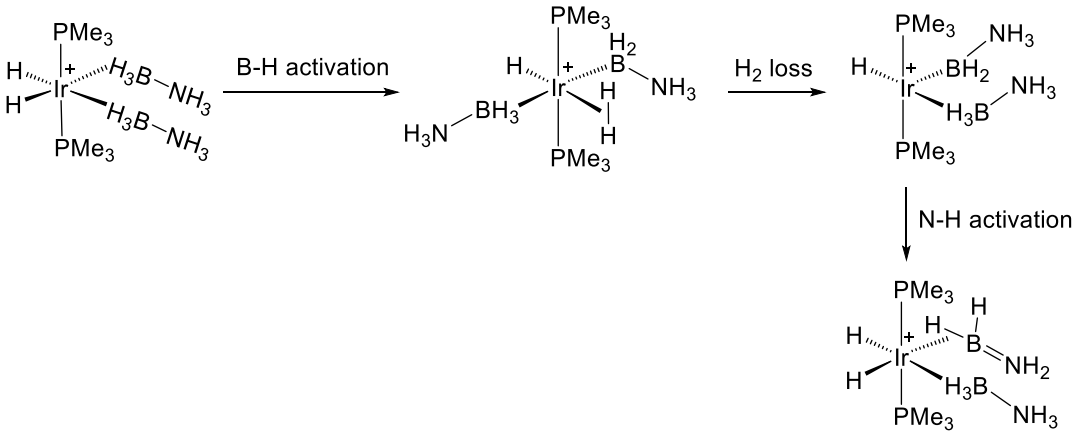


Figure 2.20 Computed structures of the rate limiting N–H activation transition states (A) in the absence of added $H_3B{\cdot}NH_3$ and (B) in the presence of one additional $H_3B{\cdot}NH_3$ molecule. Key distances are in Å and H atoms attached to PMe_3 are omitted for clarity. Figure courtesy of Dr Andrés G. Algarra and Prof. Stuart A. Macgregor and adapted from *Chem. Sci.* **2014**, *5*, 2546.

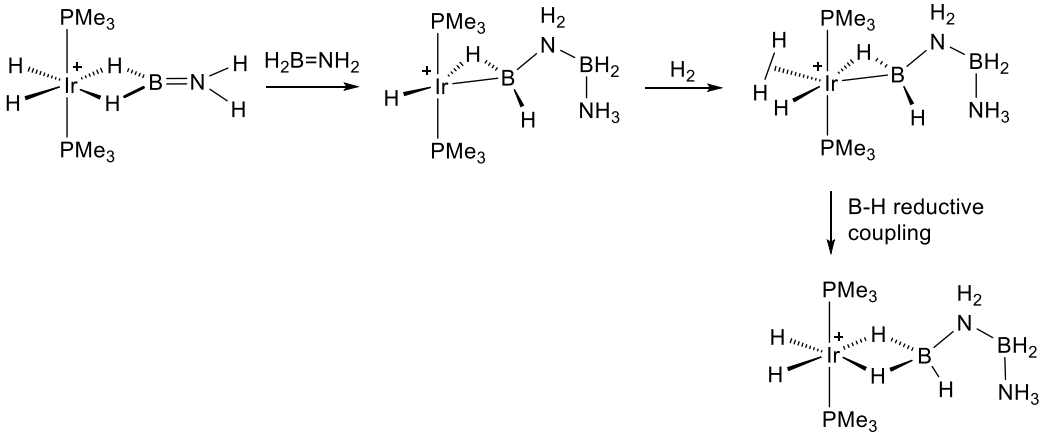
Scheme 2.13 shows the proposed mechanism for the dehydrogenation of $H_3B{\cdot}NH_3$ in the presence of an additional molecule of $H_3B{\cdot}NH_3$. $[Ir(H)_2(PMe_3)_2(\eta^1\text{-}H_3B{\cdot}NH_3)_2]^+$, formed from the coordination of $H_3B{\cdot}NH_3$ to $[Ir(H)_2(PMe_3)_2(\eta^2\text{-}H_3B{\cdot}NH_3)]^+$, undergoes a B−H activation step followed by a reductive coupling of the two hydrides. This facilitates the loss of H_2 resulting in the formation of $[Ir(H)(PMe_3)_2(H_2B{\cdot}NH_3)(\eta^1\text{-}H_3B{\cdot}NH_3)]^+$ which undergoes a rate limiting N−H activation step with a barrier of 26.7 kcal mol^{-1} to form $[Ir(H)_2(PMe_3)_2(\eta^1\text{-}H_3B{\cdot}NH_3)(\eta^1\text{-}H_2B{=}NH_2)]^+$.



Scheme 2.13 Proposed mechanism for the dehydrogenation of $H_3B{\cdot}NH_3$ in the presence of added $H_3B{\cdot}NH_3$. $[BAr^F{}_4]^-$ anions are not shown.

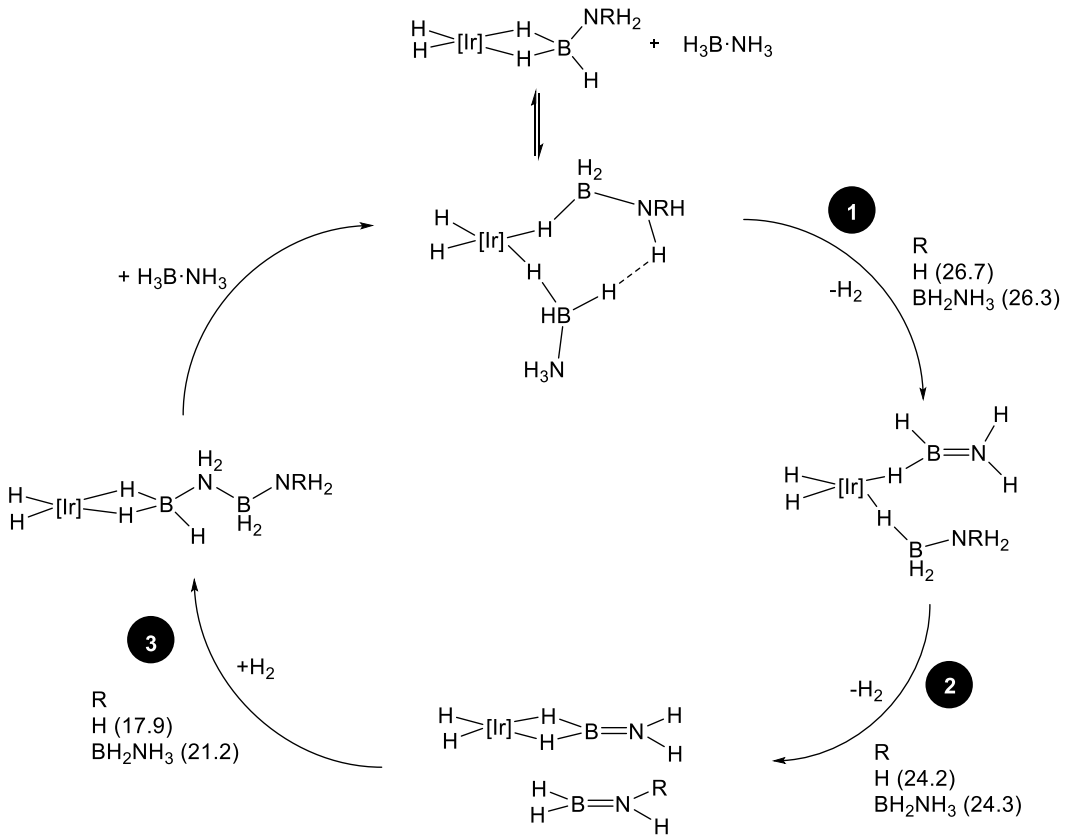
2.14.2 Mechanism for the B−N coupling step

The most accessible pathway that was characterised for the B−N coupling steps involves the coupling of two $H_2B{=}NH_2$ units requiring prior dehydrogenation of a second molecule of $H_3B{\cdot}NH_3$. The proposed mechanism is shown in Scheme 2.14, which involves the coupling of $H_2B{=}NH_2$ with $[Ir(H)_2(PMe_3)_2(\eta^2\text{-}H_2B{=}NH_2)]^+$ to form $[Ir(H)(PMe_3)_2(H_2BNH_2BH_2NH_3]^+$ with a barrier of 17.9 kcal mol^{-1}. This is closely related to the pathway characterised for the dehydrogenation of $H_3B{\cdot}NMe_2H$ by the same metal fragment.[3] Subsequent addition of H_2 followed by B−H reductive coupling then results in the formation of the bound diborazane $[Ir(H)_2(PMe_3)_2(\eta^2\text{-}H_3B{\cdot}NH_2BH_2{\cdot}NH_3)]^+$. This coupling process is similar to that reported by Schneider and co-workers for the dehydrocoupling of $H_3B{\cdot}NH_3$ using bifunctional ruthenium catalyst in which an N−H activated $H_3B{\cdot}NH_3$ undergoes B−N coupling with $H_2B{=}NH_2$.[44] An analogous mechanism for the formation of the iridium bound triborazane $[Ir(H)_2(PMe_3)_2(\eta^2\text{-}H_3B{\cdot}(NH_2BH_2)_2{\cdot}NH_3]^+$ has been postulated in which $H_2B{=}NHBH_2{\cdot}NH_3$ couples with $[Ir(H)_2(PMe_3)_2(\eta^2\text{-}H_2B{=}NH_2)]^+$ with a barrier of 21.2 kcal mol^{-1}.[52]



Scheme 2.14 Proposed mechanism for the first B−N coupling step in the dehydrocoupling of $H_3B{\cdot}NH_3$ by the $\{Ir(PMe_3)_2H_2\}^+$ fragment. $[BAr^F{}_4]^-$ anions are not shown.

An overall mechanism for the Ir-catalysed dehydrocoupling of $H_3B{\cdot}NH_3$ is summarised in Scheme 2.15. The first step is the initial dehydrogenation of $H_3B{\cdot}NH_3$ which is assisted by the $BH(\delta^-)\cdots H(\delta^+)N$ dihydrogen interaction and proceeds with the highest barrier of 26.7 kcal mol^{-1}. This is followed by the dehydrogenation of a second $H_3B{\cdot}NH_3$ molecule (step 2) with a slightly lower energy transition state (24.2 kcal mol^{-1}) forming $[Ir(H)_2(PMe_3)_2(\eta^2\text{-}H_2B{=}NH_2)]^+$ and $H_2B{=}NH_2$. The third step is the B−N coupling of the resulting amino-boranes and then addition of hydrogen, resulting in the formation of the bound dimer, $[Ir(H_2)(PMe_3)_2(\eta^2\text{-}H_3B{\cdot}NH_2BH_2{\cdot}NH_3)]^+$, which has the lowest energy barrier of all (17.9 kcal mol^{-1}). Following similar pathways, the coupling of $H_2B{=}NHBH_2{\cdot}NH_3$ with $[Ir(H)_2(PMe_3)_2(\eta^2\text{-}H_2B{=}NH_2)]^+$ can result in the formation of the bound triborazane $[Ir(H)_2(PMe_3)_2(\eta^2\text{-}H_3B{\cdot}(NH_2BH_2)_2{\cdot}NH_3]^+$ with a barrier of 21.2 kcal mol^{-1}.



Scheme 2.15 Overall mechanism for the dehydrogenation and B–N bond forming events of $H_3B{\cdot}NH_3$. R = H (first oligomerisation, i.e. to form bound dimer, **4a**); R = BH_2NH_3 (second oligomerisation forming bound trimer, **4b**). Numbers in parenthesis are calculated barriers for the model system (kcal mol^{-1}). [Ir] = $\{Ir(H)_2(PR_3)_2\}^+$ (R = Cy, experiment; R = Me, computation).

2.14.3 Effect of steric bulk on the dehydrocoupling barrier

Dehydrogenation / dehydrocoupling paths analogous to $H_3B{\cdot}NH_3$ (Scheme 2.13 - 2.15) have been calculated for $H_3B{\cdot}NMe_2H$ and $H_3B{\cdot}NMeH_2$. A general dehydrocoupling pathway is shown in Figure 2.21. DFT calculations reveal that the initial dehydrogenation barrier is similar for the three amine-boranes: 26.2 kcal mol^{-1} for $H_3B{\cdot}NMe_2H$, 25.2 kcal mol^{-1} for $H_3B{\cdot}NMeH_2$ and 26.7 kcal mol^{-1} for $H_3B{\cdot}NH_3$. This is in agreement with our experimental observations of dehydrogenation being accessible by the three amine-boranes as described in Section 2.13. Moreover, calculations show that the barrier for the B−N coupling is more substrate dependent and increases significantly on increasing size of the amine-boranes. The barriers for first B−N coupling are: 26.5 kcal mol^{-1}

($H_3B{\cdot}NMe_2H$), 19.9 kcal mol^{-1} ($H_3B{\cdot}NMeH_2$) and 17.9 kcal mol^{-1} ($H_3B{\cdot}NH_3$). This trend is consistent with our experiments where a coupling event is observed for both $H_3B{\cdot}NMeH_2$ and $H_3B{\cdot}NH_3$ but not for $H_3B{\cdot}NMe_2H$. Similarly, the barrier for the second B−N coupling step of $H_3B{\cdot}NMeH_2$ is higher (24.8 kcal mol^{-1}) than that calculated for $H_3B{\cdot}NH_3$ (19.9 kcal mol^{-1}) which is consistent with the bound triborazane being observed experimentally for $H_3B{\cdot}NH_3$ but not for $H_3B{\cdot}NMeH_2$. Interestingly, the barrier for the second B−N coupling event of $H_3B{\cdot}NH_3$ is similar to the barrier for the first B−N coupling of $H_3B{\cdot}NMeH_2$ (19.9 kcal mol^{-1}) and the barrier for the second B−N coupling event for $H_3B{\cdot}NMeH_2$ is close to the barrier for the first B−N coupling event for $H_3B{\cdot}NMe_2H$ (~26 kcal mol^{-1}). This suggests that the dehydrocoupling process is controlled by steric bulk at the nitrogen centre as $H_3B{\cdot}\mathbf{N}H_2\underline{BH_2{\cdot}NH_3}$ is sterically similar to $H_3B{\cdot}\mathbf{N}H_2\underline{Me}$, and $H_3B{\cdot}\mathbf{N}H\underline{MeBH_2{\cdot}NH_2Me}$ is sterically similar to $H_3B{\cdot}\mathbf{N}H\underline{Me_2}$ with regards to the non-hydrogen substituents attached at the nitrogen centre. Overall, based on our experimental studies and DFT calculations we propose that sterics are important in the dehydrocoupling process and dehydrocoupling tendency increases on decrease in size of amine-boranes.

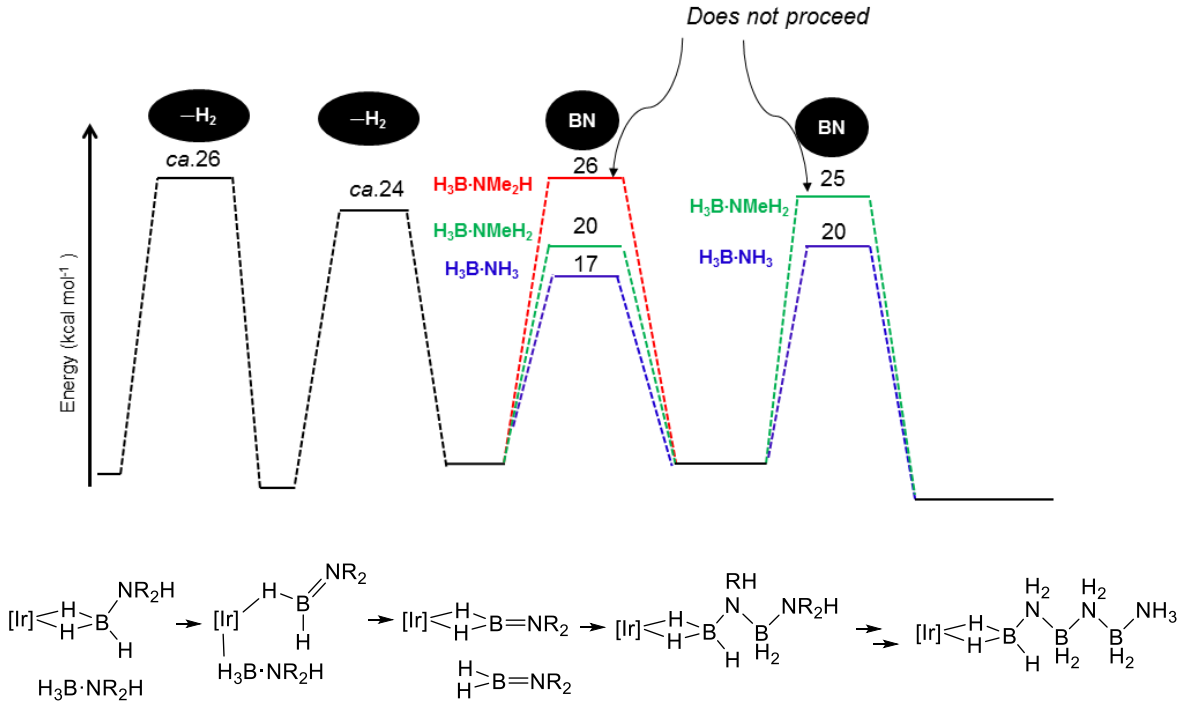


Figure 2.21 Comparison of the barriers for dehydrogenation/dehydrocoupling of amine-boranes. Numbers are calculated energy barriers for the model system (kcal mol^{-1}). [Ir] = $\{Ir(H)_2(PR'_3)_2\}^+$ (R' = Cy, experiment; R' = Me, computation).

2.15 Conclusions

In this chapter, the reactivity of $H_3B{\cdot}NH_3$ with $[Ir(H)_2(PCy_3)_2(\eta^2\text{-}H_2)_2][BAr^F{}_4]$ has been studied in detail and mechanistic aspects of the catalytic dehydrocoupling of $H_3B{\cdot}NH_3$ has been explored. Metal-bound insertion products $[Ir(H)_2(PCy_3)_2(\eta^2\text{-}H_3B{\cdot}\{NH_2BH_2\}_n{\cdot}NH_3)][BAr^F{}_4]$ (n = 0 - 4) have been observed during catalytic dehydrocoupling processes using ESI-MS and NMR spectroscopy. $Ir(H)_2(PCy_3)_2(\eta^2\text{-}H_3B{\cdot}\{NH_2BH_2\}_n{\cdot}NH_3)][BAr^F{}_4]$ (n = 0 - 2) have been independently synthesised and represent model complexes for the growing polymer chain on the metal centre. ESI-MS experiments discussed in Sections 2.8 and 2.9 suggest a reversible chain transfer mechanism for the dehydropolymerisation of $H_3B{\cdot}NH_3$. Furthermore, the effect of sterics on the dehydrocoupling of amine-boranes ($H_3B{\cdot}NH_3$, $H_3B{\cdot}NH_2Me$ and $H_3B{\cdot}NMe_2H$) has been probed using ESI-MS. The ESI-MS experiments show that $H_3B{\cdot}NMe_2H$, upon dehydrogenation by the $\{Ir(H)_2(PCy_3)_2\}^+$ fragment, forms the bound amino-borane

$[Ir(H)_2(PCy_3)_2(\eta^2\text{-}H_2B{=}NMe_2)][BAr^F{}_4]$ while $H_3B{\cdot}NMeH_2$ dehydrocouples to form $[Ir(H)_2(PCy_3)_2(H_3B{\cdot}NMeHBH_2{\cdot}NMeH_2)][BAr^F{}_4]$ and in the case of $H_3B{\cdot}NH_3$, multiple insertion products $[Ir(H)_2(PCy_3)_2(\eta^2\text{-}H_3B{\cdot}\{NH_2BH_2\}_n{\cdot}NH_3)][BAr^F{}_4]$ (n = 0 - 4) are observed. These experimental observations can be explained by the results obtained from the DFT calculations which reveal that the barrier for the initial dehydrogenation is the same for the three amine-boranes $H_3B{\cdot}NHRR'$ (R, R' = H, Me); whereas, the barrier for the B−N coupling steps depends on the steric bulk of amine-boranes with lower B−N coupling barrier for the lesser steric bulk allowing the formation of bound diborazane in case of $H_3B{\cdot}NMeH_2$ and higher order bound oligomers in the case of $H_3B{\cdot}NH_3$. Based on the results obtained from the ESI-MS experiments and the DFT calculations, we suggest that the dehydrocoupling process is favoured by the decrease in steric bulk on amine-boranes. A mechanism for the iridium-catalysed dehydrocoupling of $H_3B{\cdot}NH_3$ was also proposed upon the basis of experimental evidence and DFT calculations (Scheme 2.13 - 2.15) which highlights the role of additional equivalents of $H_3B{\cdot}NH_3$ in the dehydrogenation process (Figure 2.20).

2.16 References

1. R. H. Crabtree, M. Lavin and L. Bonneviot, *J. Am. Chem. Soc.*, 1986, **108**, 4032-4037.
2. G. Alcaraz, A. B. Chaplin, C. J. Stevens, E. Clot, L. Vendier, A. S. Weller and S. Sabo-Etienne, *Organometallics*, 2010, **29**, 5591-5595.
3. C. J. Stevens, R. Dallanegra, A. B. Chaplin, A. S. Weller, S. A. Macgregor, B. Ward, D. McKay, G. Alcaraz and S. Sabo-Etienne, *Chem. Eur. J.*, 2011, **17**, 3011-3020.
4. A. G. Algarra, L. J. Sewell, H. C. Johnson, S. A. Macgregor and A. S. Weller, *Dalton Trans.*, 2014, **43**, 11118-11128.
5. H. C. Johnson and A. S. Weller, *J. Organomet. Chem.*, 2012, **721**, 17-22.
6. H. C. Johnson, A. P. M. Robertson, A. B. Chaplin, L. J. Sewell, A. L. Thompson, M. F. Haddow, I. Manners and A. S. Weller, *J. Am. Chem. Soc.*, 2011, **133**, 11076-11079.
7. O. W. Howarth, C. H. McAteer, P. Moore and G. E. Morris, *J. Chem. Soc. Dalton Trans.*, 1981, 1481-1485.

8. P. V. Ramachandran and P. D. Gagare, *Inorg. Chem.*, 2007, **46**, 7810-7817.

9. H. C. Johnson, A. P. M. Robertson, A. B. Chaplin, L. J. Sewell, A. L. Thompson, M. F. Haddow, I. Manners and A. S. Weller, *J. Am. Chem. Soc.*, 2011, **133**, 11076-11079.

10. L. S. Santos and J. O. Metzger, *Rapid Commun. Mass Spectrom.*, 2008, **22**, 898-904.

11. D. Guironnet, L. Caporaso, B. Neuwald, I. Goettker-Schnetmann, L. Cavallo and S. Mecking, *J. Am. Chem. Soc.*, 2011, **133**, 2329-2329.

12. X. Chen, J.-C. Zhao and S. G. Shore, *J. Am. Chem. Soc.*, 2010, **132**, 10658-10659.

13. W. C. Ewing, P. J. Carroll and L. G. Sneddon, *Inorg. Chem.*, 2013, **52**, 10690-10697.

14. H. Noth and S. Thomas, *Eur. J. Inorg. Chem.*, 1999, 1373-1379.

15. C. A. Jaska, K. Temple, A. J. Lough and I. Manners, *J. Am. Chem. Soc.*, 2003, **125**, 9424-9434.

16. E. W. Hughes, *J. Am. Chem. Soc.*, 1956, **78**, 502-503.

17. S. Aldridge, A. J. Downs, C. Y. Tang, S. Parsons, M. C. Clarke, R. D. L. Johnstone, H. E. Robertson, D. W. H. Rankin and D. A. Wann, *J. Am. Chem. Soc.*, 2009, **131**, 2231-2243.

18. R. Dallanegra, A. B. Chaplin and A. S. Weller, *Angew. Chem. Int. Ed.*, 2009, **48**, 6875-6878.

19. W. C. Ewing, A. Marchione, D. W. Himmelberger, P. J. Carroll and L. G. Sneddon, *J. Am. Chem. Soc.*, 2011, **133**, 17093-17099.

20. T. B. Richardson, S. deGala, R. H. Crabtree and P. E. M. Siegbahn, *J. Am. Chem. Soc.*, 1995, **117**, 12875-12876.

21. R. H. Crabtree, P. E. M. Siegbahn, O. Eisenstein and A. L. Rheingold, *Acc. Chem. Res.*, 1996, **29**, 348-354.

22. W. T. Klooster, T. F. Koetzle, P. E. M. Siegbahn, T. B. Richardson and R. H. Crabtree, *J. Am. Chem. Soc.*, 1999, **121**, 6337-6343.

23. X. Chen, J. Gallucci, C. Campana, Z. Huang, H. K. Lingam, S. G. Shore and J.-C. Zhao, *Chem. Commun.*, 2012, **48**, 7943-7945.

24. D. Pun, E. Lobkovsky and P. J. Chirik, *Chem. Commun.*, 2007, 3297-3299.

25. M. C. Denney, V. Pons, T. J. Hebden, D. M. Heinekey and K. I. Goldberg, *J. Am. Chem. Soc.*, 2006, **128**, 12048-12049.

26. B. E. Green, C. H. L. Kennard, G. Smith, B. D. James, P. C. Healy and A. H. White, *Inorg. Chim. Acta.*, 1984, **81**, 147-150.

27. L. F. Rhodes, L. M. Venanzi, C. Sorato and A. Albinati, *Inorg. Chem.*, 1986, **25**, 3335-3337.

28. R. Komm, R. A. Geanangel and R. Liepins, *Inorg. Chem.*, 1983, **22**, 1684-1686.

29. A. Staubitz, M. E. Sloan, A. P. M. Robertson, A. Friedrich, S. Schneider, P. J. Gates, J. S. A. D. Guenne and I. Manners, *J. Am. Chem. Soc.*, 2010, **132**, 13332-13345.

30. D. L. Denton, A. D. Johnson, C. W. Hickam, R. K. Bunting and S. G. Shore, *J. Inorg. Nuc. Chem.*, 1975, **37**, 1037-1038.

31. J. Baumann, E. Baitalow and G. Wolf, *Thermochim. Acta*, 2005, **430**, 9-14.

32. C. T. Kwon and H. A. McGee, *Inorg. Chem.*, 1970, **9**, 2458-2461.

33. D. P. Kim, K. T. Moon, J. G. Kho, J. Economy, C. Gervais and F. Babonneau, *Polym. Adv. Tech.*, 1999, **10**, 702-712.

34. A. T. Lubben, J. S. McIndoe and A. S. Weller, *Organometallics*, 2008, **27**, 3303-3306.

35. L. P. E. Yunker, R. L. Stoddard and J. S. McIndoe, *J. Mass Spectrom.*, 2014, **49**, 1-8.

36. A. Goto, Y. Tsujii and T. Fukuda, *Polymer*, 2008, **49**, 5177-5185.

37. H. C. Johnson, E. M. Leitao, G. R. Whitten, I. Manners, G. C. Lloyd-Jones and A. S. Weller, *J. Am. Chem. Soc.*, 2014, **136**, 9078-9093.

38. R. J. Keaton, J. M. Blacquiere and R. T. Baker, *J. Am. Chem. Soc.*, 2007, **129**, 1844-1845.

39. A. P. M. Robertson, R. Suter, L. Chabanne, G. R. Whittell and I. Manners, *Inorg. Chem.*, 2011, **50**, 12680-12691.

40. Y. Luo and K. Ohno, *Organometallics*, 2007, **26**, 3597-3600.

41. L. J. Sewell, G. C. Lloyd-Jones and A. S. Weller, *J. Am. Chem. Soc.*, 2012, **134**, 3598-3610.

42. A. Staubitz, A. P. Soto and I. Manners, *Angew. Chem. Int. Ed.*, 2008, **47**, 6212-6215.

43. V. Pons, R. T. Baker, N. K. Szymczak, D. J. Heldebrant, J. C. Linehan, M. H. Matus, D. J. Grant and D. A. Dixon, *Chem. Commun.*, 2008, 6597-6599.

44. A. N. Marziale, A. Friedrich, I. Klopsch, M. Drees, V. R. Celinski, J. S. A. D. Guenne and S. Schneider, *J. Am. Chem. Soc.*, 2013, **135**, 13342-13355.

45. H. Dong, T. Hou, Y. Zhao, X. Fu and Y. Li, *Comp. Theor. Chem.*, 2012, **1001**, 51-59.

46. D.-P. Song, X.-C. Shi, Y.-X. Wang, J.-X. Yang and Y.-S. Li, *Organometallics*, 2012, **31**, 966-975.

47. P. Stagnaro, L. Boragno, S. Losio, M. Canetti, G. C. Alfonso, M. Galimberti, F. Piemontesi and M. C. Sacchi, *Macromolecules*, 2011, **44**, 3712-3722.

48. R. A. Stapleton, A. Al-Humydi, J. Chai, B. R. Galan and S. Collins, *Organometallics*, 2006, **25**, 5083-5092.

49. G. Li, M. Lamberti, G. Roviello and C. Pellecchia, *Organometallics*, 2012, **31**, 6772-6778.

50. A. B. Chaplin and A. S. Weller, *Acta Crystallogr. Secti. C-Cryst. Struct. Commun.*, 2011, **67**, M355-M358.

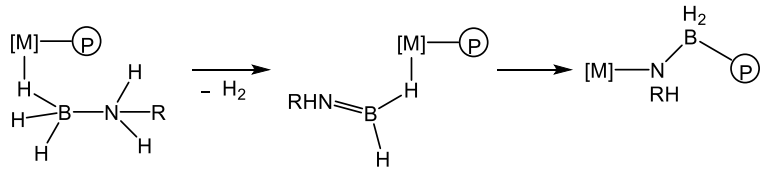
51. X. Chen, J.-C. Zhao and S. G. Shore, *Acc. Chem. Res.*, 2013, **46**, 2666-2675.

52. A. Kumar, H. C. Johnson, T. N. Hooper, A. S. Weller, A. G. Algarra and S. A. Macgregor, *Chem. Sci.*, 2014, **5**, 2546-2553.

3 The dehydrocoupling of amine-boranes catalysed by [Rh(chelating bis-phosphine)]$^+$ fragments

3.1 Introduction

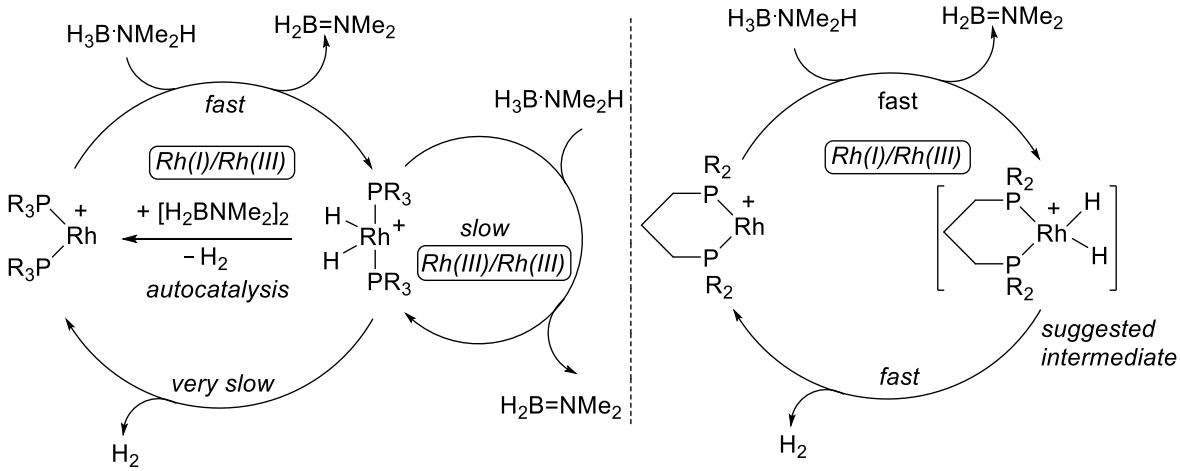
The transition metal catalysed dehydrogenation of amine-boranes ($H_3B{\cdot}NRH_2$) has been discussed in detail in Chapter 1. Amino-boranes ($H_2B{=}NRH$) are the simplest products (or more often transient intermediates) resulting from the metal catalysed dehydrogenation of amine-boranes ($H_3B{\cdot}NRH_2$) which can further dehydrocouple to produce B−N species such as polyaminoboranes, borazines or polyborazylenes.[1-5] For some dehydropolymerisation systems, a dehydrogenation/coordination/insertion mechanism has been proposed (Scheme 3.1); however, the precise mechanism of the propagation of amino-borane during dehydrocoupling is not clear.[2, 4, 6] A clear understanding of the formation of amino-borane and its role in the subsequent dehydrocoupling process, is therefore very important to fully utilise the potential of amine-borane dehydrocoupling.



Scheme 3.1 Suggested dehydrogenation/coordination/insertion mechanism for the formation of polyaminoborane, [M] = transition metal complex, P = polymer chain.

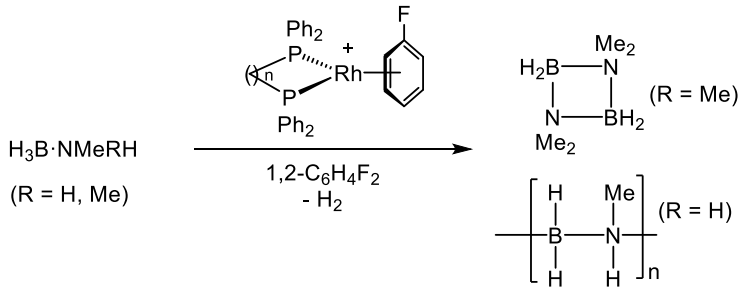
The Weller group has reported widely on the coordination chemistry and dehydrocoupling of amine-boranes using {Rh-bisphosphine}$^+$ complexes.[7-9] Dehydrogenation of $H_3B{\cdot}NMe_2H$ using monodentate phosphine complexes of Rh(I) such as $\{Rh(PR_3)_2\}^+$ (R = Cy, ^{i}Pr, ^{i}Bu) has been found to be slow.[7] This is because although $\{Rh(PR_3)_2\}^+$ rapidly

dehydrogenates amine-boranes and forms $\{RhH_2(PR_3)_2\}^+$, resulting dihydrogen loss to reform $\{Rh(PR_3)_2\}^+$ is slow and in some system has been found to be promoted by the final dehydrocoupling product $[H_2BNMe_2]_2$ (i.e. autocatalysis).[10] $\{RhH_2(PR_3)_2\}^+$ is suggested to be the resting state and is relatively a poor catalyst. Dehydrogenation, thus occurs through a fast Rh(I)/Rh(III) manifold and a considerably slower Rh(III)/Rh(III) cycle as shown in Scheme 3.2. In contrast, {Rh(chelating bis-phosphine)}$^+$ systems have been found to be faster catalysts for the dehydrocoupling of amine-boranes.[9] This is presumably because the phosphine ligands in $\{RhH_2$(chelating bis-phosphine)$\}^+$ systems do not occupy the trans position like the monodentate phosphines and facilitates the loss of dihydrogen from the dihydride Rh(III) complex to reform the starting Rh(I) complex, possibly because of its smaller bite angle. {Rh(chelating bis-phosphine)}$^+$ systems, therefore result in a constant and faster Rh(I)/Rh(III) catalytic cycle (Scheme 3.2). The effect of the bite angles in $\{Rh(PP)_2\}^+$ (PP = chelating bis-phosphine ligand) systems on the stability of the corresponding dihydride Rh(III) complex has been previously reported and the stability of $\{Rh(PP)_2(H)_2\}^+$ has been found to increase with the natural bite angles.[11, 12]



Scheme 3.2 General mechanism for the dehydrogenation of $H_3B{\cdot}NMe_2H$ using rhodium complexes containing either monodentate (left) or chelating bis-phosphine ligands (right). $[BAr^F{}_4]^-$ anions are not shown.

In 2011, the Weller and Manners groups jointly reported $[Rh(PPh_2(CH_2)_nPPh_2)(C_6H_5F)][BAr^F_4]$ (n = 3-5) complexes as efficient catalysts for the dehydrocoupling of $H_3B{\cdot}NMe_2H$ and dehydropolymerisation of $H_3B{\cdot}NMeH_2$ producing $[H_2BNMe_2]_2$ and $[H_2BNMeH]_n$, respectively (Scheme 3.3).[9]



n	TOF / h^{-1} (R = Me)	M_w (R = H)
3	1250	171, 000
4	430	180, 000
5	180	120, 000

Scheme 3.3 Dehydrocoupling of $H_3B{\cdot}NMe_2H$ using $[Rh(PPh_2(CH_2)_nPPh_2)(C_6H_5F)][BAr^F_4]$ (n = 3-5), $[BAr^F_4]^-$ anion is not shown.

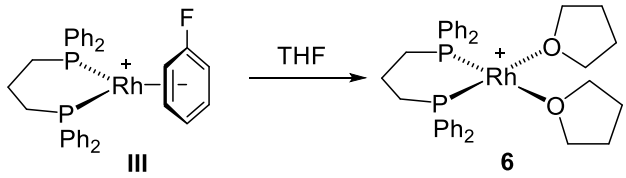
In this study, the catalytic dehydrocoupling of $H_3B{\cdot}NMe_2H$ (0.07 M) using $[Rh(PPh_2(CH_2)_3PPh_2)(C_6H_5F)][BAr^F_4]$ (**III**) in an open system was carried out and the reaction progress was monitored by ^{11}B NMR spectroscopy. Kinetic plots revealed interesting mechanistic features: (i) an induction period was observed, the origin of which was unclear and (ii) the formation of a monocationic dimer of molecular formula $[\{Rh(PPh_2(CH_2)_3PPh_2)\}_2(H_3BNMe_2)]^+$ was observed using ESI-MS. However, the role of this dimer in the catalysis was not further established due to the transient nature of this species, lack of other analytical data and the absence of suitable synthetic routes.

This chapter presents a detailed study of the catalytic dehydrocoupling of amine-boranes using $[Rh(PR_2(CH_2)_3PR_2)(C_6H_5F)][BAr^F_4]$ (R = Ph and ^{i}Pr) catalysts, addressing the issue of the formation of the previously observed dimer and its role in the catalytic dehydrocoupling. As discussed catalytic dehydrogenation of $H_3B{\cdot}NMe_2H$ and $H_3B{\cdot}NMeH_2$ using $[Rh(PPh_2(CH_2)_3PPh_2)(C_6H_5F)][BAr^F_4]$ has been previously studied,[9] however there is no report on catalytic dehydrogenation of $H_3B{\cdot}NH_3$ using this species. Motivated by this,

an investigation of the catalytic dehydrocoupling of $H_3B{\cdot}NH_3$ using $[Rh(PPh_2(CH_2)_3PPh_2)(C_6H_5F)][BAr^F{}_4]$ (**III**) was started. Due to the poor solubility of $H_3B{\cdot}NH_3$ THF was used as the solvent to study the dehydrocoupling reactions, in contrast to previously reported examples that use 1,2-$F_2C_6H_4$ or C_6H_5F.

3.2 Reactivity of III with THF

Addition of THF to $[Rh(PPh_2(CH_2)_3PPh_2)(\eta^6\text{-}C_6H_5F)][BAr^F{}_4]$ (**III**) immediately displaced the bound C_6H_5F and produced $[Rh(PPh_2(CH_2)_3PPh_2)(THF)_2][BAr^F{}_4]$ (**6**, Scheme 3.4). The newly formed complex **6** was isolated by recrystallisation from THF/pentane solution at –18ºC and characterised by NMR spectroscopy, ESI-MS, elemental analysis and single crystal X-ray diffraction. This complex **6** is likely the first formed species when **III** is dissolved in THF.



Scheme 3.4 Formation of $[Rh(PPh_2(CH_2)_3PPh_2)(THF)_2][BAr^F{}_4]$ (**6**), $[BAr^F{}_4]^-$ anions are not shown.

The $^{31}P\{^1H\}$ NMR spectrum of **6** consists of a doublet at δ 37.3 ($^1J_{RhP}$ = 192 Hz). The solid state structure of **6** is shown in Figure 3.1 and demonstrates a pseudo square planar geometry. The Rh−P [2.1723(7) and 2.1775(7) Å] and Rh−O [2.181(2) and 2.176(2) Å] distances are similar to the corresponding distances found in $[Rh(BINAP)(THF)_2][BF_4]$ (BINAP = 2,2'-bis(diphenylphosphino)-1,1'-binaphthyl) reported by Heller [Rh−P: 2.177(1) and 2.179(1) Å, Rh−O: 2.165(2) and 2.187(2) Å].[13]

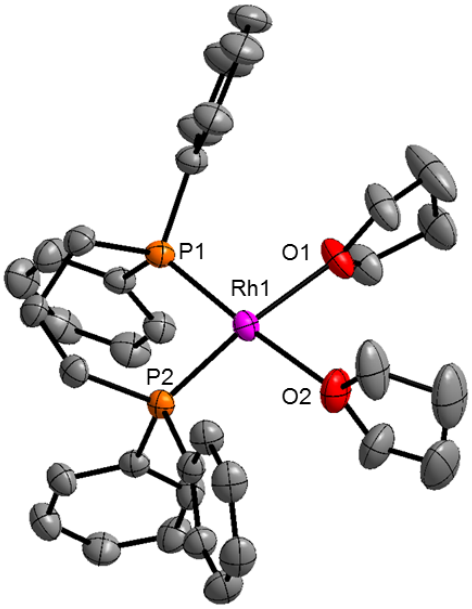
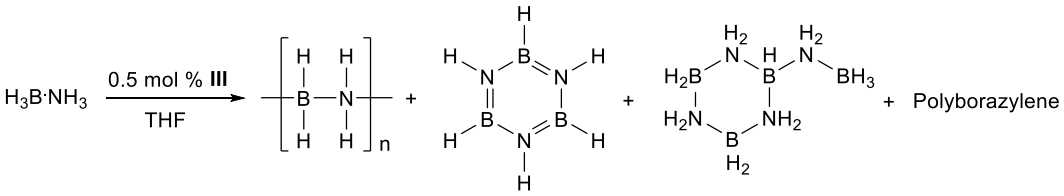


Figure 3.1 Solid state structure of the cationic portion of **6** with displacement ellipsoids at the 50% probability level. Hydrogen atoms are omitted. Selected bond lengths (Å): Rh1−P1, 2.1723(7); Rh1−P2, 2.1775(7); Rh1−O1, 2.181(2); Rh1−O2, 2.176(2). Selected bond angles (˚) O1−Rh1−O2, 81.80(9); P1−Rh1−P2, 88.47(3).

3.3 Reactivity of III with $H_3B{\cdot}NH_3$

3.3.1 Catalytic dehydrocoupling of $H_3B{\cdot}NH_3$ in an open system

The catalytic dehydrocoupling of $H_3B{\cdot}NH_3$ was studied in an open system in a 3-necked Schlenk flask connected to an argon supply and an outlet bubbler in order to prevent the build-up of hydrogen gas, as previous studies have shown that the excess hydrogen gas can cause the termination of the growing polymer chain.[14] Addition of 0.5 mol% $[Rh(PPh_2(CH_2)_3PPh_2)(C_6H_5F)][BAr^F{}_4]$ (**III**) to $H_3B{\cdot}NH_3$ (0.68 M) in THF (4 mL) immediately produced bubbles indicating the rapid start of the dehydrogenation process and lack of any significant induction period. $H_3B{\cdot}NH_3$ was completely consumed in 3 h as observed by the ^{11}B NMR spectroscopy from periodic monitoring (Scheme 3.5).



Scheme 3.5 Catalytic dehydrocoupling of $H_3B{\cdot}NH_3$ using **III** in THF.

A white precipitate was observed at the end of the reaction which was separated by filtration and was found to be insoluble in pentane, hexane, toluene, chloroform and water, suggestive of it being the polyaminoborane $[BH_2NH_2]_n$ as discussed in Chapter One. The IR spectrum of the white solid contained two sharp bands at 3301 and 3247 cm^{-1} which were assigned to the asymmetric and symmetric N−H stretches, respectively. A band at 2358 cm^{-1} was assigned to the corresponding B−H stretch, while a band at 1557 cm^{-1} was assigned to the NH_2 vibrations. These spectral features are consistent with the polyaminoborane reported by Manners and co-workers using Brookhart's $[IrH_2(POCOP)]$ catalyst, which showed bands corresponding to N−H (3299 and 3248 cm^{-1}), B−H (2356 cm^{-1}) and NH_2 (1557 cm^{-1}).[15] An ^{11}B NMR spectrum of the soluble portion of the reaction mixture after 3 hours showed the formation of borazine and polyborazylene (Figure 3.2).[16] Three unresolved broad signals at δ −5.3, −12.8 and −24.6 were also observed which could possibly be due to a mixture of B-(cyclotriborazanyl)amine-borane (BCTB, ^{11}B NMR δ −5.5 [d], −11.4 [t], −24.5 [q])[16] and short chain B−N oligomers [e.g. ^{11}B NMR of $H_3B{\cdot}(NH_2BH_2)_2{\cdot}NH_3$ δ −12.8, −13.5, −21).[17] A small amount of $[BH_4]^-$ [^{11}B NMR, δ −36.4, quintet, $^1J_{HB}$ = 80.6 Hz][18] was also observed suggesting B−N bond cleavage during the dehydrocoupling.

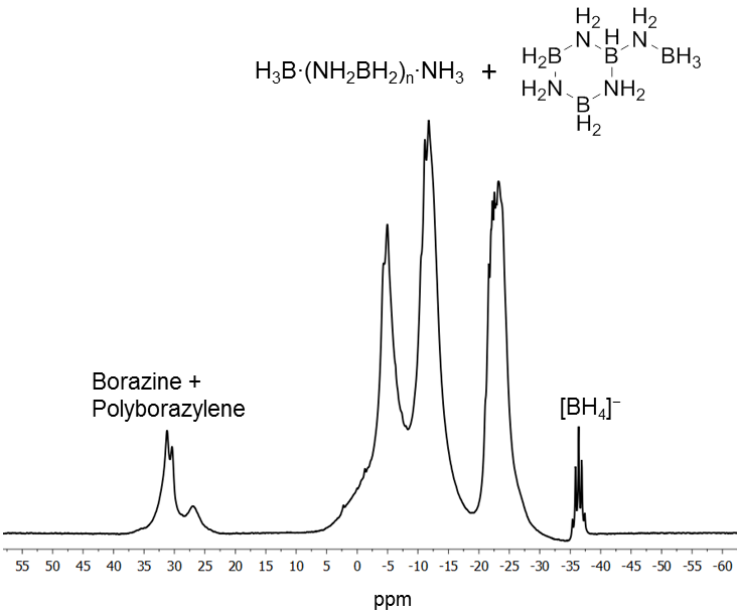


Figure 3.2 ^{11}B NMR spectrum of the reaction mixture after 3 h of dehydrocoupling of $H_3B{\cdot}NH_3$ (0.68 M) using $[Rh(PPh_2(CH_2)_3PPh_2)(C_6H_5F)][BAr^F{}_4]$ (0.5 mol%).

The evolution of hydrogen gas against time was monitored by a water filled gas burette (Figure 3.3). 1.3 equivalents of hydrogen gas were released which suggests that the major dehydrocoupling product is either polyaminoborane or BCTB as their formation releases one equivalent of hydrogen gas while the formation of borazine or polyborazylene releases two or more than two equivalents of hydrogen gas, respectively. The data from the hydrogen evolution experiment do not fit into zero, first or second order kinetics implying the occurrence of a more complex kinetics. Moreover, the release of more than one equivalent of hydrogen gas and formation of mixture of dehydrocoupling products made the detailed kinetic analysis difficult to pursue.

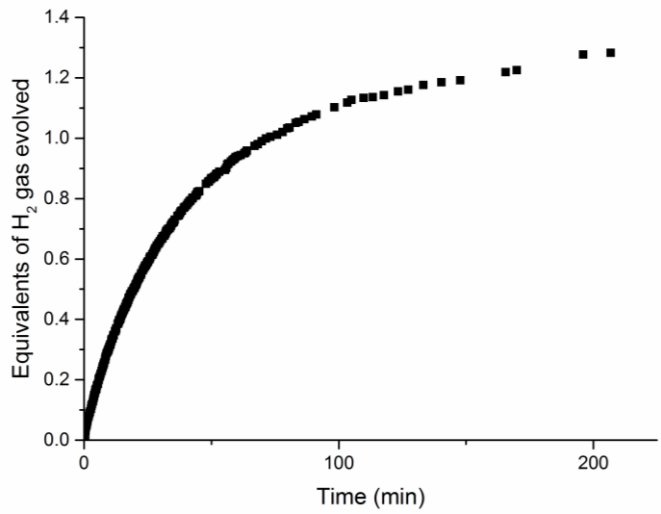
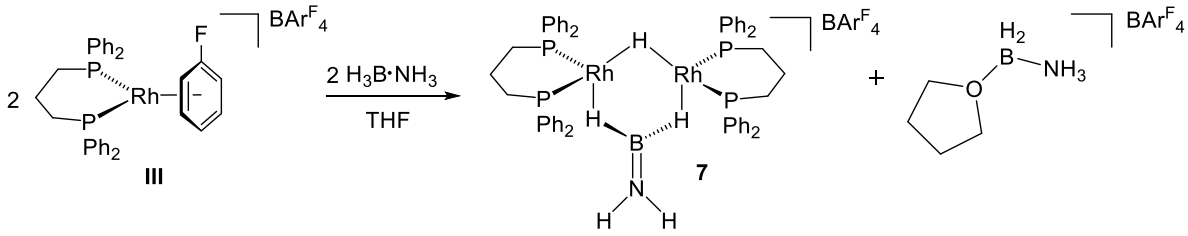


Figure 3.3 Plot of equivalents of H_2 gas produced vs time during the dehydrocoupling of $H_3B{\cdot}NH_3$ (0. 68 M) using $[Rh(PPh_2(CH_2)_3PPh_2)(C_6H_5F)][BAr^F{}_4]$ (0.5 mol %) in THF at 298 K.

3.3.2 Stoichiometric reaction of III with $H_3B{\cdot}NH_3$

In order to further probe the mechanism of the catalytic dehydrocoupling of $H_3B{\cdot}NH_3$, the reaction of **III** with $H_3B{\cdot}NH_3$ was carried out at, or near to, stoichiometric conditions. 1.1 equivalents of $H_3B{\cdot}NH_3$ was added to $[Rh(PPh_2(CH_2)_3PPh_2)(C_6H_5F)][BAr^F{}_4]$ (**III**) in d8-THF in a sealed NMR tube. After 2 min ESI-MS (m/z 1060.1612 $[M^+]$; calc. 1060.1645) and NMR spectroscopy indicated the formation of a monocationic rhodium dimer, subsequently characterised to be $[\{Rh(PPh_2(CH_2)_3PPh_2)\}_2(H)(BH_2NH_2)][BAr^F{}_4]$ (**7**, Scheme 3.6), similar to that observed previously by ESI-MS and assigned as $[\{Rh(PPh_2(CH_2)_3PPh_2)\}_2(BH_3NMe_2)]^+$, during the dehydrocoupling of $H_3B{\cdot}NMe_2H$ catalysed by **III** in 1,2-$F_2C_6H_4$.[9] ^{11}B NMR spectroscopy also showed the formation of $[BH_2(NH_3)(THF)][BAr^F{}_4]$ (δ 0.5, t, $^1J_{BH}$ = 108 Hz) in equal concentration of **7** (Scheme 3.6). $[BH_2(NH_3)(THF)][BAr^F{}_4]$ was characterised on the basis of the analogous compound $[BH_2(NH_3)(OEt_2)_2][BAr^F{}_4]$ (δ 0.21, t, $^1J_{BH}$ = 125 Hz, CD_2Cl_2) reported by Baker.[19]



Scheme 3.6 Stoichiometric reaction of **III** with $H_3B{\cdot}NH_3$ in THF and the formation of **7,** $[BAr^F{}_4]^-$ anions are not shown.

To place the structure of **7** on firm footing the reaction mixture was recrystallised, however only a few crystals (the rest being oil) could be isolated upon layering the THF solution with either pentane or hexane at –18ºC. Fortunately, this was sufficient for single crystal X-ray diffraction, although it was insufficient for characterisation by NMR spectroscopy and elemental analysis.

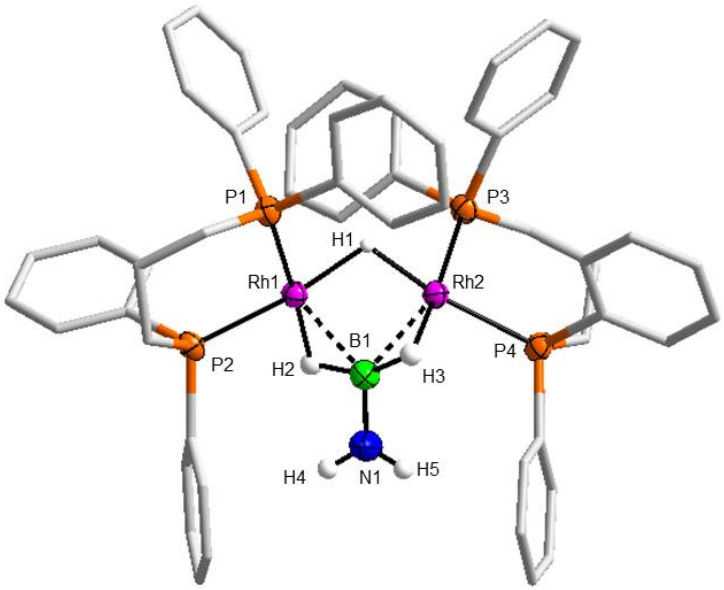


Figure 3.4 The solid state structure of the cationic portion of **7** with thermal ellipsoids at the 50% probability level. Carbon-bound H atoms are omitted, and the carbon atoms are depicted as a wireframe. Selected bond lengths (Å) and bond angles (˚): Rh1−P1, 2.2928(8); Rh1−P2, 2.2464(8); Rh2−P3, 2.2961(8); Rh2−P4, 2.2544(8); Rh1−B1, 2.111(4); Rh2−B1, 2.077(4); Rh1−Rh2, 2.7905(3); B1−N1, 1.379(5); Rh1−B1−Rh2, 83.55(14).

Figure 3.4 depicts the solid state structure of **7** and shows that two $\{Rh(PPh_2(CH_2)_3PPh_2\}^+$ fragments are bound by a bridging hydride and a bridging $H_2B{=}NH_2$ fragment. The phosphorus atoms P1/P3 and P2/P4 are related by a C_2 axis. The hydrogen atoms H1 –

H5 were located on the Fourier map and allowed to refine freely before imposing riding constraints. The B–N distance [1.379(5) Å] is consistent with a significant B–N π-interaction, and is similar to the previously reported ruthenium bound $H_2B{=}NH_2$ complexes **i-90** [1.396(3) Å] and **i-94** [1.359(8) Å, see Scheme 3.7], and also the bridging borylene complex **IV** [1.399(2) Å] (Figure 3.5).[20-22] The Rh···B distances [2.111(4), 2.077(4) Å] are similar to **i-90**, **i-94** and $[Ir(PCy_3)_2(H)_2(H_2B{=}NMe_2)][BAr^F{}_4]$[23] [1.956(2) - 2.140(13) Å], but significantly shorter than those measured in the bridging thexylborohydride complex **V** [e.g. 2.330(3) Å] reported by Baker and Marder, which is perhaps better described as a hydridoborate $[H_3BR]^-$ complex of $\{Rh(P^iPr_2(CH_2)_2P^iPr_2\}^{2+}$ dication (Figure 3.5).[24]

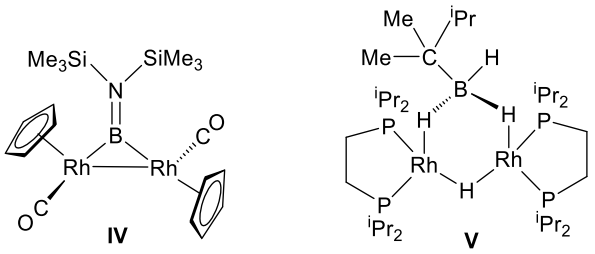
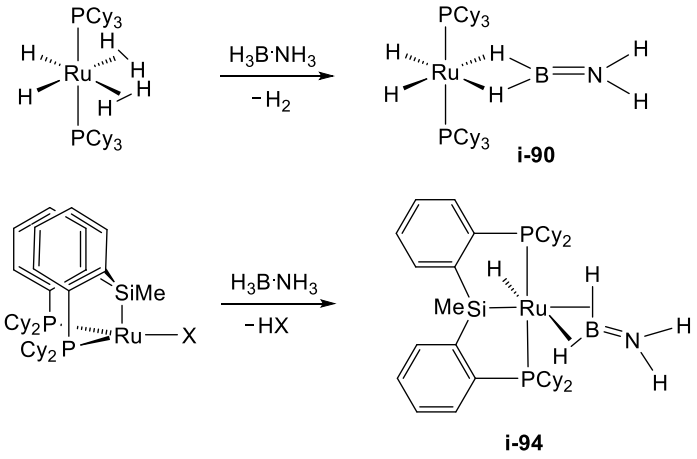


Figure 3.5 Examples of bridging borylyne (**IV**) and bridging borohydride (**V**) compounds.

The structure of complex **7** represents an unprecedented example of $H_2B{=}NH_2$ trapped on a dimeric motif. $H_2B{=}NH_2$ is highly unstable and has been prepared by subjecting borazine vapor to a radiofrequency discharge at temperatures below –150ºC[1, 25, 26], and only two examples of structurally characterised organometallic complexes coordinated to $H_2B{=}NH_2$ are known in the literature.[20, 21] Sabo-Etienne and co-workers reported the first transition metal complex coordinated to $H_2B{=}NH_2$ **i-90** by the reaction of $[Ru(PCy_3)_2(H)_2(H_2)_2]$ with $H_3B{\cdot}NH_3$ and the second example (**i-94**) was prepared by Tobisch and Turculet from the reaction of $H_3B{\cdot}NH_3$ with (Cy-PSiP)RuX [Cy-PSiP = κ^3-$(Cy_2PC_6H_4)_2SiMe$] complex as shown in Scheme 3.7.[20, 21]

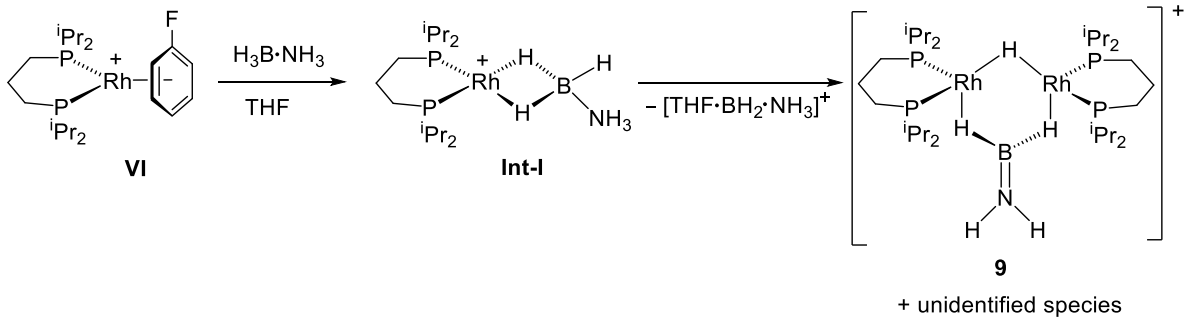


Scheme 3.7 Literature synthesis of transition metal $H_2B{=}NH_2$ complexes, X = O^{t}Bu, N(SiMe$_3$)$_2$**.**

As the isolation of **7** in good yield was not successful, it was characterised *in situ* by NMR spectroscopy at the start of the reaction when **7** is observed as the only organometallic species. In the ^{11}B NMR spectrum, a broad resonance at δ 51.7 is observed similar to the previously reported metal bound $H_2B{=}NH_2$ complexes [**i-90** (δ 47.0) and **i-94** (δ 44.1)**,** Scheme 3.7].[20, 21] In contrast, the rhodium borylene complex reported by Braunschweig (**IV**, Figure 3.5) shows a signal at δ 90 in ^{11}B NMR spectrum, which is very different from that observed for **7**.[22] In the ^{31}P{^{1}H} NMR spectrum a doublet at δ 18.3 (d, $^1J_{RhP}$ = 142 Hz) is observed showing that the phosphine groups are equivalent in solution at room temperature. ^{1}H NMR spectroscopy showed only one signal in the hydride region (δ −7.45, s) integrating for three hydrogens relative to the phenyl signals suggesting that B*H*$_2$ and Rh*H* hydrides are exchanging in solution as they are observed separately in the solid state. The N*H*$_2$ signal was observed at δ 5.67 (br, 2H) in the ^{1}H NMR spectrum. These spectral details are consistent with the formation of **7** and the boronium cation upon the reaction of **III** with $H_3B{\cdot}NH_3$ (Scheme 3.6). Changing the solvent from THF to Et_2O also resulted in the formation of **7** along with the concomitant formation of the boronium species $[BH_2(NH_3)(OEt_2)_2][BAr^F{}_4]$ (δ 1.33, broad t, $^1J_{BH}$ = 115 Hz).[19]

3.4 Reactivity of [Rh($P^iPr_2(CH_2)_3P^iPr_2$)(C_6H_5F)][BAr^F_4] (VI) with $H_3B{\cdot}NH_3$

As the synthesis of pure **7** was not successful in a bulk quantity, in order to isolate and study the dimeric species the reaction was performed using the analogous ^{i}Pr salt [Rh($P^iPr_2(CH_2)_3P^iPr_2$)(C_6H_5F)][BAr^F_4] (**VI**). Reaction of **VI** with $H_3B{\cdot}NH_3$ (1 equivalent, THF) resulted in the formation of [$BH_2(NH_3)(THF)$][BAr^F_4] (^{11}B NMR: δ 0.5, t, $^1J_{BH}$ = 108 Hz) in 15 minutes alongside a mixture of two organometallic complexes in a ratio of 7:3 as measured by the $^{31}P\{^1H\}$ NMR spectroscopy. The major product was characterised as [Rh($P^iPr_2(CH_2)_3P^iPr_2$)(η^2-$H_3B{\cdot}NH_3$)][BAr^F_4] (**Int-I**) on the basis of the analogous complex [Rh($P^iPr_2(CH_2)_3P^iPr_2$)(η^2-$H_3B{\cdot}NMe_3$)][BAr^F_4] (**8**) discussed later in Section 3.5. In the ^{1}H NMR spectrum of the mixture, a broad signal is observed at δ −1.65 characteristic of Rh···H_3B interactions of **Int-I**.[9] The $^{31}P\{^1H\}$ NMR [δ 59.03 (d, $^1J_{RhP}$ = 160 Hz)] and ^{11}B NMR [δ 24.5 (br, BH_2)] spectra both are suggestive of the formation of [Rh($P^iPr_2(CH_2)_3P^iPr_2$)(η^2-$H_3B{\cdot}NH_3$)][BAr^F_4] (**Int-I**) and are consistent with the previously reported rhodium amine-borane sigma-complexes[7, 9] The remaining complex in the mixture was assigned as the rhodium dimer [{Rh($P^iPr_2(CH_2)_3P^iPr_2$)}$_2$(μ-H)(μ-BH_2NH_2)][BAr^F_4] (**9**), similar to **7**, characterised on the basis of its independent synthesis discussed later in Section 3.7. Over time (1 h) the concentration of the two complexes changed; $^{31}P\{^1H\}$ NMR spectroscopy showed the presence of [Rh($P^iPr_2(CH_2)_3P^iPr_2$)(η^2-$H_3B{\cdot}NH_3$)][BAr^F_4] and **9** in a 6:4 ratio suggesting that over time complex **VII** proceeds to form the dimer **9** (Scheme 3.8). Formation of boronium species [$BH_2(NH_3)(THF)$][BAr^F_4] was also observed by the ^{11}B NMR spectroscopy in equal concentration as **9**.



Scheme 3.8 Reactivity of $H_3B{\cdot}NH_3$ with **VI** and the formation of **9**. $[BAr^F_4]^-$ anions are not shown.

Addition of more than one equivalent of $H_3B{\cdot}NH_3$ to **VI** favoured the formation of **9**. In a typical experiment, $[Rh(P^iPr_2(CH_2)_3P^iPr_2)(C_6H_5F)][BAr^F_4]$ (**VI**) was added to $H_3B{\cdot}NH_3$ (~4 equivalents) in THF in a sealed NMR tube. $^{31}P\{^1H\}$ NMR spectroscopy after 2 minutes showed the formation of $[Rh(P^iPr_2(CH_2)_3P^iPr_2)(\eta^2\text{-}H_3B{\cdot}NH_3)][BAr^F_4]$ (**Int-I**) and $[\{Rh(P^iPr_2(CH_2)_3P^iPr_2)\}_2(\mu\text{-}H)(\mu\text{-}BH_2NH_2)][BAr^F_4]$ (**9**) in a 1:3 ratio along with the formation of $[BH_2(NH_3)(THF)][BAr^F_4]$ (Scheme 3.8). At this stage the ^{11}B NMR signal due to excess $H_3B{\cdot}NH_3$ (δ –15.5) is broad and shifted downfield by δ 5.5 ppm compared to the free $H_3B{\cdot}NH_3$, thus suggesting rapid exchange between bound and free $H_3B{\cdot}NH_3$. After 10 minutes all the $[Rh(P^iPr_2(CH_2)_3P^iPr_2)(\eta^2\text{-}H_3B{\cdot}NH_3)][BAr^F_4]$ (**Int-I**) and $[BH_2(NH_3)(THF)][BAr^F_4]$ is consumed and dimeric **9** is the only species detected by $^{31}P\{^1H\}$ NMR spectroscopy. The consumption of $[Rh(P^iPr_2(CH_2)_3P^iPr_2)(\eta^2\text{-}H_3B{\cdot}NH_3)][BAr^F_4]$ (**Int-I**) stops the exchange between free and bound $H_3B{\cdot}NH_3$, so excess $H_3B{\cdot}NH_3$ is now observed as a sharp quartet in the ^{11}B NMR spectrum (δ −21.9, q, $^1J_{BH}$ = 100 Hz). After 4 h ^{11}B NMR spectroscopy showed that $H_3B{\cdot}NH_3$ was completely consumed to produce borazine (10% yield), a boronium species $[BH_2(NH_3)_2][BAr^F_4]$ [45% yield, δ −13.2 (t, J_{BH} = 102 Hz)] formed from the B−N cleavage of $H_3B{\cdot}NH_3$ and an unidentified product displaying a broad signal at δ −44.0 in 45% yield. $^{31}P\{^1H\}$ NMR spectroscopy at this stage showed the presence of **9** along with the formation of unidentified organometallic species [$^{31}P\{^1H\}$ NMR: δ 56 (d, $^1J_{RhP}$ = ~111 Hz) and δ 51 (d, $^1J_{RhP}$ = ~111 Hz)]. After 24 h NMR spectroscopy showed the complete consumption of **9** and the formation of a new complex

[{Rh($P^iPr_2(CH_2)_3P^iPr_2$)}$_2$(H)$_2$(μ-H)$_3$][BAr^F_4][27] as well as some unidentified complexes [$^{31}P\{^1H\}$ NMR: δ 56 (d, $^1J_{RhP}$ = ~111 Hz) and δ 51 (d, $^1J_{RhP}$ = ~111 Hz)]. Formation of [{Rh($P^iPr_2(CH_2)_3P^iPr_2$)}$_2$(H)$_2$(μ-H)$_3$][BAr^F_4] could occur from the reaction of the dimer **9** with the excess hydrogen present in the system as probed by the control experiment discussed later in Section 3.9.

These observations show that the formation of the dimer is slow in the case of the ^{i}Pr-substituted phosphine complex **VI** compared to that of the Ph-substituted complex **III** and its formation is promoted by the presence of excess amine-borane. This is likely via N−H···H−B interactions that promote B−H / N−H activation.[28]

3.5 Synthesis of [Rh($P^iPr_2(CH_2)_3P^iPr_2$)(η^2-$H_3B{\cdot}NMe_3$)][BAr^F_4] (8)

[Rh($P^iPr_2(CH_2)_3P^iPr_2$)(η^2-$H_3B{\cdot}NH_3$)][BAr^F_4] (**Int-I**) was observed as an intermediate during the formation of the dimer [{Rh($P^iPr_2(CH_2)_3P^iPr_2$)}$_2$(μ-H)(μ-BH_2NH_2)][BAr^F_4] (**9**) and could not be isolated due to its transient nature. In order to put the structure of **Int-I** on firm footing, we carried out the synthesis of its stable analogue [Rh($P^iPr_2(CH_2)_3P^iPr_2$)(η^2-$H_3B{\cdot}NMe_3$)][BAr^F_4] (**8**). Complex **8** was synthesised by the addition of one equivalent of $H_3B{\cdot}NMe_3$ to [Rh($P^iPr_2(CH_2)_3P^iPr_2$)(C_6H_5F)][BAr^F_4] (**VI**) in Et_2O solvent and was characterised by NMR spectroscopy, ESI-MS, elemental analysis and single crystal X-ray diffraction. In the ^{1}H NMR spectrum of the isolated complex **8**, a broad signal is observed at δ −1.9 (3 H) corresponding to B*H*$_3$ hydrides suggesting that the terminal and bridging B−H hydrides are exchanging in the solution as previously noted experimentally and also computed theoretically for the sigma-$H_3B{\cdot}NMe_3$ complexes of iridium and rhodium.[29] The ^{11}B NMR spectrum showed a signal at δ 24.5 corresponding to the Rh···H_3B interaction and the $^{31}P\{^1H\}$ NMR spectrum consisted of a doublet at δ 59.2 (d, $^1J_{RhP}$ = 163 Hz). These spectral features are consistent with the previously reported sigma-complexes of rhodium with $H_3B{\cdot}NMe_3$.[8, 9] Figure 3.6 shows the solid state structure of the cationic portion of **8** which shows that $H_3B{\cdot}NMe_3$ is coordinated to a pseudo-square planar Rh(I) centre

through two Rh···H−B 3c-2e interactions. Bond lengths Rh1−B1 2.283(9), B1−N1 1.535(5) Å and bond angle P1−Rh1−P2 93.56(4)˚ are consistent with a rhodium(I) η^2-amine-borane complexes resembling closely $[Rh(PPh_2(CH_2)_3PPh_2)(\eta^2\text{-}H_3B{\cdot}NMe_3)][BAr^F{}_4]$: Rh1−B1 2.199(3) Å, B1−N1 1.592(7) Å and P1−Rh1−P2 91.14(3)˚.[8, 9]

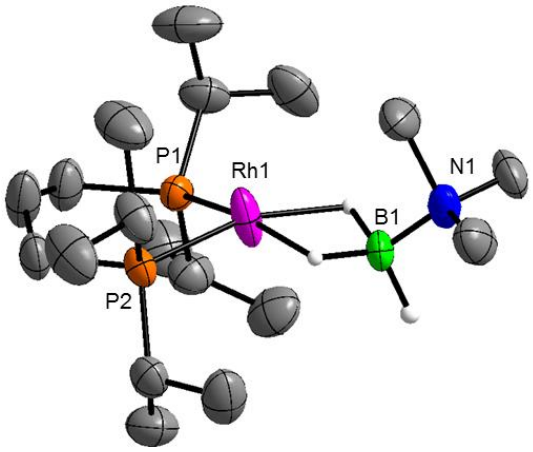
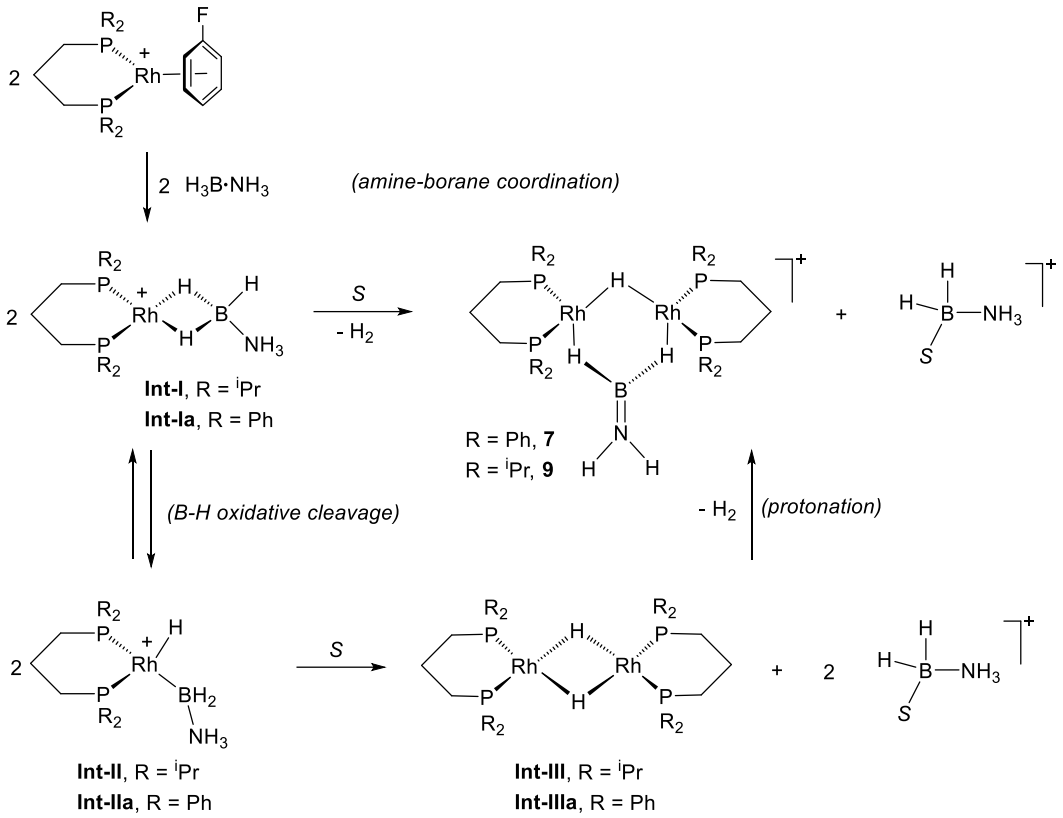


Figure 3.6 Solid state structure of the cationic portion of **8** with displacement ellipsoids at the 50% probability level. For clarity carbon-bound H atoms are omitted, and only one of the disordered (NMe_3 and carbon backbone of the bis-phosphine ligands) components are shown. Selected bond lengths (Å): Rh1−P1, 2.2085(11); Rh1−P2, 2.2013(10); Rh1−B1, 2.283(9); B1−N1, 1.535(5). Selected bond angle (˚): P1−Rh1−P2, 93.56(4).

3.6 The mechanism of the formation of the dimers

Understanding the mechanism of the formation of the dimeric species **7** and **9** and their onward reactivity is important in exploring their role in the catalytic dehydrocoupling of $H_3B{\cdot}NH_3$. Scheme 3.9 shows a proposed mechanism for the dimer formation that takes into account the concomitant formation of the boronium cation and the dimer. The first step is the formation of an amine-borane sigma-complex (**Int-I** or **Int-Ia**) which then undergoes a B–H activation step to form a Rh(III) species (**Int-II** or **Int-IIa**). Nucleophilic solvent (*S* = THF or Et_2O) can then react with **Int-II** or **Int-IIa**, abstract $\{BH_2(NH_3)\}^+$ and form a boronium species $[BH_2(NH_3)(S)][BAr^F{}_4]$ along with a neutral rhodium hydride $[Rh(PR_2(CH_2)_3PR_2)(H)]$ which can dimerize to produce a Fryzuk-type dimer $[Rh(PR_2(CH_2)_3PR_2)(\mu\text{-}H)]_2$ (**Int-III** or **Int-IIIa**).[30] Subsequent protonation by

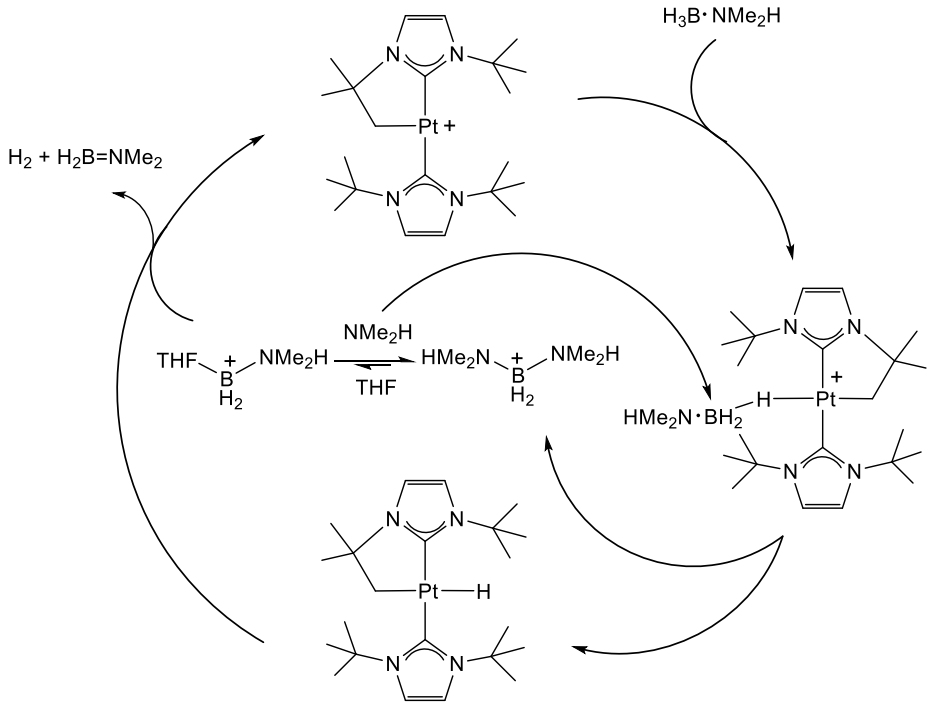
$[BH_2(NH_3)(S)][BAr^F{}_4]$ could release H_2 and result in the formation of **7** (R = Ph) or **9** (R = ^{i}Pr).



Scheme 3.9 Mechanism for the formation of the dimers **7** and **9**. $[BAr^F{}_4]^-$ anions are not shown. *S* = THF or Et_2O.

The concomitant formation of a metal hydride and the boronium cation has also been reported by Conejero for the dehydrocoupling of $H_3B{\cdot}NMe_2H$ catalysed by the Pt(II) complex $[Pt(I^tBu')(I^tBu)][BAr^F{}_4]$ (Scheme 3.10, I^tBu is the N-heterocyclic carbene ligand 1,3-di-*tert*-butylimidazol-2-ylidene, and I^tBu' denotes the cyclometalated I^tBu ligand).[31] The mechanism involves hydride abstraction from $H_3B{\cdot}NMe_2H$ at the metal centre which is assisted by NMe_2H and yields a platinum-hydride complex $[PtH(I^tBu')(I^tBu)]$ along with the boronium cation $[(NHMe_2)_2BH_2]^+$. $[(NHMe_2)_2BH_2]^+$ is suggested to be in equilibrium with $[(NHMe_2)(THF)BH_2]^+$ which protonates the platinum hydride through the acidic N−H

proton, produces H_2 and the amino-borane $H_2B{=}NMe_2$, and regenerates the catalyst (Scheme 3.10).

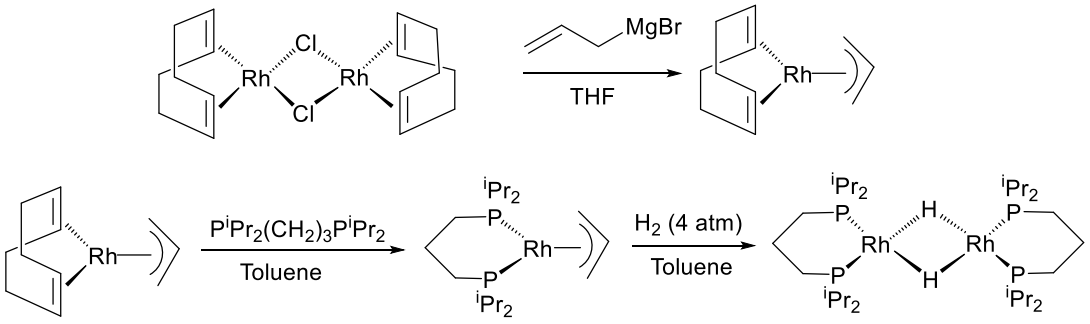


Scheme 3.10 Proposed mechanism for the dehydrocoupling of $H_3B{\cdot}NMe_2H$ catalysed by Pt(II) complex.[31] $[BAr^F{}_4]^-$ anions are not shown.

3.7 Independent synthesis of the dimer 9

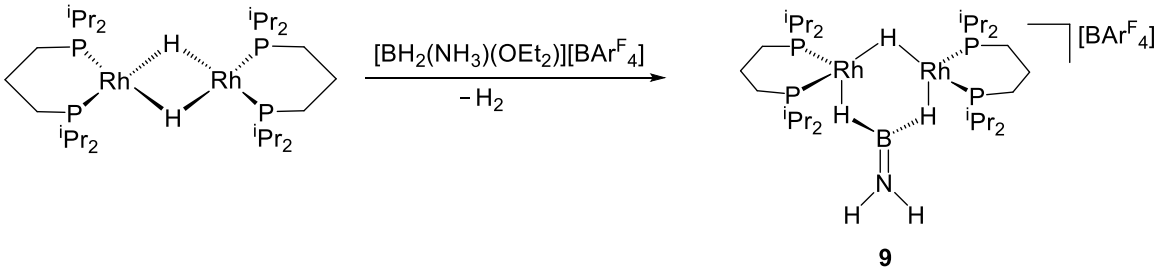
In order to test the proposed mechanism described in Scheme 3.9 the reaction of the Fryzuk dimer $[Rh(PR_2(CH_2)_3PR_2)_2(\mu\text{-}H)_2]$ (**IX**) with the boronium cation was targetted. $[BH_2(NH_3)(OEt_2)][BAr^F{}_4]$ was prepared by the method reported by Baker through the reaction of $H_3B{\cdot}NH_3$ with $[H(OEt_2)_2][BAr^F{}_4]$.[19] $[Rh(P^iPr_2(CH_2)_3P^iPr_2)_2(\mu\text{-}H)_2]$ was synthesised by the method reported by Fryzuk in 1989.[30] Addition of $P^iPr_2(CH_2)_3P^iPr_2$ in toluene to $[Rh(COD)(\eta^3\text{-}C_3H_5)]$ resulted in the formation of $[Rh(P^iPr_2(CH_2)_3P^iPr_2)(\eta^3\text{-}C_3H_5)]$ which was then hydrogenated (4 atm, 3 days) to produce $[Rh(P^iPr_2(CH_2)_2P^iPr_2)_2(\mu\text{-}H)_2]$. Synthesis of $[Rh(COD)(\eta^3\text{-}C_3H_5)]$ was reported by Muetterties in 1979 by the reaction of $[Rh(COD)(\mu\text{-}Cl)]_2$ with allylmagnesium bromide in THF (Scheme 3.11).[32] Attempts to synthesise

$[Rh(PPh_2(CH_2)_3PPh_2)_2(\mu\text{-}H)_2]$ using the same methodology was not successful and instead resulted in a mixture of uncharacterised complexes.



Scheme 3.11 Synthesis of $[Rh(P^iPr_2(CH_2)_2P^iPr_2)_2(\mu\text{-}H)_2]$.

Reaction of white $[BH_2(NH_3)(OEt_2)][BAr^F{}_4]$ with green $[Rh(P^iPr_2(CH_2)_3P^iPr_2)(\mu\text{-}H)]_2$ in Et_2O solvent resulted in immediate bubbling, presumed to be due to the release of hydrogen gas, and formed an orange solution, which was characterised to be $[\{Rh(P^iPr_2(CH_2)_3P^iPr_2)\}_2(\mu\text{-}H)(\mu\text{-}BH_2NH_2)][BAr^F{}_4]$ (**9**) (Scheme 3.12). This confirms the postulated mechanism shown in Scheme 3.5 showing that the dimer **7** or **9** can be formed by the protonation of the neutral dimer $[Rh(PR_2(CH_2)_2PR_2)_2(H)_2]$ by $[BH_2(NH_3)(THF)][BAr^F{}_4]$.



9

Scheme 3.12 Synthesis of $[(Rh(P^iPr_2(CH_2)_3P^iPr_2))_2(\mu\text{-}H)(\mu\text{-}BH_2NH_2)][BAr^F{}_4]$ (**9**).

Orange crystals of complex **9** were isolated by recrystallisation from Et_2O/pentane solution at −18˚C and characterised by NMR spectroscopy, ESI-MS, elemental analysis and single crystal X-ray diffraction. Figure 3.8 shows the solid state structure of **9** which shows that

the amino-borane unit is bridging two pseudo-square planar Rh(I) centres. Hydrogen atoms H1 - H5 were located on the Fourier map and allowed to refine freely before applying the riding constraints. Bond lengths B–N [1.377(6) Å], Rh–B [2.070(5)Å] and Rh1–Rh2 [2.7874(4) Å] are all consistent with a bridging $H_2B{=}NH_2$ fragment bound to two rhodium centers similar to the solid state structure of **7** shown in Figure 3.4.

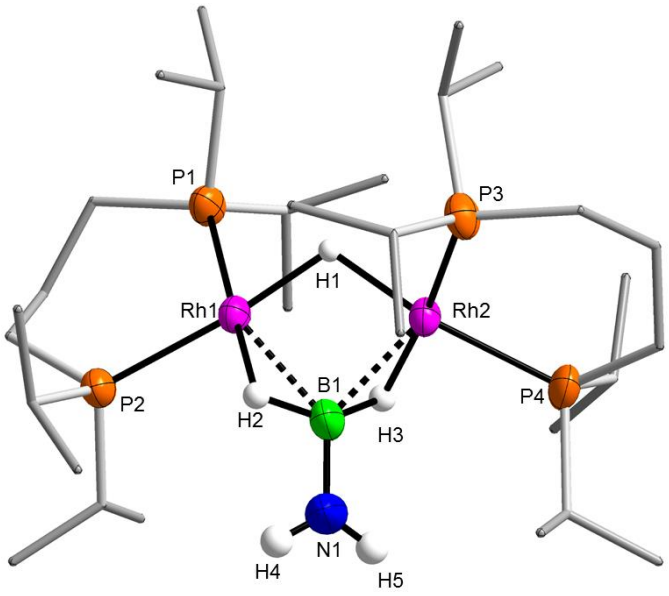


Figure 3.7 Solid state structure of the cationic portion of **9** with thermal ellipsoids at the 50% probability level. For clarity carbon-bound H atoms are omitted, and the carbon atoms are depicted as a wireframe. Selected bond lengths (Å) and bond angles (˚): Rh1−P1, 2.2550(10); Rh1−P2, 2.3063(10); Rh2−P3, 2.2912(10); Rh2−P4, 2.2674(10); Rh1−B1, 2.070(5); Rh2−B1, 2.055(5); Rh1−Rh2, 2.7874(4); B1−N1, 1.377(6); Rh1−B1−Rh2, 85.02(19).

The coordination geometry around the rhodium centres is explicitly shown in Figure 3.8. The NH_2 group is twisted by 24˚ with respect to the BH_2 group and the $H_2B{=}NH_2$ fragment is twisted by 54.1˚ with respect to the Rh···Rh vector (Figure 3.8 A). This is presumably in order to accommodate the appropriate overlap between the B−H moieties and the two rhodium centres. Each pseudo square plane containing phosphines and the hydrides e.g. P1/P2/H1/H2 is twisted with respect to one another by 102˚ (Figure 3.8 B) similar to that observed for the hydridoborate complex **V** (Figure 3.5) reported by Baker and Marder.[24]

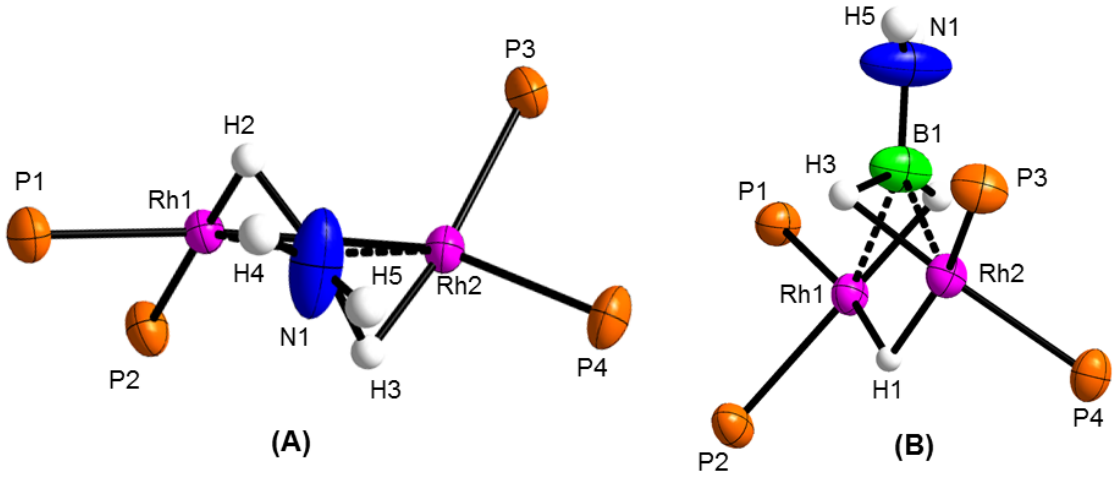


Figure 3.8 Portion of the solid state structure of **9** showing the coordination chemistry around metal centres. ∠plane(N1B1H2H2)/plane(N1B1Rh1Rh2), 54.1; ∠plane(Rh1P1P2)/plane(Rh2P3P4), 100.2; ∠plane(NH_2)/plane(BH_2), 24.3º.

The ^{11}B NMR spectrum of **9** consisted of a broad signal at δ 51.1 corresponding to the bound H_2B=NH_2 fragment. At 298 K, a single resonance at δ −8.64 (s, 3H) was observed in the hydride region of the ^{1}H NMR spectrum. On cooling to 180 K, this resonance splits into two broad signals at δ −8.16 (2H, BH_2) and δ −9.02 (1H, Rh*H*) suggestive of a fluxional process resulting in the fast exchange of the bridging BH_2 and Rh*H* hydrides at room temperature. At room temperature, the ^{31}P{^{1}H} NMR spectrum shows a single resonance at δ 40.8 (d, $^{1}J_{RhP}$ = 142 Hz). However, gradual cooling of the sample allows the observation of two distinct phosphorus environments as shown in Figure 3.9. The coalescence temperature was observed at 210 K and the low temperature limit was reached at 180 K where the two broad doublets were observed at δ 41.6 ($^{1}J_{RhP}$ = 140 Hz) and 36.1 ($^{1}J_{RhP}$ = 140 Hz). The experimentally observed ^{31}P{^{1}H} NMR spectra were simulated using G-NMR[33] through which the rate constants of the exchange process at different temperatures were obtained. An Eyring plot[34] of ln(k/T) against 1/T (Figure 3.10) provided the values of activation parameters for the fluxional process: $\Delta H^{\ddagger}$ = 31.07 ± 1.3 kJ mol^{-1}, $\Delta S^{\ddagger}$ = −27.44 ± 0.99 J K^{-1} mol^{-1}, $\Delta G^{\ddagger}$ = 39.25 ± 1.6 kJ mol^{-1}. A negative entropy suggests that the fluxional process is not operating through a dissociative mechanism.[35]

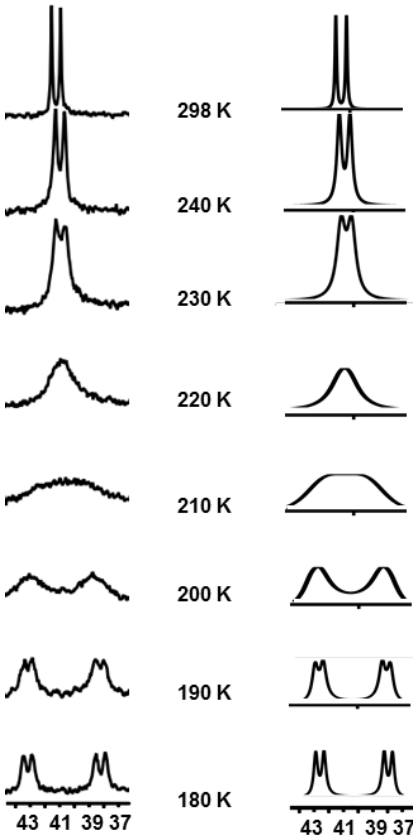


Figure 3.9 Representative $^{31}P\{^{1}H\}$ NMR spectra of **9** in THF at a range of temperatures (left) and their g-NMR simulations (right).

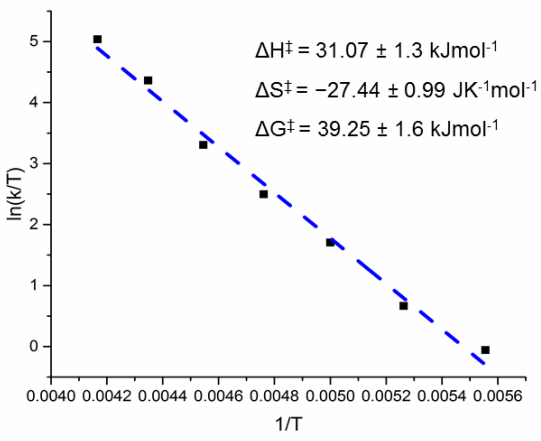
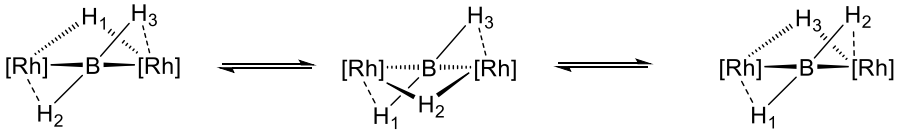


Figure 3.10 Eyring analysis for 9**.** ln(k/T) = −3736.85(1/T) + 20.46.

Aldridge has reported a similar energy barrier ($\Delta G^{\ddagger}$ = 41.4 kJ mol^{-1}) for the fluxionality of amino-borane in [CpRu(PPh$_3$)$_2$(η^1-H$_2$BNCy$_2$)][BAr$^F{}_4$] (**i-89**) in which the H$_2$BNCy$_2$ fragment rotates about the Ru−(BH centroid) axis making both the phosphine groups spectroscopically equivalent at room temperature.[36]

3.8 Mechanism of the fluxional process in 9

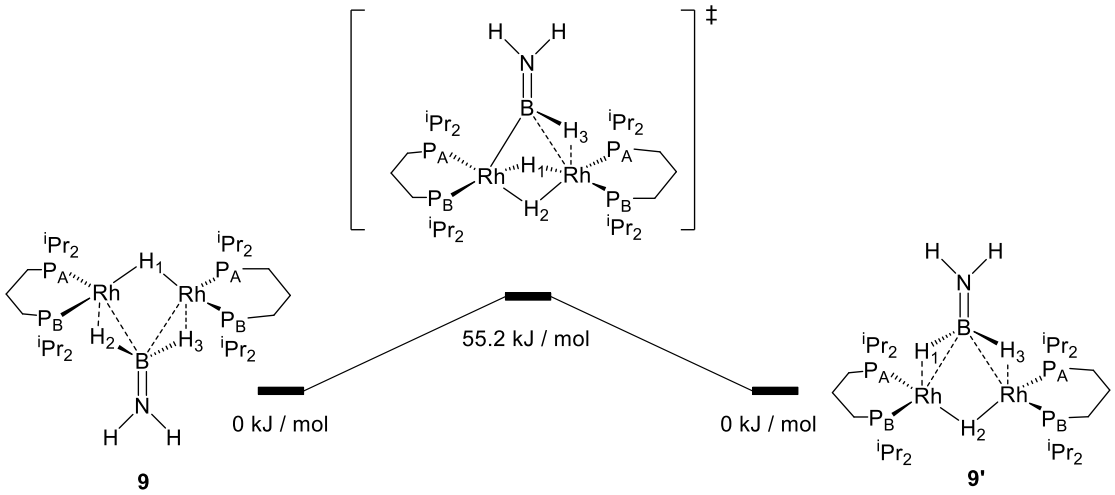
The mechanism of the room temperature fluxional process in **9** was probed by the DFT calculations carried out by Prof. Stuart Macgregor and Nicholas Beattie (Heriot Watt University, Edinburgh). A mechanism shown in Scheme 3.13 is suggested for the fluxional process which involves cleavage of a B−H (e.g. B−H$_2$) bond and formation of a Rh−H−Rh (e.g. Rh−H$_2$−Rh) bond followed by the movement of the original rhodium bridging hydride (e.g. Rh−H$_1$−Rh) to a Rh−H−B position. This results in the exchange of two hydrides e.g. H$_1$ and H$_2$. A degenerate transformation can result in the exchange between the remaining two hydrides (Scheme 3.13). This mechanism explains the observation of a single resonance in the hydride region of the ^{1}H NMR spectrum of the dimers **7** or **9** as the "BNH$_2$" unit effectively precesses around RhH$_3$Rh moiety.



Scheme 3.13 Proposed fluxional process occurring in the dimers **7** or **9**.

A single transition state as shown in Scheme 3.14 was identified for this fluxional process. The exchange of hydrides (such as H$_1$ and H$_2$ in **9** and **9'**) is accompanied by the rotation of the H$_2$B=NH$_2$ fragment around the Rh···Rh vector which makes both the phosphorus atoms (P$_A$ and P$_B$) equivalent. This is consistent with the observation of single phosphorus environment in the ^{31}P{^{1}H} NMR spectrum of the dimer **7** or **9**. The magnitude of the DFT-computed thermodynamic parameters for the exchange process ($\Delta H^{\ddagger}$ = 45.6 kJ mol^{-1}, $\Delta S^{\ddagger}$

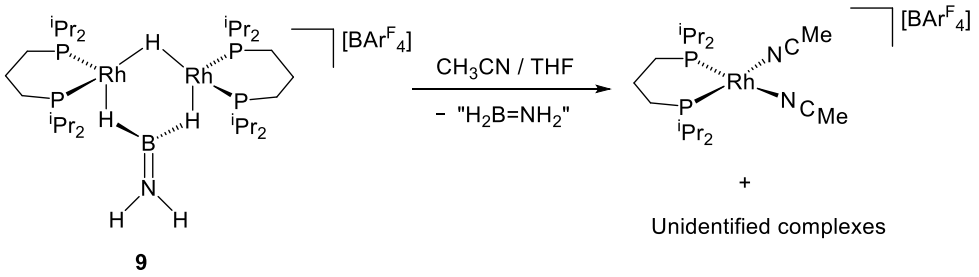
= –32.2 J K^{-1} mol^{-1} and $\Delta G^{\ddagger}$ = 55.2 kJ mol^{-1}) are slightly higher than those obtained from the Eyring analysis ($\Delta H^{\ddagger}$ = 31.07 ± 1.3 kJ mol^{-1}, $\Delta S^{\ddagger}$ = −27.44 ± 0.99 J K^{-1} mol^{-1}, $\Delta G^{\ddagger}$ = 39.25 ± 1.6 kJ mol^{-1}) but still consistent with the process being feasible at room temperature.



Scheme 3.14 Transition state for the fluxionality of $H_2B{=}NH_2$, charges are not shown.

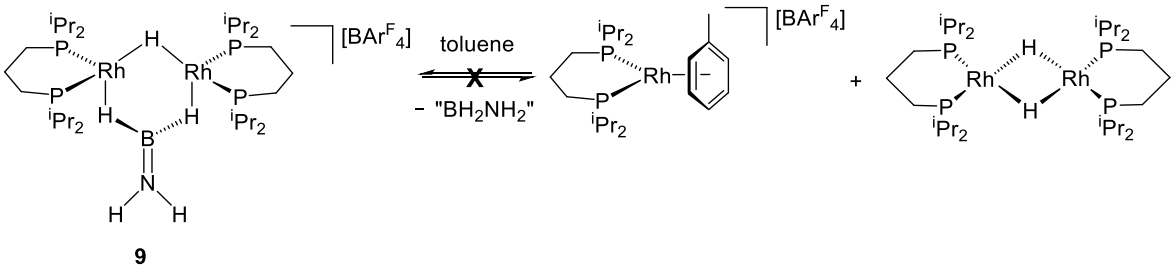
3.9 Reactivity of 9 towards $H_3B{\cdot}NMe_3$, CH_3CN, toluene and H_2

η^2-Amine-borane or amino-borane sigma-complexes feature weak binding of amine-boranes / amino-boranes at the metal centres and thus can be easily displaced by the addition of excess strong donor ligands such as CH_3CN (for example, see Section 2.2, Chapter 2).[37-40] However, complex **9** does not show any reactivity with $H_3B{\cdot}NMe_3$ (5 equivalents) and only very slowly ($t_{1/2}$ = ~8 h) reacts with CH_3CN (100 equivalents) to form the known monomeric complex $[Rh(P^iPr_2(CH_2)_3P^iPr_2)(NCMe)_2][BAr^F{}_4]$[27] (Scheme 3.15) and an unidentified complexes showing broad hydride resonances at δ −11.67 and −20.69. This shows that the $H_2B{=}NH_2$ fragment in **9** is very strongly bound suggesting a strong degree of Rh−B backbonding.



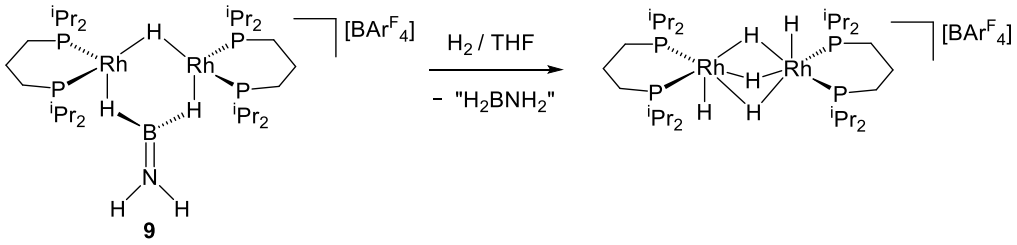
Scheme 3.15 Reactivity of **9** with CH_3CN.

When isolated, pure [{Rh(P^{i}Pr$_2$(CH$_2$)$_3$P^{i}Pr$_2$)}$_2$(μ-H)(μ-BH$_2$NH$_2$)][BAr$^F_4$] (**9**) was found to be stable in THF for two days by NMR spectroscopy. A slow dimer-monomer equilibrium in solution can be probed by the addition of toluene which could result in the formation of a cationic complex [Rh(P^{i}Pr$_2$(CH$_2$)$_3$P^{i}Pr$_2$)(C$_6$H$_5$Me)][BAr$^F_4$] and a neutral Fryzuk dimer [Rh(P^{i}Pr$_2$(CH$_2$)$_3$P^{i}Pr$_2$)(H)]$_2$ (Scheme 3.16). However, addition of toluene (100 equivalents) to the THF solution of **9** did not show any reaction as monitored by the $^{31}P\{^1H\}$ NMR spectroscopy. This argues against a dimer-monomer equilibrium operating in the solution.



Scheme 3.16 Probing the dimer-monomer equilibrium by the addition of toluene.

In contrast, addition of H_2 (4 atm) to a THF solution of **9** resulted in the quantitative formation of [{Rh(P^{i}Pr$_2$(CH$_2$)$_3$P^{i}Pr$_2$)}$_2$(H)$_2$(*μ*-H)$_3$][BAr$^F_4$][27] in 15 minutes by NMR spectroscopy (Scheme 3.17). The ^{11}B NMR spectroscopy did not show any signals (to the detectable limit) corresponding to B−N products resulting from the loss of $H_2B{=}NH_2$.



9

Scheme 3.17 Reactivity of the complex **9** with H_2.

This experiment suggests that the reaction of **9** with H_2 follows a different kinetic pathway compared to that with the Lewis base ligands such as CH_3CN. Formation of $[\{Rh(P^iPr_2(CH_2)_3P^iPr_2)\}_2(H)_2(\mu\text{-}H)_3][BAr^F_4]$ can occur by the coordination of one dihydrogen ligand on each rhodium centre of **9** followed by their oxidative cleavage. One of the two hydrides thus formed on each rhodium centre can bridge with the other rhodium centre forming two additional Rh−H−Rh hydrides resulting in the formation of $[\{Rh(P^iPr_2(CH_2)_3P^iPr_2)\}_2(H)_2(\mu\text{-}H)_3][BAr^F_4]$.

3.10 Structure and bonding of 9 using DFT calculations

As discussed above, **9** represents a cationic rhodium dimer containing the strongly bound $H_2B{=}NH_2$ unit. The valence bond model for **9** is shown in Figure 3.11 in which one of the rhodium centres is considered cationic while the other one is considered neutral. Donation from the $Rh_{neutral}$−H bond to the $Rh_{cationic}$ centre gives two 16 electron metal centres suggesting that a metal−metal bond is not required, whereas, donation from the $Rh_{cationic}$−H bond to the $Rh_{neutral}$ centre results in a 17 electron and a 15 electron metal centre which is highly unlikely and not commensurate with the diamagnetic NMR spectrum observed.

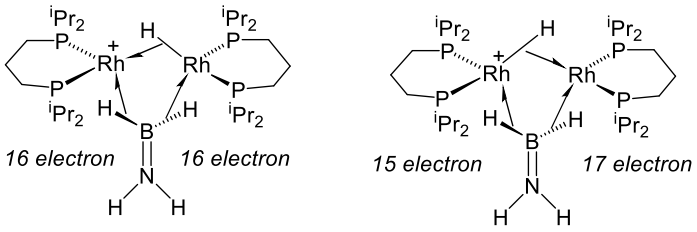


Figure 3.11 Valence bond electron counting models for the dimer **9**. $[BAr^F_4]^-$ anions are not shown.

In order to understand the structure of **9** in terms of the coordination chemistry of amino-borane, Nicholas Beattie and Prof. Stuart Macgregor (Heriot-Watt University, Edinburgh) carried out 'Atoms in Molecules'[41] calculations which provide information on the nature of the electron density in the interaction between atoms. Figure 3.12 shows the two plausible limiting structures of the complex **9**: a bridging amino-borane Rh(I) complex and a bridging borylene dihydride Rh(III) complex.

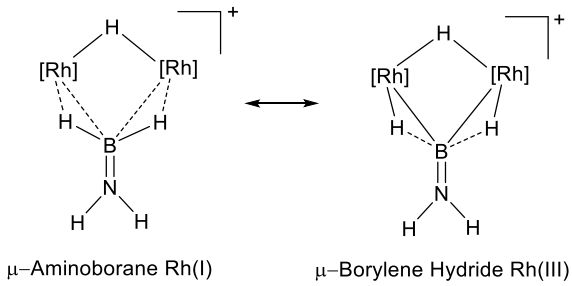


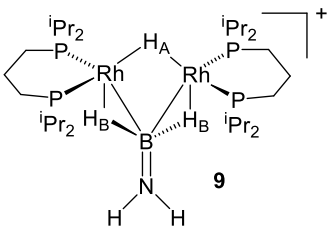
Figure 3.11 Limiting valence bond descriptions for complex **9**. $[BAr^F_4]^-$ anions are not shown.

Two important parameters obtained from these calculations are ρ (e $Å^{-3}$, electrons per cubic angstrom) and ε. ρ is a measure of the bond strength and therefore higher ρ is indicative of a stronger bond, while ε (ellipticity) is a measure of the bond asymmetricity. A symmetric bond will have very low ellipticity (close to zero) while an asymmetric bond for example, a three-centre two-electron bond, will have greater ellipticity. Table 3.1 represents the values of ρ and ε obtained for the complex **9** as well as the related bridging borylene complex **IV** and the hydrididoborate complex **V**. The values of ρ obtained for $Rh{-}H_A$ (0.09) and $Rh{-}H_B$ (0.11) bonds in **9** are similar to the corresponding values in **V**

and represent significant Rh···H interactions. A significant B−H_B interaction is also observed in **9**, similar to **V**, along with a higher ellipticity which suggests that the B−H_B bond is involved in a 3c-2e bond. The values of ρ for the B−H_B bond in **9** (0.11) and **V** (0.13) are smaller than that of the B−H_C terminal bond (0.15) which is consistent with the bridging bonds being stretched compared to the terminal bond. The higher values of ρ (0.20) and the smaller ε (0.13) obtained for the B−N bond in **9** are found to be similar to **IV** and are consistent with it being a double bond. Interestingly, a significant Rh···B interaction similar to **IV** is also observed in **9**, however, a higher ellipticity (0.62) compared to that obtained for **IV** (0.08) provides strong evidence for the absence of a direct 2c-2e Rh−B bond in **9**, thus discounting a bridging borylene dihydride Rh(III) structure. Based on all this evidence, we suggest that the complex **9** is a bridging amino-borane complex with stretched B−H bonds and significant Rh···B interactions.

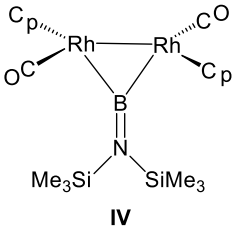
Table 3.1 'Atoms in Molecules' calculated parameters for **9**, **IV** and **V**.

Bond	**ρ**	**ε**
Rh−B	0.11	0.62
B−H_B	0.11	0.38
Rh−H_B	0.11	0.46
Rh−H_A	0.09	0.10
B−N	0.20	0.13



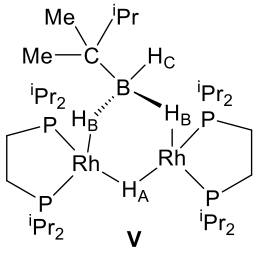
9

Bond	**ρ**	**ε**
Rh−B	0.11	0.08
B−N	0.21	0.10



IV

Bond	ρ	ε
Rh−B	-	-
B−H_B	0.13	0.17
Rh−H_B	0.09	0.37
Rh−H_A	0.09	0.11
B−H_C	0.15	0.11



V

Mid summary

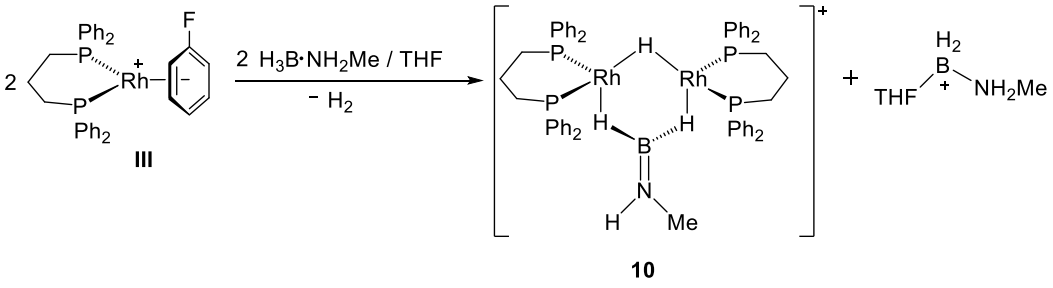
*Up until this point, we have established that the dimers **7** or **9** forms from the reaction of $H_3B{\cdot}NH_3$ with the monomers **III** or **VI**, respectively. We have also studied the structure and bonding of the isolatable dimeric complex **9** by the NMR spectroscopy, single crystal X-ray diffraction and DFT calculations in great detail. The remaining sections in this chapter will explore the formation of the dimer with the N-substituted amine-boranes such as $H_3B{\cdot}NHRMe$ (R = H, Me) and their role in the catalytic dehydrocoupling of amine-boranes.*

3.11 Reactivity of III with $H_3B{\cdot}NH_2Me$ in THF and 1,2-$F_2C_6H_4$

3.11.1 Reactivity of III with 1 - 4 equivalents of $H_3B{\cdot}NH_2Me$

Addition of 1.2 equivalents of $H_3B{\cdot}NH_2Me$ to $[Rh(PPh_2(CH_2)_3PPh_2)(C_6H_5F)][BAr^F{}_4]$ (**III**) in THF showed the immediate formation of $[\{Rh(PPh_2(CH_2)_3PPh_2)\}_2(\mu\text{-}H)(\mu\text{-}BH_2NHMe)][BAr^F{}_4]$ (**10**, Scheme 3.18), which is proposed to be directly analogous to **7**, as the only organometallic product by NMR spectroscopy and ESI-MS (m/z 1074.1340 $[M^+]$, calc. 1074.1801). ^{1}H NMR spectroscopy showed a resonance at δ −6.84 (s, 3H) corresponding to both hydride environments (B*H*$_2$ and Rh*H*) suggesting a fast exchange between the three hydrides. The $^{31}P\{^1H\}$ NMR spectrum displayed two broad signals at δ 22.2 and 21.6, integrating equally relative to each other, suggesting two inequivalent phosphorus environments presumably due to the asymmetry now imposed by the NMe

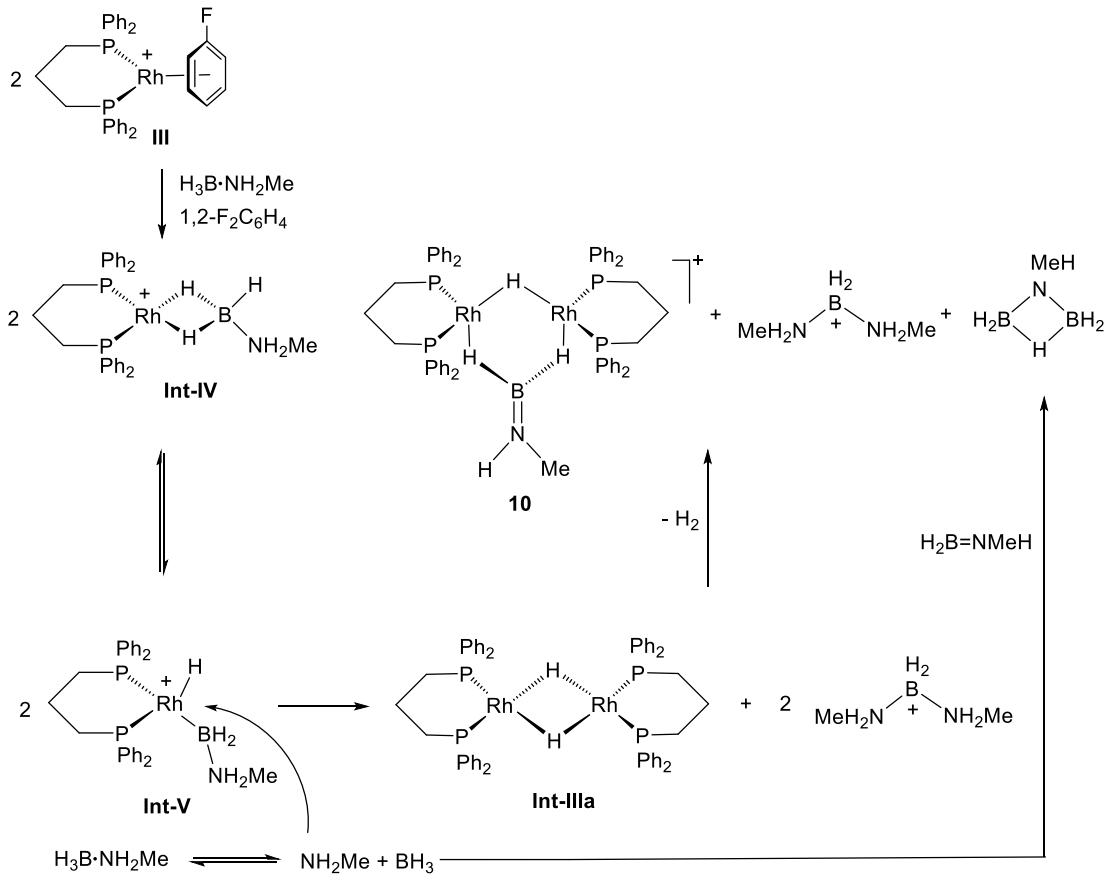
group. The bound H_2B=NHMe unit was observed at δ 50.6 as a broad signal in the ^{11}B NMR spectrum similar to that observed for the complexes **7** and **9**. A signal corresponding to $[BH_2(NH_2Me)(THF)][BAr^F{}_4]$ was also observed in the ^{11}B NMR spectrum at δ 2.8 (t, $^1J_{BH}$ = 123 Hz), which is consistent with $[BH_2(NH_2Me)(OEt_2)][B(C_6F_5)_4]$ (CD_2Cl_2, δ 1.70, t, J_{BH} = 121 Hz) reported by Manners and coworkers.[42] Over 1 h complex **10** decomposes to give a number of unidentified complexes. Due to this instability, **10** could not be isolated as pure solid.



Scheme 3.18 Reactivity of **III** with $H_3B{\cdot}NH_2Me$ in THF. $[BAr^F{}_4]^-$ anions are not shown.

The formation of **10** was also observed in 1,2-$F_2C_6H_4$ solvent. Addition of 4 equivalents of $H_3B{\cdot}NH_2Me$ to $[Rh(PPh_2(CH_2)_3PPh_2)(C_6H_5F)][BAr^F{}_4]$ (**III**) in 1,2-$F_2C_6H_4$ solution resulted in the immediate formation of $[\{Rh(PPh_2(CH_2)_3PPh_2)\}_2(\mu\text{-}H)(\mu\text{-}BH_2NHMe)][BAr^F{}_4]$ (**10**) which decomposed after 20 minutes to give a mixture of unidentified compounds. ^{11}B NMR spectroscopy also showed the formation of $[(NH_2Me)_2BH_2][BAr^F{}_4]$ [δ −7.7 (t, J_{BH} = 115 Hz)][31, 43], $H_2B(\mu\text{-}H)(\mu\text{-}NMeH)BH_2$[44] and polymethylaminoborane ($[H_2BNMeH]_n$, δ −5.5, br).[15] We suggest a mechanism (Scheme 3.19) inspired by Conejero's mechanism (Scheme 3.10) that explains the formation of **10** along with the B−N products in 1,2-$F_2C_6H_4$ solvent. Complex **III** reacts with $H_3B{\cdot}NH_2Me$ to form the sigma-complex $[Rh(P^iPr_2(CH_2)_3P^iPr_2)(\eta^2\text{-}H_3B{\cdot}NH_2Me)][BAr^F{}_4]$ (**Int-IV**) which undergoes oxidative cleavage to form a Rh(III) complex **Int-V** similar to that proposed for the THF solvent (Scheme 3.9). NH_2Me produced from the B−N cleavage of $H_3B{\cdot}NH_2Me$ reacts with the Rh(III) intermediate **Int-V** to form the boronium cation $[(NH_2Me)_2BH_2][BAr^F{}_4]$ and the neutral

Fryzuk dimer $[Rh(PPh_2(CH_2)_3PPh_2)(\mu\text{-}H)]_2$ (**Int-IIIa**). The boronium cation can then react with $[Rh(PPh_2(CH_2)_3PPh_2)(H)]_2$ to form **10**. The remaining BH_3 from the dissociation of $H_3B{\cdot}NMeH_2$ reacts with the amino-borane $H_2B{=}NHMe$ produced from the dehydrogenation of $H_3B{\cdot}NH_2Me$ to form the hydrido bridged product $H_2B(\mu\text{-}H)(\mu\text{-}NMeH)BH_2$.



Scheme 3.19 Proposed mechanism for the formation of **10** in 1,2-$F_2C_6H_4$ solvent. $[BAr^F{}_4]^-$ anions are not shown.

However, when one equivalent of **III** is reacted with $H_3B{\cdot}NH_2Me$, formation of **10** is observed in only 5% yield, rest being the starting complex **III**.

The different B−N products formed on reaction of **III** with $H_3B{\cdot}NH_2Me$ in 1,2-$F_2C_6H_4$ and THF could be due to the difference in stability of $[BH_2(NH_2Me)(S)][BAr^F{}_4]$ (S = solvent) which is formed concomitantly with **10**. $[BH_2(NH_2Me)(S)][BAr^F{}_4]$ would be expected to be

more stable in the presence of nucleophilic solvents like THF and less stable in the presence of 1,2-$F_2C_6H_4$. Thus formation of $[(NH_2Me)_2BH_2][BAr^F_4]$ instead of $[BH_2(NH_2Me)(S)][BAr^F_4]$ is observed in 1,2-$F_2C_6H_4$.

The experimental details discussed above suggest that the formation of **10** is assisted by a nucleophilic solvent and occurs via the formation of $[BH_2(NH_2Me)(S)][BAr^F_4]$. In 1,2-$F_2C_6H_4$, where $[BH_2(NH_2Me)(S)][BAr^F_4]$ is not stable, **10** is formed with the concomitant formation of $[(NH_2Me)_2BH_2][BAr^F_4]$ and the process is favoured by the presence of excess $H_3B{\cdot}NH_2Me$.

3.11.2 Catalytic dehydrocoupling of $H_3B{\cdot}NH_2Me$ using III and *in situ* prepared 10

Catalytic dehydrocoupling experiments were carried out in an open system using the method described in Section 3.3.1 using **III** and *in situ* prepared **10** catalysts. In a typical experiment, 0.5 mol% **III** (2.0 x 10^{-3} M) or 0.25 mol% **10** (1.0 x 10^{-3} M) was used as a catalyst for the dehydrocoupling of $H_3B{\cdot}NH_2Me$ (0.41 M) in THF and hydrogen evolution was measured using a gas-burette method. Both showed similar dehydrogenation profiles and released ~1.1 equivalents of hydrogen gas with a TOF of ~200 h^{-1} (Figure 3.13).

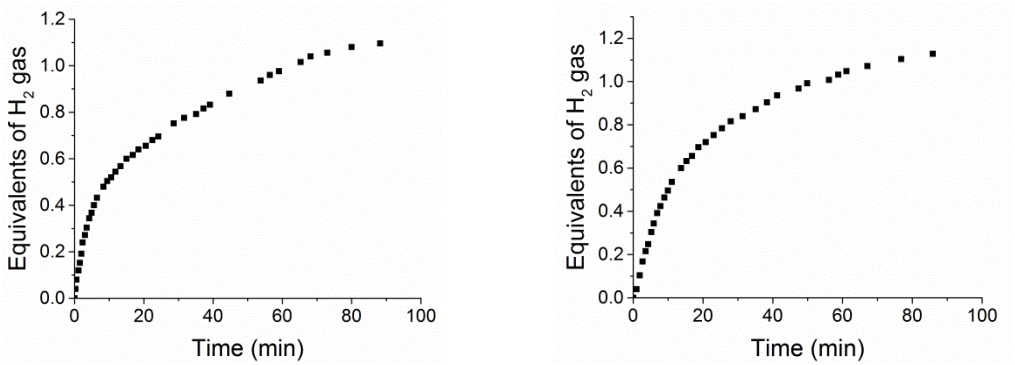
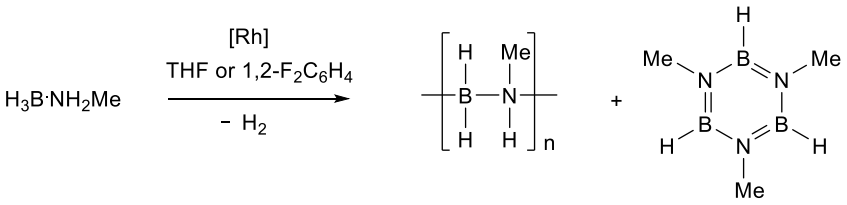


Figure 3.13 Plots of equivalents of H_2 gas produced against time during dehydrocoupling of $H_3B{\cdot}NH_2Me$ (0. 41 M) using **III** (2.0 x 10^{-3} M, 0.5 mol%, left) or *in situ* prepared **10** (1.0 x 10^{-3} M, 0.25 mol%, right) in THF.

The formation of polyaminoborane ($[BH_2NMeH]_n$, ~95%) and borazine ($[BHNMe]_3$, ~5%) was observed at the end of both the dehydrocoupling experiments through ^{11}B NMR spectroscopy (Scheme 3.20, Figure 3.14).



Scheme 3.20 [Rh] catalysed dehydrocoupling of $H_3B{\cdot}NH_2Me$. [Rh] = 0.5 mol% **III** or 0.25 mol% **10.**

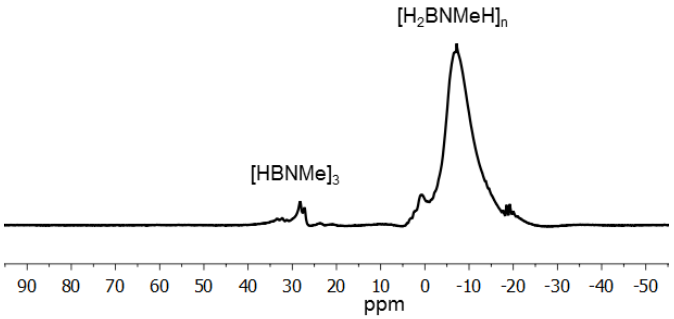


Figure 3.14 The ^{11}B NMR spectrum at the end of the catalytic dehydrocoupling of $H_3B{\cdot}NH_2Me$ (0.41 M) using $[Rh(PPh_2(CH_2)_3PPh_2)(C_6H_5F)][BAr^F{}_4]$ (**III**, 2 x 10^{-3} M, 0.5 mol%) in THF.

Polymer from the catalytic dehydrocoupling of $H_3B{\cdot}NH_2Me$ using **III** was isolated by precipitating it in hexane and then subsequently working up by washing with hexane and then drying under vacuum. The isolated polymer showed M_w = 30,600 $gmol^{-1}$ and Đ = 2.6 as measured by Gel Permeation Chromatography.

Changing the solvent to 1,2-$F_2C_6H_4$ showed a slightly different dehydrocoupling profile as that observed with THF, although similar profile was observed for both the catalysts **III** or **10** in this solvent (Figure 3.15). Using either catalyst resulted in the release of ~1.1 equivalents of hydrogen gas with a faster TOF of ~800 h^{-1} (for one equivalent of hydrogen gas) and produced polyaminoborane ($[BH_2NMe]_n$, ~95%) and borazine ($[BHNMeH]_3$, ~5

%) at the end of dehydrocoupling as measured by ^{11}B NMR spectroscopy. The dehydrogenation profiles in both cases show apparent zero order kinetics (for ~ one equivalent of H_2 release) suggesting saturation kinetics[45] as also observed for the dehydropolymerisation of $H_3B{\cdot}NH_2Me$ using a $[Rh(Xantphos)]^+$ catalyst where the active catalyst, proposed to be a Rh-amido-borane complex reversibly binds the additional $H_3B{\cdot}NH_2Me$ and thus shows zero order dependence on amine-borane.[14]

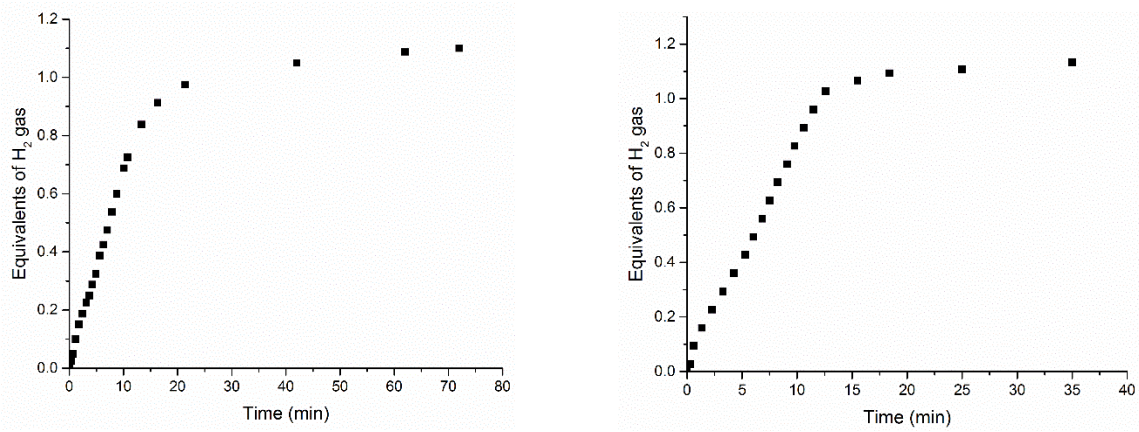


Figure 3.15 Plots of equivalents of H_2 gas produced against time during dehydrocoupling of $H_3B{\cdot}NH_2Me$ (0.41 M) using **III** (2 x 10^{-3} M, 0.5 mol%, left) or *in situ* prepared **10** (1 x 10^{-3} M, 0.25 mol%, right) in 1,2-$F_2C_6H_4$.

These experiments suggest that the dimer (**10**) is also a competent catalyst for the dehydrocoupling of $H_3B{\cdot}NH_2Me$ exhibiting a similar kinetic profile to the monomer (**III**). The lack of induction period suggests that the formation of the dimer from the monomer (**III**) is rapid in presence of the excess $H_3B{\cdot}NH_2Me$. This is in direct contrast to Xantphos-based rhodium catalysts that show induction period for the dehydrocoupling of $H_3B{\cdot}NH_2Me$ in C_6H_5F proposed to be due to N−H activation to form the active species.[14, 46]

3.12 Reactivity of III with $H_3B{\cdot}NMe_2H$

Addition of 1.2 equivalents of $H_3B{\cdot}NMe_2H$ to $[Rh(PPh_2(CH_2)_3PPh_2)(C_6H_5F)][BAr^F{}_4]$ (**III**) in THF resulted in the formation of a mixture of species (unlike $H_3B{\cdot}NMeH_2$ and $H_3B{\cdot}NH_3$, which immediately proceeded to give **10** and **7**, respectively). One of these complexes is tentatively characterised as $[\{Rh(PPh_2(CH_2)_3PPh_2)\}_2(\mu\text{-}H)(\mu\text{-}BH_2NMe_2)][BAr^F{}_4]$ (**11**, 60% yield by $^{31}P\{^1H\}$ NMR spectroscopy). In the ^1H NMR spectrum, a signal is observed at δ −7.05 (s), that is assigned to the bound hydrides (BH_2 and RhH). $^{31}P\{^1H\}$ NMR spectroscopy showed a doublet at δ 23.5 ($^1J_{RhP}$ = 140 Hz). The bound $H_2B{=}NMe_2$ unit was observed at δ 52.8 in the ^{11}B NMR spectrum. These spectral data are consistent with the formation of $[\{Rh(PPh_2(CH_2)_3PPh_2)\}_2(\mu\text{-}H)(\mu\text{-}BH_2NMe_2)][BAr^F{}_4]$ (**11**) and are similar to the well-characterised complexes **7** and **9**. Signals corresponding to $[BH_2(NMe_2)(THF)][BAr^F{}_4]$ and $[BH_2(NMe_2)_2][BAr^F{}_4]$ were also observed in the ^{11}B NMR spectrum as broad triplets at δ 4.9 (t, $^1J_{BH}$ = 110 Hz) and δ −2.8 (t, $^1J_{BH}$ = 113 Hz), respectively.[31] ESI-MS showed signals corresponding to **11** consistent with its simulated isotopic pattern (m/z 1088.1990 [M^+], calc. 1088.1958). Complex **11** decomposed in an hour to give a number of unknown degradation products.

3.13 Reactivity of VI with $H_3B{\cdot}NMeHR$ (R = H, Me)

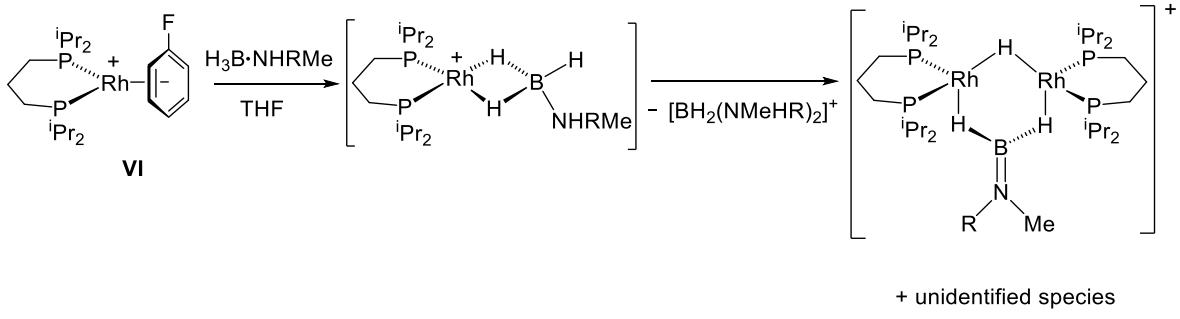
As discussed above, **III** reacts with $H_3B{\cdot}NHRR'$ (R, R' = H, Me) to form the dimer $[\{Rh(PPh_2(CH_2)_3PPh_2)\}_2(\mu\text{-}H)(\mu\text{-}BH_2NRR')][BAr^F{}_4]$. **VI** has also been found to react with $H_3B{\cdot}NH_3$ to form the dimer $[\{Rh(P^iPr_2(CH_2)_3P^iPr_2)\}_2(\mu\text{-}H)(\mu\text{-}BH_2NH_2)][BAr^F{}_4]$ (**9**). In order to expand the dimer formation event with the N-alkyl substituted amine-boranes, we explored the reactivity of **VI** with $H_3B{\cdot}NMeHR$ (R = H, Me).

3.13.1 Reactivity of VI with $H_3B{\cdot}NMeH_2$

$H_3B{\cdot}NMeH_2$ (1.2 equivalents, THF) immediately reacts with **VI** to form a mixture of $[Rh(P^iPr_2(CH_2)_3P^iPr_2)(\eta^2\text{-}H_3B{\cdot}NMeH_2)][BAr^F{}_4]$ and $[(Rh(P^iPr_2(CH_2)_3P^iPr_2))_2(\mu\text{-}H)(\mu\text{-}$

$BH_2NMeH)][BAr^F_4]$ in a 9:1 ratio, characterised by NMR spectroscopy on the basis of the analogous complexes **8** and **9**, respectively. ^{11}B NMR spectroscopy at this stage showed a broad signal at δ 8.2 suggestive of the rapid exchange between bound and free $H_3B{\cdot}NMeH_2$. After 2.5 h when all the $H_3B{\cdot}NMeH_2$ is consumed by dehydrocoupling and the exchange process stops, $[Rh(P^iPr_2(CH_2)_3P^iPr_2)(\eta^2\text{-}H_3B{\cdot}NMeH_2)][BAr^F_4]$ is observed at δ 15 in the ^{11}B NMR spectrum. An uncharacterised boron species was also observed through ^{11}B NMR spectroscopy displaying a resonance at δ –13.3 (t, $^1J_{BH}$ = 106 Hz). $^{31}P\{^1H\}$ NMR spectroscopy and ESI-MS at this stage also showed the presence of $[\{Rh(P^iPr_2(CH_2)_3P^iPr_2)\}_2(\mu\text{-}H)(\mu\text{-}BH_2NMeH)][BAr^F_4]$ along with the formation of some unidentified organometallic complexes.

However, when four equivalents of $H_3B{\cdot}NMeH_2$ are used, **VI** immediately converts to the dimer $[\{Rh(P^iPr_2(CH_2)_3P^iPr_2)\}_2(\mu\text{-}H)(\mu\text{-}BH_2NMeH)][BAr^F_4]$, which in 15 minutes decomposes to give unidentified species. This is consistent with the dimer **9** being unstable in presence of excess $H_3B{\cdot}NH_3$ in THF as discussed earlier in Section 3.14 but a much shorter time scale for $H_3B{\cdot}NH_2Me$ as described here. Formation of $[(NH_2Me)_2BH_2][BAr^F_4]$ was also observed by ^{11}B NMR spectroscopy [δ −7.7 (t, $^1J_{BH}$ = 115 Hz)].[31, 43]



Scheme 3.21 Reactivity of **VI** with $H_3B{\cdot}NMeRH$ (R = H, Me). $[BAr^F_4]^-$ anions are not shown.

3.13.2 Reactivity of VI with $H_3B{\cdot}NMe_2H$

Reaction of 4 equivalents of $H_3B{\cdot}NMe_2H$ with **VI** in THF resulted in the rapid formation of $[Rh(P^iPr_2(CH_2)_3P^iPr_2)(\eta^2\text{-}H_3B{\cdot}NMe_2H)][BAr^F{}_4]$ and $[\{Rh(P^iPr_2(CH_2)_3P^iPr_2)\}_2(\mu\text{-}H)(\mu\text{-}BH_2NMe_2)][BAr^F{}_4]$ in a 1:2 ratio as well as the formation of $[BH_2(NMe_2H)_2][BAr^F{}_4]$ [δ −2.8 (t, $^1J_{BH}$ = 113 Hz)][31] as observed by the NMR spectroscopy and ESI-MS after 5 minutes of reaction progress. The spectral details are consistent with the analogous compounds $[Rh(P^iPr_2(CH_2)_3P^iPr_2)(\eta^2\text{-}H_3B{\cdot}NMe_3)][BAr^F{}_4]$ (**8**) and $[\{Rh(P^iPr_2(CH_2)_3P^iPr_2)\}_2(\mu\text{-}H)(\mu\text{-}BH_2NH_2)][BAr^F{}_4]$ (**9**). At this stage NMR signals due to free $H_3B{\cdot}NMe_2H$ are broad in ^{11}B NMR spectrum thus suggesting a rapid exchange between the bound and free $H_3B{\cdot}NMe_2H$. $[\{Rh(P^iPr_2(CH_2)_3P^iPr_2)\}_2(\mu\text{-}H)(\mu\text{-}BH_2NMe_2)][BAr^F{}_4]$ decomposes to uncharcaterized complexes in 1 h as observed by $^{31}P\{^1H\}$ NMR spectroscopy. $H_3B{\cdot}NMe_2H$ undergoes slow dehydrocoupling to the cyclic dimer $[H_2B{\cdot}NMe_2]_2$ via $H_2B{=}NMe_2$ and $H_3B{\cdot}NMe_2BH_2{\cdot}NMe_2H$ intermediates (70% in 2 days and complete conversion in 5 days, Figure 3.16). Formation of NMe_2BHNMe_2 [δ 38.1, $^1J_{BH}$ = 130 Hz][7] and $[BH_2(NHMe_2)_2][BAr^F{}_4]$ were also observed by ^{11}B NMR spectroscopy during and at the end of the dehydrocoupling.

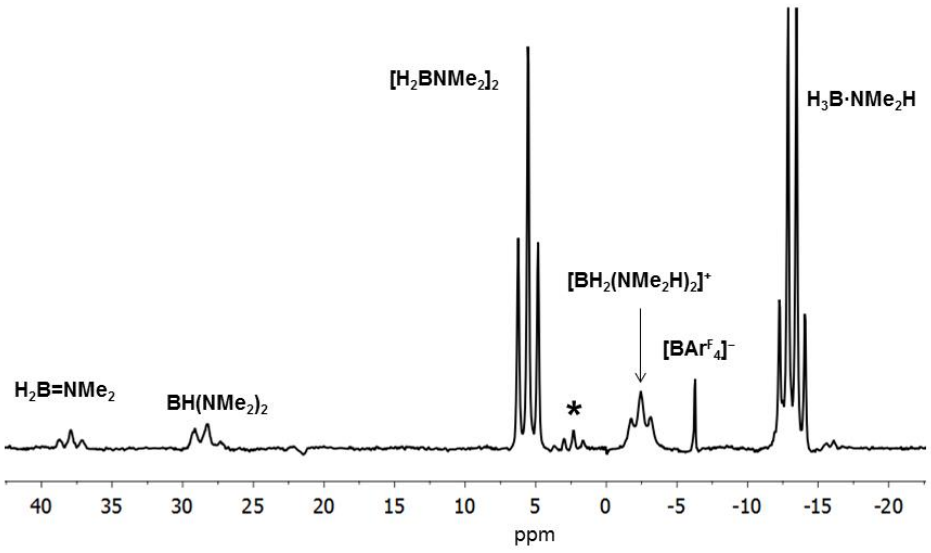


Figure 3.16 The ^{11}B NMR spectrum after 24 h of reaction of **VI** with 4 equivalents of $H_3B{\cdot}NMe_2H$, * corresponds to BH_2 signal due to $H_3B{\cdot}NMe_2BH_2{\cdot}NMe_2H$. The remaining BH_3 signal is overlapped by the signal due to $H_3B{\cdot}NMe_2H$.[7]

3.14 Reactivity of 9 with $H_3B{\cdot}NH_3$

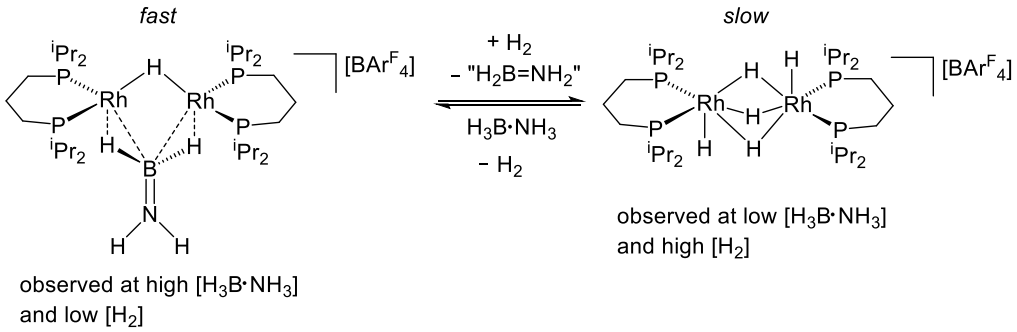
In order to understand the role of dimers in the catalytic dehydrocoupling experiments, we aimed to carry out stoichiometric experiments utilising the pure dimers. However, as the phenyl substituted dimers $[\{Rh(PPh_2(CH_2)_3PPh_2)\}_2(\mu\text{-}H)(\mu\text{-}BH_2NRR')][BAr^F{}_4]$ (**7**, **10** or **11**) could not be isolated, we carried out stoichiometric and catalytic experiments using the ^{i}Pr substituted dimer $[\{Rh(P^iPr_2(CH_2)_3P^iPr_2)\}_2(\mu\text{-}H)(\mu\text{-}BH_2NH_2)][BAr^F{}_4]$ (**9**) which could be isolated in pure form.

The reaction of four equivalents of $H_3B{\cdot}NH_3$ with **9** in THF solvent resulted in its conversion to a number of unidentified products after 45 minutes. ^{11}B NMR spectroscopy after 45 minutes showed 20% conversion of $H_3B{\cdot}NH_3$ to unidentified species [^{11}B NMR: δ −43.0 (br) and −38.0 (br)] and borazine. After 24 h all the $H_3B{\cdot}NH_3$ was converted to borazine and polyamino-borane. $^{31}P\{^1H\}$ NMR spectroscopy showed the presence of **9** (30%), $[\{Rh(P^iPr_2(CH_2)_3P^iPr_2)\}_2(H)_2(\mu\text{-}H)_3][BAr^F{}_4]$ (44%) and uncharacterised complexes (26%). These spectral details suggest that: (i) **9** is not stable in presence of excess $H_3B{\cdot}NH_3$; (ii) **9** is either an actual catalyst or a precatalyst for the dehydrocoupling of $H_3B{\cdot}NH_3$ and (iii) **9** decomposes in the presence of excess hydrogen to produce $[\{Rh(P^iPr_2(CH_2)_3P^iPr_2)\}_2(H)_2(\mu\text{-}H)_3][BAr^F{}_4]$ (consistent with the reaction of pure **9** with hydrogen as shown in Scheme 3.17).

3.15 Reactivity of $[\{Rh(P^iPr_2(CH_2)_3P^iPr_2)\}_2(H)_2(\mu\text{-}H)_3][BAr^F{}_4]$ with $H_3B{\cdot}NH_3$

As $[\{Rh(P^iPr_2(CH_2)_3P^iPr_2)\}_2(H)_2(\mu\text{-}H)_3][BAr^F{}_4]$ is observed as the end product in the catalytic dehydrocoupling of $H_3B{\cdot}NH_3$ using either the monomer (**VI**) or the dimer (**9**) as catalysts, we carried out its reaction with $H_3B{\cdot}NH_3$ in order to understand its role in the catalytic dehydrocoupling process. Addition of two equivalents of $H_3B{\cdot}NH_3$ to $[\{Rh(P^iPr_2(CH_2)_3P^iPr_2)\}_2(H)_2(\mu\text{-}H)_3][BAr^F{}_4]$ resulted in the immediate formation of

[(Rh(P^{i}Pr$_2$(CH$_2$)$_3$P^{i}Pr$_2$))$_2$(μ-H)(μ-BH$_2$NH$_2$)][BAr$^F_4$] (**9**, 42%) and some uncharacterised organometallic complexes (12%), with the rest being the starting complex [{Rh(P^{i}Pr$_2$(CH$_2$)$_3$P^{i}Pr$_2$)}$_2$(H)$_2$(*μ*-H)$_3$][BAr$^F_4$] (46%) as observed by the ^{31}P{^{1}H} NMR spectroscopy. The H$_3$B·NH$_3$ was completely converted to borazine and polyaminoborane over 24 h. The ^{31}P{^{1}H} NMR spectrum at this point showed the presence of **9** (23%), [{Rh(P^{i}Pr$_2$(CH$_2$)$_3$P^{i}Pr$_2$)}$_2$(H)$_2$(*μ*-H)$_3$][BAr$^F_4$] (43%) and some uncharacterised organometallic complexes (34%). This experiment, combined with the reaction of **9** with hydrogen to form [{Rh(P^{i}Pr$_2$(CH$_2$)$_3$P^{i}Pr$_2$)}$_2$(H)$_2$(*μ*-H)$_3$][BAr$^F_4$] (Scheme 3.17), suggests an equilibrium between [{Rh(P^{i}Pr$_2$(CH$_2$)$_3$P^{i}Pr$_2$)}$_2$(H)$_2$(*μ*-H)$_3$][BAr$^F_4$] and **9** in the presence of H$_3$B·NH$_3$ and H$_2$ (Scheme 3.22) so that the resting state of the catalysis changes through the course of catalysis. [{Rh(P^{i}Pr$_2$(CH$_2$)$_3$P^{i}Pr$_2$)}$_2$(H)$_2$(*μ*-H)$_3$][BAr$^F_4$] under catalytic conditions (1.7 x 10^{-3} M, 2 mol%) resulted in 30% conversion of H$_3$B·NH$_3$ to polyamino-borane and borazine in 4 h, slower than **9** under identical conditions (see section 3.16).

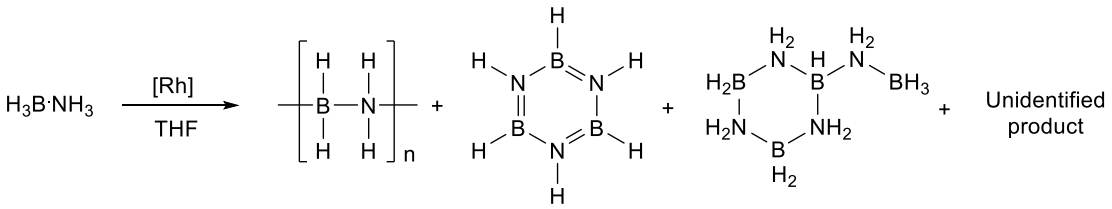


Scheme 3.22 Equilibrium between [{Rh(P^{i}Pr$_2$(CH$_2$)$_3$P^{i}Pr$_2$)}$_2$(H)$_2$(*μ*-H)$_3$][BAr$^F_4$] and **9**.

3.16 Catalytic dehydrocoupling of H$_3$B·NH$_3$ using VI and 9 in THF

The catalytic dehydrocoupling of H$_3$B·NH$_3$ was conducted using [Rh(P^{i}Pr$_2$(CH$_2$)$_3$P^{i}Pr$_2$)(C$_6$H$_5$F)][BAr$^F_4$] (**VI**) (4 mol%) or [{Rh(P^{i}Pr$_2$(CH$_2$)$_3$P^{i}Pr$_2$)}$_2$(μ-H)(μ-BH$_2$NH$_2$)][BAr$^F_4$] (**9**) (2 mol%) in THF in a sealed NMR tube. Both showed similar kinetic profiles (as measured by the concentration of H$_3$B·NH$_3$ using ^{11}B NMR spectroscopy). No induction period was observed suggesting that the formation of the dimer **9** from **VI** is

rapid in the presence of a large excess of $H_3B{\cdot}NH_3$. Complex **VI** gave ~50% conversion while **9** resulted in ~70% conversion of $H_3B{\cdot}NH_3$ in 4 (Figure 3.17). ^{11}B NMR spectroscopy showed the formation of a mixture of species containing borazine, B-(cyclotriborazanyl)amine-borane and short chain B−N oligomers (Scheme 3.23) similar to that obtained using the catalyst **III** discussed in Section 3.3.1. A broad unidentified resonance at δ −43 was also observed in the ^{11}B NMR spectrum at the end of both dehydrocoupling experiments. This is suggestive of similar catalytic action for both the complexes **VI** and **9** with regards to formation of the dehydrocoupling products.



Scheme 3.23 [Rh] catalysed dehydrocoupling of $H_3B{\cdot}NH_3$ in THF. [Rh] = 4 mol% **III** or 2 mol% **9**.

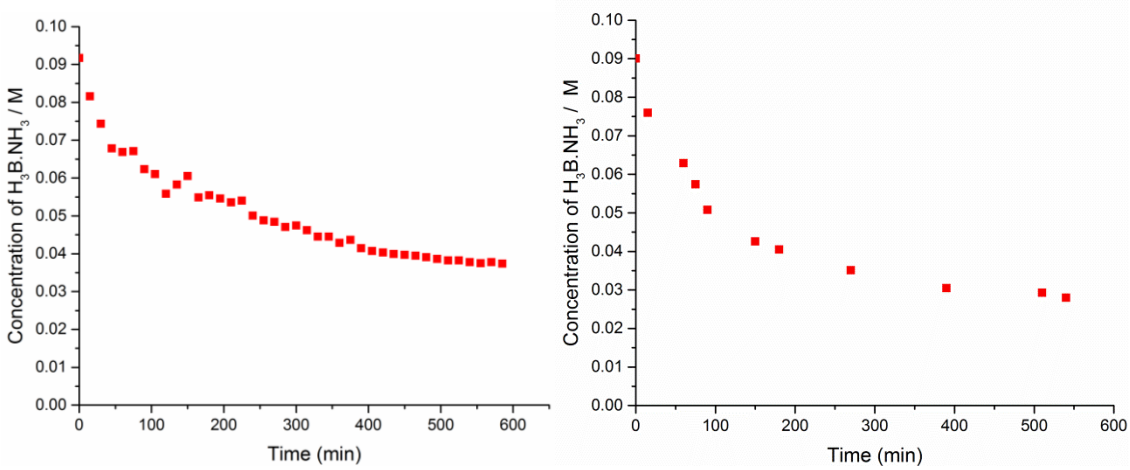


Figure 3.17 Plot of concentration of $H_3B{\cdot}NH_3$ against time for the catalytic dehydrocoupling of $H_3B{\cdot}NH_3$ (9 x 10^{-2} M) in THF (sealed system). Left: **VI** (3.6 x 10^{-3} M, 4 mol%); Right: **9** (1.7 x 10^{-3} M, 2 mol%).

We suggest that the poor catalytic activity of **VI** is due to the catalyst deactivation by the presence of excess H_2 leading to the formation of $[\{Rh(P^iPr_2(CH_2)_3P^iPr_2)\}_2(H)_2(\mu\text{-}H)_3][BAr^F{}_4]$ as discussed in Scheme 3.22. To probe into this hypothesis we monitored the

dehydrocoupling of $H_3B{\cdot}NH_3$ using ^{11}B NMR spectroscopy in a sealed system under the same catalytic condition: $H_3B{\cdot}NH_3$, 9 x 10^{-2} M; **VI**, 4 mol%; THF. Almost 50% conversion of $H_3B{\cdot}NH_3$ was obtained in 3.5 h after which the sample was degassed using freeze-pump-thaw method. Further monitoring the reaction using ^{11}B NMR spectroscopy revealed that the rate of dehydrogenation after degassing is faster than that the rate just before degassing (Figure 3.18). We suggest this is because on degassing, the deactivated catalyst $[\{Rh(P^iPr_2(CH_2)_3P^iPr_2)\}_2(H)_2(\mu\text{-}H)_3][BAr^F{}_4]$ forms $[\{Rh(P^iPr_2(CH_2)_3P^iPr_2)\}_2(\mu\text{-}H)(\mu\text{-}BH_2NH_2)][BAr^F{}_4]$ which shows greater catalytic activity consistent with the equilibrium shown in Scheme 3.22.

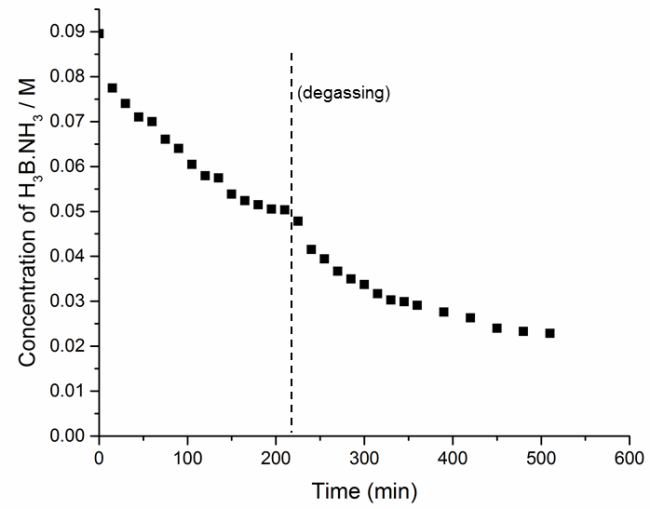


Figure 3.18 Plot of concentration of $H_3B{\cdot}NH_3$ against time for the dehydrocoupling of $H_3B{\cdot}NH_3$ (9 x 10^{-2} M) using catalyst **VI** (3.6 x 10^{-3} M, 4 mol%) in THF (sealed system).

3.17 Catalytic dehydrocoupling of $H_3B{\cdot}NH_3$ using 0.5 mol% $[BH_2(NH_3)(OEt_2)][BAr^F{}_4]$ in THF

Baker has reported the catalytic dehydrocoupling of $H_3B{\cdot}NH_3$ using the Lewis acid $B(C_6F_5)_3$ as a catalyst (0.5 mol%, 60˚C, 20 h) where $[BH_2(NH_3)(S)][HB(C_6F_5)_3]$ (*S* = solvent e.g. Et_2O or THF) has been proposed as an initiator for the dehydrogenation process.[19] Under our conditions, $[BH_2(NH_3)(OEt_2)][BAr^F{}_4]$ (3.4 X 10^{-3} M, 0.5 mol%) did not lead to any dehydrogenation of $H_3B{\cdot}NH_3$ (0.68 M) as monitored by gas-burette method for 3 h. The

^{11}B NMR spectrum after 3 h showed only the signal corresponding to $H_3B{\cdot}NH_3$ (δ −21.9, q, $^1J_{BH}$ = 100 Hz). This suggests that $[BH_2(NH_3)(THF)][BAr^F{}_4]$, which is formed during the formation of the dimer **7** or **9** (Scheme 3.3, 3.4), is not the sole catalyst for the dehydrocoupling of $H_3B{\cdot}NH_3$, which confirms the direct involvement of the rhodium complex in the catalytic cycle.

3.18 Kinetic studies using initial rate methods

In order to explore the nature of the active catalyst and understand the role of the dimer during the dehydrogenation, the dehydrogenation kinetics using an initial rate method was studied.[47] Initial rates at different concentrations of $H_3B{\cdot}NH_2R$ (R = H, Me) and **9** in THF solvent were calculated from the pseudo zero-order region of the temporal consumption of amine-borane as measured by the ^{11}B NMR spectroscopy over the first 20 minutes of catalysis (~5% conversion of amine-boranes). Initial rates obtained at different concentrations of either $H_3B{\cdot}NH_2R$ or **9** are plotted against the concentration values in order to obtain the corresponding order of the reaction (Tables 3.2, 3.3; Figures 3.19, 3.20).

Table 3.2 Initial rates upon variation of the concentration of $H_3B{\cdot}NH_3$ and catalyst (**9**).

[Catalyst] (10^{-3} M)	**[$H_3B{\cdot}NH_3$] (10^{-2} M)**	**Initial rate (10^{-5} Ms^{-1})**
1.7	4.6	2.2 ± 0.21
1.7	9.2	3.7 ± 0.62
1.7	18.4	8.0 ± 0.13
0.85	9.2	2.0 ± 0.24
3.4	9.2	8.3 ± 0.41

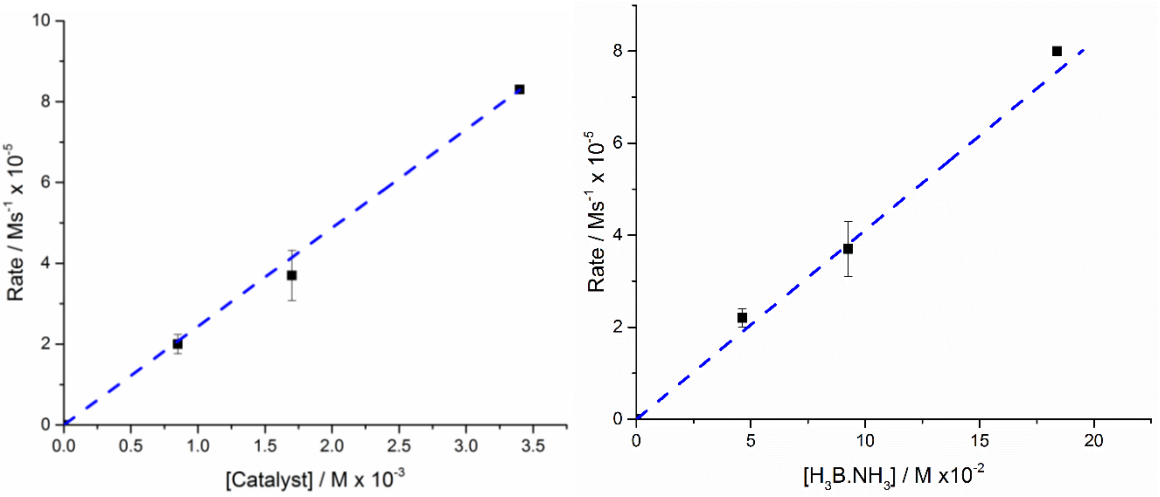


Figure 3.19 Plots of initial rates against concentrations of **9** (left) and $H_3B{\cdot}NH_3$ (right).

Table 3.3 Initial rates upon variation of the concentration of $H_3B{\cdot}NH_2Me$ and catalyst (**9**).

[Catalyst] (10^{-3} M)	[$H_3B{\cdot}NH_2Me$] (10^{-2} M)	Initial rate (10^{-5} Ms^{-1})
1.7	4.5	1.0 ± 0.21
1.7	9.0	1.9 ± 0.62
1.7	18	3.8 ± 0.13
0.85	9.0	0.9 ± 0.11
3.4	9.0	3.5 ± 0.32

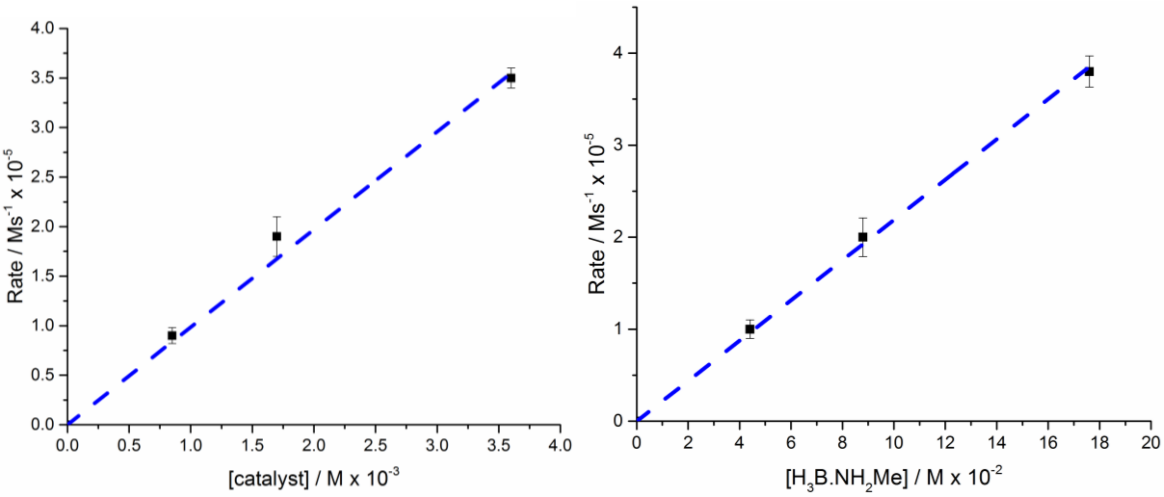


Figure 3.20 Plots of initial rates against concentrations of **9** (left) and $H_3B{\cdot}NH_2Me$ (right).

Initial rate experiments showed a first order dependence for both $H_3B{\cdot}NH_2R$ (R = H, Me) and the dimer **9**. This is in contrast to a rapid dimer-monomer equilibrium for which an order of half (relative to **9**) would be expected, as discussed in Chapter 5.[30, 48] However, we cannot distinguish between dimer **9** or a monomer undergoing irreversible and fast consumption to form the dimer being the actual catalyst, which would also show the first order kinetics.

3.19 Conclusions

This chapter presents the catalytic dehydrocoupling of amine-boranes using $[Rh(PR_2(CH_2)_3PR_2)(C_6H_5F)][BAr^F{}_4]$ (R = Ph and ^{i}Pr) catalysts. The central observation is the initial formation of dimers from the reactions of monomers **III** and **VI** with amine-boranes. The mechanism of the formation of the dimer has been explored which highlights the role of nucleophilic solvents such as THF through the formation of solvent stabilized boronium species $[BH_2(NH_3)(THF)][BAr^F{}_4]$. As the direct isolation of the dimer (**9**) from the reaction was not successful, **9** was isolated by an independent synthetic route and its structure and bonding has been studied in detail by NMR spectroscopy, single crystal X-ray diffraction and DFT calculations. These studies reveal that the dimer consists of a bridging $H_2B{=}NH_2$ and a bridging hydride unit bound to two rhodium centres. $H_2B{=}NH_2$ is bound to the metal centres mainly through H−B sigma bonds in which there is significant Rh···B interaction. Eyring analysis and DFT calculations show that the $H_2B{=}NH_2$ fragment in the dimer is fluxional at room temperature and rotates around Rh···Rh vector making the hydrides (BH_2 and Rh*H*) and the phosphine groups equivalent at room temperature in solution. Similar formation of dimers has also been observed with $H_3B{\cdot}NH_2Me$ and $H_3B{\cdot}NHMe_2$.

Catalytic dehydrocoupling experiments show that both monomers (**III** or **VI**) and dimers (**7**, **9**, **10** or **11**) are active in catalysis. Kinetic experiments showed the first order dependence

for both $H_3B{\cdot}NH_2R$ (R = H, Me) and the pure dimer **9**. Nevertheless, we cannot currently distinguish between the actual catalyst derived from the dimer or from a monomer resulting from the irreversible but fast dissociation of the dimer, the finding of which remains a challenge for the future.

3.20 Future work

Future work involves the exploration into the role of dimer (**7** or **9**) in the catalytic dehydrocoupling of $H_3B{\cdot}NH_3$ and establishing a mechanism of how the dimer reacts and dehydrogenates the amine-boranes. For the simplicity of mechanistic investigation an attempt to isolate the dimer with the bound $H_2B{=}NMe_2$ or $H_2B{=}NMeH$ (using the methodology analogous to Scheme 3.12) can be made which can then be used to study the amine-borane dehydrocoupling mechanism using kinetic studies and stoichiometric reactions.

3.21 References

1. V. Pons, R. T. Baker, N. K. Szymczak, D. J. Heldebrant, J. C. Linehan, M. H. Matus, D. J. Grant and D. A. Dixon, *Chem. Commun.*, 2008, 6597.

2. A. Staubitz, M. E. Sloan, A. P. M. Robertson, A. Friedrich, S. Schneider, P. J. Gates, J. R. S. auf der Günne and I. Manners, *J. Am. Chem. Soc.*, 2010, **132**, 13332-13345.

3. R. T. Baker, J. C. Gordon, C. W. Hamilton, N. J. Henson, P.-H. Lin, S. Maguire, M. Murugesu, B. L. Scott and N. C. Smythe, *J. Am. Chem. Soc.*, 2012, **134**, 5598-5609.

4. H. C. Johnson, E. M. Leitao, G. R. Whittell, I. Manners, G. C. Lloyd-Jones and A. S. Weller, *J. Am. Chem. Soc.*, 2014, **136**, 9078-9093.

5. A. N. Marziale, A. Friedrich, I. Klopsch, M. Drees, V. R. Celinski, J. R. S. auf der Günne and S. Schneider, *J. Am. Chem. Soc.*, 2013, **135**, 13342-13355.

6. A. Glüer, M. Förster, V. R. Celinski, J. Schmedt auf der Günne, M. C. Holthausen and S. Schneider, *ACS Catal.*, 2015, **5**, 7214-7217.

7. T. M. Douglas, A. B. Chaplin, A. S. Weller, X. Yang and M. B. Hall, *J. Am. Chem. Soc.*, 2009, **131**, 15440-15456.

8. T. M. Douglas, A. B. Chaplin and A. S. Weller, *J. Am. Chem. Soc.*, 2008, **130**, 14432-14433.

9. R. Dallanegra, A. P. M. Robertson, A. B. Chaplin, I. Manners and A. S. Weller, *Chem. Commun.*, 2011, **47**, 3763-3765.

10. L. J. Sewell, G. C. Lloyd-Jones and A. S. Weller, *J. Am. Chem. Soc.*, 2012, **134**, 3598-3610.

11. A. D. Wilson, A. J. M. Miller, D. L. DuBois, J. A. Labinger and J. E. Bercaw, *Inorg. Chem.*, 2010, **49**, 3918-3926.

12. M. R. Nimlos, C. H. Chang, C. J. Curtis, A. Miedaner, H. M. Pilath and D. L. DuBois, *Organometallics*, 2008, **27**, 2715-2722.

13. A. Preetz, C. Fischer, C. Kohrt, H.-J. Drexler, W. Baumann and D. Heller, *Organometallics*, 2011, **30**, 5155-5159.

14. H. C. Johnson, E. M. Leitao, G. R. Whitten, I. Manners, G. C. Lloyd-Jones and A. S. Weller, *J. Am. Chem. Soc.*, 2014, **136**, 9078-9093.

15. A. Staubitz, M. E. Sloan, A. P. M. Robertson, A. Friedrich, S. Schneider, P. J. Gates, J. S. A. D. Guenne and I. Manners, *J. Am. Chem. Soc.*, 2010, **132**, 13332-13345.

16. H. A. Kalviri, F. Gaertner, G. Ye, I. Korobkov and R. T. Baker, *Chem.Sci.*, 2015, **6**, 618-624.

17. W. C. Ewing, P. J. Carroll and L. G. Sneddon, *Inorg. Chem.*, 2013, **52**, 10690-10697.

18. J.-s. Li, C.-r. Zhang, B. Li, F. Cao and S.-q. Wang, *Inorg. Chim. Acta*, 2011, **366**, 173-176.

19. F. H. Stephens, R. T. Baker, M. H. Matus, D. J. Grant and D. A. Dixon, *Angew. Chem. Int. Ed.*, 2007, **46**, 746-749.

20. M. C. MacInnis, R. McDonald, M. J. Ferguson, S. Tobisch and L. Turculet, *J. Am. Chem. Soc.*, 2011, **133**, 13622-13633.

21. G. Alcaraz, L. Vendier, E. Clot and S. Sabo-Etienne, *Angew. Chem. Int. Ed.*, 2010, **49**, 918-920.

22. H. Braunschweig, M. Forster, T. Kupfer and F. Seeler, *Angew. Chem. Int. Ed.*, 2008, **47**, 5981-5983.

23. G. Alcaraz, A. B. Chaplin, C. J. Stevens, E. Clot, L. Vendier, A. S. Weller and S. Sabo-Etienne, *Organometallics*, 2010, **29**, 5591-5595.

24. R. T. Baker, D. W. Ovenall, R. L. Harlow, S. A. Westcott, N. J. Taylor and T. B. Marder, *Organometallics*, 1990, **9**, 3028-3030.

25. H. A. McGee and C. T. Kwon, *Inorg. Chem.*, 1970, **9**, 2458-2461.

26. J. S. Wang and R. A. Geanangel, *Inorg. Chim. Acta*, 1988, **148**, 185-190.

27. See Chapter 5, Section 5.7.1.

28. A. Kumar, H. C. Johnson, T. N. Hooper, A. S. Weller, A. G. Algarra and S. A. Macgregor, *Chem. Sci.*, 2014, **5**, 2546-2553.

29. A. G. Algarra, L. J. Sewell, H. C. Johnson, S. A. Macgregor and A. S. Weller, *Dalton Trans.*, 2014, **43**, 11118-11128.

30. M. D. Fryzuk, W. E. Piers, F. W. Einstein and T. Jones, *Can. J. Chem.*, 1989, **67**, 883-896.

31. M. Rosello-Merino, J. Lopez-Serrano and S. Conejero, *J. Am. Chem. Soc.*, 2013, **135**, 10910-10913.

32. A. J. Sivak and E. L. Muetterties, *J. Am. Chem. Soc.*, 1979, **101**, 4878-4887.

33. J. M. Rummey and M. C. Boyce, *J. Chem. Ed.*, 2004, **81**, 762-763.

34. K. J. Laidler and M. C. King, *J. Phys. Chem.*, 1983, **87**, 2657-2664.

35. V. Fernandez-Moreira, F. L. Thorp-Greenwood, R. J. Arthur, B. M. Kariuki, R. L. Jenkins and M. P. Coogan, *Dalton Trans.*, 2010, **39**, 7493-7503.

36. D. Vidovic, D. A. Addy, T. Kraemer, J. McGrady and S. Aldridge, *J. Am. Chem. Soc.*, 2011, **133**, 8494-8497.

37. C. J. Stevens, R. Dallanegra, A. B. Chaplin, A. S. Weller, S. A. Macgregor, B. Ward, D. McKay, G. Alcaraz and S. Sabo-Etienne, *Chem. Eur. J.*, 2011, **17**, 3011-3020.

38. A. B. Chaplin and A. S. Weller, *Angew. Chem. Int. Ed.*, 2010, **49**, 581-584.

39. A. B. Chaplin and A. S. Weller, *Inorg. Chem.*, 2010, **49**, 1111-1121.

40. H. C. Johnson and A. S. Weller, *J. Organomet. Chem.*, 2012, **721**, 17-22.

41. R. J. Gillespie and P. L. A. Popelier, *Chemical bonding and Molecular geometry, Oxford University Press*.

42. O. J. Metters, A. M. Chapman, A. P. M. Robertson, C. H. Woodall, P. J. Gates, D. F. Wass and I. Manners, *Chem. Commun.*, 2014, **50**, 12146-12149.

43. A. R. Dodds and G. Kodama, *Inorg. Chem.*, 1977, **16**, 2900-2903.

44. H. C. Johnson, A. P. M. Robertson, A. B. Chaplin, L. J. Sewell, A. L. Thompson, M. F. Haddow, I. Manners and A. S. Weller, *J. Am. Chem. Soc.*, 2011, **133**, 11076-11079.

45. R. B. Jordan, *Reaction Mechanisms of Inorganic and Organometallic Systems; Oxford University Press: New York*, 2007.

46. H. C. Johnson and A. S. Weller, *Angew. Chem. Int. Ed.*, 2015, **54**, 10173-10177.

47. J. H. Espenson, *Chemical Kinetics and Reaction Mechanisms*, McGraw-Hill, Inc., 1995.

48. Z. Lu, B. L. Conley and T. J. Williams, *Organometallics*, 2012, **31**, 6705-6714.

4 Sigma-complexes and dehydrogenation of *B*-phenyl amine-boranes

4.1 Introduction

N-alkyl substituted amine-boranes ($H_3B{\cdot}NRR'H$; R = R' = Me, H) have received the majority of attention in terms of the transition metal catalysed dehydrogenation of amine-boranes as discussed in Chapter 1 - 3.[1] On the other hand, dehydrogenation of *B*-substituted amine-boranes has not been explored in much detail mainly due to the instability resulting from the weaker B–N bonds.[2,3] Botalib and co-workers have theoretically predicted the dissociation energies of $H_3B{\cdot}NMe_xH_{3-x}$ and $Me_{3-x}H_xB{\cdot}NH_3$ (x = 0 - 3) and reported that the stability of an amine-borane increases on increasing the methyl substitution on nitrogen whereas the stability decreases on increasing the methyl substituents on the boron.[4]

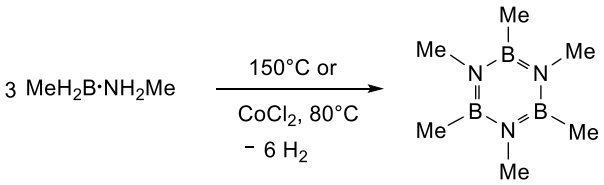
Nevertheless, there are handful of reports for the synthesis and the dehydrogenation of *B*-substituted amine-boranes. Manners reported the synthesis and dehydrogenation of $RR'HB{\cdot}NH^iPr_2$ [RR' = H(SPh) and $(C_6F_5)_2$] to produce the amino-boranes $RR'B{=}N^iPr_2$ (Scheme 4.1).[5, 6]

$$H(C_6F_5)_2B{\cdot}NH^iPr_2 \xrightarrow{100°C} (C_6F_5)_2B{=}N^iPr_2$$

$$PhSH_2B{\cdot}NH^iPr_2 \xrightarrow[[Rh(Cl)(COD)]_2,\ 20°C]{100°C\ or} PhSHB{=}N^iPr_2$$

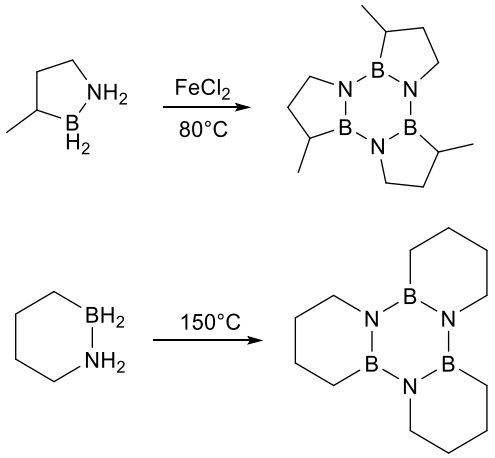
Scheme 4.1 Dehydrogenation of $(C_6F_5)_2HB{\cdot}NH^iPr_2$ and $PhSH_2B{\cdot}NH^iPr_2$ reported by Manners.

Liu and Manners have independently reported the synthesis of *B*-alkyl substituted amine-boranes such as $MeH_2B{\cdot}NMe_xH_{3-x}$ (x = 0 - 2) and their thermal or transition-metal catalysed dehydrogenation.[7, 8] $MeH_2B{\cdot}NH_2Me$ was found to dehydrocouple to form methyl-substituted borazine under thermal or catalytic conditions (Scheme 4.2).



Scheme 4.2 Dehydrogenation of $MeH_2B{\cdot}NH_2Me$ reported by Liu.

The Liu group have also reported the synthesis and the dehydrocoupling of BN-methyl cyclopentane or BN-cyclohexane, which can be considered as the amine-boranes bearing substituents on both boron and nitrogen atoms (Scheme 4.3).[9, 10] The transition metal catalysed dehydrogenation of BN-cyclohexanes is discussed in detail in Chapter 5.



Scheme 4.3 Dehydrogenation of BN-methylcyclopentane[9] and BN-cyclohexane.[10]

Reports on aryl substituted amine-boranes, in particular *B*-phenyl substituted ones, are scarce. Manners has reported the dehydrocoupling of the *N*-aryl substituted amine-boranes $H_3B{\cdot}NArH_2$ (Ar = Ph, *p*-$MeOC_6H_4$, c: *p*-$CF_3C_6H_4$) at ambient temperature to afford borazine $[HBNArH]_3$ as the final product along with the B−N cleavage product diamino-borane.[11] Although the synthesis of $H_2PhB{\cdot}NMe_3$ was first reported by Nöth and coworkers in 1958[12], only in 2007 was its coordination chemistry with the metal fragments $[M(CO)_5]$ (M = Cr and W) and $[CpMn(CO)_2]$ (Figure 4.1) reported, in which the amine-borane binds in an η^1-mode through the B-H sigma bonds.[13] Shimoi, on the basis of the equilibrium constants of $[M(CO)_5(\eta^1\text{-}H_2RB{\cdot}NMe_3)]$ (M = Cr, W), also showed that the

stability of the borane complexes increases upon increasing the electron donating capacity of the R groups. For example, the stability of both the chromium and tungsten complexes increases in the following order: $H_2ClB{\cdot}NMe_3$ ≈ $H_2IB{\cdot}NMe_3$ < $H_2(m\text{-}C_6H_4F)B{\cdot}NMe_3$ < $H_2PhB{\cdot}NMe_3$ < $H_3B{\cdot}NMe_3$ < $H_2MeB{\cdot}NMe_3$, which suggests that the steric factors are not of significant importance and the stability of sigma-complexes for these amine-boranes depends primarily on the electron donating capacity of the borane moiety. Mikhailov and Dorokhov reported the synthesis of $H_2PhB{\cdot}NMe_2H$ in 1962. However, the dehydrogenation chemistry of this species is still unexplored.[14] Michalak and Kang reported the catalytic dehydrogenation of $H_2PhB{\cdot}NH_3$ using $[Pd(NCMe)_4][BF_4]_2$ to form a material which was tentatively characterised as $\{BPhNH_x\}_n$, although no further characterisation was reported.[15] Compared to the *N*-substituted amine-boranes, there is thus a distinct lack of sigma-complexes of *B*-substituted amine-boranes.

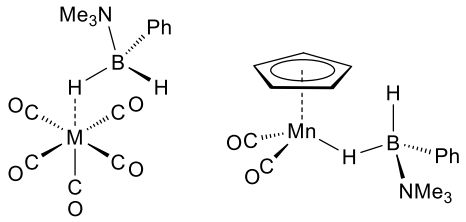
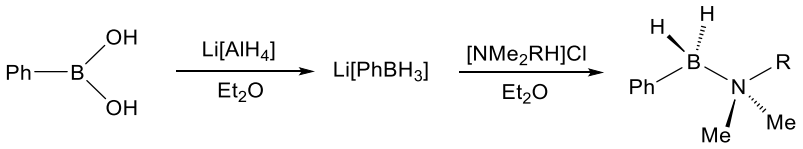


Figure 4.1 Previously reported sigma-complexes of $H_2PhB{\cdot}NMe_3$; M = Cr, W.

Here, we report the detailed coordination chemistry and catalytic dehydrogenation of *B*-phenyl amine-boranes $H_2PhB{\cdot}NMe_3$ and $H_2PhB{\cdot}NMe_2H$ using {Rh-bisphosphine}$^+$ fragments. $H_2PhB{\cdot}NMe_2R$ (R = Me, H) are particularly interesting as they possess two different coordination modes: η^6-phenyl coordination mode and η^2-H_2B coordination mode. {Rh-bisphosphine}$^+$ fragments of different bite angles have been used to study the variable coordination mode of the amine-borane.

4.2 Synthesis of $H_2PhB{\cdot}NMe_3$ and $H_2PhB{\cdot}NMe_2H$

The known complexes $H_2PhB{\cdot}NMe_3$ and $H_2PhB{\cdot}NMe_2H$ were synthesised using the method reported by Liu[7] by the reaction of the ammonium salt, $[NMe_3H]Cl$ or $[NMe_2H_2]Cl$ with $Li[PhBH_3]$ in diethyl ether.[4] $Li[PhBH_3]$ was prepared by the reaction of phenylboronic acid with lithium aluminium hydride in diethyl ether (Scheme 4.4).[16]



Scheme 4.4 Synthesis of $H_2PhB{\cdot}NMe_2R$; R = Me, H.

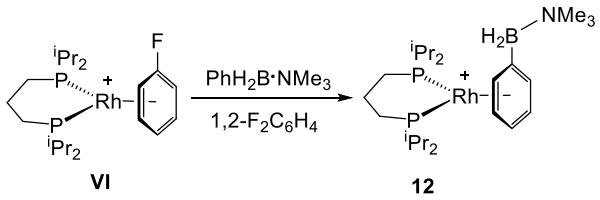
The amine-boranes were obtained as white solids in good yield (~60%) and characterised by NMR spectroscopy. ^{11}B NMR spectroscopy showed triplets at δ −0.8 (J_{BH} = 97 Hz) and δ −4.7 (J_{BH} = 95 Hz) for $H_2PhB{\cdot}NMe_3$ and $H_2PhB{\cdot}NMe_2H$ respectively, consistent with the literature data.[13, 14] $H_2PhB{\cdot}NMe_3$ and $H_2PhB{\cdot}NMe_2H$ were found to be stable in fluorobenzene solution at room temperature. Heating these samples (80°C, 12 h) did not result in the B-N bond cleavage or decomposition/dehydrogenation as monitored by NMR spectroscopy. This is in contrast to the *N*-aryl amine-boranes such as $H_3B{\cdot}NPhH_2$ which shows spontaneous dehydrogenation at ambient temperature.[17]

4.3 Coordination Chemistry of $H_2PhB{\cdot}NMe_3$

4.3.1 Reactivity of $H_2PhB{\cdot}NMe_3$ with $[Rh(P^iPr_2(CH_2)_3P^iPr_2)(C_6H_5F)][BAr^F_4]$ (VI)

The reaction of a stoichiometric amount of $H_2PhB{\cdot}NMe_3$ with $[Rh(P^iPr_2(CH_2)_3P^iPr_2)(C_6H_5F)][BAr^F_4]$ (**VI**) in 1,2-$F_2C_6H_4$ solvent resulted in the displacement of C_6H_5F by $H_2PhB{\cdot}NMe_3$ and the formation of $[Rh(^iPr_2P(CH_2)_3P^iPr_2)(\eta^6\text{-}PhH_2BNMe_3)][BAr^F_4]$ (**12**, Scheme 4.5). Complex **12** was isolated by recrystallisation from

1,2-$F_2C_6H_4$/pentane solution as an orange solid in 77% yield and characterised by NMR spectroscopy, ESI-MS, elemental analysis and single crystal X-ray diffraction.



Scheme 4.5 Reaction of **VI** with $H_2PhB{\cdot}NMe_3$. $[BAr^F{}_4]^-$ anions are not shown.

Figure 4.2 shows the solid state structure of the cationic portion of **12** which shows the η^6 binding of $H_2PhB{\cdot}NMe_3$ and shows the formulation as $[Rh(^iPr_2P(CH_2)_3P^iPr_2)(\eta^6\text{-}PhH_2B{\cdot}NMe_3)][BAr^F{}_4]$ (**12**). The distances between Rh1 and the phenyl carbons [2.267(3)-2.408(3)] in **12** are similar to that found for **VI** [2.285(3)-2.395(3)].[18] The ligand bite angle was found to be 94.04(4)°.

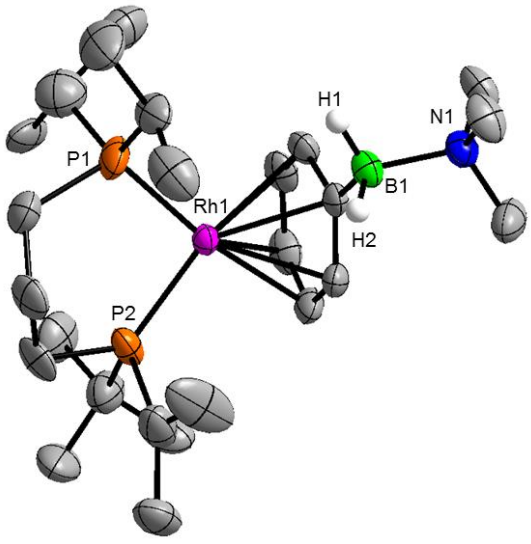
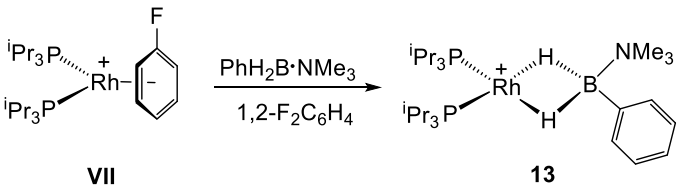


Figure 4.2 X-ray molecular structure of $[Rh(^iPr_2P(CH_2)_3P^iPr_2)(\eta^6\text{-}PhH_2B{\cdot}NMe_3)][BAr^F{}_4]$ (**12**). $[BAr^F{}_4]^-$ anion and selected H atoms omitted for clarity. Only major components of disorder for the isopropyl substituents and the C−C backbone of the chelating bis-phosphine ligand are shown. Ellipsoids shown at 50% probability level. Selected bond lengths (Å) and angles (°): Rh(1)-P(1) 2.2340(9), Rh(1)-P(2) 2.2403(8), Rh(1)-C_{arene} 2.267(3)-2.408(3), B(1)-N(1) 1.635(4); P(1)-Rh(1)-P(2) 94.04(4).

The ^{11}B NMR spectrum of **12** showed a broad resonance at δ −2.1, shifted only slightly by 1.3 ppm relative to the free $H_2Ph\mathit{B}{\cdot}NMe_3$ (δ −0.8, br). A signal corresponding to a Rh···H_2B interaction was not observed in the ^{1}H NMR spectrum in the expected region of δ −4 to δ −10,[19-24] but the phenyl resonances [δ 6.93 (1 H) and 6.31 (4 H, a 2 + 2 coincidence)] were observed as broad multiplets and also shifted upfield relative to that observed for the free $H_2\mathit{Ph}B{\cdot}NMe_3$ [δ 7.30, t, $^3J_{HH}$ = 8 Hz, 1 H; 7.41, m, 2H and 7.74, d, $^3J_{HH}$ = 7 Hz, 2 H][25] confirming the interaction of rhodium with the phenyl moiety of $H_2\mathit{Ph}B{\cdot}NMe_3$. The $^{31}P\{^1H\}$ NMR spectrum of **12** contained a doublet at δ 45.0 ($^1J_{RhP}$ = 195 Hz) which is slightly shifted from the starting η^6–C_6H_5F complex **VI** but shows the similar $^1J_{RhP}$ coupling constant [δ 55.5 ($^1J_{RhP}$ = 210 Hz in C_6H_5F solvent)].[26] This is consistent with the previously reported rhodium bis-phosphine η^6–aryl complexes that show $^1J_{RhP}$ coupling constants in the range of 195 - 205 Hz.[27-29]

4.3.2 Reactivity of $H_2PhB{\cdot}NMe_3$ with $[Rh(P^iPr_3)_2(C_6H_5F)][BAr^F_4]$ (VII)

Changing the ligand motif from the chelating bis-phosphine $P^iPr_2(CH_2)_3P^iPr_2$ to monodentate phosphine $(P^iPr_3)_2$, which has similar electronic properties but a different bite angle, had an interesting effect on the coordination chemistry of $H_2PhB{\cdot}NMe_3$. Reaction of $[Rh(P^iPr_3)_2(C_6H_5F)][BAr^F_4]$ (**VII**) with a slight excess of $H_2PhB{\cdot}NMe_3$ (1.5 equivalents) resulted in the immediate formation of a deep purple solution which was characterised as $[Rh(P^iPr_3)_2(\eta^2\text{-}H_2PhB{\cdot}NMe_3)][BAr^F_4]$ (**13**) in which the amine-borane was bound in an η^2 fashion rather than the η^6 mode as observed for **12**.



VII **13**

Scheme 4.6 Reaction of **VII** with $H_2PhB{\cdot}NMe_3$. $[BAr^F_4]^-$ anions are not shown.

The ^{11}B NMR spectrum of the isolated pure material (in CD_2Cl_2) displayed a single peak at δ 34.8 (br) with a downfield shift of 35.6 ppm compared to that of free $H_2PhB{\cdot}NMe_3$ (δ −0.8). The downfield shift of amine-borane chemical shift in the ^{11}B NMR spectrum upon coordination with metal through η^2-H_2B moiety is diagnostic and has been previously noted.[30, 31] The ^{1}H NMR spectrum contained a broad signal at δ −6.36 (2 H relative integral) corresponding to the B*H*$_2$ resonance but the aryl protons (δ 7.37, 3H; δ 7.25, 2H) were not significantly shifted compared to those of the free ligand. The ^{31}P{^{1}H} NMR spectrum displayed a doublet at δ 69.6 ($^1J_{RhP}$ = 176 Hz), shifted 14.1 ppm downfield from that of the starting material.[26] These observations are consistent with three-centre two-electron $\eta^2{\cdots}H_2B$ interactions and the formation of $[Rh(P^iPr_3)_2(\eta^2\text{-}H_2PhB{\cdot}NMe_3)][BAr^F{}_4]$ (**13**). Crystals suitable for a single crystal X-ray diffraction study were obtained by layering a 1,2-difluorobenzene solution of **13** with pentane and storing at −30 °C for 24 h. The solid state structure of **13** reveals the occupancy of 2 cations (and 2 anions) in the asymmetric unit both showing similar amine-borane geometry, but with a slight variation in the position and conformation of the P^iPr_3 ligands [P(1)-Rh(1)-P(2), 106.19(3)°; P(3)-Rh(2)-P(4), 101.86(3)°]. We suggest this is due to crystal packing effects as only one set of ^{i}Pr resonances could be observed in the ^{1}H NMR spectrum in solution. The presence of two molecules in the asymmetric unit of a solid state structure has been noted in related sigma-complexes of $H_3B{\cdot}NMe_2BH_2{\cdot}NMe_2H$ and $[Me_2NBH_2]_2$ with the $\{Rh(P^iBu_3)_2\}^+$ fragment.[21] In the solid state, Rh···B distances of 2.150(3) and 2.159(3) Å are observed in the independent cations, consistent with an η^2 three-centre two-electron binding of amine-boranes, comparing closely with the previously reported $[Rh(P^iPr_3)_2(\eta^2\text{-}H_3B{\cdot}NMe_3)][BAr^F{}_4]$ [Rh···B = 2.1376(3) Å].[19-24] The P–Rh–P bite angle [101.83(3)º and 106.19(3)º] is significantly larger than in the η^6-bound complex **12** [94.04(4)°].

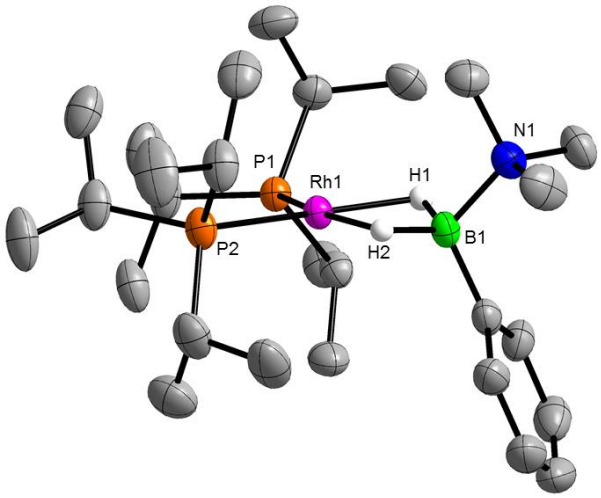
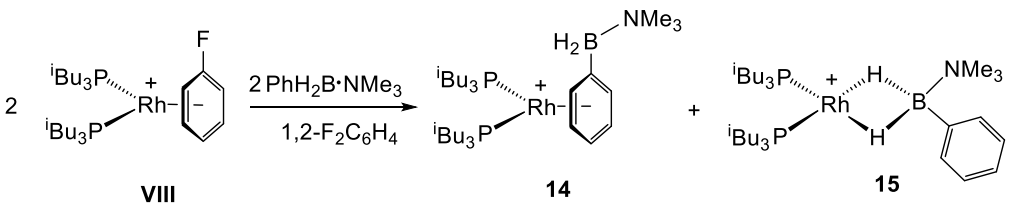


Figure 4.3 X-ray molecular structure of $[Rh(P^iPr_3)_2(\eta^2\text{-}H_2PhB{\cdot}NMe_3)][BAr^F{}_4]$ (**13**). The second cation in the asymmetric unit, $[BAr^F{}_4]^-$ anions and selected H atoms are omitted for clarity. Ellipsoids shown at 50% probability level. Selected bond lengths (Å) and angles (°) (values are given for both cations in the asymmetric unit which is not shown in the figure): Rh(1)-P(1) 2.2581(6), Rh(1)-P(2) 2.2748(7), Rh(1)-B(1) 2.150(3), B(1)-N(1) 1.623(4), Rh(2)-P(3) 2.2628(7), Rh(2)-P(4) 2.2655(7), Rh(2)-B(2) 2.159(3), B(2)-N(2) 1.629(4); P(1)-Rh(1)-P(2) 106.19(3), P(3)-Rh(2)-P(4) 101.86(3).

4.3.3 Reactivity of $H_2PhB{\cdot}NMe_3$ with $[Rh(P^iBu_3)_2(C_6H_5F)][BAr^F{}_4]$ (VIII)

In order to further probe the coordination chemistry of $H_2PhB{\cdot}NMe_3$ with respect to its ability to adopt an η^2 or η^6 binding mode, we explored its reactivity with $[Rh(P^iBu_3)_2(C_6H_5F)][BAr^F{}_4]$ (**VIII**); the idea being that P^iBu_3 ligands have similar electronic properties but a less demanding steric profile in comparison to P^iPr_3 (ligand cone angle: P^iPr_3 160°; P^iBu_3 143°).[32] The stoichiometric reaction of $H_2PhB{\cdot}NMe_3$ with $[Rh(P^iBu_3)_2(C_6H_5F)][BAr^F{}_4]$ (**VIII**) resulted in the formation of a mixture of $[Rh(P^iBu_3)_2(\eta^6\text{-}PhH_2BNMe_3)][BAr^F{}_4]$ (**14**) and $[Rh(P^iBu_3)_2(\eta^2\text{-}H_2PhB{\cdot}NMe_3)][BAr^F{}_4]$ (**15**) in approximately equal concentrations (Scheme 4.7).



Scheme 4.7 Reactivity of $H_2PhB{\cdot}NMe_3$ with $[Rh(P^iBu_3)_2(C_6H_5F)][BAr^F{}_4]$ (**VIII**). $[BAr^F{}_4]^-$ anions are not shown.

The $^{11}B\{^1H\}$ NMR spectrum displayed two broad resonances at δ –2.1 and 29.5 in equal concentration. The resonance at δ –2.1 is only slightly shifted compared to the free $H_2PhB{\cdot}NMe_3$ (δ −0.8, br), similar to that of complex **12** and is suggested to be due to the formation of η⁶-aryl complex $[Rh(P^iBu_3)_2(\eta^6\text{-}PhH_2BNMe_3)][BAr^F{}_4]$ (**14**). The signal at δ 29.5 is suggested to be due to the η²-Rh···H_2B interaction of $[Rh(P^iBu_3)_2(\eta^2\text{-}H_2PhB{\cdot}NMe_3)][BAr^F{}_4]$ (**15**), shifted 30.3 ppm downfield compared to $H_2PhB{\cdot}NMe_3$, similar to the η² amine-borane sigma-complex **13**. The ^1H NMR spectrum is also consistent with this description and showed two singlets at δ 2.76 and 2.50 corresponding to N*Me₃* protons in the different coordination modes of $H_2PhB{\cdot}NMe_3$. A resonance corresponding to Rh···H_2B interaction of **15** was observed at δ –5.06 (br) and the resonances due to the η⁶-coordinated aryl moiety of **14** were observed in the upfield aryl region compared with the free $H_2PhB{\cdot}NMe_3$. The $^{31}P\{^1H\}$ NMR spectroscopy showed two doublets at δ 25.2 [d, $^1J_{RhP}$ = 202 Hz] and δ 34.1 [d, $^1J_{RhP}$ = 177 Hz] in equal concentration, suggested to be due to the complexes **14** and **15**, respectively, on the basis of the analogous η⁶-complex **12** and the η²-sigma-complex **13**.

A variable temperature NMR spectroscopy study was carried out to understand if these two isomers were exchanging slowly on the NMR time scale and to calculate the thermodynamic parameters of binding. At 298 K in 1,2-difluorobenzene, **14** (η⁶) and **15** (η²) were found to be in approximately equal concentrations as measured by $^{31}P\{^1H\}$ NMR spectroscopy. Lowering the temperature to 240 K resulted in a relative increase in the

concentration of **14** (η^6) while **15** (η^2) was favoured at elevated temperatures, suggesting a dynamic equilibrium between the two isomers (Figure 4.4).

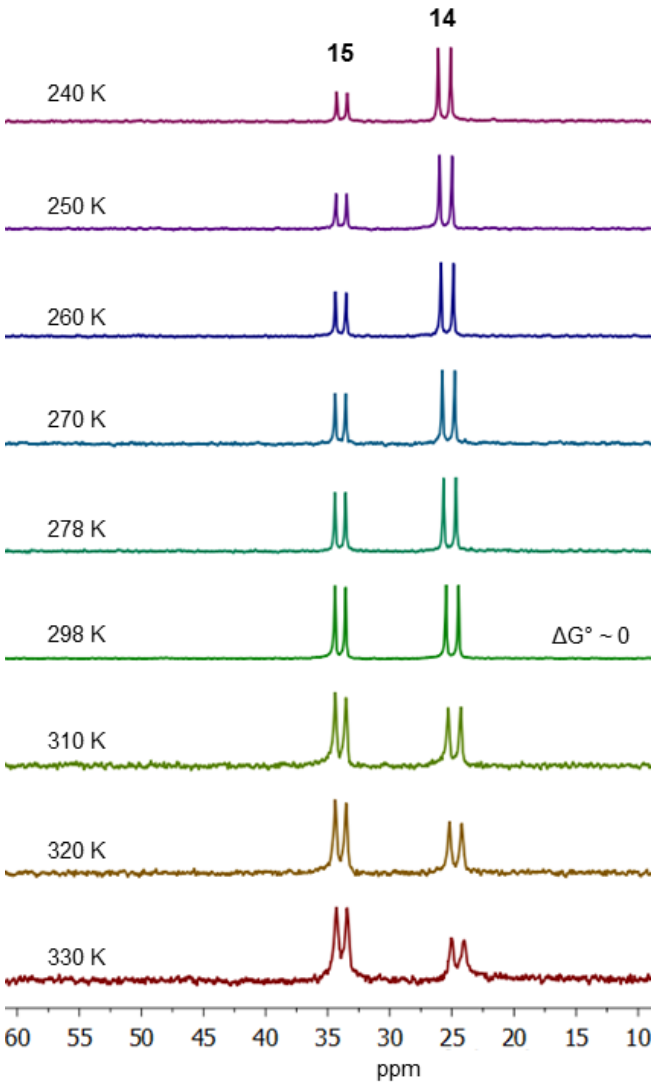


Figure 4.4 $^{31}P\{^1H\}$ NMR spectra of $[Rh(P^iBu_3)_2(PhH_2BNMe_3)][BAr^F{}_4]$ in 1,2-$C_6H_4F_2$ at temperatures ranging from 240 K to 330 K.

The equilibrium constants K_{eq} = [**14**]/[**15**] at different temperatures were calculated from integration of the $^{31}P\{^1H\}$ NMR spectra, which we suggest are reliable as the phosphorus environments in each complex are very similar. A Van't Hoff plot of ln(K_{eq}) vs 1/T allowed the determination of the thermodynamic parameters for this exchange. For the forward reaction (Figure 4.5), the obtained thermodynamic parameters are $\Delta H°$ = –11.3 ± 0.5 kJ

mol^{-1} and $\Delta S°$ = –39.1 ± 1.7 J K^{-1} mol^{-1}. The value for $\Delta G°$ at 298 K was calculated to be 0.4 ± 0.4 kJ mol^{-1}, consistent with the formation of both the complexes in equal concentration at room temperature. The negative enthalpic value of −11.3 ± 0.5 kJ mol^{-1} suggests stronger binding of η^6-aryl group than the η^2-BH_2 group which is balanced by the negative entropic value. The negative value of the entropy is possibly due to the loss of free rotation of the phenyl group upon η^6-binding, but we also cannot discount the possibility of greater solvation of **14**.

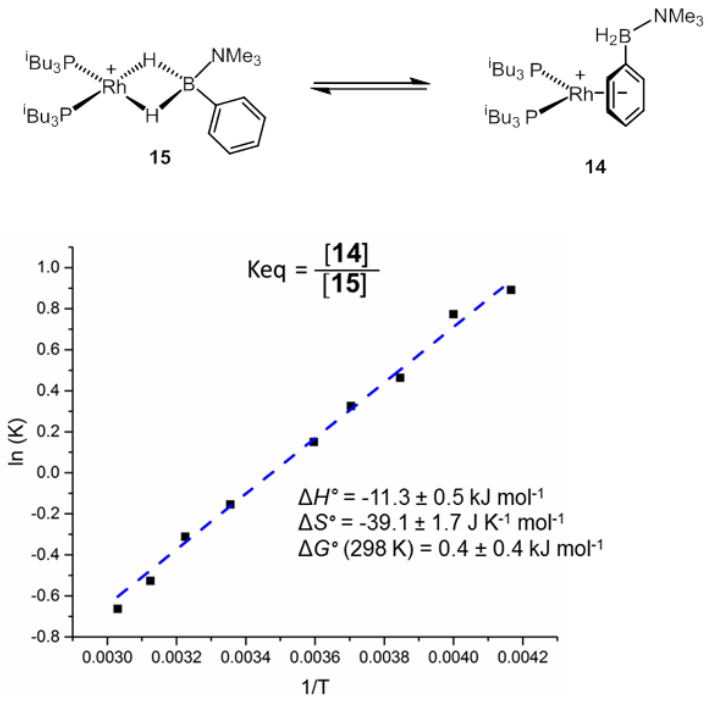
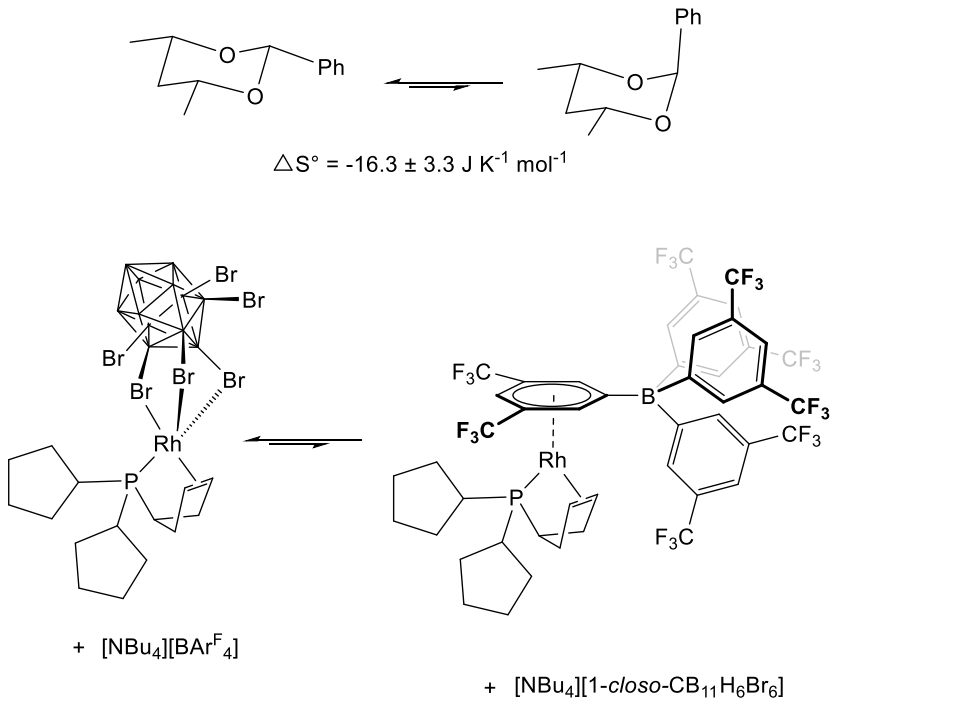


Figure 4.5 Van't Hoff plot (ln Keq against 1/T) for the equilibrium between [Rh(P^{i}Bu$_3$)$_2$(η^2-H_2BPh·NMe$_3$)][BAr$^F{}_4$] (**15**) and [Rh(P^{i}Bu$_3$)$_2$(η^6-PhH$_2$B·NMe$_3$)][BAr$^F{}_4$] (**14**). [BAr$^F{}_4$]$^-$ anions are not shown.

A similar change in entropy ($\Delta S°$ = –16.3 ± 3.3 J K^{-1} mol^{-1}) was observed in the epimerisation of 2-phenyl-4,6-dimethyl-1,3-dioxane, which is attributed to the loss of free rotation of the phenyl group (Scheme 4.7).[33] Similar findings were also reported for the anion exchange equilibrium between [Rh{P(Cyp$_2$)(η^2-C_5H_7)}(1-closo-$CB_{11}H_6Br_6$)] and [Rh{P(Cyp$_2$)(η^2-C_5H_7)}{η^6-($C_6H_3(CF_3)_2$)BAr$^F{}_3$], in which enthalpically the [BAr$^F{}_4$]$^-$ anion is

shown to bind more strongly than the carborane anion ($\Delta H°$ = –19.0 ± 0.3 kJ mol^{-1}) but a large negative entropic contribution and solvation of the carborane anion shifts the overall equilibrium towards the formation of the carborane complex. (Scheme 4.8).[34]

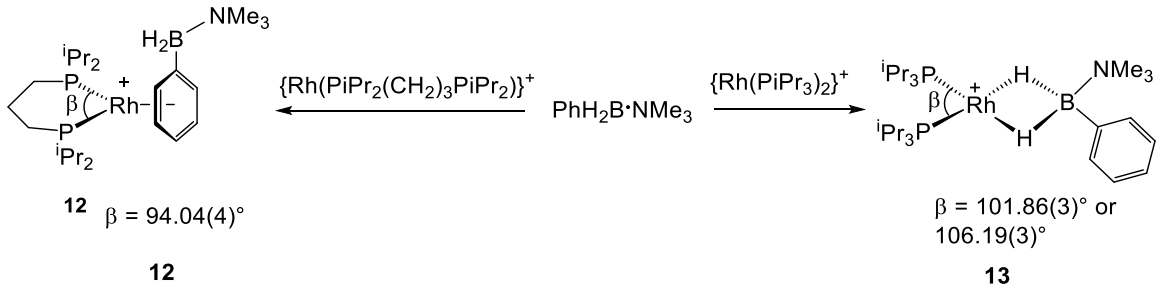


△H° = –19.0 ± 0.3 KJ mol^{-1}, △S° = –87.6 ± 0.8 J K^{-1} mol^{-1} and △G° (298 K) = 7.0 ± 0.5 KJ mol^{-1}

Scheme 4.8 Equilibrium between the isomers of 2-phenyl4,6-dimethyl-1,3-dioxane and between [Rh{P(Cyp$_2$)(η^2-C$_5$H$_7$)}(1-closo-CB$_{11}$H$_6$Br$_6$)] and [Rh{P(Cyp$_2$)(η^2-C$_5$H$_7$)}{η^6-(C$_6$H$_3$(CF$_3$)$_2$)BAr$^F_3$].

4.3.4 Effect of bite angle on the coordination mode of $H_2PhB{\cdot}NMe_3$

As discussed above, the rhodium complex containing chelating phosphine P^{i}Pr$_2$(CH$_2$)$_3$P^{i}Pr$_2$ prefers η^6-arene binding with $H_2PhB{\cdot}NMe_3$ whereas the monodentate phosphine (P^{i}Pr$_3$)$_2$ exhibits η^2-borane coordination mode. As the electronic factors are essentially the same, we suggest that this is due to the variation in the bite angle; the smaller bite angle of the {Rh(P^{i}Pr$_2$(CH$_2$)$_3$P^{i}Pr$_2$)}$^+$ fragment [94.04(4)°] enables η^6-arene coordination of the phenyl moiety while the {Rh(P^{i}Pr$_3$)$_2$}$^+$ exhibits a significantly larger bite angle [101.86(3)° or 106.19(3)°], thus enforcing the η^2-borane coordination mode (Scheme 4.9).



12 β = 94.04(4)°

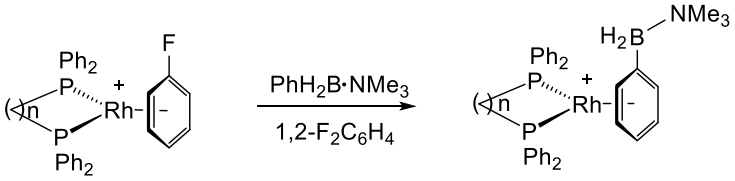
12

β = 101.86(3)° or 106.19(3)°

13

Scheme 4.9 Formation of η⁶ and η² sigma-complexes of $H_2PhB{\cdot}NMe_3$; $[BAr^F{}_4]^-$ anions are not shown.

This has been further probed by Isobel Priest using $[Rh(PPh_2(CH_2)_3PPh_2)(C_6H_5F)][BAr^F{}_4]$ (**III**) and $[Rh(PPh_2(CH_2)_5PPh_2)(C_6H_5F)][BAr^F{}_4]$ (I**X**) complexes which formed η⁶-arene sigma-complexes $[Rh(PPh_2(CH_2)_3PPh_2)(\eta^6\text{-}PhH_2BNMe_3)][BAr^F{}_4]$ (**16**) and $[Rh(PPh_2(CH_2)_5PPh_2)(\eta^6\text{-}PhH_2BNMe_3)][BAr^F{}_4]$ (**17**, Scheme 4.10) and exhibited bite angles of 87.96(2)° and 92.21(4)°, respectively which are essentially smaller than that of η²-borane complex $[Rh(P^iPr_3)_2(\eta^2\text{-}H_2PhB{\cdot}NMe_3)][BAr^F{}_4]$ (**13**).[35]



III, n = 3; **IX**, n = 5

16, n = 3; **17**, n = 5

Scheme 4.10 Reactivity of $[Rh(PPh_2(CH_2)_nPPh_2)(C_6H_5F)][BAr^F{}_4]$ (n = 3, 5) fragments with $H_2PhB{\cdot}NMe_3$; $[BAr^F{}_4]^-$ anions are not shown.

The relationship between the bite angles and the coordination mode (η⁶-arene/η²-borane) for the isolated complexes **12**, **13** and **15**-**17** has been shown in Figure 4.6. On the basis of this empirical evidence we suggest that the higher bite angle in the $[RhL_2]^+$ complex favours the η²-borane coordination mode of $H_2PhB{\cdot}NMe_3$, whereas the smaller bite angle favours the η⁶-arene coordination mode.

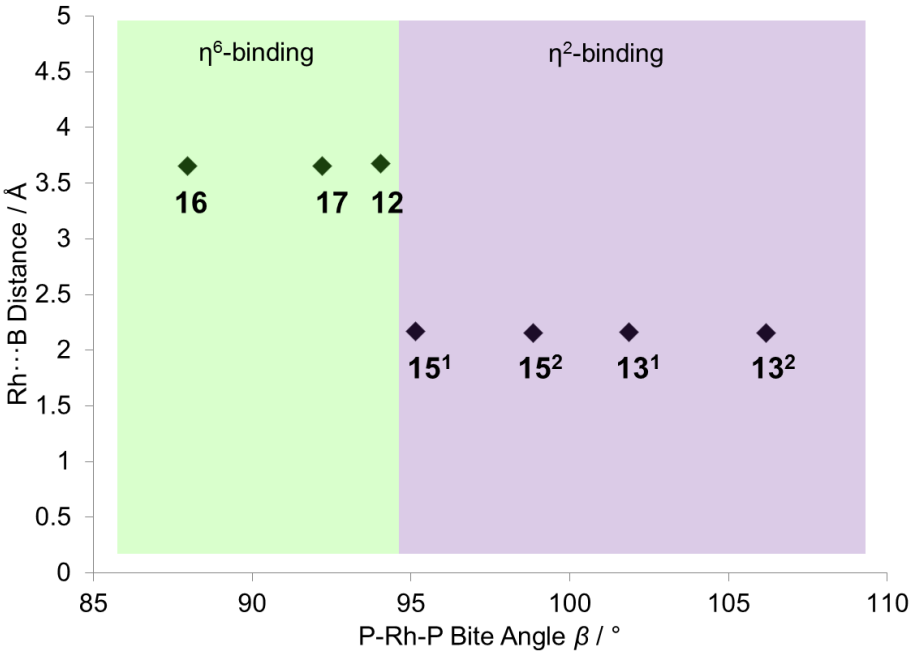
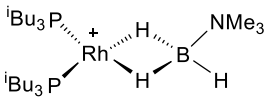
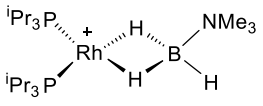
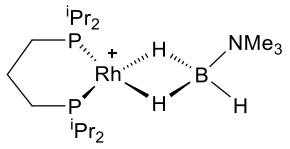
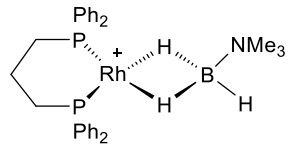
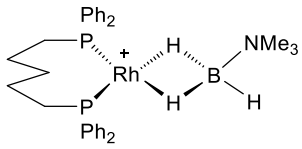


Figure 4.6 Plot of Rh···B distance (Å) against bite angle *β* (°) showing different binding modes for complexes **12**, **13**, **15, 16** and **17**. The values for independent cations in the asymmetric units of **13** and **15** are given separately. The bite angle for $[Rh(P^iBu_3)_2(\eta^2\text{-}H_2PhB{\cdot}NMe_3)][BAr^F{}_4]$ (**15**) [95.14(5)° or 98.84(5)°] has been taken from the part II thesis of Isobel Priest.[36]

The effect of bite angles on the strength of amine-borane binding has been previously commented upon in the case of $[Rh(L_2)(\eta^2\text{-}H_3B{\cdot}NMe_3)][BAr^F{}_4]$ (L_2 = bisphosphine ligand) with the stronger binding observed on increasing the bite angle (Table 4.1). For example, $[Rh(P^iPr_3)_2(\eta^2\text{-}H_3B{\cdot}NMe_3)][BAr^F{}_4]$ with the larger bite angle [106.08 (5)°] than that observed in $[Rh(P^iBu_3)_2(\eta^2\text{-}H_3B{\cdot}NMe_3)][BAr^F{}_4]$ [97.35 (9)°] shows stronger Rh···B interaction as measured by the ^{11}B NMR chemical shift and the Rh···B bond distance in the solid state (Entries I and II, Table 4.1). A similar conclusion can be drawn by comparing the complexes containing the monodentate and the chelating phosphine ligands of similar electronic nature but different bite angles such as $[Rh(P^iPr_3)_2(\eta^2\text{-}H_3B{\cdot}NMe_3)][BAr^F{}_4]$ and $[Rh(^iPr_2P(CH_2)_3P^iPr_2)(\eta^2\text{-}H_3B{\cdot}NMe_3)][BAr^F{}_4]$ (Entries II and III, Table 4.1). Finally, the increase in bite angle by increasing the backbone carbon chain length in $[Rh(Ph_2P(CH_2)_nPPh_2)(\eta^2\text{-}H_3B{\cdot}NMe_3)][BAr^F{}_4]$ (n = 3-5) complexes shows the stronger binding of amine-borane by the ^{11}B NMR spectroscopy but the Rh···B bond distance does not change within error (Entries IV and V, Table 4.1).

Table 4.1 Bite angles (P−Rh−P), Rh···B bond distances and the ^{11}B NMR chemical shifts for the selected $[Rh(L_2)(\eta^2\text{-}H_3B{\cdot}NMe_3)][BAr^F{}_4]$ complexes.

		P−Rh−P / °	Rh···B / Å	δ $^{11}B(CD_2Cl_2)$	Δ [δ ^{11}B]
I		97.35 (4)	2.180 (4)	23.1	30.4
II		106.08 (5)	2.1376 (3)	28.8	36.1
III		93.56 (4)	2.283 (9)	24.5	31.8
IV		91.14 (3)	2.199(3)	16.4	23.7
V		98.18(3)	2.189(3)	20.3	27.3

In contrast, the Rh···arene binding strength decreases on increasing the bite angle in $[Rh(L_2)(\eta^6\text{-arene})][BAr^F{}_4]$ (L_2 = bisphosphine ligand) complexes as measured by collision–induced dissociation in Electrospray Mass Spectrometry (ESI-MS) and solution equilibrium measurements.[37, 38] These trends perhaps reflect the optimisation of bonding between a d^8-$\{RhL_2\}^+$ fragment and either a π-arene orbitals or a B–H sigma-bonding

donating orbital. Figure 4.7 represents a qualitative Walsh diagram for a linear and a bent (C_2V) $\{ML_2\}^+$ fragment system.[39, 40] The LUMO ($1b_1$) which is of π symmetry gets stabilized as the bite angle increases. This results in a worse match of $\{ML_2\}^+$-LUMO with the arene HOMO[41] and a better one with that of low lying B–H sigma orbital. This is consistent with our experimental findings of the formation of η^6-arene complexes with the smaller bite angles while η^2-borane complexes with the higher bite angle $\{RhL_2\}^+$ fragments. It is hoped that theoretical calculations in the near future will put these ideas on a firmer footing.

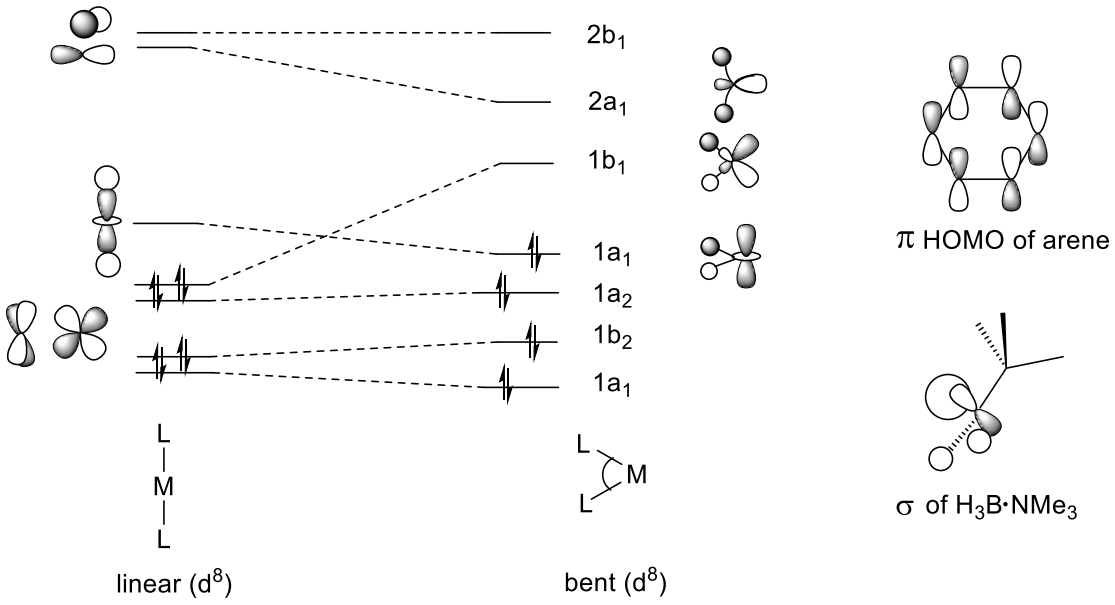
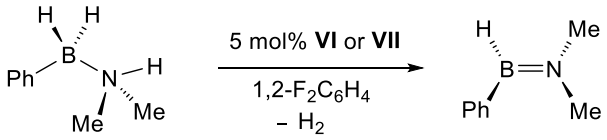


Figure 4.7 Adapted qualitative Walsh diagram[39] showing the frontier metal orbitals for the bending of a ML_2 d^8 fragment. Energies are approximate, and the specific ordering is for illustration only.

4.4 Catalytic dehydrogenation of $H_2PhB{\cdot}NMe_2H$ using VI and VII

The Weller group has previously reported the effect of bite angles on the rate of catalytic dehydrogenation of $H_3B{\cdot}NMe_2H$ using $[Rh(PPh_2(CH_2)_nPPh_2)(C_6H_5F)][BAr^F{}_4]$ (n = 3 - 5) catalysts.[29] The complex which was found to have the weakest binding with the amine-borane $H_3B{\cdot}NMe_3$ showed the highest turnover frequency for formation of $[H_2BNMe_2]_2$ under catalytic conditions. In order to explore the effect of variable coordination modes (η^6

or η^2) on the catalytic dehydrogenation of amine-boranes, we carried out the dehydrogenation of $H_2PhB{\cdot}NMe_2H$ using $[Rh(P^iPr_2(CH_2)_3P^iPr_2)(C_6H_5F)][BAr^F_4]$ (**VI**) and $[Rh(P^iPr_3)_2(C_6H_5F)][BAr^F_4]$ (**VII**) catalysts.



Scheme 4.11 Catalytic dehydrogenation of $H_2PhB{\cdot}NMe_2H$ to form aminoborane $PhBH{=}NMe_2$.

Catalytic dehydrogenation experiments were carried out in a sealed NMR tube using 5 mol% catalytic loading of **VI** or **VII** and 0.1 M $H_2PhB{\cdot}NMe_2H$ in 1,2-$F_2C_6H_4$ solvent and monitored by ^{11}B NMR spectroscopy. At 298 K, **VI** showed very slow dehydrogenation (6% conversion in five hours) of $H_2PhB{\cdot}NMe_2H$ (Figure 4.8, Scheme 4.11). ^{11}B NMR spectroscopy showed the appearance of a new signal at δ 39.4 (d, $^1J_{BH}$ = 123 Hz) which is characteristic of amino-boranes bearing two alkyl groups at nitrogen (e.g. ^{11}B NMR: $H_2B{=}NMe_2$, δ 37.5; $H_2B{=}NEt_2$, δ 36.6; $H_2B{=}N^iPr_2$, δ 35.1)[42, 43] as well as the recently reported $HMeB{=}NMe_2$ containing additional *B*-substitution (δ 41.2 d, $^1J_{BH}$ = 123 Hz)[8]. It was thus assigned to be the amino-borane $HPhB{=}NMe_2$. When **VII** was used for the dehydrogenation of $H_2PhB{\cdot}NMe_2H$ under identical catalytic conditions, a slightly faster rate of dehydrogenation was revealed, resulting in 15% conversion of $H_2PhB{\cdot}NMe_2H$ to $HPhB{=}NMe_2$ in 5 h (Figure 4.8, Scheme 4.11). Coupling of the amino-borane to form the cyclic dimer $[HPhBNMe_2]_2$ was not observed, presumably due to the bulky phenyl group present at the borane fragment.

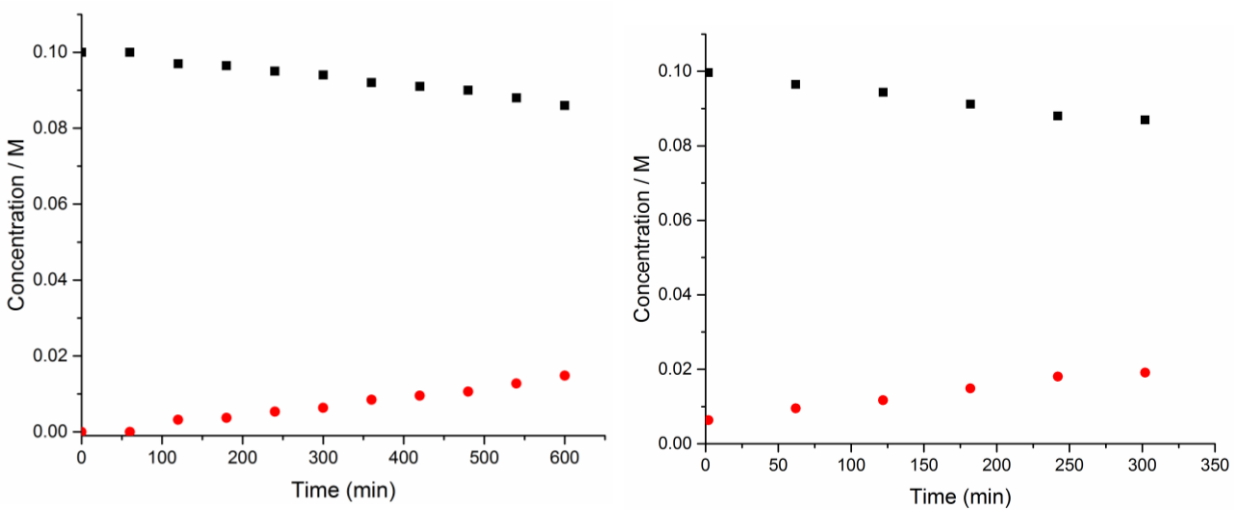


Figure 4.8 Plot of concentration (by ^{11}B NMR spectroscopy) against time for the catalytic dehydrogenation of $H_2PhB{\cdot}NMe_2H$ (initial concentration 0.1 M) using 5 mol% **VI** (left) and 5 mol% **VII** (right) at 298 K, • = $HPhB{=}NMe_2$, ■ = $H_2PhB{\cdot}NMe_2H$.

Increasing the temperature increased the rate of dehydrogenation. **VI** (5 mol%, sealed system) in 1,2-$F_2C_6H_4$ solvent at 350 K effected complete dehydrogenation of $H_2PhB{\cdot}NMe_2H$ (0.05 M) in 60 minutes [TOF for 50% conversion: 40 h^{-1}] while **VII** showed complete dehydrogenation in only 30 minutes [TOF for 50% conversion: 500 h^{-1}], both producing the amino-borane $HPhB{=}NMe_2$ (Figure 4.9).

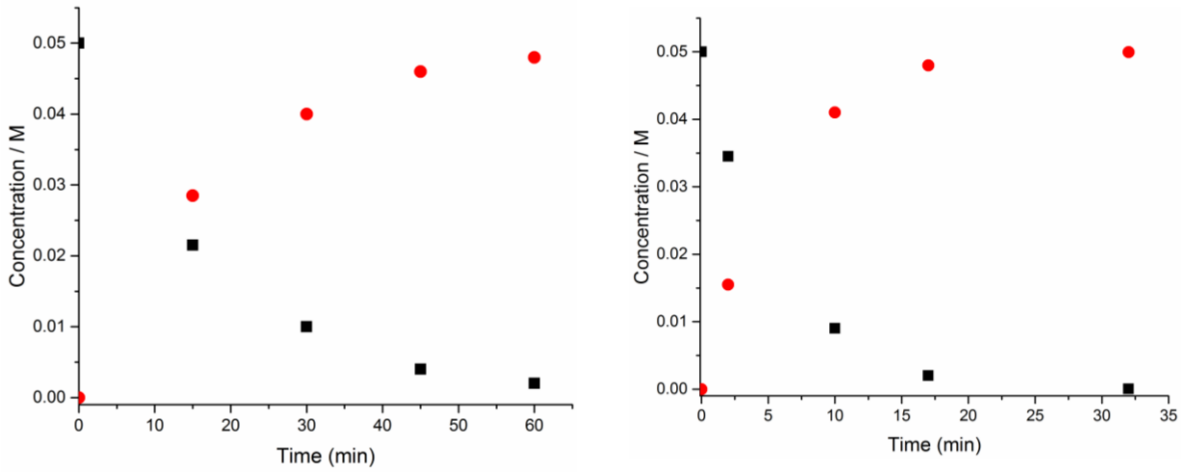


Figure 4.9 Plot of concentration (by ^{11}B NMR spectroscopy) against time for the catalytic dehydrogenation of $H_2PhB{\cdot}NMe_2H$ (initial concentration 0.05 M) using 5 mol% **VI** (left) and 5 mol% **VII** (right) at 350 K in 1,2-$C_6H_4F_2$, • = $PhBH{=}NMe_2$, ■ = $H_2PhB{\cdot}NMe_2H$.

Attempts to isolate the amino-borane $HPhB{=}NMe_2$ as a pure compound was not successful due to its volatile nature, although the metal catalyst was separated by the vacuum distillation technique to obtain $HPhB{=}NMe_2$ as a mixture with the 1,2-$F_2C_6H_4$ solvent. The ^1H NMR spectrum of $HPhB{=}NMe_2$ in 1,2-$F_2C_6H_4$ solvent showed a broad quartet at δ 5.05 ($^1J_{HB}$ = 120 Hz, 1H) corresponding to B*H* hydrogen similar to that reported for $H_2B{=}N^iPr_2$ in $CDCl_3$ solvent [δ 4.32, $^1J_{HB}$ = 125 Hz, 2H].[44] The two methyl resonances were observed as two distinct signals at δ 3.02 (s, 3H) and 2.88 (s, 3H) due to the restricted rotation around B=N bond.

If the dehydrogenation occurs via an inner sphere mechanism, the BH_2 fragment of amine-borane would be required to interact with the metal centre in order to undergo initial B−H activation. We suggest that the η^6-Phenyl binding of $H_2PhB{\cdot}NMe_2H$ prevents this step and results in the slower catalytic activity of $\{Rh(P^iPr_2(CH_2)_3P^iPr_2)\}^+$ fragment. In order to verify the hypothesis that the poor catalytic activity of **VI** is due to the η^6-binding of amine-borane and probe into the dehydrogenation mechanism we conducted the reaction of $H_2PhB{\cdot}NMe_2H$ (1 and 3 equivalents) with **VI** and monitored the reaction progress by NMR spectroscopy.

4.5 Reactivity of $H_2PhB{\cdot}NMe_2H$ with VI

The reaction of 1.2 equivalents of $H_2PhB{\cdot}NMe_2H$ with $[Rh(P^iPr_2(CH_2)_3P^iPr_2)(C_6H_5F)][BAr^F{}_4]$ (**VI**) in 1,2-$F_2C_6H_4$ solvent resulted in the displacement of the fluorobenzene ligand by $H_2PhB{\cdot}NMe_2H$ and the formation of $[Rh(^iPr_2P(CH_2)_3P^iPr_2)(\eta^6\text{-}PhH_2B{\cdot}NMe_2H)][BAr^F{}_4]$ (**18**). Formation of a small quantity of $HPhB{=}NMe_2$ was also observed by the ^{11}B NMR spectroscopy. Orange crystals were isolated by layering the reaction mixture with pentane at −25 °C in 62% yield. The ^1H NMR spectral data of the isolated **18** is similar to that observed for $[Rh(^iPr_2P(CH_2)_3P^iPr_2)(\eta^6\text{-}PhH_2B{\cdot}NMe_3)][BAr^F{}_4]$ (**12**) with an additional NH resonance observed in the ^1H NMR spectrum at δ 3.55. The solid state structure of the cationic portion of **18** is shown in Figure 4.10 which confirms the η^6 binding mode of

$H_2PhB{\cdot}NMe_2H$. Distances between the Rh and the aryl carbons [2.270(4)-2.373(4) Å] are similar to that observed for the η^6-complex **12** [2.267(3)-2.408(3) Å]. The P(1)-Rh(1)-P(2) angle [94.27(4)°] is also very similar to that in **12** [(94.04(4)°)].

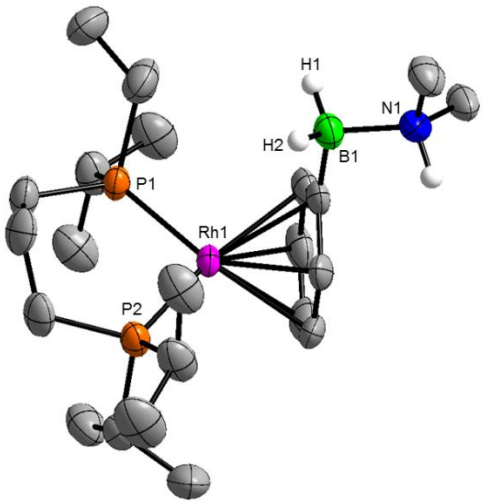
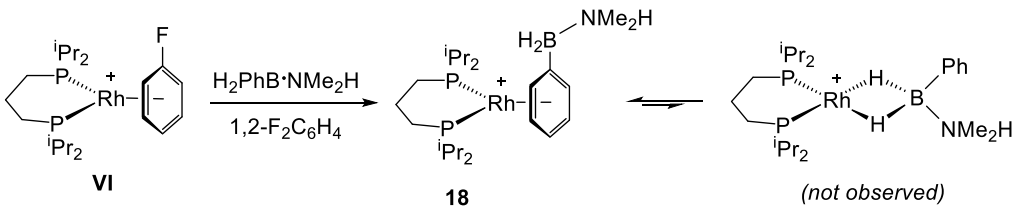


Figure 4.10 X-ray molecular structure of $[Rh(^iPr_2P(CH_2)_3P^iPr_2)(\eta^6\text{-}PhH_2B{\cdot}NMe_2H)][BAr^F{}_4]$ (**18**). $[BAr^F{}_4]^-$ anion and selected H atoms omitted for clarity. Ellipsoids shown at 50% probability level. Selected bond lengths (Å) and angles (°)Rh(1)-P(1) 2.2441(11), Rh(1)-P(2) 2.2422(10), Rh(1)-C_{arene} 2.270(4)-2.373(4), B(1)-N(1) 1.618(6); P(1)-Rh(1)-P(2) 94.27(4).

When three equivalents of $H_2PhB{\cdot}NMe_2H$ were reacted with **VI** at 350 K, the complete conversion of $H_2PhB{\cdot}NMe_2H$ to $HPhB{=}NMe_2$ was obtained in 15 minutes by the ^{11}B NMR spectroscopy. **18** was observed as the only organometallic species at the end of the dehydrogenation by $^{31}P\{^1H\}$ NMR spectroscopy. The fact that no η^2-amine-borane complex $[Rh(^iPr_2P(CH_2)_3P^iPr_2)(\eta^2\text{-}H_2BPh{\cdot}NMe_2H)][BAr^F{}_4]$ was observed at the end of dehydrogenation is consistent with our hypothesis of **VI** being a poor catalyst for the dehydrogenation of $H_2PhB{\cdot}NMe_2H$ due to binding of the amine-borane via the η^6-aryl coordination mode. Nevertheless, if the dehydrogenation occurs through an inner sphere mechanism, a switch to an η^2-borane coordination mode from an η^6-aryl coordination mode would be required. This is possible if there is an equilibrium between both the isomers which lies heavily towards η^6-aryl coordination mode (Scheme 4.12) as the dehydrogenation of $H_2PhB{\cdot}NMe_2H$ by **VI** is relatively slow. Considering the η^6-aryl

coordination mode of amine-borane, we also cannot discount the possibility of an outer sphere mechanism that operates via B−H$^{\delta-}\cdots$ $^{\delta+}$HN interactions. However, the N*H* resonance does not change significantly on coordination with the metal centre [^{1}H NMR: δ 3.55 for **18** versus δ 3.52 for $H_2PhB{\cdot}NMe_2H$] suggesting only minimal perturbation of this bond.

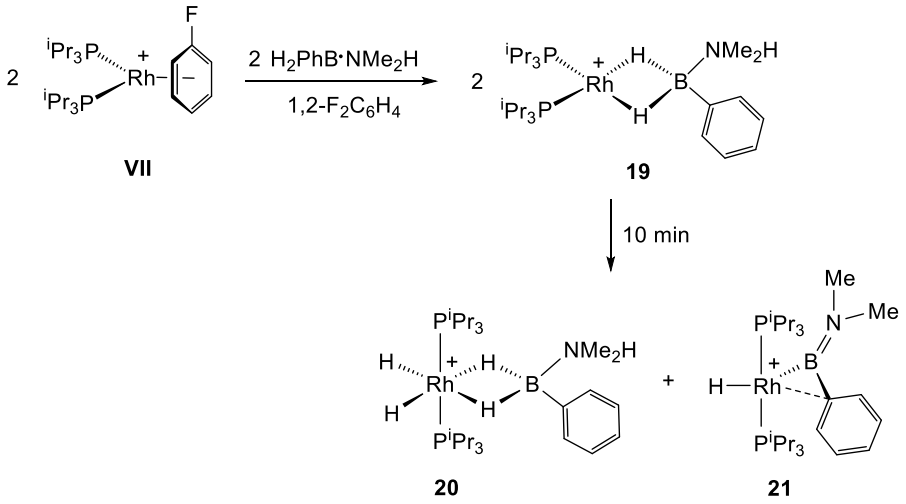


Scheme 4.12 Reactivity of $H_2PhB{\cdot}NMe_2H$ with **VI** and the proposed equilibrium between the isomers of $[Rh(^iPr_2P(CH_2)_3P^iPr_2)(\eta^6\text{-}PhH_2B{\cdot}NMe_2H)][BAr^F{}_4]$ in case of inner sphere dehydrogenation mechanism; $[BAr^F{}_4]^-$ anions not shown.

4.6 Stoichiometric reactivity of $H_2PhB{\cdot}NMe_2H$ with VII

The addition of a stoichiometric amount of $[Rh(P^iPr_3)_2(C_6H_5F)][BAr^F{}_4]$ (**VII**) to $H_2PhB{\cdot}NMe_2H$ in 1,2-$F_2C_6H_4$ resulted in the immediate formation of a transient blue solution which turned colourless in 5 minutes. The $^{31}P\{^1H\}$ NMR spectrum after 2 minutes showed three doublets at δ 69.29 ($^1J_{RhP}$ = 174 Hz), δ 64.36 (J_{RhP} = 109 Hz) and δ 48.46 ($^1J_{RhP}$ = 116 Hz) in an approximate ratio of 10:45:45 respectively. It is proposed that the doublet at δ 69.29 ($^1J_{RhP}$ = 174), which is similar to that observed for the complex **13** $[Rh(P^iPr_3)_2(\eta^2\text{-}H_2BPhNMe_3)][BAr^F{}_4]$ (δ 69.6 [d, $^1J_{RhP}$ = 176 Hz]), is due to the formation of $[Rh(^iPr_3P)_2(\eta^2\text{-}H_2BPhNHMe_2)][BAr^F{}_4]$ (**19**). The $^{31}P\{^1H\}$ NMR spectrum after 10 minutes showed the complete disappearance of the resonances attributed to **19**, however the remaining two products persisted in an equimolar ratio for the next 24 h. The formation of $HPhB{=}NMe_2$ or the presence of any unreacted $H_2PhB{\cdot}NMe_2H$ was not observed by ^{11}B NMR spectroscopy. Layering this solution with pentane and storage at –26°C for 24 h resulted in the formation of two distinct crystalline products: colourless block crystals and pale yellow plate crystals. The colourless crystals were identified as $[RhH_2(P^iPr_3)_2(\eta^2\text{-}$

$H_2PhB{\cdot}NMe_2H)][BAr^F{}_4]$ (**20**) and the pale yellow crystals as $[RhH(P^iPr_3)_2(BPhNMe_2)][BAr^F{}_4]$ (**21**) using NMR spectroscopy, ESI-MS and single crystal X-ray diffraction as discussed below (Scheme 4.13).



Scheme 4.13 Reactivity of $H_2PhB{\cdot}NMe_2H$ with **VII**. $[BAr^F{}_4]^-$ anions are not shown.

The $^{31}P\{^1H\}$ NMR (CD_2Cl_2) spectrum of isolated **20** showed a signal at δ 64.7 (d, $^1J_{RhP}$ = 108 Hz) confirming it to be one of the products observed in the stoichiometric reaction of **VII** with $H_2PhB{\cdot}NMe_2H$. We suggest that the equivalent phosphorus environment in **20** is due to the fluxionality of amine-borane through a mechanism that involves the change of amine-borane coordination mode from η^2 to η^1 and then rotation around the Rh−H bond.[45] The ^1H NMR spectrum showed the sigma-bound B*H*$_2$ resonance at δ –2.08 (br, 2H). A broad multiplet was also observed at δ –19.05 (2 H) in ^1H NMR spectrum corresponding to Rh*H*$_2$ which changed to a broad doublet ($^1J_{RhH}$ = 17) upon ^{31}P decoupling. The bound *B*H_2 was observed at δ 8.0 (br) in the ^{11}B NMR spectrum. Figure 4.11 depicts the solid state structure of the cationic portion of **20** which confirms the trans orientation of the P^iPr_3 ligands. The asymmetric unit of **20** contains two independent cations (and two anions) with broadly similar metric parameters as observed for **13**. The presence of the N–*H*, B–*H* and Rh–*H* hydrogen atoms were confirmed by NMR spectroscopy and ESI-MS, although crystallographically they could not be located in the electron density map. The N–*H* and

B–*H* hydrogen atoms were placed in calculated positions, whereas the Rh–*H* hydride ligands could not be reliably placed and so were omitted. Rh···B distances of 2.274(9) and 2.333(8) Å were observed for the two cations present in the asymmetric unit. The formation of dihydride Rh (III) complexes from the dehydrogenation of $H_3B{\cdot}NMe_2H$ using $\{Rh(PR_3)_2\}^+$ (R = ^{i}Pr, ^{i}Bu and Cy) fragments have been previously reported by the Weller group[39, 46, 47] and **20** is structurally similar to $[RhH_2(P^iPr_3)_2(\eta^2\text{-}H_3B{\cdot}NMe_3)][BAr^F{}_4]$[23] which has Rh···B distance of 2.325(4) Å, similar to that of **20**.

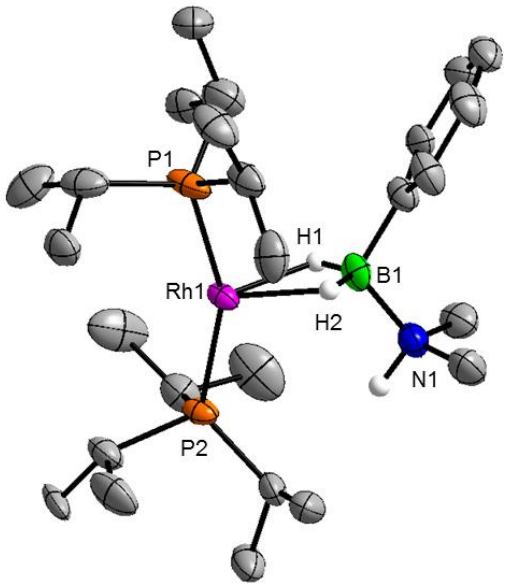


Figure 4.11 The solid state structure of **20**. $[BAr^F{}_4]^-$ anion and selected H atoms omitted for clarity. Ellipsoids shown at 50% probability level. Selected bond lengths (Å) and angles (°) for both the cations in the asymmetric unit: Rh(1)−P(1) 2.336(2), Rh(1)−P(2) 2.330(2), Rh(1)−B(1) 2.274(9), B(1)−N(1) 1.650(11), Rh(2)−P(3) 2.3227(19), Rh(2)−P(4) 2.327(2), Rh(2)−B(2) 2.333(8), B(2)−N(2) 1.608(11); P(1)−Rh(1)−P(2) 158.35(8), P(3)−Rh(2)−P(4) 155.75(8).

The second product isolated from the reaction mixture was characterised as $[RhH(P^iPr_3)_2(BPhNMe_2)][BAr^F{}_4]$ (**21**) by NMR spectroscopy and single crystal X-ray diffraction. The solid state structure is depicted in Figure 4.12 which confirms the formulation proposed on the basis of spectroscopic data.

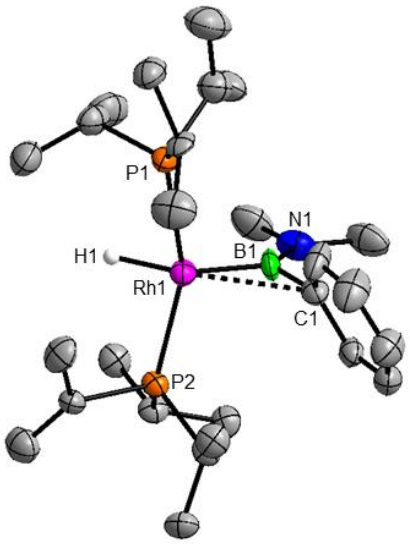


Figure 4.12 The solid state structure of **21**. $[BAr^{F}{}_{4}]^{-}$ anion and selected H atoms omitted for clarity. Ellipsoids shown at 50% probability level. Selected bond lengths (Å) and angles (°) for both the cations in the asymmetric unit: Rh(1)−P(1) 2.3292(18), Rh(1)−P(2) 2.350(2), Rh(1)−B(1) 1.929(9), B(1)−N(1) 1.411(14); P(1)−Rh(1)−P(2) 157.55(7), P(1)−Rh(1)−B(1) 100.2(3), P(2)−Rh(1)−B(1) 100.6(3), Rh(1)−B(1)−N(1) 138.0(8), Rh(1)−B(1)−C(1) 98.3(7), N(1)−B(1)−C(1) 123.7(8).

The B–N distance was found to be 1.411(14) Å which suggests that there is significant π character in the B–N bond. The Rh(1)–C(1) distance was found to be 2.634(8) Å which is significantly longer than the Rh–C_{ipso} bond (1.85 - 2.0 Å) in rhodium(III) aryl complexes[48, 49] such as bis(imino)aryl rhodium(III) halide (**X**) suggesting that Rh(1)–C(1) interaction in **21** is weaker than a usual Rh···C_{ipso} interaction. Longer Rh···C_{ipso} [2.377(4) / 2.3535 Å] interaction has been reported earlier for the zwitterionic rhodium(I) complexes [(WCA-NHC)Rh(L_2)] [L_2 = COD or $(CO)_2$; WCA = weakly coordinating anions, $\{B(C_6F_5)_3\}^{-}$, e.g. **XI**] in which the rhodium metal shows an intramolecular interaction with the N-aryl groups of the carbene ligands exhibiting weaker Rh···C_{ortho} interactions of 2.624(5) / 3.061(4) Å similar to the Rh(1)–C(1) interaction in **21**.[50] The Rh(1)–B(1)–C(1) angle [98.3(7)°] was found to be significantly smaller than the ideal sp^2-hybridised angle of 120°. This also indicates the presence of Rh(1)–C(1) interaction in **21**. The phenyl group is twisted 62° compared to the Rh/B/N plane possibly due to Rh···C_{ipso} interaction. The Rh–B bond distance was found to be 1.929(9) Å which is consistent with a rhodium-boryl bond such

as that observed in complex **XII** [Rh–B 1.981(4) Å, Figure 4.13].[51, 52] Complex **21** closely resembles [Ir(IMes)$_2$(H$_2$B=NCy$_2$)][BAr$^F{}_4$] (IMes = *N,N′*-bis(2,4,6-trimethylphenyl)imidazol-2-ylidene) (**XIII**) reported by Aldridge, which contains a direct Ir–B bond stabilised by a B–H α-agostic interaction (Figure 4.13).[53] The Ir–B [2.012(8) Å] and B–N [1.365(9) Å] bond lengths in **XIII** are only slightly different from the Rh–B [1.929(9) Å] and B–N [1.411(14) Å] bond lengths observed for **21**. The Weller group has also reported a similar rhodium-boryl complex [Rh(κ^3-$_{POP}$-Xantphos)(H)(BH=N^{i}Pr$_2$)(NCMe)][BAr$^F{}_4$] (**XIV**). The solid state structure of **XIV** showed the Rh–B distance of 2.034(3) Å which is slightly longer than the 1.929(9) Å found in **21**, but the B=N bond [1.378(4) Å] is similar to the B=N bond length observed in **21** [1.411(14) Å].

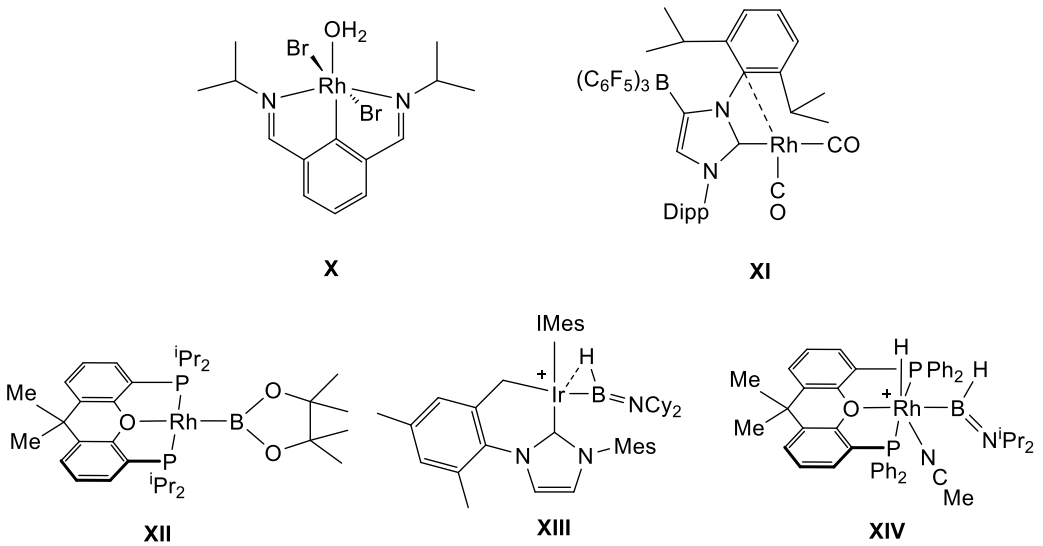


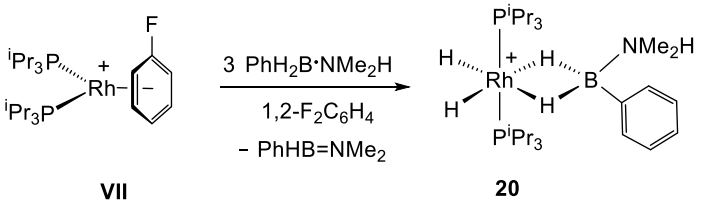
Figure 4.13 Examples of iridium and rhodium amino-boryl complexes. [BAr$^F{}_4$]$^-$ anions are not shown.

The ^{31}P{^{1}H} NMR spectrum (in CD_2Cl_2) of isolated **21** shows a doublet at δ 48.8 ($^1J_{RhP}$ = 120 Hz) confirming it to be one of the products (other than **20**) formed from the stoichiometric reaction of **VII** with $H_2PhB{\cdot}NMe_2H$ (Scheme 4.13). The ^{1}H NMR spectrum showed a signal at δ –21.71 (doublet of triplets, $^1J_{HRh}$ = 64 Hz, $^2J_{HP}$ = 12 Hz, 1H) corresponding to the terminal Rh–*H*. The large Rh–H coupling constant is characteristic of a hydride ligand bound to an electron deficient Rh(III) centre and thus consistent with a

rhodium hydride of a 14-electron complex **21**, similar to the 14-electron amino-boryl rhodium hydride $[Rh(IMes)_2(H)(BHNMe_2)][BAr^F{}_4]$ reported by Aldridge that shows the rhodium hydride signal at δ –23.59 with the $^1J_{HRh}$ = 43.5 Hz.[54] Two separate resonances at δ 3.07 (s, 3H) and 2.95 (s, 3H) are observed for the N*Me* groups, demonstrating a lack of rotation about the B–N bond on the ^{1}H NMR timescale. Three distinct phenyl-hydrogen resonances [δ 7.67 (m, 1H), 7.55 (broad d, 2H) and 7.54 (br, 2H)] were observed in the ^{1}H NMR spectrum due to the three inequivalent C–*H* arene environments [ortho (2H), meta (2H) and para (1H)]. The ^{13}C NMR spectrum of **21** also showed three distinct resonances at δ 132.2 (s, Ph), 130.7 (s, Ph), and 127.8 (s, Ph) for the phenyl carbon atoms. The resonance corresponding to the B−*C* was not observed presumably due to the quadrupolar broadening of boron. The N*Me*$_2$ carbon atoms were also observed as two separate resonances at δ 43.3 (s) and 40.4 (s) consistent with the observation of the inequivalent methyl resonances in its ^{1}H NMR spectrum. Bound Ph*B*=NMe_2 was observed at δ 54.8 in the ^{11}B NMR spectrum consistent with other rhodium···boryl interactions reported in the literature [^{11}B NMR for **XII**: 41.9;[51] **XIII**: δ 38.0;[53] for **XIV**: 49.0,[52] Figure 4.13].

4.7 Mechanism for the formation of 21

In order to understand the transformation of organometallic species during the dehydrogenation of $H_2PhB{\cdot}NMe_2H$ catalysed by **VII**, reaction of three equivalents of $H_2PhB{\cdot}NMe_2H$ with $[Rh(P^iPr_3)_2(C_6H_5F)][BAr^F{}_4]$ (**VII**) was carried out and followed by NMR spectroscopy. $H_2PhB{\cdot}NMe_2H$ was completely consumed in 24 h producing amino-borane $HPhB{=}NMe_2$ as observed by the ^{11}B NMR spectroscopy. $[RhH_2(P^iPr_3)_2(\eta^2\text{-}H_2PhB{\cdot}NMe_2H)][BAr^F{}_4]$ (**20**) was the only organometallic species observed during dehydrogenation, suggesting that **20** is the resting state during the catalytic dehydrogenation of $H_2PhB{\cdot}NMe_2H$ (Scheme 4.14). Complex **20** could also be isolated from this reaction in 57% yield by layering the reaction mixture with pentane and storing at −25°C.

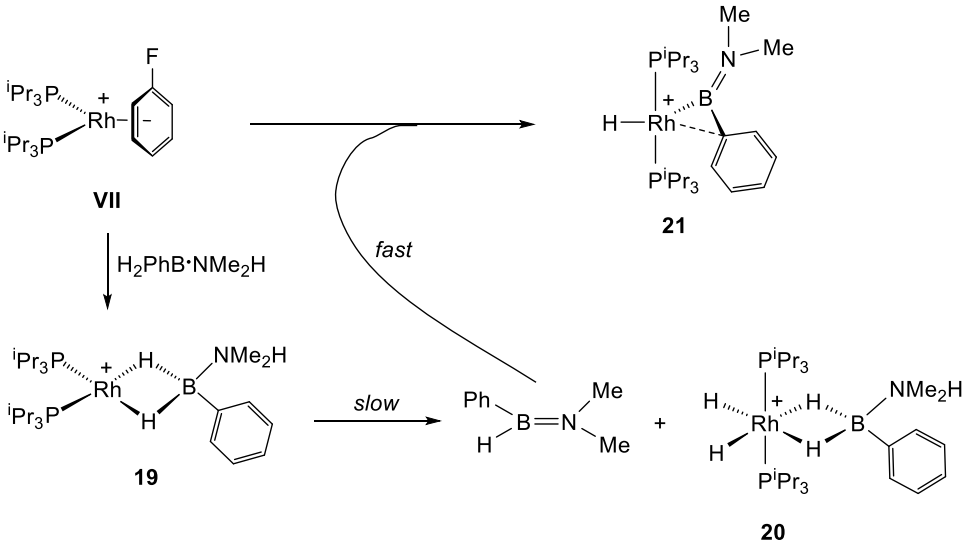


VII **20**

Scheme 4.14 Reaction of **VII** with 3 equivalents of $H_2PhB{\cdot}NMe_2H$; $[BAr^F{}_4]^-$ anions are not shown.

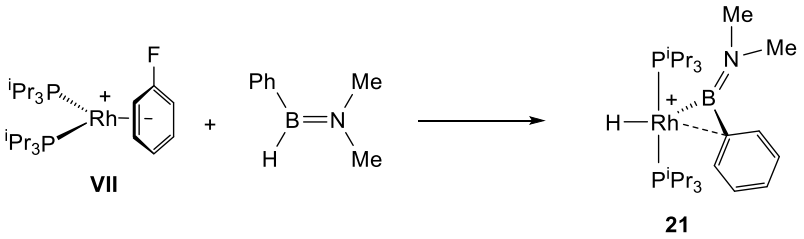
The addition of three equivalents of $H_2PhB{\cdot}NMe_2H$ to the 1,2-$F_2C_6H_4$ solution of pure **20** resulted in the dehydrogenation of $H_2PhB{\cdot}NMe_2H$ to form $HPhB{=}NMe_2$. Complex **20** was the only organometallic species observed during the catalytic dehydrogenation, which persisted till the end, consistent with the previous observation of **20** being the resting state. Formation of **21** was not observed during the catalytic dehydrogenation experiment suggesting that **21** can only be formed or observed from the stoichiometric reaction of $H_2PhB{\cdot}NMe_2H$ (1 equivalent) with **VII**.

We propose that in the stoichiometric reaction of $H_2PhB{\cdot}NMe_2H$ (1 equivalent) with **VII**, half an equivalent of the $\{Rh(P^iPr_3)_2\}^+$ fragment reacts with one equivalent of $H_2PhB{\cdot}NMe_2H$ to form half an equivalent of **20** and half an equivalent of the aminoborane $HPhB{=}NMe_2$. This half equivalent of $HPhB{=}NMe_2$ may then B−H oxidatively add to the remaining half equivalent of $\{Rh(P^iPr_3)_2\}^+$ to form **21** in an equal ratio to **20** (Scheme 4.15). No free $HPhB{=}NMe_2$ was observed during the course of the reaction, suggesting that the oxidative addition of the amino-borane occurs at a significantly faster rate than its formation.



Scheme 4.15 Proposed reaction mechanism showing tandem formation of **20** and **21** from a stoichiometric reaction of **VII** and $H_2PhB{\cdot}NMe_2H$; $[BAr^F{}_4]^-$ anions are not shown.

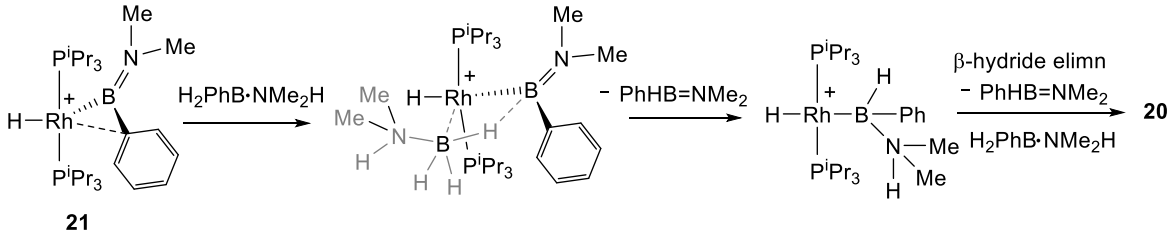
To confirm this hypothesis, the reaction of **VII** with the independently synthesised $HPhB{=}NMe_2$ was performed which led to the rapid and quantitative formation of complex **21** as observed by NMR spectroscopy (Scheme 4.16).



Scheme 4.16 Reaction of $HPhB{=}NMe_2$ with $[Rh(P^iPr_3)_2(C_6H_5F)][BAr^F{}_4]$ (**VII**). $[BAr^F{}_4]^-$ anions are not shown.

In an additional experiment, reaction of independently synthesised **21** with the amine-borane $H_2PhB{\cdot}NMe_2H$ (2 equivalents) resulted in the formation of complex **20** and the amino-borane $HPhB{=}NMe_2$. This is consistent with the previous observation of complex **20** being the only organometallic species observed in the presence of excess amine-boranes. Formation of **20** from **21** could occur through a sigma-bond metathesis reaction between **21** and $H_2PhB{\cdot}NMe_2H$ followed by the β–hydride elimination and the subsequent

coordination of $H_2PhB{\cdot}NMe_2H$ as shown in Scheme 4.17. However, we cannot discount an alternative mechanism in which the complex **21** undergoes a reversible reductive elimination of $HPhB{=}NMe_2$ to afford the $\{Rh(P^iPr_3)_2\}^+$ fragment which reacts with $H_2PhB{\cdot}NMe_2H$ as discussed in Scheme 4.15.



Scheme 4.17 Formation of complex **20** from the reaction of **21** with $H_2PhB{\cdot}NMe_2H$; $[BAr^F_4]^-$ anions are not shown.

4.8 Conclusions

In conclusion, we have reported here the reactivity of *B*-phenyl substituted amine-boranes $H_2PhB{\cdot}NMe_2R$ (R = Me, H) with rhodium bis-phosphine fragments. In the case of $H_2PhB{\cdot}NMe_3$, we have observed that the amine-borane coordination mode depends on the bite angle of the phosphine ligands. For example, chelating ligands such as $PR_2(CH_2)_3PR_2$ (R = Ph, ^{i}Pr) with the bite angles in the range of 88 - 94° form η^6-aryl complexes, while non-chelating phosphines such as $(P^iPr_3)_2$ with comparatively higher bite angles 102 - 106° form η^2-borane complexes. The balance of the two binding modes comes with $(P^iBu_3)_2$ ligands which has the bite angle of 95 or 99° (from two independent cations present in the asymmetric unit) and forms an equilibrium mixture of the both η^6-aryl and η^2-borane complexes $[Rh(P^iBu_3)_2(\eta^6\text{-}C_6H_5BH_2NMe_3)][BAr^F_4]$ (**14**) and $[Rh(P^iBu_3)_2(\eta^2\text{-}H_2PhB{\cdot}NMe_3)][BAr^F_4]$ (**15**). Dehydrogenation of $H_2PhB{\cdot}NMe_2H$ has also been studied using catalysts **VI** and **VII** which showed TOF of 20 h^{-1} and 40 h^{-1} respectively forming amino-borane $HPhB{=}NMe_2$. A stoichiometric reaction of $H_2PhB{\cdot}NMe_2H$ with **VI** showed the formation of η^6-aryl complex $[Rh(^iPr_2P(CH_2)_3P^iPr_2)(\eta^6\text{-}PhH_2B{\cdot}NMe_2H)][BAr^F_4]$ (**18**) similar to **12**, while the stoichiometric reaction with **VII** resulted

in the formation of a mixture of complexes $[RhH_2(P^iPr_3)_2(\eta^2\text{-}H_2PhB{\cdot}NMe_2H)][BAr^F{}_4]$ (**20**) and $[RhH(P^iPr_3)_2(BPhNMe_2)][BAr^F{}_4]$ (**21**). Complex **20** was found to be the resting state during the catalytic dehydrogenation of $H_2PhB{\cdot}NMe_2H$ using **VII**. Complex **21** features an unusual amino-boryl binding to the Rh(III) centre and is proposed to form by the oxidative addition of $HPhB{=}NMe_2$. We hope that the DFT calculations in near future will keep these observations on firmer footing.

4.9 References

1. A. Staubitz, A. P. M. Robertson, M. E. Sloan and I. Manners, *Chem. Rev.*, 2010, **110**, 4023-4078.

2. H. Anane, A. Jarid, A. Boutalib, I. Nebot-Gil and F. Tomás, *J. Mol. Struct.: Thermochem*, 1998, **455**, 51-57.

3. D. J. Grant, M. H. Matus, K. D. Anderson, D. M. Camaioni, S. R. Neufeldt, C. F. Lane and D. A. Dixon, *J. Phys. Chem. A*, 2009, **113**, 6121-6132.

4. H. Anane, A. Jarid, A. Boutalib, I. Nebot-Gil and F. Tomas, *J. Mol. Struct.: Thermochem*, 1998, **455**, 51-57.

5. A. P. M. Robertson, G. R. Whittell, A. Staubitz, K. Lee, A. J. Lough and I. Manners, *European Journal of Inorganic Chemistry*, 2011, **2011**, 5279-5287.

6. A. P. M. Robertson, M. F. Haddow and I. Manners, *Inorganic Chemistry*, 2012, **51**, 8254-8264.

7. P. G. Campbell, J. S. A. Ishibashi, L. N. Zakharov and S.-Y. Liu, *Aust. J. Chem.*, 2014, **67**, 521-524.

8. N. E. Stubbs, A. Schäfer, A. P. M. Robertson, E. M. Leitao, T. Jurca, H. A. Sparkes, C. H. Woodall, M. F. Haddow and I. Manners, *Inorg. Chem.*, 2015, **54**, 10878-10889.

9. W. Luo, P. G. Campbell, L. N. Zakharov and S.-Y. Liu, *J. Am. Chem. Soc.*, 2013, **135**, 8760-8760.

10. W. Luo, L. N. Zakharov and S.-Y. Liu, *J. Am. Chem. Soc.*, 2011, **133**, 13006-13009.

11. C. A. Jaska, K. Temple, A. J. Lough and I. Manners, *J. Am. Chem. Soc.*, 2003, **125**, 9424-9434.

12. E. Wiberg, J. E. F. Evans and H. Noth, *Zeitschrift Fur Naturforschung Part B-Chemie Biochemie Biophysik Biologie Und Verwandten Gebiete*, 1958, **13**, 263-264.

13. Y. Kawano, K. Yamaguchi, S.-y. Miyake, T. Kakizawa and M. Shimoi, *Chem. Eur. J.*, 2007, **13**, 6920-6931.

14. B. M. Mikhailov and V. A. Dorokhov, *Russ. Chem. Bull.*, 1962, **11**, 1138-1142.

15. S.-K. Kim, W.-S. Han, T.-J. Kim, T.-Y. Kim, S. W. Nam, M. Mitoraj, Ł. Piekoś, A. Michalak, S.-J. Hwang and S. O. Kang, *J. Am. Chem. Soc.*, 2010, **132**, 9954-9955.

16. B. Singaram, T. E. Cole and H. C. Brown, *Organometallics*, 1984, **3**, 774-777.

17. H. Helten, A. P. M. Robertson, A. Staubitz, J. R. Vance, M. F. Haddow and I. Manners, *Chem. Eur. J.*, 2012, **18**, 4665-4680.

18. I. Pernik, J. F. Hooper, A. B. Chaplin, A. S. Weller and M. C. Willis, *Acs Catal.*, 2012, **2**, 2779-2786.

19. G. Alcaraz, E. Clot, U. Helmstedt, L. Vendier and S. Sabo-Etienne, *J. Am. Chem. Soc.*, 2007, **129**, 8704-8705.

20. T. M. Douglas, A. B. Chaplin and A. S. Weller, *J. Am. Chem. Soc.*, 2008, **130**, 14432-14433.

21. T. M. Douglas, A. B. Chaplin, A. S. Weller, X. Yang and M. B. Hall, *J. Am. Chem. Soc.*, 2009, **131**, 15440-15456.

22. R. Dallanegra, A. B. Chaplin and A. S. Weller, *Angew. Chem. Int. Ed.*, 2009, **48**, 6875-6878.

23. A. B. Chaplin and A. S. Weller, *Inorg. Chem.*, 2010, **49**, 1111-1121.

24. R. Dallanegra, A. B. Chaplin, J. Tsim and A. S. Weller, *Chem. Commun.*, 2010, **46**, 3092-3094.

25. Y. Kawano, K. Yamaguchi, S.-y. Miyake, T. Kakizawa and M. Shimoi, *Chem. Eur. J.*, 2007, **13**, 6920-6931.

26. A. B. Chaplin, A. I. Poblador-Bahamonde, H. A. Sparkes, J. A. K. Howard, S. A. Macgregor and A. S. Weller, *Chem. Commun.*, 2009, DOI: 10.1039/B816739G, 244-246.

27. A. Meissner, H.-J. Drexler, S. Keller, C. Selle, V. Ratovelomanana-Vidal and D. Heller, *Eur. J. Inorg. Chem.*, 2014, 4836-4842.

28. M. T. Whited, A. J. Kosanovich and D. E. Janzen, *Organometallics*, 2014, **33**, 1416-1422.

29. R. Dallanegra, A. P. M. Robertson, A. B. Chaplin, I. Manners and A. S. Weller, *Chem. Commun.*, 2011, **47**, 3763-3765.

30. G. Alcaraz and S. Sabo-Etienne, *Coord. Chem. Rev.*, 2008, **252**, 2395-2409.

31. N. Merle, G. Koicok-Köhn, M. F. Mahon, C. G. Frost, G. D. Ruggerio, A. S. Weller and M. C. Willis, *Dalton Trans.*, 2004, 3883-3892.

32. C. A. Tolman, *Chem. Rev.*, 1977, **77**, 313-348.

33. W. F. Bailey, H. Connon, E. L. Eliel and K. B. Wiberg, *J. Am. Chem. Soc.*, 1978, **100**, 2202-2209.

34. T. M. Douglas, E. Molinos, S. K. Brayshaw and A. S. Weller, *Organometallics*, 2007, **26**, 463-465.

35. I. Priest, *Complex **17** was synthesized by Tom Hooper and the complex **16** was synthesized by Isobel Priest, Part II thesis*, 2015, University of Oxford.

36. I. Priest, *Part II Thesis*, 2015, University of Oxford.

37. S. D. Pike, I. Pernik, R. Theron, J. S. McIndoe and A. S. Weller, *J. Organomet.Chem.*, 2015, **784**, 75-83.

38. I. Pernik, J. F. Hooper, A. B. Chaplin, A. S. Weller and M. C. Willis, *ACS Catal.*, 2012, **2**, 2779-2786.

39. A. B. Chaplin and A. S. Weller, *Inorg. Chem.*, 2010, **49**, 1111-1121.

40. M. D. Su and S. Y. Chu, *Inorg. Chem.*, 1998, **37**, 3400-3406.

41. J. Silvestre and T. A. Albright, *J. Am. Chem. Soc.*, 1985, **107**, 6829-6841.

42. Y. Kawano, M. Uruichi, M. Shimoi, S. Taki, T. Kawaguchi, T. Kakizawa and H. Ogino, *J. Am. Chem. Soc.*, 2009, **131**, 14946-14957.

43. L. Pasumansky, D. Haddenham, J. W. Clary, G. B. Fisher, C. T. Goralski and B. Singaram, *J. Org. Chem.*, 2008, **73**, 1898-1905.

44. C. A. Jaska, K. Temple, A. J. Lough and I. Manners, *J. Am. Chem. Soc.*, 2003, **125**, 9424-9434.

45. A. G. Algarra, L. J. Sewell, H. C. Johnson, S. A. Macgregor and A. S. Weller, *Dalton Trans.*, 2014, **43**, 11118-11128.

46. T. M. Douglas, A. B. Chaplin, A. S. Weller, X. Yang and M. B. Hall, *J. Am. Chem. Soc.*, 2009, **131**, 15440-15456.

47. L. J. Sewell, G. C. Lloyd-Jones and A. S. Weller, *J. Am. Chem. Soc.*, 2012, **134**, 3598-3610.

48. A. Damas, H. Sesolis, M. N. Rager, L. M. Chamoreau, M. P. Gullo, A. Barbieri and H. Amouri, *Rsc Adv.*, 2014, **4**, 23740-23748.

49. W. J. Hoogervorst, K. Goubitz, J. Fraanje, M. Lutz, A. L. Spek, J. M. Ernsting and C. J. Elsevier, *Organometallics*, 2004, **23**, 4550-4563.

50. E. L. Kolychev, S. Kronig, K. Brandhorst, M. Freytag, P. G. Jones and M. Tamm, *J. Am. Chem. Soc.*, 2013, **135**, 12448-12459.

51. M. A. Esteruelas, M. Olivan and A. Velez, *Organometallics*, 2015, **34**, 1911-1924.

52. H. C. Johnson, E. M. Leitao, G. R. Whittell, I. Manners, G. C. Lloyd-Jones and A. S. Weller, *J. Am. Chem. Soc.*, 2014, **136**, 9078-9093.

53. C. Y. Tang, A. L. Thompson and S. Aldridge, *J. Am. Chem. Soc.*, 2010, **132**, 10578-10591.

54. C. Y. Tang, N. Phillips, J. I. Bates, A. L. Thompson, M. J. Gutmann and S. Aldridge, *Chem. Commun.*, 2012, **48**, 8096-8098.

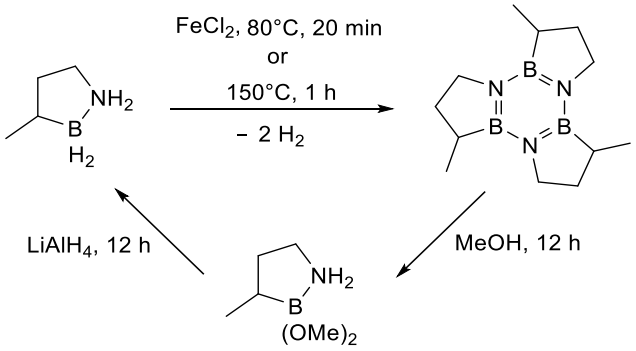
5 The Synthesis and Dehydrogenation of Sigma-Complexes of BN−Cyclohexanes

5.1 Introduction

Amine-boranes ($H_3B{\cdot}NHRR'$), in particular $H_3B{\cdot}NH_3$, have attracted significant interest towards the development of chemical hydrogen storage materials because of their high gravimetric hydrogen density (*e.g.* 19.6 wt% for $H_3B{\cdot}NH_3$), as discussed in Chapter One.[1] However, these acyclic amine-boranes ($H_3B{\cdot}NHRR'$) are solid and cannot serve as liquid fuels, similar to gasoline, therefore their transportation would require the development of new infrastructure facilities. Moreover, the regeneration of charged fuel, such as $H_3B{\cdot}NH_3$, from the spent fuel such as borazine or polyaminoborane is thermodynamically disfavoured and requires energy-rich agents such as hydrazine in liquid ammonia which leads to the poor energy efficiency of the overall process.[2, 3] Thus, development of a liquid amine-borane system which can discharge and recharge hydrogen with the minimum thermodynamic overpotential would be of significant importance to the current hydrogen economy.

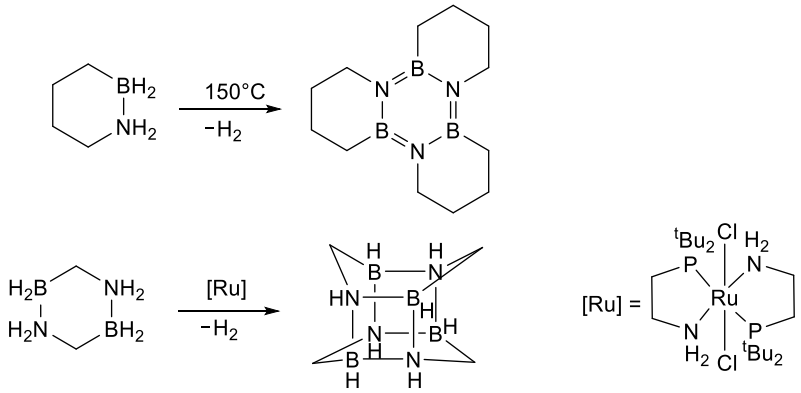
A breakthrough in this area was achieved by Liu in 2011, who reported an air and moisture stable amine-borane, BN-methylcyclopentane, which was a liquid at room temperature and released two equivalents of hydrogen gas under thermal or catalytic conditions to form a tricyclic borazine.[4] Regeneration of the starting fuel BN-methylcyclopentane from the dehydrogenated product borazine was also possible in an overall yield of 92% using a two-step methodology as shown in Scheme 5.1. Liu and Autrey later reported the properties of BN-methylcyclopentane which are relevant to hydrogen storage materials such as thermal stability, viscosity and hydrogen gas stream purity.[5] The results such as stability below 40ºC, viscocity of 25 centipoise (comparable to

ethylene glycol) and a pure hydrogen stream produced upon thermal dehydrogenation showed BN-methylcyclopentane to be a viable hydrogen storage material.



Scheme 5.1 Dehydrogenation and regeneration of BN-methylcyclopentane.

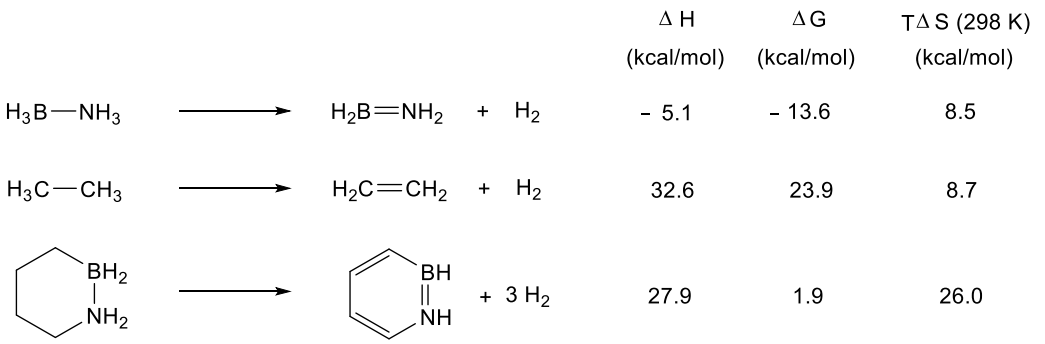
Liu and co-workers have also reported the synthesis of other cyclic amine-boranes such as 1,2-BN cyclohexane[6] and bis-BN cyclohexane[7] and their dehydrocoupling to produce a tricyclic borazine and a cage-like structure respectively (Scheme 5.2).



Scheme 5.2 Dehydrocoupling of 1,2-BN cyclohexane (top) and bis-BN cyclohexane(bottom).

A major advantage of using cyclic amine-boranes over acyclic amine-boranes such as $H_3B{\cdot}NH_3$ is the thermodynamic feasibility of the regeneration of cyclic amine-boranes from the discharged amino-borane. The dehydrogenation of $H_3B{\cdot}NH_3$ is exergonic by −13.6 kcal mol^{-1} while the dehydrogenation of its alkane isostere $H_3C{-}CH_3$ is endergonic by 23.9 kcal mol^{-1} (Scheme 5.3).[8] A hybrid system designed by combining both BN and CC fragments can thus result in a material that can dehydrogenate with the minimum

thermodynamic overpotential. Liu has shown that a cyclic amine-borane such as 1,2-BN cyclohexane, containing both BN and CC moieties leads to a thermodynamically reversible hydrogen storage pathway (taking account of the aromatic stabilization) with ΔG (dehydrogenation) = 1.9 kcal mol^{-1} (Scheme 5.3).[8]



Scheme 5.3 Thermodynamic parameters for the dehydrogenation reactions.

Although 1,2-BN cyclohexane is a potential candidate for the reversible hydrogen storage material, dehydrogenation without a catalyst requires a high temperature (150°C) as shown in Scheme 5.2. The use of a transition-metal catalyst can lower the dehydrogenation barrier reducing the operating temperature and controlling the final product distribution. Here, we report the reactivity of 1,2-BN cyclohexane (**A**) and its N-substituted analogues (**B** and **C**) with iridium and rhodium bis-phosphine complexes (**II**, **III** and **VI**; Figure 5.1). This gives insight into the coordination mode and the activation chemistry. As far as we are aware, this is the first report on the coordination chemistry and subsequent transition metal catalysed dehydrogenation of BN cyclohexanes using well-defined catalysts.

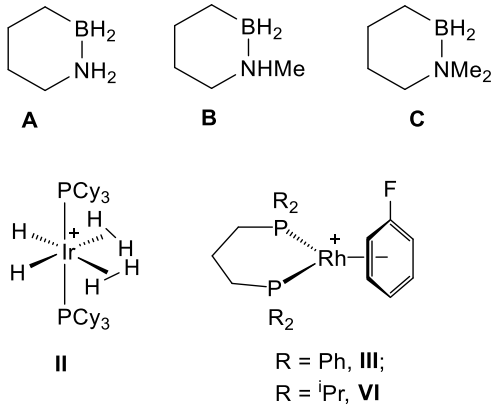
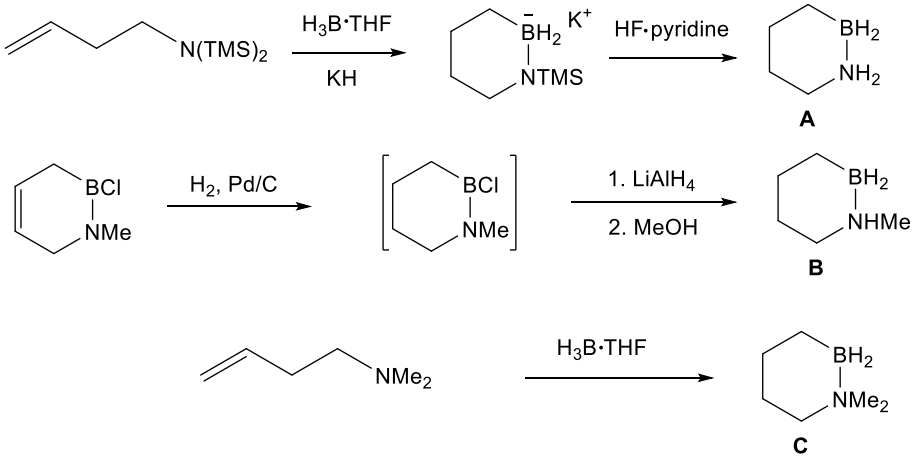


Figure 5.1 Cyclic amine-boranes and metal-complexes used in this project. $[BAr^F{}_4]^-$ anions are not shown.

5.2 Synthesis of cyclic amine-boranes

The cyclic amine-boranes **A**-**C** were prepared by Jacob S. A. Ishibashi from the Liu research group, Boston College, USA (Scheme 5.4). 2,2-H_2-1,2-B,N-C_4H_{10} (**A**) was synthesised using the method previously reported by Liu and co-workers[6] by the hydroboration of bistrimethylsilyl-substituted homoallylamine. 2,2-H,Me-1,2-B,N-C_4H_{10} (**B**), to the best of our knowledge, has not been reported yet in the open literature as an isolated compound but has been implicated as an intermediate during the synthesis of amino-borane **F** (*vide infra*).[9] **B**, here, has been synthesised by the hydrogenation of *B*-Cl-N-Me-1,2-BN-cyclohexene and its subsequent reaction with $LiAlH_4$. Preparation of 2,2-Me_2-1,2-B,N-C_4H_{10} (**C**) was adapted from that of Wille and Goubeau[9], and was synthesised by the hydroboration of N,N-dimethylhomoallylamine (Scheme 5.4).



Scheme 5.4 Synthesis of the cyclic amine-boranes **A**-**C**.

Compounds **A** and **B** were isolated as analytically pure white solids while **C** was isolated as a colorless liquid. The three cyclic amine-boranes **A**-**C** were characterised by the NMR spectroscopy and high resolution mass spectroscopy. The ^{11}B NMR and ^{1}H{^{11}B} B–*H* chemical shifts for these three compounds are shown in Table 5.1.

Table 5.1 ^{11}B NMR and ^{1}H{^{11}B} B–*H* chemical shifts for **A**-**C**.

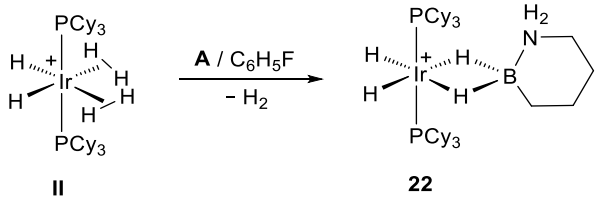
Compound	δ(^{11}B)	δ[1H{^{11}B}]
A	–11.3 [$^{1}J_{BH}$ = 95 Hz]	1.81
B	–6.5 [$^{1}J_{BH}$ = 96 Hz]	2.05
C	–3.0 [$^{1}J_{BH}$ = 97 Hz]	2.54

5.3 Reactivity of cyclic amine-boranes (A-C) with [Ir(PCy$_3$)$_2$(H$_2$)$_2$(H)$_2$][BAr$^F_4$] (II)

5.3.1 Formation of [Ir(PCy$_3$)$_2$(H)$_2$(η^2-H$_2$BNH$_2$C$_4$H$_8$)][BAr$^F_4$] (22)

The bis-dihydrogen dihydride complex [Ir(PCy$_3$)$_2$(H$_2$)$_2$(H)$_2$][BAr$^F_4$] (**II**) was prepared *in situ* by the hydrogenation of [IrHPCy$_2$(η^2-C$_6$H$_9$)PCy$_2$(η^3-C$_6$H$_8$)][BAr$^F_4$] in C$_6$H$_5$F as discussed in Chapter 2, section 2.1. Reaction of **A** to a C$_6$H$_5$F solution of the *in situ* generated **II**, resulted in the formation of [Ir(PCy$_3$)$_2$(H)$_2$(η^2-H$_2$BNH$_2$C$_4$H$_8$)][BAr$^F_4$] (**22**) in quantitative yield

as measured by NMR spectroscopy (Scheme 5.5). Analytically pure, crystalline, material was isolated in 43% yield by recrystallisation from C_6H_5F/pentane solution at –30˚C. Complex **22** was characterised by NMR spectroscopy, ESI-MS, single crystal X-ray diffraction and elemental analysis.



II **22**

Scheme 5.5 Formation of **22**; $[BAr^F_4]^-$ anions are not shown.

The solid-state structure of complex **22** is shown in Figure 5.2 which shows it to be a Shimoi-type sigma-amine-borane complex.[10-12] The Ir–*H* protons were located in the final difference map, while the bridging B–*H*–Ir protons were not located with any reliability and hence were placed in their calculated positions meaning that the nature of the Ir···H_3B interaction needs to be probed by other metrics. The Ir···B [2.216(5) Å] and B1–N1 [1.604(6) Å] distances are consistent with a sigma-amine-borane complex, comparing closely with the η^2-sigma-complexes of $H_3B{\cdot}NMe_3$ with the same metal fragment [Ir···B, 2.207(7) Å],[13] $H_3B{\cdot}NMeH_2$ [2.210(7) Å][14] and $H_3B{\cdot}NH_3$ [2.209(5) Å].[15] An η^1-sigma amine-borane complex, or a boryl complex, would be expected to have significantly longer (ca. 2.6 Å or longer)[16, 17] and shorter M–B distances (less than 2.1 Å) respectively.[18, 19] The cyclic amine-borane adopts a chair conformation, Figure 5.2B, showing that there is no plane of symmetry in the molecule in the solid-state.

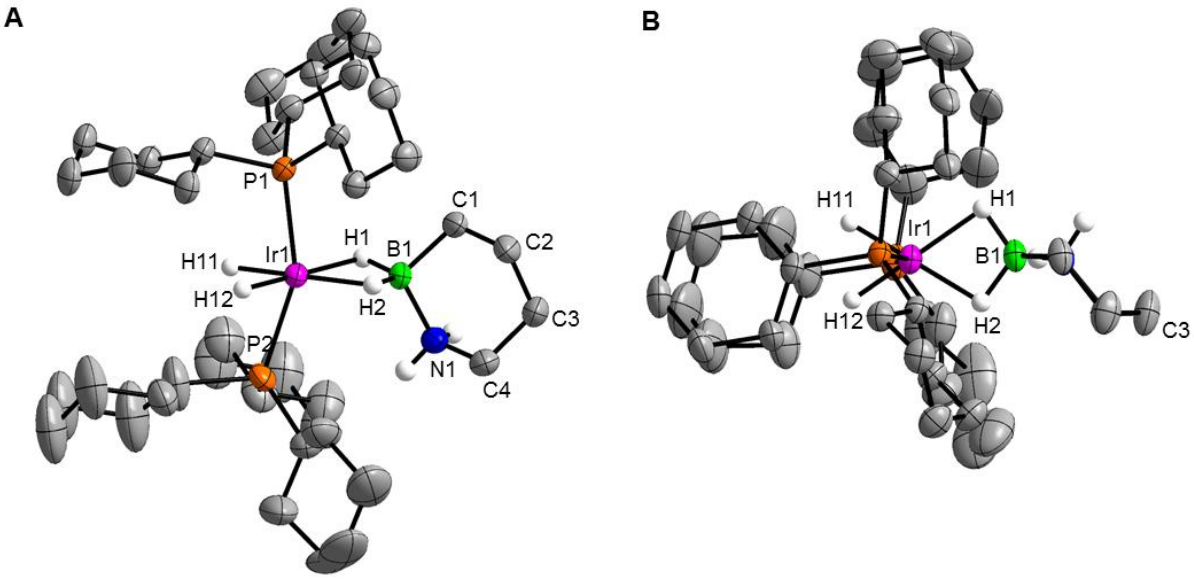


Figure 5.2 The solid–state structure of the cationic portion of complex **22**. Side (A) and Plan (B) views. Displacement ellipsoids are shown at the 50% probability level. Selected bond lengths (Å) and angles (º): Ir1–B1, 2.216(5); Ir1–P1, 2.3146(11); Ir1–P2, 2.3244(10); B1–C1, 1.590(6); B1–N1,1.604(6); P1–Ir1–P2, 155.88(4).

The ^{11}B NMR spectrum (in CD_2Cl_2) of **22** shows a broad signal (fwhm = 350 Hz) at δ 19.8, shifted downfield, when compared to the free ligand (**A**) that is observed at δ –11.3. The downfield movement of the amine-borane chemical shift in ^{11}B NMR spectrum upon coordination with a metal centre is diagnostic of an $\eta^{2}\cdots H_3B$ interaction and has been previously noted.[20, 21] The ^{1}H NMR spectrum (CD_2Cl_2) displays a triplet at δ –20.53 (2H, $^{2}J_{PH}$ = 16 Hz) corresponding to Ir*H*$_2$ hydrides and a broad signal corresponding to IrB*H*$_2$ hydrides at δ –6.23 (br, 2H) that sharpens on ^{11}B decoupling and is shifted 8.04 ppm upfield from **A**. The N*H*$_2$ protons are observed at δ 4.07 and CH_2 resonances of amine-borane moiety were observed at δ 3.23 (br, 2H), ~1.70 (br m, 2H, overlapping with PCy_3 protons) and 0.92 (m, 4H) in the ^{1}H NMR spectrum. NH_2/CH_2 resonances were further discriminated on the basis of the number of cross-peaks in the ^{1}H/^{1}H COSY spectrum. The ^{1}H/^{1}H COSY spectrum in the aliphatic region shows interaction of the signal at δ 4.07 (N*H*$_2$) with the signal at δ 3.23 (C^{1}*H*$_2$), while the resonance at δ 3.23 (C^{1}*H*$_2$) interacts with two different sets of protons resonating at δ 4.07 (N*H*$_2$) and δ 1.70 (C^{2}*H*$_2$) confirming that the resonance at δ 4.07 is due to NH_2 proton while that at δ 3.23 is due to CH_2 protons (Figure 5.3).

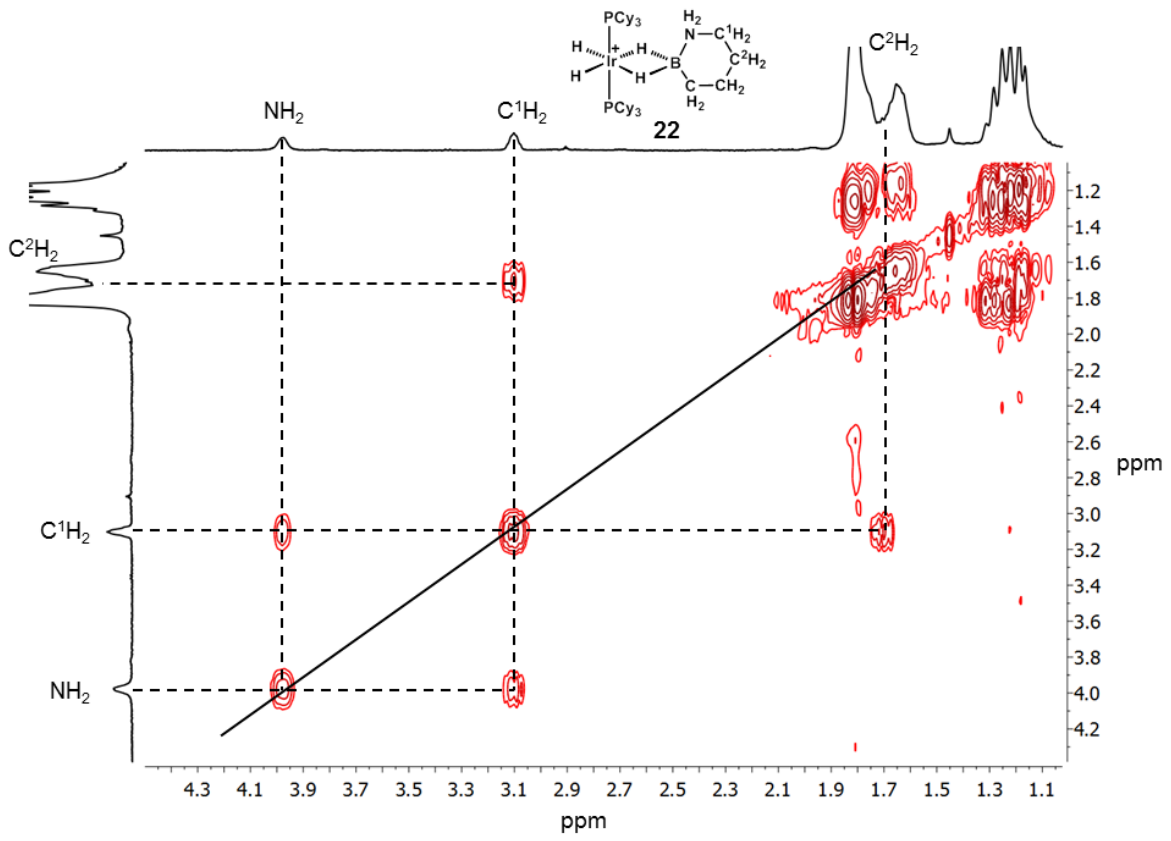
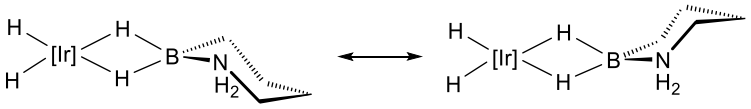


Figure 5.3 $^{1}H/^{1}H$ COSY spectrum showing correlation between NH_2, C^1H_2 and C^2H_2 protons in **22**. $[BAr^F{}_4]^-$ anion is not shown.

Furthermore, the HSQC (^{1}H - ^{13}C) spectrum shows no cross peak between the signal at δ 4.07 (br, 2H), while the signal at δ 3.23 is coupled to a ^{13}C NMR signal at 48.0 ppm confirming that the resonance at δ 4.07 is due to the N*H*$_2$ protons while the signal at δ 3.23 is due to the C*H*$_2$ hydrogens. The $^{31}P\{^{1}H\}$ NMR spectrum displays two inequivalent phosphorus environments at δ 37.12 (d, $^{2}J_{PP}$ = 268 Hz, 1P) and 35.26 (d, $^{2}J_{PP}$ = 268 Hz, 1P), consistent with a *trans* orientation. These solution data suggest that the η^2-bound cyclic amine-borane is undergoing a fluxional process that gives a time-averaged mirror plane, making the two sets of hydride ligands (Ir*H*$_2$ and B*H*$_2$) equivalent. We propose that this fluxional process is occurring through the ring flipping of cyclic amine-borane as shown in Scheme 5.6, rather than just a rotation around the B1–Ir1 vector that would also make the phosphine ligands equivalent.[22] The Liu group has shown that the ring-flip in the free 1,2-BN cyclohexane ligand proceeds via a low activation barrier of $\Delta G^{\neq}$ = 8.8 ± 0.2

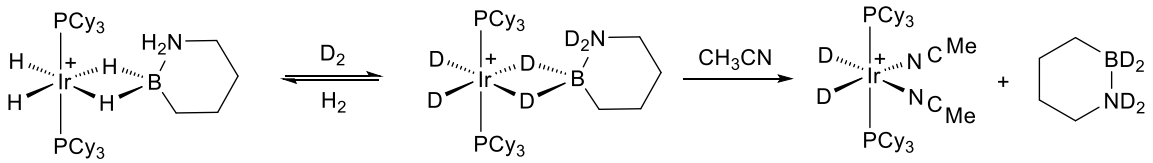
kcal/mol which is similar to the ring flipping energy of activation for cyclohexane ($\Delta G^{\neq}$ = 10.5 ± 0.2 kcal/mol).[23]



Scheme 5.6 Ring flipping of the bound cyclic amine borane moiety in **22**. Stereochemistry is adapted from Figure 5.2 B, [Ir] = $\{Ir(PCy_3)_2\}^+$ and the $[BAr^F{}_4]^-$ anions are not shown.

5.3.2 Reactivity of $[Ir(PCy_3)_2(H)_2(\eta^2\text{-}H_2BNH_2C_4H_8)][BAr^F{}_4]$ (22) with D_2

Addition of D_2 (4 atm, 1 h) to a C_6H_5F solution of **22** in a sealed NMR tube resulted in a loss of the N*H*$_2$ (δ 3.96), B*H*$_2$ (δ –6.23) and Ir*H*$_2$ (δ –20.53) resonances in the ^{1}H NMR spectrum and the appearance of the corresponding signals in the ^{2}H NMR spectrum (Scheme 5.7, Figure 5.4 - 5.5). Dissolved HD and H_2 were also observed at δ 4.47 (t, $^1J_{HD}$ = 43 Hz) and δ 4.50 respectively in the ^{1}H NMR spectrum. Deuterium incorporation was also observed at the C–H hydrogens of PCy_3 and C_6H_5F in the ^{2}H NMR spectrum (Figure 5.4). The $^{31}P\{^1H\}$ NMR spectrum is unchanged on deuterium addition. A ^{2}H NMR spectrum was also taken after degassing the sample in order to eliminate HD, H_2 and D_2 as the resonances corresponding to these species appear appear close to that expected for the N*D*$_2$ resonance. This confirmed the scrambling of deuterium into the N*H*$_2$ protons. Addition of 100 equivalents of acetonitrile immediately displaced the bound cyclic amine-borane resulting in the formation of $[Ir(PCy_3)_2(D)_2(CH_3CN)_2][BAr^F{}_4]$[24] (Scheme 5.7). The displaced cyclic amine-borane ($BD_2ND_2C_4H_8$) showed the same chemical shift as that of $BH_2NH_2C_4H_8$ (**A**, δ: –11.3) in the ^{11}B NMR spectrum and did not show any B–H coupling showing the complete transformation of BH_2 to BD_2.



Scheme 5.7 Addition of D_2/H_2 to the complex **22** and the subsequent addition of acetonitrile. $[BAr^F_4]^-$ anions are not shown.

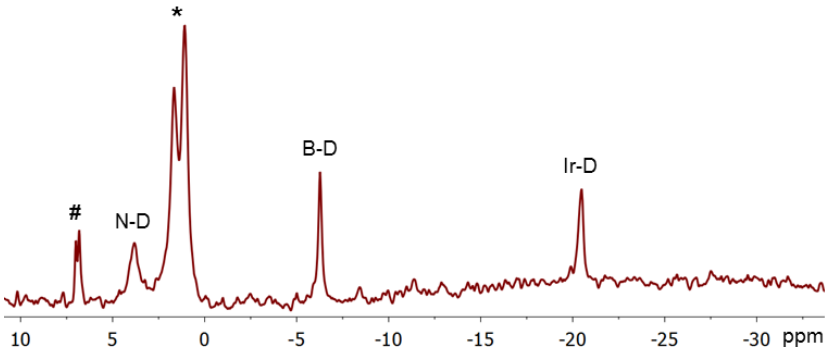


Figure 5.4 The ^2H NMR spectrum after 1 h of the addition of D_2 to complex **22** in C_6H_5F solvent. *: D-incorporation in PCy_3 ligand, #: D-incorporation in C_6H_5F solvent.

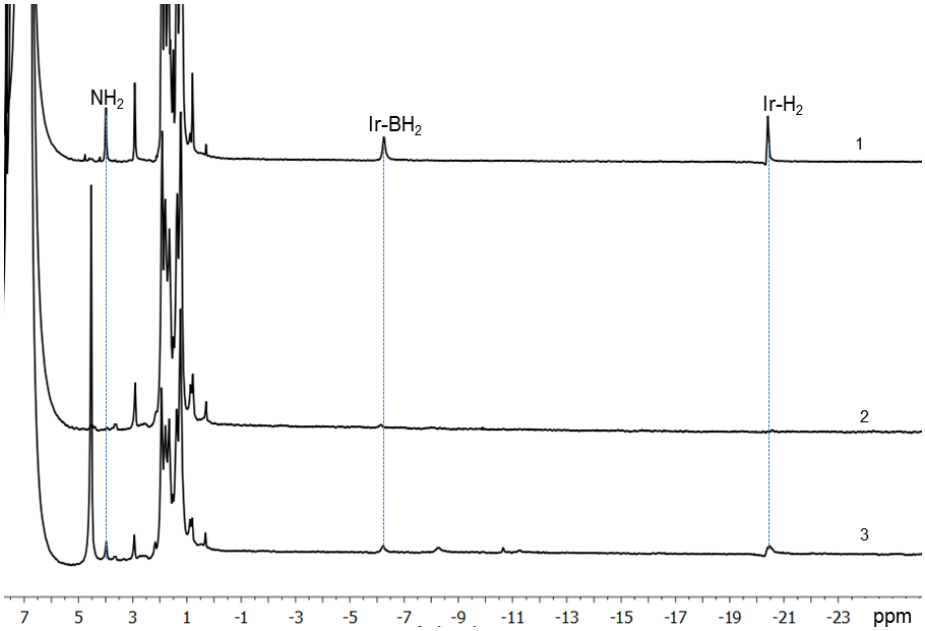
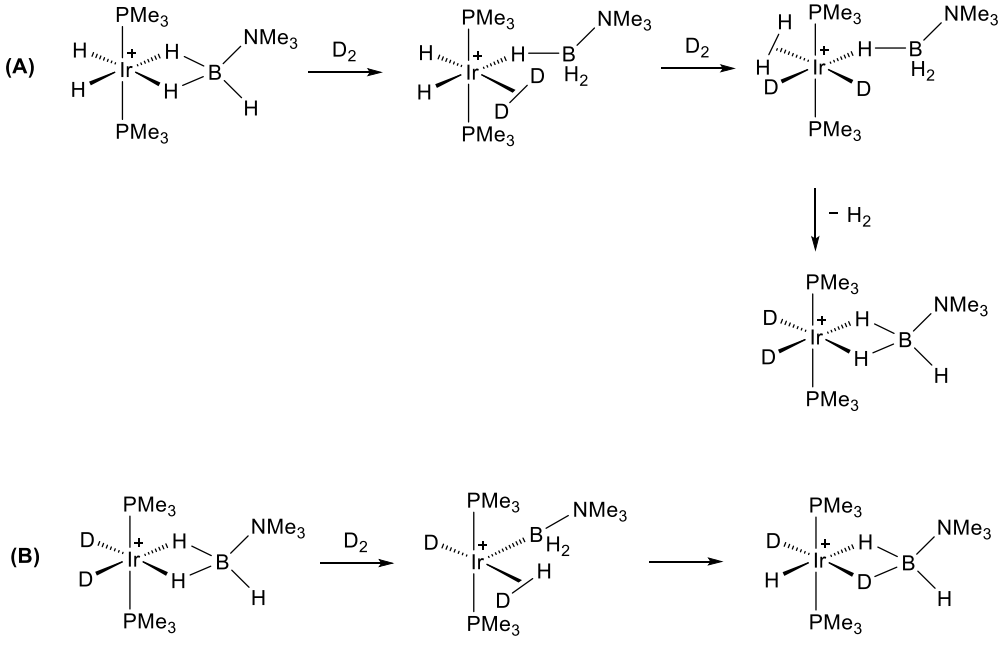


Figure 5.5 The ^1H NMR spectrum in C_6H_5F solvent. **1**: Complex **22**, **2**: After 1 h of the addition of D_2 to complex **22** (signals due to IrH_2, BH_2 and NH_2 disappear), **3**: After 30 minutes of adding H_2 to the sample corresponding to Figure **5.5-2** (signals due to IrH_2, BH_2 and NH_2 reappear). Signals at δ −8 and −11 are some decomposition products due to multiple manipulations.

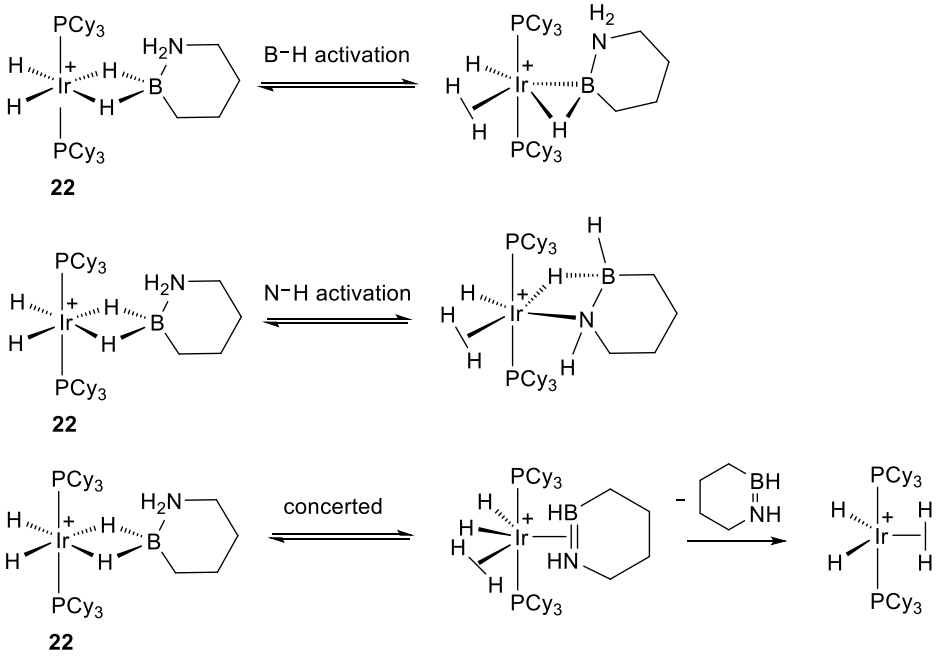
Addition of D_2 followed by H_2 regenerates the N*H*$_2$, B*H*$_2$ and Ir*H*$_2$ signals in the ^{1}H NMR spectrum (Figure 5.5). These experimental observations unusually suggest that rapid Ir–*H*/*D* exchange and sequential N–H or B–H activation (in either order) are of approximately similar energies and are therefore reversible. Weller and Macgregor have previously proposed a mechanism for the exchange between the exogenous *D*$_2$ and Ir*H*$_2$ hydrides in $[Ir(PR_3)_2(H)_2(\eta^2\text{-}H_3B{\cdot}NMe_3)][BAr^F{}_4]$ (R = Cy, experiment and Me, computation) which involves the sigma coordination of a D_2 ligand to $[Ir(PMe_3)_2(H)_2(\eta^2\text{-}H_3B{\cdot}NMe_3)][BAr^F{}_4]$ and the formation of $[Ir(PMe_3)_2(H)_2(\eta^2\text{-}D_2)(\eta^1\text{-}H_3B{\cdot}NMe_3)][BAr^F{}_4]$ followed by the reductive elimination of the two terminal hydride ligands (Scheme 5.8A).[22] A mechanism for the exchange between the Ir–H and B–H hydrides involving B–H activation has also been proposed which explains the incorporation of deuterium to the bridging B*H*$_2$ moiety (Scheme 5.8B).[22]



Scheme 5.8 Ir–H/D_2 exchange (**A**) and Ir–H/B–H (**B**) exchange in $[Ir(PMe_3)_2(H)_2(\eta^2\text{-}H_3B{\cdot}NMe_3)][BAr^F{}_4]$. $[BAr^F{}_4]^-$ anions are not shown.

N–H activation has been previously proposed to occur through a relatively higher energy barrier compared to the B–H activation; for example addition of D_2 (4 atm, 2 h) to

$[Ir(PCy_3)_2(H)_2(\eta^2–H_3BNMeH_2)][BAr^F_4]$ results in H/D exchange only at Ir–H and B–H and not at N–H.[14] DFT calculations on the model complex $[Ir(PMe_3)_2(H)_2(\eta^2–H_3BNMe_2H)][BAr^F_4]$ have revealed a barrier of 21.3 kcal mol^{-1} for the B–H activation and a significantly higher barrier of 30.1 kcal mol^{-1} for the N–H activation.[24] Similarly, a higher barrier for the N–H activation (ΔG = 19.9 kcal mol^{-1}) than the B–H activation (ΔG = 6.0 kcal mol^{-1}) has been calculated for a rhodium sigma-complex $[Rh(P^iBu_3)_2(H)_2(\eta^2–H_3BNMe_2H)][BAr^F_4]$.[25] However, the occurrence of N–H activation over B–H activation has been observed for neutral titanium and zirconium systems and the corresponding amido-borane products have been isolated,[26, 27] or postulated.[28] The complex **22**, here, represents an unprecedented example of an amine-borane sigma-complex exhibiting a similar barrier for the B–H and the N–H activation step (Scheme 5.9). An alternative mechanism for the H/D exchange in both BH_2 and NH_2 moieties of $[Ir(PCy_3)_2(H)_2(\eta^2-H_2BNH_2C_4H_8)][BAr^F_4]$ (**22**) would be a concerted and reversible N–H and B–H activation resulting in the formation of amino-borane (**D**) and the subsequent addition of D_2 to the amino-borane (Scheme 5.9). However, the observation of no free amino-borane or any other dehydrogenation product in the ^{11}B NMR spectrum argues against this. As deuterium is also incorporated into the PCy_3 ligand, we cannot discount more complicated mechanisms for H/D exchange that involve cyclometallated phosphine ligands. DFT calculations are required to put these mechanistic details on firmer footing.



Scheme 5.9 Activation of B−H and N−H bonds in **22**. $[BAr^F_4]^-$ anions are not shown.

5.3.3 Formation of $[Ir(PCy_3)_2(H)_2(\eta^2\text{-}H_2BNRMeC_4H_8)][BAr^F_4]$ (R = H, Me)

The addition of 2,2-H,Me-1,2-B,N-C_4H_{10} (**B**) to $[Ir(PCy_3)_2(H_2)_2(H)_2][BAr^F_4]$ (**II**) resulted in a relatively slow displacement of the dihydrogen ligands by the amine-borane **B** compared to that of **A**, which displaces hydrogen immediately. NMR spectroscopy after 90 minutes showed the formation of $[Ir(PCy_3)_2(H)_2(\eta^2\text{-}H_2BNHMeC_4H_8)][BAr^F_4]$ (**23**) and $[Ir(H_5)(PCy_3)_2]$[29] in a 20:1 ratio. Recrystallisation from C_6H_5F/pentane solution resulted in only a few crystals (the rest being an oil) which were sufficient for single crystal X-ray diffraction but not for elemental analysis. The solid–state structure of complex **23** is shown in Figure 5.6, which shows that the structure is very similar to that of **22** with the cyclic amine-borane adopting a chair-conformation. Unlike **22**, the BN–cyclohexane ligand in **23** is disordered, occupying four chemically identical, but crystallographically different sites with equal contributions. The Ir···B distance [2.230(4) Å] and the P1–Ir–P2 angle [155.13(3)] are within error the same as for **22**.

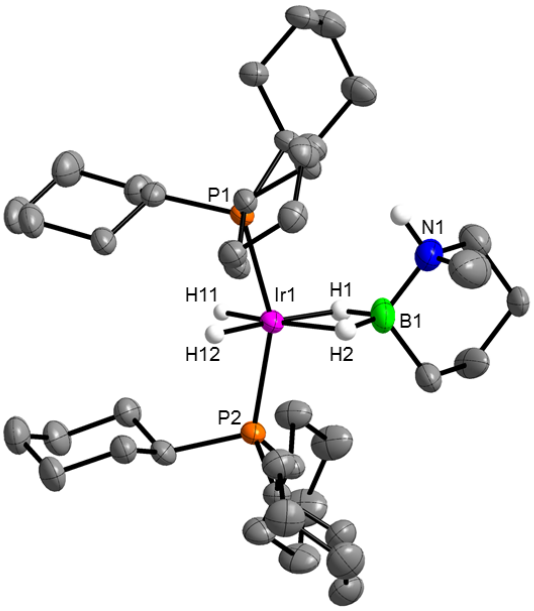
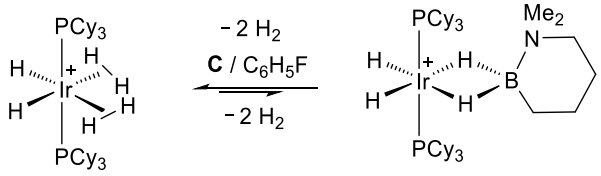


Figure 5.6 The solid–state structure of the cationic portion of complex **23**. Only one disordered component of the cyclic amine–borane ligand is shown. Displacement ellipsoids are shown at the 30% probability level. Selected bond lengths (Å) and angles (º): Ir1–B1, 2.230(4); Ir1–P1, 2.3269(7); Ir1–P2, 2.3266(7); B1–C1, 1.588(5); B1–N1, 1.566(6); P1–Ir1–P2, 155.13(3).

Despite isolating only a few crystals, NMR spectroscopy demonstrates that mainly **23** is formed in the bulk. In the ^{1}H NMR spectrum two broad signals are observed at δ –20.58 (1H) and –20.82 (1H) suggesting that Ir–*H* hydrides in **23** are spectroscopically inequivalent. This is due to the asymmetry enforced by the NMe moiety on the cyclic amine-borane that would not be removed by a low energy ring-flip. Similarly, the Ir–*H*–B signals are observed separately at δ –6.24 (br) and –6.35 (br), and a more complicated aliphatic region compared with **22** is noted, as all the methylene C–H groups are now distinct. The ^{11}B NMR spectrum shows a signal at δ 22.4, corresponding to the bound *B*H$_2$ moiety which is shifted downfield by 28.9 ppm from the free amine-borane **B**. As for **22,** two distinct phosphorus environments are observed in the ^{31}P{^{1}H} NMR spectrum, exhibiting *trans* P–P coupling [δ 36.5 (d, $^{2}J_{PP}$ = 276 Hz, 1P), 33.2 (d, $^{2}J_{PP}$ = 276 Hz, 1P)].

Addition of 2,2-Me$_2$-1,2-B,N-C$_4$H$_{10}$ (**C**) to a C$_6$H$_5$F solution of [Ir(PCy$_3$)$_2$(H$_2$)$_2$(H)$_2$][BAr$^{F}_4$] (**II**) resulted in a very slow displacement of the dihydrogen ligand, and NMR spectroscopy

showed the formation of $[Ir(PCy_3)_2(H)_2(\eta^2\text{-}H_2BNMe_2C_4H_8)][BAr^F{}_4]$ in less than 5% yield after one hour. The resonance corresponding to the B*H*$_2$ hydrides [δ –4.06 (br)] in the ^{1}H NMR spectrum is consistent with that observed for the well characterised complexes **22** and **23**. However, over time (8 h) decomposition to $[Ir(H)_5(PCy_3)_2]$[29] and $[\{Ir(PCy_3)_2\}_2(H)_2(\mu\text{-}H)_3][BAr^F{}_4]$[13] is observed by the ^{1}H and ^{31}P{^{1}H} NMR spectroscopy. The slow reactivity of **C** towards **II** suggests that an initial equilibrium is established between the starting complex $[Ir(PCy_3)_2(H_2)_2(H)_2][BAr^F{}_4]$ (**II**) and the corresponding amine-borane sigma-complex $[Ir(PCy_3)_2(H)_2(\eta^2\text{-}H_2BNMe_2C_4H_8)][BAr^F{}_4]$ which is in favour of the starting material **II** (Scheme 5.10). This could be due to the steric clash between the PCy_3 and the NMe_2 groups. This is similar to the previously reported analogous complex $[Ir(PCy_3)_2(H)_2(\eta^2\text{-}H_3B{\cdot}NMe_3)][BAr^F{}_4]$, that shows rapid exchange of the terminal and the bridging H−B bonds at room temperature. The fluxionality in $[Ir(PCy_3)_2(H)_2(\eta^2\text{-}H_3B{\cdot}NMe_3)][BAr^F{}_4]$ cannot be frozen at 190 K due to the steric clash between the PCy_3 and the NMe_3 group whereas the fluxionality in $[Ir(PCy_3)_2(H)_2(\eta^2\text{-}H_3B{\cdot}NMe_2H)][BAr^F{}_4]$ can be frozen out at 190 K.[13]



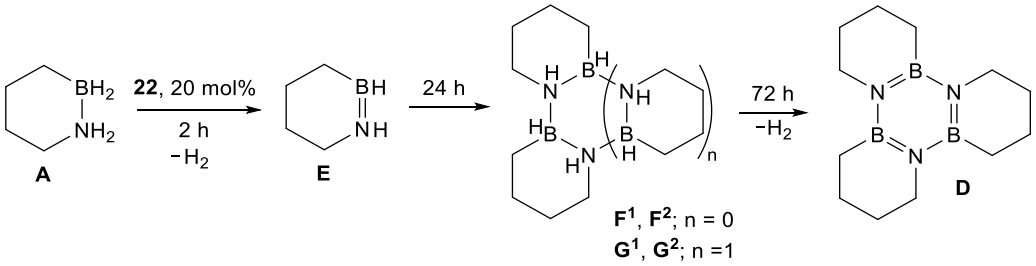
Scheme 5.10 Formation of $[Ir(PCy_3)_2(H)_2(\eta^2\text{-}H_2BNMe_2C_4H_8)][BAr^F{}_4]$; $[BAr^F{}_4]^-$ anions are not shown.

5.4 Catalytic dehydrogenation of A and B using Ir-BN complexes

5.4.1 Catalytic dehydrogenation of A using 22

$[Ir(PCy_3)_2(H)_2(\eta^2\text{-}H_2BNH_2C_4H_8)][BAr^F{}_4]$ (**22**) was found to be stable in 1,2-$F_2C_6H_4$ solution for at least 24 h as observed by NMR spectroscopy. However, addition of 5 equivalents of the cyclic amine-borane **A** to the complex **22** (i.e. 20 mol%) in a sealed NMR tube results in a slow (72 h, TOF ~0.07 h^{-1}) dehydrocoupling of **A** to form the tricyclic borazine $[BNC_4H_8]_3$ **D** [δ 34.5, s; lit. 34.8, s, C_6D_6].[23, 30] The dehydrocoupling experiment was

followed by ^{11}B NMR spectroscopy – the temporal plot shown in Figure 5.7 demonstrates that the amine-borane **A** first dehydrogenates to form a new monomeric amino-borane $HBNHC_4H_8$ (**E**). **E** has been tentatively characterised by ^{11}B NMR spectroscopy by a characteristic resonance at δ 41.1 (d, $^1J_{BH}$ 124 Hz) that is consistent with other transient amino-boranes such as $^iPr_2N{=}BHMe$ that show a doublet at δ 39.2 ($^1J_{BH}$ = 119 Hz) in the ^{11}B NMR spectrum,[13, 31-33] as well as stable $HBNMeC_4H_8$, **H** (*vide infra*, δ 40.8 [$^1J_{BH}$ = 125 Hz]). After 24 h the signal arising from **E** is completely consumed, with **D** now observed as a significant product. The ^{11}B NMR spectrum at this stage also shows broad peaks centred around δ –5 which show $^1J_{BH}$ coupling (~110 Hz). Over a further 48 h (72 h in total) these signals get completely converted to **D**. The temporal behaviour of the species suggest that these signals are due to intermediates that follow **E** and precede **D** (Scheme 5.11). Due to the transient and structurally similar nature of these intermediates, we have not been able to employ NMR spectroscopy and ESI-MS for their full characterisation. Using DFT geometry optimization coupled with GIAO ^{11}B chemical shift calculations, Tanya Mikulas and Prof. David Dixon (The University of Alabama) have computed the ^{11}B NMR chemical shifts of likely intermediates as shown in Table 5.2. Based on these calculations we suggest that the broad signals centred around δ –5 could be due to the cyclic diborazanes (F^1 and F^2) and triborazanes (G^1 and G^2). Partially dehydrogenated trimers would be expected to show an additional signal at ca. δ 37 which could get obscured by the broad signal (~ δ 34) arising due to the cyclic triborazine **D**. ^{1}H and ^{31}P{^{1}H} NMR spectroscopy show that the final organometallic product is the pentahydride complex $Ir(PCy_3)_2H_5$.[29]



Scheme 5.11 Dehydrocoupling of **A** catalysed by **22**.

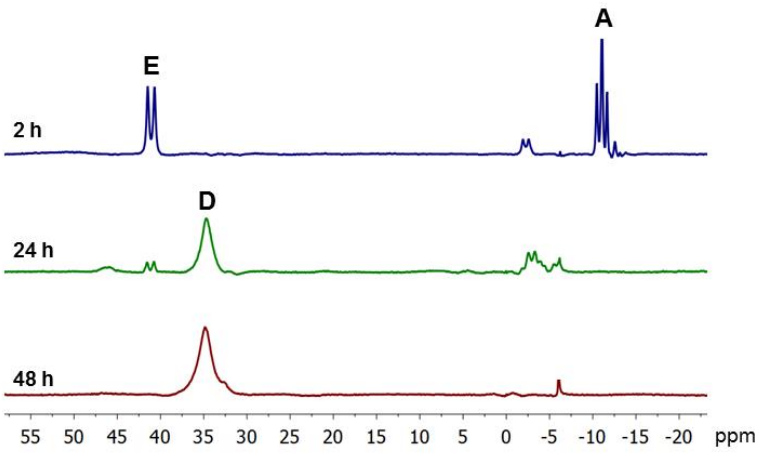
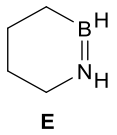
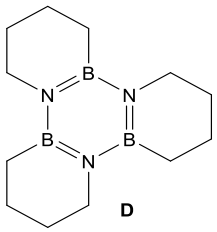
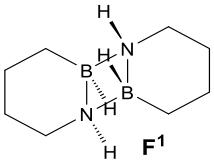
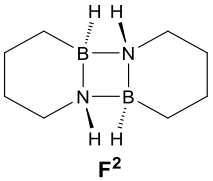
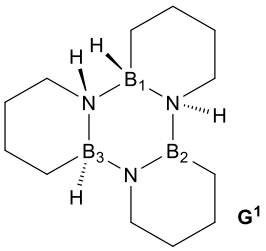
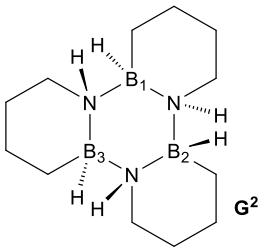


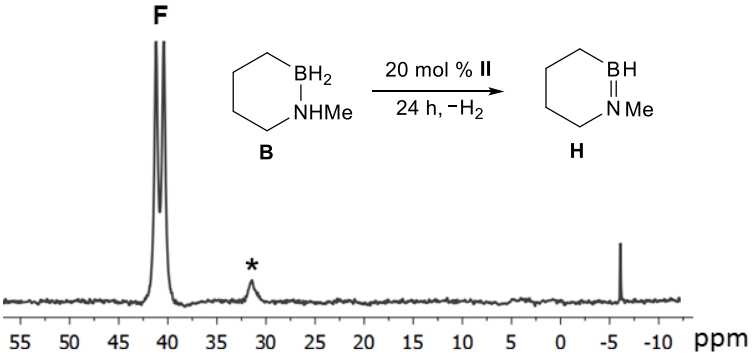
Figure 5.7 Temporal ^{11}B NMR spectra for the dehydrocoupling of **A** catalysed by **22**.

Table 5.2 Calculated ^{11}B NMR chemical shifts in ppm of representative dimers and trimers (σ = standard ($BF_3{\cdot}OEt_2$) – molecule).

Molecule	σ / ppm	Molecule	σ / ppm
 **E**	+38.4 [exp. +41.1]	 **D**	+31.9 [exp. 34.5]
 **F¹**	–9.3	 **F²**	–2.2
 **G¹**	–10.7 (B1) +34.3 (B2) –9.1 (B3)	 **G²**	–11.0 (B1) –9.3 (B2) –5.6 (B3)

5.4.2 Catalytic dehydrogenation of B using $[Ir(PCy_3)_2(H_2)_2(H)_2][BAr^F_4]$ (II)

Addition of a 1,2-$F_2C_6H_4$ solution of **II** (as a precursor to **23**) to 5 equivalents of 2,2-H,Me-1,2-B,N-C_4H_{10} (**B**, ~0.08 M) in a sealed NMR tube resulted in the complete dehydrogenation of **B** to form the cyclic amino-borane $HBNMeC_4H_8$ **H** in 24 h (TOF ~ 0.2 h^{-1}, Scheme 5.12). ^1H and $^{31}P\{^1H\}$ NMR spectroscopy showed the presence of **23** and $Ir(PCy_3)_2H_5$[29] at the end of dehydrogenation in a 0.6:1 ratio respectively. $HBNMeC_4H_8$ (**H**) was first reported by Wille and Goubeau,[30] and also independently synthesised by the Liu group via intramolecular hydroboration of the *N*-methylhomoallylamine-borane adduct and subsequent one-pot thermal dehydrogenation.[34] **H** does not undergo any B−N coupling reaction to give linear or cyclic dimer and is found to be stable in the solution, as evidenced by a characteristic downfield chemical shift in the ^{11}B NMR spectrum δ 40.8 [$^1J_{BH}$ = 125 Hz], similar to **E**. This is consistent with sterically bulky amino-boranes such as $H_2B{=}N^iPr_2$[35] or $PhHB{=}NMe_2$ (see Chapter 4) which do not cyclise or polymerise under thermal or catalytic conditions.



Scheme 5.12 Dehydrogenation of **B** catalysed by **II.** ^{11}B NMR spectrum after 24 h. * Assigned to trace 1-OH-2-Me-1,2-B,N-C_4H_8[30] (confirmed by EI-MS). The signal at δ –6.1 is assigned to the residual $[BAr^F_4]^-$.

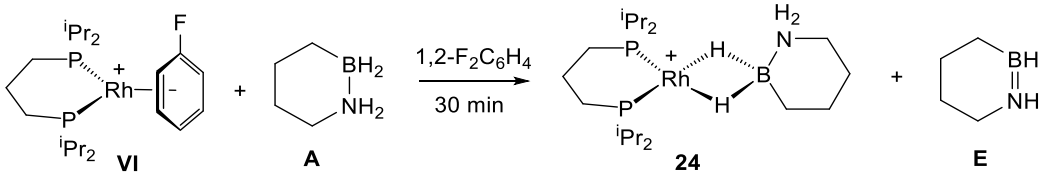
5.5 Reactivity of the cyclic amine-boranes A-C with VI

The reactivity of the cyclic amine-boranes **A**-**C** with the $\{Ir(PCy_3)_2(H)_2\}^+$ fragment has been discussed above. Under catalytic conditions, **A** dehydrocouples to yield the cyclic trimer **D** while **B** dehydrogenates to form the amino-borane **H**. However, $[Ir(PCy_3)_2(H_2)_2(H)_2][BAr^F_4]$

(**II**) has been found to be a poor catalyst giving a TOF of ~0.07 h^{-1} for the dehydrocoupling of **A** and 0.2 h^{-1} for the dehydrogenation of **B**. In order to expand the coordination chemistry of these cyclic amine-boranes and develop the catalysis, we explored the reactivity of **A**-**C** with the $\{Rh(^{i}Pr_2P(CH_2)_3P^{i}Pr_2)\}^{+}$ fragment.

5.5.1 Formation of $[Rh(^{i}Pr_2P(CH_2)_3P^{i}Pr_2)(\eta^2\text{-}H_2BNH_2C_4H_8)][BAr^F{}_4]$ (24)

Addition of two equivalents of 2,2-H_2-1,2-B,N-C_4H_{10} (**A**) to the 1,2-$F_2C_6H_4$ solution of $[Rh(^{i}Pr_2P(CH_2)_3P^{i}Pr_2)(C_6H_5F)][BAr^F{}_4]$ (**VI**) completely displaces the fluorobenzene ligand to form $[Rh(^{i}Pr_2P(CH_2)_3P^{i}Pr_2)(\eta^2\text{-}H_2BNH_2C_4H_8)][BAr^F{}_4]$ (**24**) and the corresponding amino-borane $HBNHC_4H_8$ (**E**) after 30 minutes (Scheme 5.13).



Scheme 5.13 Reactivity of **A** with **VI**; $[BAr^F{}_4]^-$ anions are not shown.

At the beginning of this reaction, the signals due to the amine-borane **A** and the sigma-complex **24** are too broad to be observed in the ^{1}H and ^{11}B NMR spectra, but the $^{31}P\{^{1}H\}$ NMR spectrum is well resolved. This suggests that there is a rapid exchange between the bound and the free amine-borane. This is further confirmed after 30 minutes when all of the amine-boranes is consumed and the opportunity for exchange is reduced, at which point the sigma-complex **24** displays a characteristic broad signal at δ 29.3 in the ^{11}B NMR spectrum. The ^{1}H NMR spectrum also displays a broad signal at δ –4.83 (relative integral of 2H) corresponding to the Rh–*H*–B groups. Broad overlapping multiplets in the ^{1}H NMR spectrum [δ 1.23-1.16] are observed corresponding to the two distinct sets of CH_3 resonances of the isopropyl groups. $^{31}P\{^{1}H\}$ NMR spectroscopy shows equivalent phosphorus environment as observed by a doublet at δ 57.1 ($^{1}J_{RhP}$ = 160 Hz). We suggest that the ring flipping of the BN-cyclohexane moiety provides a time averaged mirror plane

which makes both the BH_2 hydrides and the phosphine ligands equivalent. Diffusion of pentane to the reaction mixture at –35°C afforded the red crystals of **24** which were mechanically separated from the co-crystallized orange crystals of **VI**. Figure 5.8 shows the solid-state structure of the cationic portion of **24** which confirms its formulation. The Rh···B 2.155(5) and B–N 1.588(6) Å distances are similar to that in closely related complex [Rh(^{i}Pr$_2$P(CH$_2$)$_3$P^{i}Pr$_2$)(η^2-H$_3$B·NMe$_3$)][BAr$^F{}_4$], 2.283(9) and 1.535(5) Å, respectively.[36] The cyclic amine-borane adopts a chair conformation in **24** similar to that of the iridium sigma-complexes **22** and **23**.

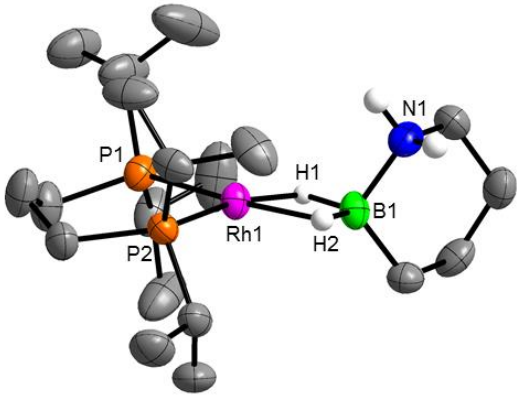


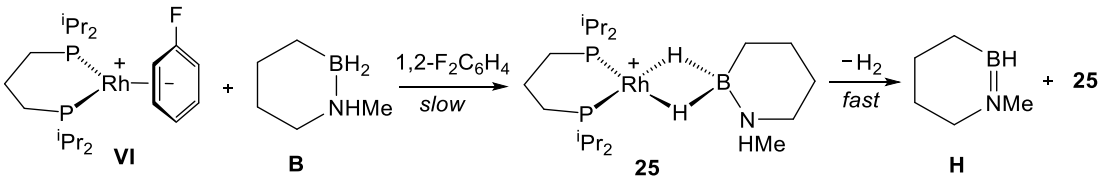
Figure 5.8 Solid-state structure of the cationic portion of complex **24**. Only hydrogen atoms associated with the Rh···HB interaction are shown. Displacement ellipsoids are shown at the 50% probability level. Selected bond lengths and angles: Rh1–B1, 2.155(5); Rh1–P1, 2.2174(12); Rh1–P2, 2.2170(12); B1–N1, 1.588(6); P1–Rh1–P2, 93.52(5).

Over 8 h, the amino-borane **E** formed from the reaction of **VI** and **A** (Scheme 5.13) dehydrocouples to form the cyclic triborazine **D**. ^{31}P{^{1}H} NMR spectroscopy, at the end of dehydrocoupling, showed a mixture of organometallic species consisting of **24** (44%), **VI** (18%), [{Rh(P^{i}Pr$_2$(CH$_2$)$_3$P^{i}Pr$_2$)}$_2$(H)$_2$(μ-H)$_3$][BAr$^F{}_4$], *vide infra* (18%) and an uncharacterised complex (20%).

5.5.2 Formation of [Rh(^{i}Pr$_2$P(CH$_2$)$_3$P^{i}Pr$_2$)(η^2-H$_2$BNHMeC$_4$H$_8$)][BAr$^F{}_4$] (25)

Similar to the formation of **24**, addition of two equivalents of the cyclic amine-borane 2,2-HMe-1,2-B,N-C$_4$H$_{10}$ (**B**) to [Rh(^{i}Pr$_2$P(CH$_2$)$_3$P^{i}Pr$_2$)(η^6-C$_6$H$_5$F)][BAr$^F{}_4$] (**VI**) in 1,2-F$_2$C$_6$H$_4$

solvent resulted in the formation of a new complex [Rh(^{i}Pr$_2$P(CH$_2$)$_3$P^{i}Pr$_2$)(η^2-H$_2$BNHMeC$_4$H$_8$)][BAr$^F_4$] (**25**), alongside unreacted **VI** and **B**, and the amino-borane HBNMeC$_4$H$_8$ (**H**) in 5 minutes. The observation of both the starting material **VI** and the amino-borane **H**, under conditions of excess **B**, suggests that the initial substitution of the fluorobenzene ligand is slower than the dehydrogenation of the amine-borane. ^{11}B NMR spectroscopy after 8 h showed the complete conversion of **VI** and **B** to the sigma-complex **25** and the amino-borane **H**, but did not show any further cyclisation or the oligomerisation of **H** even when the reaction mixture was left for longer (18 h, Scheme 5.14, Figure 5.9). Formation of a small amount of the dimer [{Rh(P^{i}Pr$_2$(CH$_2$)$_3$P^{i}Pr$_2$)}$_2$(H)$_2$(*μ*-H)$_3$][BAr$^F_4$] (*vide infra*) was also observed in ~5% yield by ^{31}P{^{1}H} and ^{1}H NMR spectroscopy.



Scheme 5.14 Reactivity of **VI** with **B**; [BAr$^F_4$]$^-$ anions are not shown.

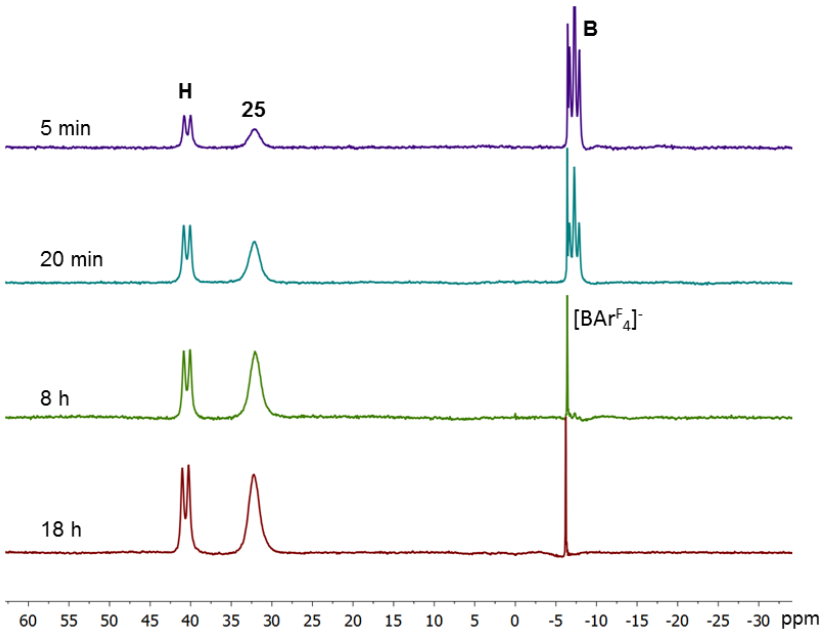
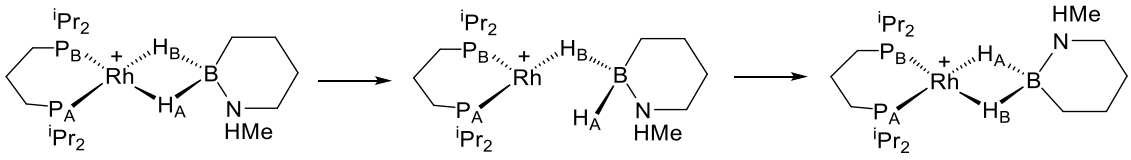


Figure 5.9 ^{11}B NMR spectra showing the temporal evolution of the dehydrogenation of **B** (2 equivalents) by **VI** to form [Rh(^{i}Pr$_2$P(CH$_2$)$_3$P^{i}Pr$_2$)(η^2-H$_2$BNHMeC$_4$H$_8$)][BAr$^F_4$], **25**, and amino–borane **F**. [BAr$^F_4$]$^-$ anions are not shown.

Recrystallisation of the reaction mixture from 1,2-$F_2C_6H_4$ / pentane at −35ºC allowed the isolation of complex **25** as an analytically pure red solid in 40% yield. Complex **25** was characterised by NMR spectroscopy, ESI-MS, elemental analysis and single crystal X-ray diffraction. The ^{1}H NMR spectrum of complex **25** displays two distinct broad signals at δ –4.9 and δ –5.4 which are assigned to the Rh–H–B groups suggesting that both of the *H*–B hydrides are inequivalent, presumably due to the asymmetry enforced by the NMe group that would not be removed by a low energy ring flip. The aliphatic region of the ^{1}H NMR spectrum shows more complex signals compared to that of **24** due to the inequivalent C*H* protons of the cyclic amine-borane fragment and the inequivalent CH_3 groups of the isopropyl substituents (see Chapter 6 for the spectral details). The ^{31}P{^{1}H} NMR spectrum at room temperature displays only one doublet at δ 57.9 ($^1J_{RhP}$ = 162 Hz), but on cooling to 190 K splits into two doublet of doublets at δ 57.8 and δ 56.9 ($^2J_{PP}$ = 56 Hz and $^1J_{RhP}$ = 160 Hz). These NMR spectra suggest that the amine-borane is undergoing a fluxional process. A mechanism that involves a change of amine-borane binding from η^2 to η^1 mode and then rotation around the Rh–H bond would make both the phosphorus atoms equivalent but the hydrides would still be inequivalent (Scheme 5.15).[22] The ^{11}B NMR spectrum displays a broad signal at δ 32.1, shifted downfield from free cyclic amine-borane **B** by 38.6 ppm, consistent with a bidentate binding mode of the amine–borane at a Rh(I) center.[37]



Scheme 5.15 Suggested fluxional process for [Rh(^{i}Pr$_2$P(CH$_2$)$_3$P^{i}Pr$_2$)(η^2-H$_2$BNHMeC$_4$H$_8$)][BAr$^F_4$] (**25**). [BAr$^F_4$]$^-$ anions are not shown.

Figure 5.10 shows the solid-state structure of the cationic portion of complex **25** demonstrating the formation of an η^2-amine-borane sigma-complex through two Rh–H–B interactions at a pseudo square planar Rh(I) centre. The cyclic amine-borane moiety was

found to be equally disordered over two positions, which was modelled as either the NMe pointing axial or equatorial with respect to the RhP_2 plane. The Rh···B [2.150(6) Å] and B−N [1.518(8) Å] distances are similar to that of the complex **23** and are consistent with a rhodium η^2-sigma-amine-borane complex.[25, 38, 39]

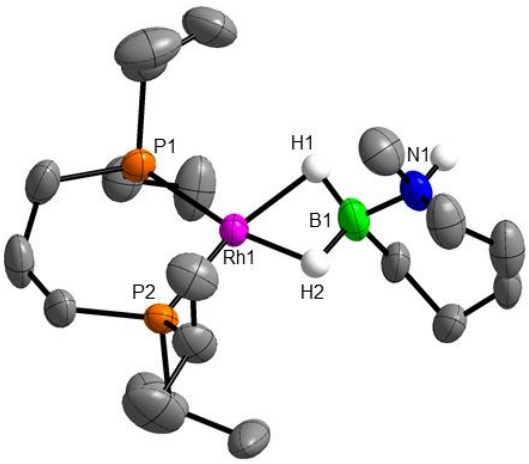


Figure 5.10 Solid-state structure of the cationic portion of complex **25**. Only hydrogen atoms associated with the NH and Rh···HB interaction are shown, and only one disordered component of the cyclic amine-borane ligand is shown. Displacement ellipsoids are shown at the 50% probability level. Selected bond lengths (Å) and angles (º): Rh1–B1, 2.150(6); Rh1–P1, 2.2167(12); Rh1–P2, 2.2030(12); B1–N1, 1.518(8); P1–Rh1–P2, 92.95(5).

5.5.3 Formation of $[Rh(^iPr_2P(CH_2)_3P^iPr_2)(\eta^2\text{-}H_2BNMe_2C_4H_8)][BAr^F{}_4]$ (26)

Addition of the cyclic amine-borane 2,2-Me_2-1,2-B,N-C_4H_{10} (**C**) to $[Rh(^iPr_2P(CH_2)_3P^iPr_2)(\eta^6\text{-}C_6H_5F)][BAr^F{}_4]$ (**VI**) in 1,2-$F_2C_6H_4$ solvent resulted in a slow (24 h) substitution of the fluorobenzene ligand and the formation of $[Rh(^iPr_2P(CH_2)_3P^iPr_2)(\eta^2\text{-}H_2BNMe_2C_4H_8)][BAr^F{}_4]$ (**26**) as monitored by NMR spectroscopy. Complex **26** was isolated by recrystallization from 1,2-$F_2C_6H_4$/pentane solution and characterised by NMR spectroscopy, ESI-MS, elemental analysis and single crystal X-ray diffraction, and shows very similar data to that of **24** and **25**. The ^{1}H NMR spectrum shows a singlet at δ 2.85 (6 H) assigned to the N*Me*$_2$ hydrogens. A single Rh–*H*–B environment at δ –5.17 was also observed in the ^{1}H NMR spectrum. Broad overlapping signals centred at δ 1.23 were observed corresponding to the C*H*$_3$ resonances of the isopropyl groups. The ^{31}P{^{1}H} NMR spectrum showed a

doublet at δ 58.0 ($^1J_{RhP}$ = 163 Hz) suggestive of equivalent phosphorus environments similar to that of [Rh(^{i}Pr$_2$P(CH$_2$)$_3$P^{i}Pr$_2$)(η^2-H$_2$BNH$_2$C$_4$H$_8$)][BAr$^F{}_4$] (**24**) and [Rh(^{i}Pr$_2$P(CH$_2$)$_3$P^{i}Pr$_2$)(η^2-H$_2$BNHMeC$_4$H$_8$)][BAr$^F{}_4$] (**25**). We suggest that the ring flipping of the BN-cyclohexane moiety provides a time averaged mirror plane which makes both the B*H$_2$* hydrides and the phosphine ligands equivalent. The ^{11}B NMR spectrum shows a downfield shifted signal at δ 34.4 characteristic to the bound amine-borane fragment similar to **24** (δ 29.3) and **25** (δ 32.1). Figure 5.11 shows the solid state structure of the cationic portion of **26** which depicts that the cyclic amine-borane is coordinated to a pseudo-square planar Rh(I) center in a bidentate mode. The Rh···B bond distance 2.172(3) Å is essentially the same as that of complex **24**, 2.155(5) Å and **25**, 2.150(6) Å within experimental error.

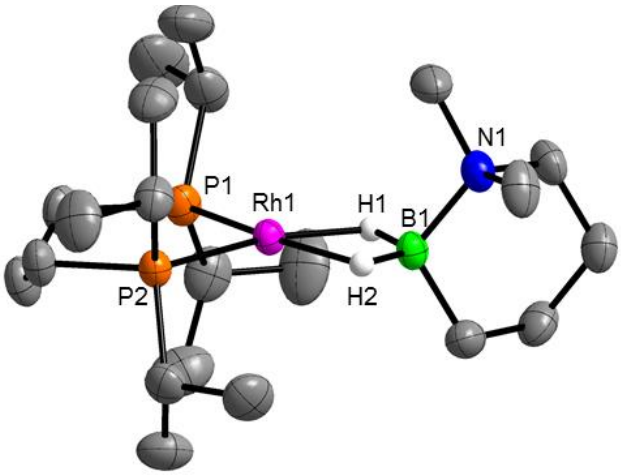


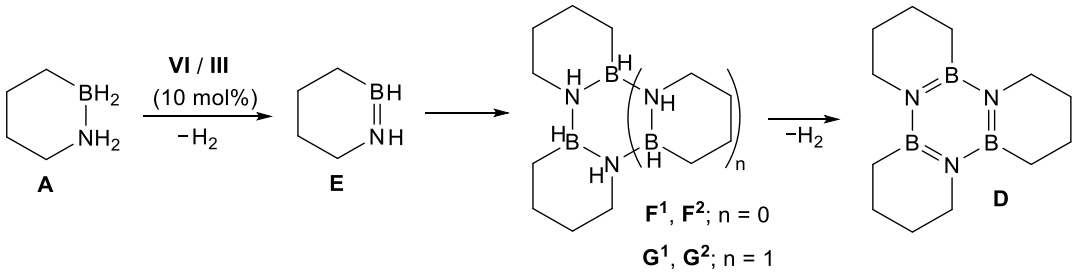
Figure 5.11 Solid–state structures of the cationic portion of **26**. Only hydrogen atoms associated with the Rh···HB interaction are shown. Displacement ellipsoids are shown at the 50% probability level. Selected bond lengths (Å) and angles (º): Rh1–B1, 2.172(3); Rh1–P1, 2.2204(8); Rh1–P2, 2.2182(8); B1–N, 1.599(4); P1–Rh1–P2, 94.14(3).

5.6 Catalytic dehydrogenation of A and B using VI and III

5.6.1 Catalytic dehydrocoupling of A using VI and III

A 10 mol% catalytic loading of [Rh(^{i}Pr$_2$P(CH$_2$)$_3$P^{i}Pr$_2$)(η^6-C$_6$H$_5$F)][BAr$^F{}_4$] (**VI**) (1,2-F$_2$C$_6$H$_4$, sealed NMR tube) resulted in the slow dehydrocoupling (4 days, TOF ~ 0.1 h^{-1}) of **A** to ultimately form the cyclic triborazine (**D**). Following the reaction using ^{11}B NMR

spectroscopy showed that amine-borane **A**, first, undergoes rapid dehydrogenation to afford the amino-borane **E** in two minutes. **E** then proceeds to form the cyclic diborazanes (F^1 and F^2) or triborazanes (G^1 and G^2, Table 5.2) as observed by the overlapping resonances centred on δ −5 exhibiting $^1J_{BH}$ coupling of ~110Hz. These signals slowly (over four days) disappears to form the cyclic triborazine **D** (Scheme 5.16, Figure 5.12).



Scheme 5.16 Dehydrocoupling of **A** catalysed by **VI** (10 mol%). See table 5.2 for the structures of F^1, F^2, G^1 and G^2.

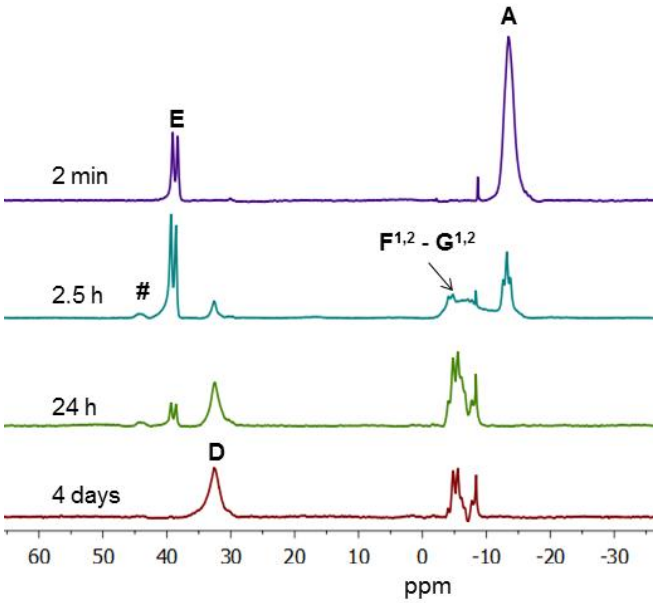


Figure 5.12 ^{11}B NMR spectra showing the temporal evolution of the dehydrocoupling of **A** catalysed by **VI** (10 mol%). # is an uncharacterised B–N product. The signal at δ –6.1 is assigned to the residual $[BAr^F{}_4]^-$.

As **VI** is a poor catalyst for the dehydrocoupling of **A**, we moved towards using the analogous complex $[Rh(Ph_2P(CH_2)_3PPh_2)(\eta^6\text{-}C_6H_5F)][BAr^F{}_4]$ (**III**), which has been previously shown to be a relatively fast catalyst for the dehydrocoupling of $H_3B{\cdot}NMe_2H$

(1250 h^{-1}).[39] A 10 mol% catalytic loading of **III** (sealed NMR tube), resulted in the complete dehydrocoupling of **A** (0.08 M) in 15 h with a TOF of ~0.7 h^{-1}, which is approximately seven times faster than that of **VI**. The ^{11}B NMR spectroscopy showed the formation of the similar intermediates as those observed for **VI** (Scheme 5.16, Figure 5.13).

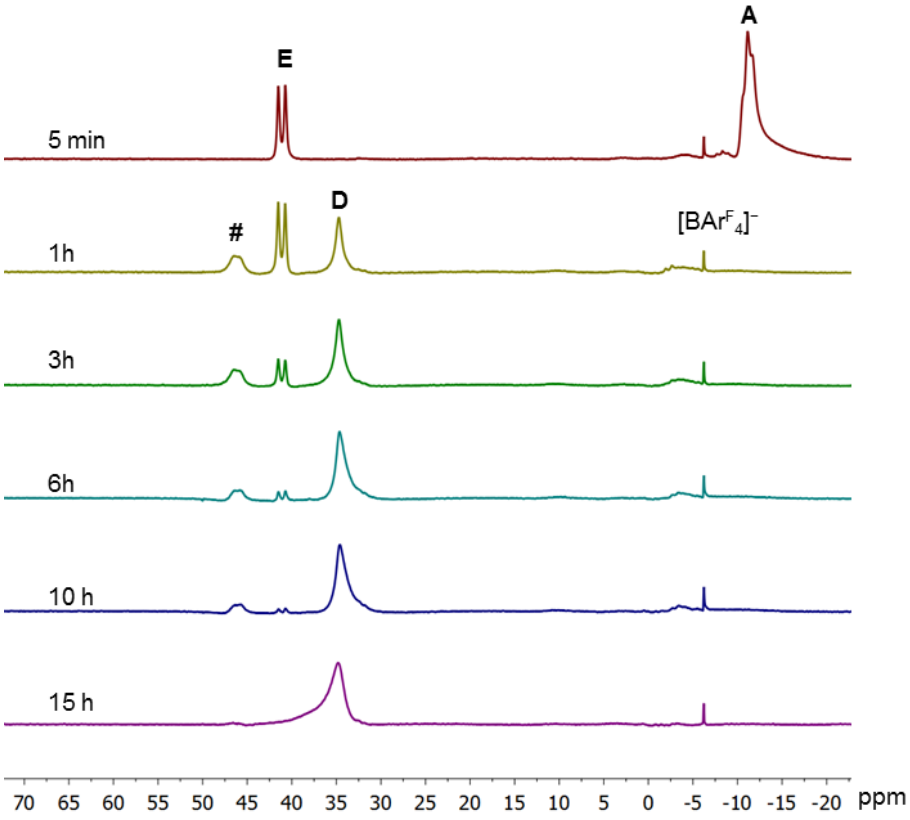
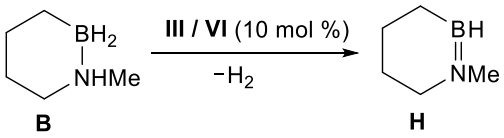


Figure 5.13 ^{11}B NMR spectra showing the temporal evolution of the dehydrocoupling of **A** catalysed by by **VI** (10 mol%). # is an uncharacterised B–N product.

Catalytic dehydrocoupling (10 mol% **III**, 0.26 M **A**) in an open system using gas-burette method to follow the reaction resulted in the evolution of 1.8 equivalents of hydrogen gas in ~80 minutes (TOF = ~7 h^{-1}). The ^{11}B NMR spectrum of the reaction mixture at the end of dehydrocoupling showed the presence of the cyclic triborazine **D**, however formation of 1-OH-2-H-1,2-B,N-C_4H_8[30] (δ ~31, confirmed by EI–MS) in less than 10% yield was also observed which possibly occurs through the reaction of the amino-borane **E** with any trace of oxygen or water present in the system.

5.6.2 Catalytic dehydrogenation of B using III and VI

The catalytic dehydrogenation of **B** was carried out in a sealed NMR tube using 10 mol% $[Rh(PPh_2(CH_2)_3PPh_2)(C_6H_5F)][BAr^F{}_4]$ (**III**) and monitored by ^{11}B NMR spectroscopy. The complete conversion of the cyclic amine-borane **B** (initial concentration: 0.08 M) to the amino-borane **H** (Scheme 5.17) was obtained in 3 h (TOF ~3 h^{-1}), and thus is a much faster catalyst than iridium complex $[Ir(PCy_3)_2(H_2)_2(H)_2][BAr^F{}_4]$ (**II**), which gives a TOF of 0.2 h^{-1} under identical catalytic conditions.



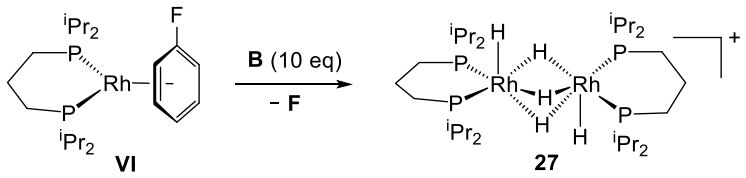
Scheme 5.17 Catalytic dehydrogenation of **B** to form **F** using 10 mol% **III** or **VI**.

However, when $[Rh(P^iPr_2(CH_2)_3P^iPr_2)(C_6H_5F)][BAr^F{}_4]$ (**VI**) was used under the same catalytic conditions, the dehydrogenation was found to be slower than that with catalyst **III** but still faster than the iridium catalyst **II**. Under the catalytic conditions of 10 mol% **VI** and 0.08 M **B**, complete conversion of **B** to **H** was obtained in 17 h giving a TOF of 0.6 h^{-1}. The dehydrogenation process was monitored using ^{11}B and $^{31}P\{^1H\}$ NMR spectroscopy. $[Rh(P^iPr_2(CH_2)_3P^iPr_2)(C_6H_5F)][BAr^F{}_4]$ (**VI**) was found to be completely consumed in less than 45 minutes leading to the formation of the sigma-complex $[Rh(^iPr_2P(CH_2)_3P^iPr_2)(\eta^2\text{–}H_2BNHMeC_4H_8)][BAr^F{}_4]$ (**25**) and a Rh (III) dimer, $[\{Rh(P^iPr_2(CH_2)_3P^iPr_2)\}_2(H)_2(\mu\text{-}H)_3][BAr^F{}_4]$ (*vide infra*, **27**) in an approximately equal concentration. Over time during the dehydrogenation process, the concentration of the dimer (**27**) increases (80% after 8 h and 90% after 17 h) suggesting that the dimer formation is promoted by the dehydrogenation of amine-boranes.

5.7 Mechanistic investigation for the dehydrogenation of B catalysed by VI

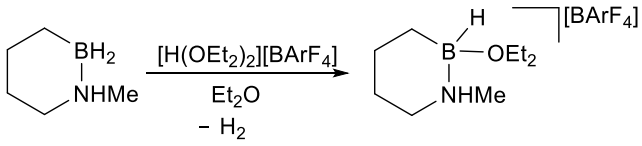
5.7.1 Formation of [{Rh(P^{i}Pr$_2$(CH$_2$)$_3$P^{i}Pr$_2$)}$_2$(H)$_2$(μ-H)$_3$][BAr$^F_4$] (27)

As discussed in Section 5.6.2, the formation of the dimer [{Rh(P^{i}Pr$_2$(CH$_2$)$_3$P^{i}Pr$_2$)}$_2$(H)$_2$(μ-H)$_3$][BAr$^F_4$] (**27**) is observed at the end of the dehydrogenation of **B** catalyzed by [Rh(P^{i}Pr$_2$(CH$_2$)$_3$P^{i}Pr$_2$)(C$_6$H$_5$F)][BAr$^F_4$] (**VI**, Scheme 5.18).



Scheme 5.18 Formation of **27** from the catalytic dehydrogenation of **B**. [BAr$^F_4$]$^-$ anions are not shown.

We speculate that the formation of **27** is accompanied by the formation of either [H(S)][BAr$^F_4$] or the cyclic amine-boronium cation [(S)BHNHMe(CH$_2$)$_4$)][BAr$^F_4$] [(S) = Solvent], so that the cation-anion ratio remains balanced in the reaction. To test this hypothesis, the cyclic amine-boronium cation [(Et$_2$O)BHNHMe(CH$_2$)$_4$)][BAr$^F_4$] was *in situ* synthesised by the addition of the Brookhart's acid [H(OEt$_2$)$_2$][BAr$^F_4$][40] to **B** (Scheme 5.19) using a similar strategy as described by Baker for the synthesis of ammonia-boronium cation [BH$_2$(NH$_3$)(OEt$_2$)][BAr$^F_4$].[41]

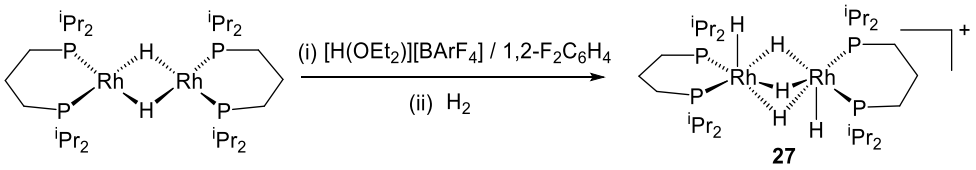


Scheme 5.19 Synthesis of the cyclic amine-boronium cation [(Et$_2$O)BHNHMe(CH$_2$)$_4$)][BAr$^F_4$].

The *in situ* prepared [(Et$_2$O)BHNHMe(CH$_2$)$_4$)][BAr$^F_4$] showed a signal at δ 10.7 (d, $^1J_{BH}$ = 121 Hz) in the ^{11}B NMR spectrum. Monitoring the catalytic dehydrogenation of **B** using ^{11}B NMR spectroscopy in either 1,2-F$_2$C$_6$H$_4$ or Et$_2$O solvent did not show the presence of the cyclic amine-boronium cation [(CH$_2$)$_4$BH(OEt$_2$)NHMe)][BAr$^F_4$]. [H(S)][BAr$^F_4$], therefore

remains the only sensible choice.

In order to put **27** on a firm structural footing it was independently synthesised. Reaction of $[H(OEt_2)_2][BAr^F{}_4]$[40] with Fryzuk's dinuclear neutral complex $[Rh(^iPr_2P(CH_2)_3P^iPr_2)(\mu\text{–}H)]_2$[42] under an atmosphere of H_2 resulted in the formation of complex **27** in 70% yield (Scheme 5.20). This is similar to the reaction of the rhodium dimer $[\{Rh(P^iPr_2(CH_2)_3P^iPr_2)\}_2(\mu\text{-}H)(\mu\text{-}BH_2NH_2)][BAr^F{}_4]$ (**9**) with hydrogen that results in the formation of $[\{Rh(P^iPr_2(CH_2)_3P^iPr_2)\}_2(H)_2(\mu\text{-}H)_3][BAr^F{}_4]$ (**27**) as discussed in Chapter 3.



Scheme 5.20 Synthesis of complex **27**, $[BAr^F{}_4]^-$ anion is not shown.

The ^{1}H NMR spectrum (at 298 K) of isolated **27** shows a broad signal at δ −8.25 (3H) corresponding to the bridging Rh−*H* hydrides. On cooling to 250 K, this signal splits into two different resonances at δ −7.91 (br, 2H) and δ −9.52 (br, 1H), suggesting a rapid exchange between the bridging Rh−*H* hydrides at room temperature. The terminal hydrides resonate further upfield at δ −18.71 (br, 2H) and remain equivalent even at low temperature (250 K). This is similar to the cationic rhodium dimer $[\{Rh(PCy_2(CH_2)_2PCy_2)\}_2(H)_2(\mu\text{-}H)_3][BF_4]$ previously reported by Heller that shows two inequivalent sets of bridging hydrides at 183 K resonating at δ −7.80 (2H) and −8.50 (1H) with the signal at δ −7.80 (2H) assigned to the bridging hydrides located trans to the phosphorus atoms.[43] The terminal hydrides were found to be equivalent at room temperature and also at low temperature (183 K) resonating at δ −17.90 (2H). The $^{31}P\{^1H\}$ NMR spectrum of **27** displays two broad signals at δ 66.5 and 62.2 which sharpen to the two broad doublets at δ 66.4 ($^1J_{RhP}$ = 100 Hz) and δ 60.0 ($^1J_{RhP}$ = 100 Hz) showing that there are two different phosphorus environments. Crystals suitable for single crystal X-ray diffraction were obtained by layering the 1,2-$F_2C_6H_4$ solution of **27** with pentane and

storing the solution at –18ºC for 24 h. However, due to poor crystal quality and significant structural disorder, the structure obtained is only suitable for showing connectivity and discussion of the precise bond lengths and angles would be inappropriate. Figure 5.14B represents the gross structure of the cationic portion of **27** which shows a rhodium dimer consisting of two $\{Rh(^{i}Pr_2P(CH_2)_3P^{i}Pr_2\}^+$ fragments twisted with respect to each other by ~67º similar to that observed for the dimer $[\{Rh(P^{i}Pr_2(CH_2)_3P^{i}Pr_2)\}_2(\mu\text{-}H)(\mu\text{-}BH_2NH_2)][BAr^F{}_4]$ (**9**) as discussed in Chapter 3. Due to the disordered rhodium atoms we are unable to comment upon the Rh−Rh distance. However, the presence of the three bridging and the two terminal hydrides as detected by the ^{1}H NMR spectroscopy results in the two 18 electron rhodium centers (Figure 5.14A), suggesting that a formal Rh−Rh bond is not required. Complex **27** is similar to the previously reported $[Rh_2(\text{bis-phosphine})_2H_5]^+$ cations such as $[\{Rh(PCy_2(CH_2)_2PCy_2)\}_2(H)_2(\mu\text{-}H)_3][BF_4]$ that are formed by the hydrogenation of $[Rh(\text{bis–phosphine})]^+$ precursors such as $[Rh(PCy_2(CH_2)_2PCy_2)(COD)][BF_4]$, via dimerization/deprotonation steps.[44-46]

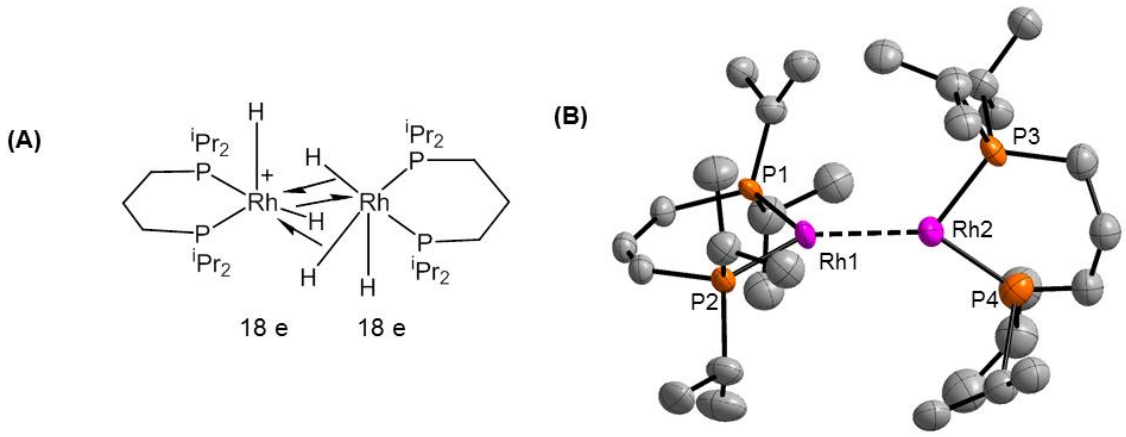
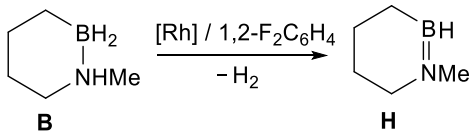


Figure 5.14 (A) Valence bond electron counting model for the dimer **27**. $[BAr^F{}_4]^-$ anion is not shown. **(B)** Solid-state structure of the cationic portion of the complex **27** showing connectivity of the non-hydrogen atoms. Only one of the disordered components (rhodium atoms, isopropyl groups and the C−C backbone of the chelating bis-phosphine ligands) are shown. Displacement ellipsoids are shown at the 30% probability level. Approximate bond lengths (Å) and angles (º): Rh1–P1, 2.324(5); Rh1–P2, 2.20(2); Rh2–P3, 2.388(13); Rh2–P4, 2.269(13); P1–Rh1–P2, 95.3(5); P3–Rh2–P4, 93.7(4); ∠plane(Rh1P1P2)/plane(Rh2P3P4), ~67.

5.7.2 Catalytic dehydrogenation of B using monomeric 25 and dimeric 27

As the monomeric sigma-complex (**25**) and the dimer (**27**) were both observed during the dehydrogenation of **B** catalysed by [Rh($P^iPr_2(CH_2)_3P^iPr_2$)(C_6H_5F)][BAr^F_4] (**VI**), in order to investigate the nature of the active catalyst in terms of the dimer or the monomer, we carried out the catalytic dehydrogenation of **B** using complexes **25** and **27** independently. We were unable to monitor the dehydrogenation rate in an open system due to the partial decomposition of the amino-borane on sampling.[9] Dehydrogenation, was therefore carried out in a sealed NMR tube under the catalytic conditions of [**B**] = 0.08 M, [**25**] = 0.008 M or [**27**] = 0.004 M (*i.e.* 10 mol% of rhodium) in 1,2-$F_2C_6H_4$ solvent. The reaction progress was monitored using ^{11}B NMR spectroscopy.



Scheme 5.21 Catalytic dehydrogenation of **B** to form **H**, [Rh] = 10 mol% **25** or 5 mol% **27**.

Dehydrogenation was found to be faster in case of the rhodium dimer (**27**) and the complete conversion of the cyclic amine-borane **B** to the amino-borane **H** was obtained in 100 minutes (Scheme 5.21, Figure 5.15). ^{1}H and ^{31}P{^{1}H} NMR spectra at the end of catalysis showed the presence of the Rh-dimer (**27**, 95%) along with some uncharacterised organometallic species (5%). However, when [Rh($^iPr_2P(CH_2)_3P^iPr_2$)(η^2–$H_2BNHMeC_4H_8$)][BAr^F_4] (**25**) was used as the catalyst, only 60% conversion of **B** to **H** was obtained in 8 h (Figure 5.16). Interestingly, the dimer [{Rh($P^iPr_2(CH_2)_3P^iPr_2$)}$_2$($H)_2$(μ-$H)_3$][BAr^F_4] (**27**) was observed as the major organometallic species (80% yield, with the rest being the starting complex **25**) by ^{31}P{^{1}H} NMR spectroscopy. This is consistent with our previous hypothesis that the formation of the dimer from the monomer is assisted by the dehydrogenation of the amine-boranes. Kinetic plots for the dehydrogenation of **B** using both catalysts are shown in Figures 5.15 and 5.16. Both show a lack of induction period and the first order kinetics relative to the amine-borane, with the dimer **27**

[k = 2.16(7) x 10^{-4} s^{-1}] being a much faster catalyst than the monomer **25** [k = 1.18(3) x 10^{-5} s^{-1}].

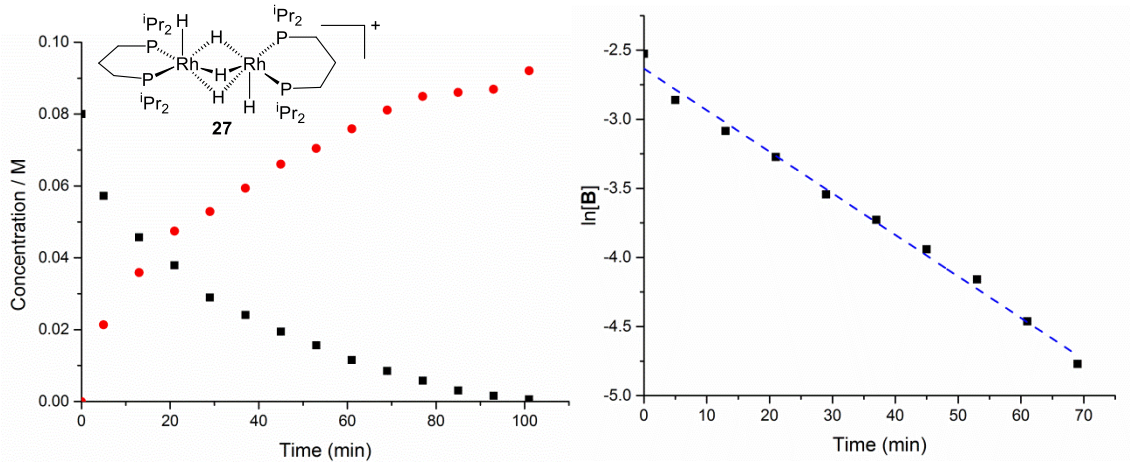


Figure 5.15 Kinetic plot for the catalytic dehydrogenation of **B** (initial concentration 0.08 M) using the complex **27** (0.004 M, 5 mol%). Left: Plot of concentration against time. • = amino-borane (**H**), ■ = amine-borane (**B**). Right: Plot of ln [**B**] against time.

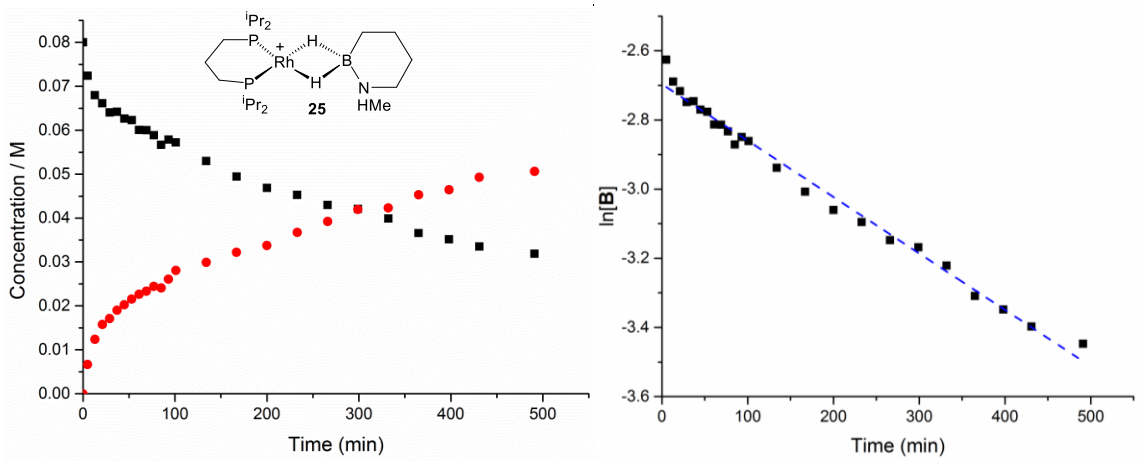


Figure 5.16 Kinetic plot for the catalytic dehydrogenation of **B** (initial concentration 0.08 M) using complex **25** (0.008 M, 10 mol%). Left: Plot of concentration against time. • = amino-borane (**H**), ■ = amine-borane (**B**). Right: Plot of ln [**B**] against time.

5.7.3 Dimer (27) - monomer (25) equilibrium

We hypothesised that the slow dehydrogenation in the case of [Rh(^{i}Pr$_2$P(CH$_2$)$_3$P^{i}Pr$_2$)(η^2-H$_2$BNHMeC$_4$H$_8$)][BAr$^F_4$] (**25**) is due to the inhibition by the acid [H(S)][BAr$^F_4$] which is formed concomitantly with [{Rh(P^{i}Pr$_2$(CH$_2$)$_3$P^{i}Pr$_2$)}$_2$(H)$_2$(μ-H)$_3$][BAr$^F_4$] (**27**), as discussed previously in Section 5.7.1. To test this hypothesis, we carried out the dehydrogenation of

B under the same catalytic conditions as above (**B**: 0.08 M; **25**: 0.008 M, 10 mol%) but in the presence of a hindered base 2,6-di-tert-butylpyridine (5 equivalents relative to **25**) which would be expected to consume the acid and speed up the dehydrogenation. Monitoring the dehydrogenation progress by the ^{11}B NMR spectroscopy revealed that the cyclic amine-borane **B** gets completely dehydrogenated to the amino-borane **H** in ~ 3 h with the rate constant k = 1.4(1) x 10^{-4} s^{-1}, which is more than ten times higher than that observed in the absence of base under the same catalytic conditions. Moreover, the dehydrogenation rate constant in the presence of the base using catalyst **25** [k = 1.4(1) x 10^{-4} s^{-1}] is similar to that observed when pure dimer **27** is used as the catalyst [k = 2.16(7) x 10^{-4} s^{-1}]. A $^{31}P\{^{1}H\}$ NMR spectrum of the reaction mixture at the end of the dehydrogenation (using **25** in the presence of the base) showed **27** as the only organometallic species present in the solution. This suggests that the external base enhances the dehydrogenation rate by promoting the formation of the dimer (**27**, which is a more active catalyst than **25**) from **25** by consuming the acid by-product of the formation of **27**, likely to be [H(S)][BAr^{F}_{4}].

In order to further probe these processes, the catalytic dehydrogenation of B was performed using 5 mol% dimer **27** in the presence of [$H(OEt_2)_2$][BAr^{F}_{4}] (1 equivalent relative to **27**). The ^{11}B NMR spectroscopy showed 75% conversion of the amine-borane **B** to the amino-borane **H** in 8 h (Figure 5.17). First order kinetics with respect to **B** is observed with the rate constant k = 2.3(1) x 10^{-5} s^{-1} which is almost ten times smaller than that observed in the absence of the acid *i.e.* with the pure dimer [k = 2.16(7) x 10^{-4} s^{-1}] but only slightly different to the dehydrogenation observed using the monomer, [$Rh(^{i}Pr_2P(CH_2)_3P^{i}Pr_2)(\eta^2–H_2BNHMeC_4H_8)$][$BAr^{F}_{4}$] (25) [$k$ = 1.18(3) x 10^{-5} s^{-1}].

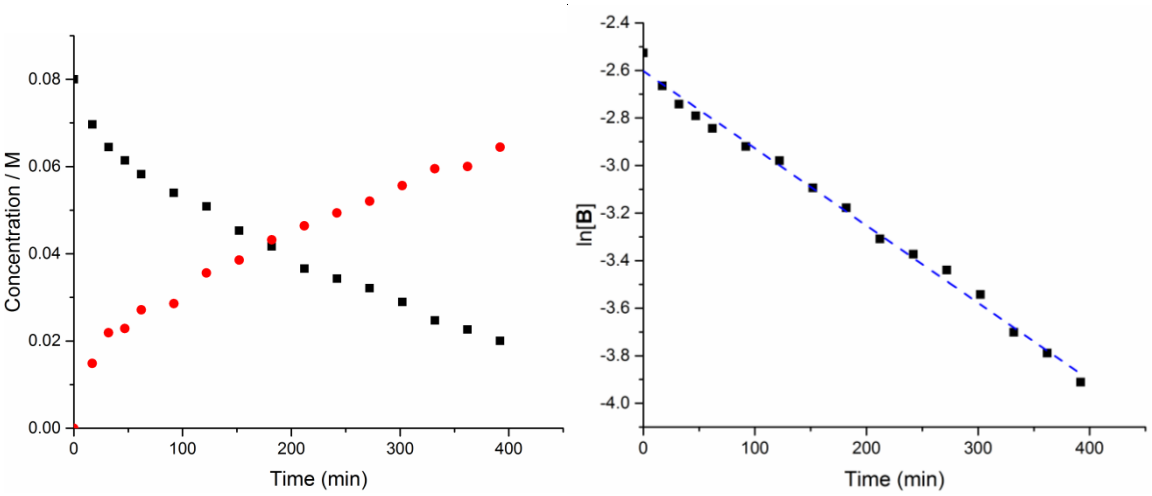
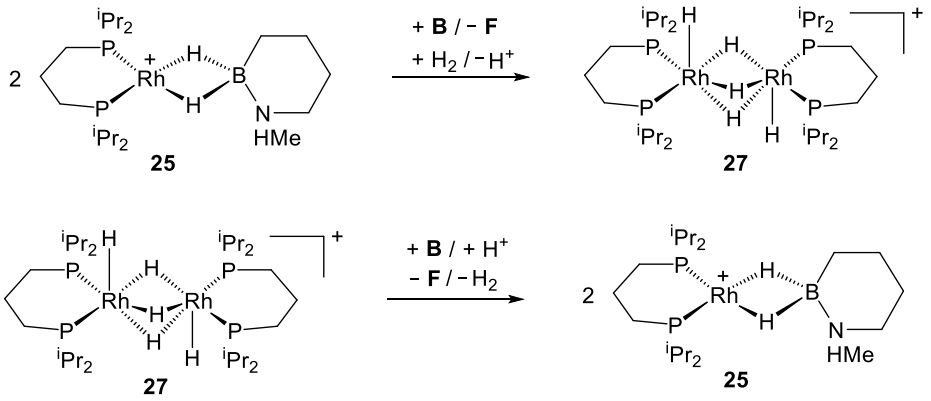


Figure 5.17 Kinetic plot for the catalytic dehydrogenation of **B** (initial concentration: 0.08 M) using complex **25** (0.004 M, 5 mol%) in presence of $[H(OEt_2)_2][BAr^F_4]$ (0.004 M). Left: Plot of concentration against time. • = amino-borane (**H**), ■ = amine-borane (**B**). Right: Plot of ln[**B**] against time.

A summary of the rate constants for the catalytic dehydrogenation of **B** using different catalysts is provided in the Table 5.3. These observations support our hypothesis that the acid $[H(S)][BAr^F_4]$ inhibits the dehydrogenation of **B** presumably by driving the resting state away from the dimer **27** towards **25**.The relationship between **25** and **27** in presence of acid/base is shown in Scheme 5.22.

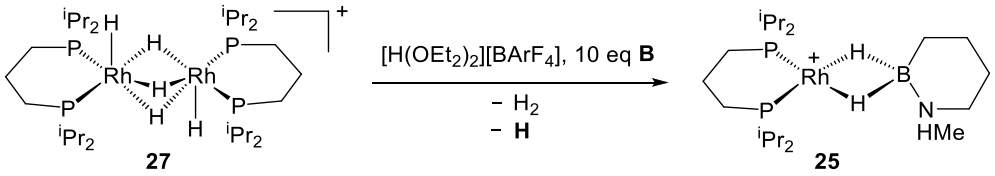
Table 5.3 Rate constants (s^{-1}) for the catalytic dehydrogenation of **B** (initial concentration: 0.08 M).

Catalyst	**Rate constant (s^{-1})**
25 (10 mol%)	$1.18(3) \times 10^{-5}$
27 (10 mol%)	$2.16(7) \times 10^{-4}$
25 (10 mol%) + 2,6-di-tert-butylpyridine (5 equivalents relative to **25**)	$1.4(1) \times 10^{-4}$
27 (10 mol%) + $[H(OEt_2)_2][BAr^F_4]$ (10 mol%)	$2.3(1) \times 10^{-5}$



Scheme 5.22 The relationship between **25** and **27**. $[BAr^F_4]^-$ anions are not shown.

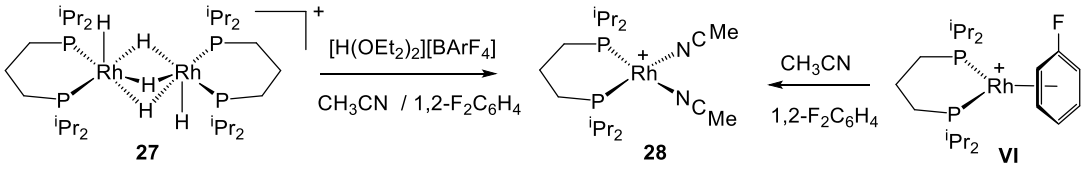
We further probed the above discussed dimer-monomer relationship by trapping the monomeric species $\{Rh(^iPr_2P(CH_2)_3P^iPr_2)\}^+$ by the addition of $[H(OEt_2)_2][BAr^F_4]$ and **B** or $[H(OEt_2)_2][BAr^F_4]$ and CH_3CN to the dimer **27**. Addition of one equivalent of $[H(OEt_2)_2][BAr^F_4]$ to $[\{Rh(P^iPr_2(CH_2)_3P^iPr_2)\}_2(H)_2(\mu\text{-}H)_3][BAr^F_4]$ (**27**) in the 1,2-$F_2C_6H_4$ solvent, followed by the addition of 10 equivalents of **B** resulted in the immediate formation of the sigma-complex **25** (Scheme 5.23). The formed sigma-complex **25** catalyses the dehydrogenation of the cyclic amine-borane **B** to form the amino-borane **H** (complete conversion in ~17 h).



Scheme 5.23 Reaction of **27** with $[H(OEt_2)_2][BAr^F_4]$ and **B**. $[BAr^F_4]^-$ anions are not shown.

Addition of excess acetonitrile (20 equivalents) to the mixture of $[H(OEt_2)_2][BAr^F_4]$ and **27** resulted in the formation of $[Rh(P^iPr_2(CH_2)_3P^iPr_2)(NCCH_3)_2][BAr^F_4]$ (**28**). Complex **28** was also synthesised independently by the addition of acetonitrile to $[Rh(P^iPr_2(CH_2)_3P^iPr_2)(C_6H_5F)][BAr^F_4]$ (**VI**) in 1,2-$F_2C_6H_4$ solvent (Scheme 5.24) and characterised by NMR spectroscopy, ESI-mass spectroscopy and elemental analysis. The $^{31}P\{^1H\}$ NMR spectrum of the isolated complex **28** displays a doublet at δ 42.5 ($^1J_{RhP}$ = 167

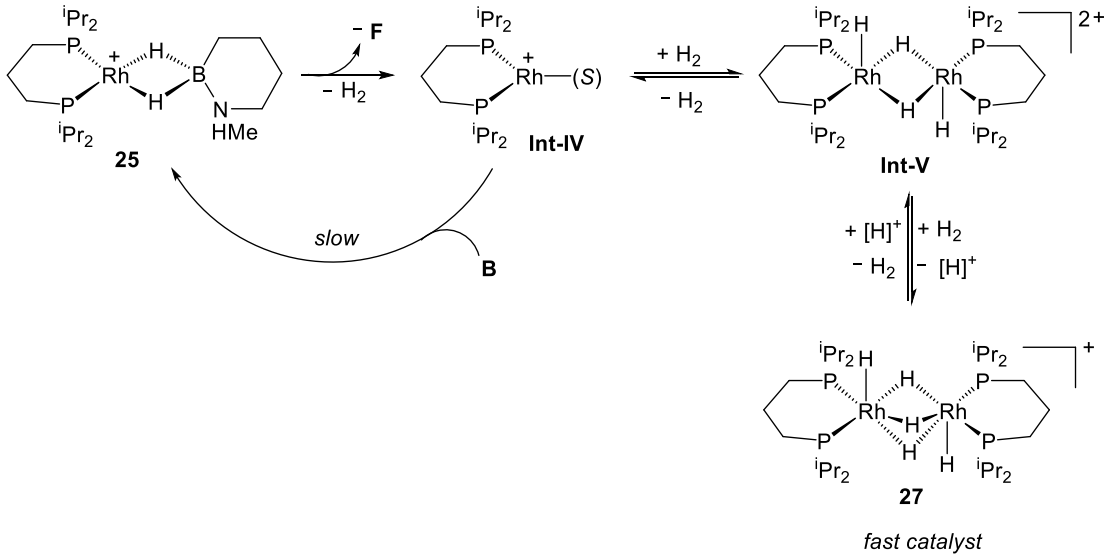
Hz) similar to that observed for $[Rh(PPh_2(CH_2)_3PPh_2)(NCCH_3)_2][Bbutcat_2]$ (butcat = 3,5-di-tert-butylcatecholato) which displays a resonance at δ 29.7 ($^1J_{RhP}$ = 163 Hz).[47]



Scheme 5.24 Formation of $[Rh(P^iPr_2(CH_2)_3P^iPr_2)(NCCH_3)_2][BAr^F_4]$ (**28**) from the dimer **27** or **VI**. $[BAr^F_4]^-$ anions are not shown.

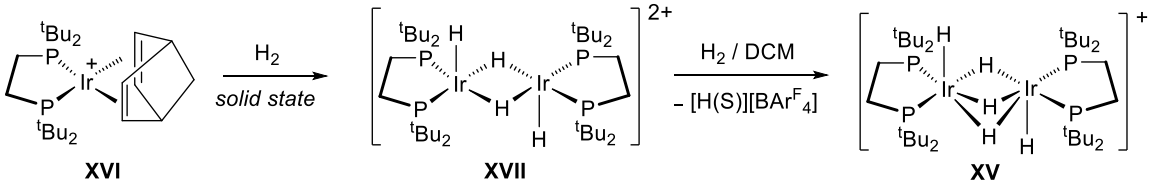
Trapping of a monomeric organometallic species from the dissociation of a dimer in acetonitrile has been observed before.[47] Westcott and co-workers have reported that the reaction of the *in situ* prepared $[Rh(\mu\text{-}Cl)(PPh_2(CH_2)_3PPh_2)]_2$ with $Tl(Bbutcat_2)$ in acetonitrile results in the loss of TlCl salt and the formation of the bis-acetonitrile adduct $[Rh(PPh_2(CH_2)_3PPh_2)(NCCH_3)_2][Bbutcat_2]$.

The overall relationship between **25** and **27** is summarised in Scheme 5.25. Complex **25** slowly dehydrogenates the cyclic amine-borane **B** to produce the amino-borane **H** and a Rh(I) complex **Int-IV**. In a sealed system, hydrogen produced from the dehydrogenation of **B** can reversibly react with **Int-IV** to form a dicationic rhodium dimer **Int-V**. The dicationic complex **Int-V** can then reversibly react with further one equivalent of hydrogen gas to release one equivalent of acid, likely to be $[H(S)][BAr^F_4]$ to form the monocationic dimer **27** which is a faster catalyst (Section 5.7.2). The presence of acid pushes the resting state towards **25** and results in the slow dehydrogenation of **B**, while the presence of a hindered base such as 2,6-di-tert-butylpyridine drives the equilibrium towards **27** and results in the faster dehydrogenation of **B**.



Scheme 5.25 Proposed relationship between **25** and **27**, (*S*) = solvent. $[BAr^F{}_4]^-$ anions are not shown.

The postulated mechanism to the formation of the dimer **27** from the monomer **25** is similar to the formation of the analogous complex $[\{Ir(P^tBu_2(CH_2)_2P^tBu_2)\}_2(H)_2(\mu\text{-}H)_3][BAr^F{}_4]$ (**XV**) upon hydrogenation of $[Ir(P^tBu_2(CH_2)_2P^tBu_2)(NBD)][BAr^F{}_4]$ (**XVI**) as recently reported by Weller and co-workers.[48] Hydrogenating the crystals of $[Ir(P^tBu_2(CH_2)_2P^tBu_2)(NBD)][BAr^F{}_4]$ (**XVI**) in the solid state results in the formation of a dicationic iridium dimer $[\{Ir(P^tBu_2(CH_2)_2P^tBu_2)\}_2(H)_2(\mu\text{-}H)_2][BAr^F{}_4]_2$ (**XVII**). Further hydrogenation of $[\{Ir(P^tBu_2(CH_2)_2P^tBu_2)\}_2(H)_2(\mu\text{-}H)_2][BAr^F{}_4]_2$ (**XVII**) in dichloromethane solvent results in the formation of a monocationic iridium dimer $[\{Ir(P^tBu_2(CH_2)_2P^tBu_2)\}_2(H)_2(\mu\text{-}H)_3][BAr^F{}_4]$ (**XV**) analogous to **27** presumably via the loss of $[H(S)][BAr^F{}_4]$ (Scheme 5.26). This is because H_2 on coordination to metal becomes very acidic (pK_a measured as low as −6) and can be deprotonated even by the presence of very weak base.[49] Hydrogenating the monomeric complex $[Ir(P^tBu_2(CH_2)_2P^tBu_2)(NBD)][BAr^F{}_4]$ (**XVI**) in dichloromethane solvent leads to the direct formation of $[\{Ir(P^tBu_2(CH_2)_2P^tBu_2)\}_2(H)_2(\mu\text{-}H)_3][BAr^F{}_4]$ (**XV**).



Scheme 5.26 Formation of [{Ir(P^{t}Bu$_2$(CH$_2$)$_2$P^{t}Bu$_2$)}$_2$(H)$_2$(μ-H)$_3$][BAr$^F_4$] (**XV**) from the hydrogenation of [Ir(P^{t}Bu$_2$(CH$_2$)$_2$P^{t}Bu$_2$)(NBD)][BAr$^F_4$] (**XVI**). [BAr$^F_4$] anions are not shown.

5.7.4 Kinetic studies

In order to explore the nature of the active catalyst in terms of the dimer or the monomer, we carried out initial rate[50] studies to find the order of the dehydrogenation reaction with respect to the amine-borane **B** and the catalyst [{Rh(P^{i}Pr$_2$(CH$_2$)$_3$P^{i}Pr$_2$)}$_2$(H)$_2$(μ-H)$_3$][BAr$^F_4$] (**27**) in a sealed system. Initial rates at different concentrations of **B** and **27** were calculated from the pseudo zero order region of the temporal consumption of **B** as measured by ^{11}B NMR spectroscopy for 5 minutes (~10% conversion of the amine-borane **B** to the amino-borane **F**). Initial rates obtained at different concentrations of either **B** or **27** are plotted against the concentration (Table 5.4, Figure 5.18). Figure 5.18A shows that initial rates vary linearly with the concentrations of **B** suggesting a first order kinetics relative to **B**. The plot of the initial rates against the catalyst (**27**) concentrations gives a curve (Figure 5.18C), whereas, when the initial rates are plotted against the square root of the concentration of **27** a straight line is obtained, suggesting half order kinetics relative to the dimer **27** (Figure 5.18B).

Table 5.4 Initial rates upon variation of concentrations of **B** and **27**.

[**B**] x 10^{-2} (M)	[**27**] x 10^{-3} (M)	Initial rate x 10^{-5} (Ms^{-1})
3.4	1.7	1.87 ± 0.16
3.4	0.85	1.01 ± 0.08
3.4	3.4	2.32 ± 0.17
1.7	1.7	1.04 ± 0.28
6.8	1.7	3.96 ± 0.24

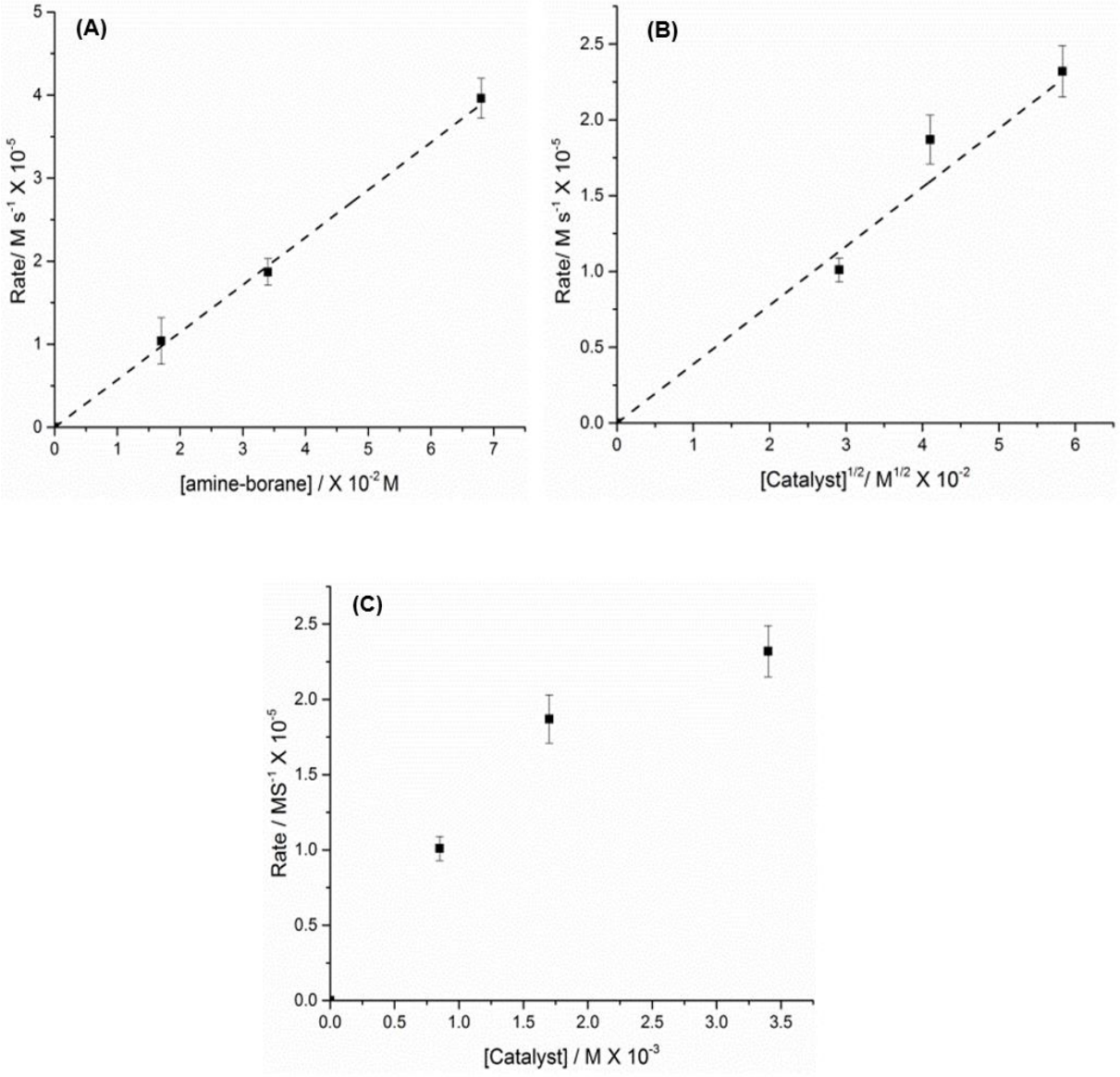
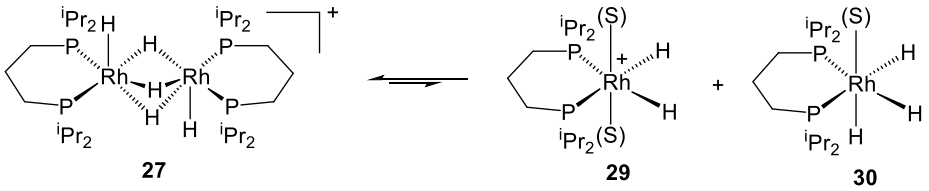


Figure 5.18 (A): Plot of initial rates against concentration of amine-borane; **(B)**: plot of initial rates against concentration of [catalyst]$^{1/2}$; **(C)**: plot of initial rates against concentration of [catalyst]. Amine-borane = **B** and catalyst = [{Rh($P^iPr_2(CH_2)_3P^iPr_2$)}$_2$(H)$_2$(μ-H)$_3$][BAr^F_4] (**27**).

The half order dependence on **27** suggests the occurrence of a rapid dimer-monomer equilibrium in which the dimer sits off the catalytic cycle and a monomer is the actual catalytic species. The Weller group has previously reported the catalytic dehydrocoupling of $H_3B{\cdot}NMe_2H$ to form the cyclic dimer $[H_2BNMe_2]_2$ using $[Rh(PCy_3)H_2Cl]_2$.[51] Kinetic studies revealed a first order dependence on $H_3B{\cdot}NMe_2H$ and a half order dependence on $[Rh(PCy_3)H_2Cl]_2$ suggesting a rapid equilibrium between the inactive dimer $[Rh(PCy_3)H_2Cl]_2$ and the active monomer $Rh(PCy_3)H_2Cl$. Similar kinetics have been

reported for the dimeric rhodium complex $[Rh(H_2C{=}CHAr)_2(Cl)_2]_2$ (aryl = *p*-$MeOC_6H_4$) catalyzed hydroboration of alkenes in which the first order dependence on borane and a half order dependence on the rhodium dimer has been observed.[52] A rapid equilibrium between the dimer $[Rh(H_2C{=}CHAr)_2(Cl)_2]_2$ and the monomer $[Rh(H_2C{=}CHAr)_2(Cl)_2]$ has been suggested in which the later has been proposed to be the active catalyst. Similar equilibria have been suggested earlier for alkene hydrogenation[42] arene alkylations,[53] and C–S bond activations.[54]

In this case, we speculate a rapid equilibrium between the dimer **27** and the two monomeric rhodium complexes: a cationic complex **29** and a neutral complex **30** in which one of the two monomers is the active catalyst (Scheme 5.26). We discount the other possibilities for half order dependence that involve the dissociation of either chelating phosphine or H_2 from **27** as we do not observe any such dissociation while monitoring the catalytic dehydrogenation experiment using NMR spectroscopy.[55] To confirm this hypothesis, MeCN (10 equivalents) was added to **27** which resulted in the immediate formation of a monomeric MeCN-adduct $[Rh(P^iPr_2(CH_2)_3P^iPr_2)(NCCH_3)_2][BAr^F{}_4]$ (**28**) with liberation of some gas, presumably hydrogen, which could arise from an intermediate dihydride **29**. ^{1}H NMR spectroscopy also showed some unidentified hydride signals [δ –11.79 and –17.45] which could arise from a neutral species such as **30**.



Scheme 5.26 Suggested dimer/monomer equilibrium for **27**. (S) = solvent. $[BAr^F{}_4]^-$ anions are not shown.

5.8 Conclusions

In this chapter, the reactivity of the cyclic amine-boranes (**A**-**C**) with the transition metal fragments $\{Ir(PCy_3)_2(H)_2\}^+$ and $\{Rh(R_2P(CH_2)_3PR_2)\}^+$ (R = ^{i}Pr, Ph) have been reported. Amine-boranes **A**-**C** form iridium and rhodium η^2-sigma complexes (**22**-**26**) which have been isolated and characterised in the solid state and in solution. The dehydrocoupling of **A** to form the cyclic triborazine **D** has been reported earlier at the temperature 150ºC[6] but the use of transition metal fragment, here has resulted in the dehydrocoupling to occur at room temperature and also allowed the observation of the involved B-N intermediates. Under catalytic conditions, cyclic amine-borane **A** catalytically dehydrocouples at room temperature to ultimately form the cyclic triborazine **D** via the cyclic amino-borane **E** and the cyclic diborazane (**F^1** and **F^2**) or triborazanes (**G^1** and **G^2**), whereas the cyclic amine-borane **B** dehydrogenates at room temperature to form the amino-borane **H**. A summary of the TOF for the catalytic dehydrogenation of **A** and **B** are mentioned below:

Table 5.5 TOF for the catalytic dehydrocoupling of **A** and the catalytic dehydrgenation of **B**.

Amine-borane	Catalyst	~ToF (h^{-1})
A	**II**	0.07
A	**VI**	0.1
A	**III**	0.7
B	**II**	0.2
B	**VI**	0.6
B	**III**	3
B	**27**	5

The mechanism for the dehydrogenation of **B** using $\{Rh(^iPr_2P(CH_2)_3P^iPr_2)\}^+$ fragment has been investigated which reveals an equilibrium between the dimeric species $[\{Rh(P^iPr_2(CH_2)_3P^iPr_2)\}_2(H)_2(\mu\text{-}H)_3][BAr^F{}_4]$ (**27**) and the monomeric species $[Rh(^iPr_2P(CH_2)_3P^iPr_2)(\eta^2\text{–}H_2BNHMeC_4H_8)][BAr^F{}_4]$ (**25**). The equilibrium is affected by the presence of acid/base, with acid driving the equilibrium towards the monomeric complex

25, and the base driving the equilibrium in favour of the dimer. Kinetic studies have been carried out to understand the nature of actual catalyst (dimer or monomer) which shows a first order dependence on **B** and a half order dependence on the dimer **27** suggesting a rapid equilibrium between the dimer **27** and the monomers **29** and **30**, for which one of the latter is the active catalyst (Scheme 5.26).

Overall, this is the first report on the coordination chemistry and the catalytic dehydrogenation of B,N-cyclohexane type amine-boranes using the transition metal complexes. Changing the metal or ligand framework influences the catalytic activity as shown in Table 5.5. Development of catalysts that can dehydrocouple **A** to form **D** at a faster rate or dehydrogenate the C−C backbone of **D** to offer a hydrogen storage material of 9.4 wt% capacity (current gravimetric hydrogen density: 4.7 wt%) remains a challenge for the future.

5.9 References

1. F. H. Stephens, V. Pons and R. T. Baker, *Dalton Trans.*, 2007, 2613-2626.
2. K. Mueller, K. Stark, B. Mueller and W. Arlt, *Energy Fuels*, 2012, **26**, 3691-3696.
3. A. D. Sutton, A. K. Burrell, D. A. Dixon, E. B. Garner, III, J. C. Gordon, T. Nakagawa, K. C. Ott, P. Robinson and M. Vasiliu, *Science*, 2011, **331**, 1426-1429.
4. W. Luo, P. G. Campbell, L. N. Zakharov and S.-Y. Liu, *J. Am. Chem. Soc.*, 2011, **133**, 19326-19329.
5. W. Luo, D. Neiner, A. Karkamkar, K. Parab, E. B. Garner, III, D. A. Dixon, D. Matson, T. Autrey and S.-Y. Liu, *Dalton Trans.*, 2013, **42**, 611-614.
6. W. Luo, L. N. Zakharov and S.-Y. Liu, *J. Am. Chem. Soc.*, 2011, **133**, 13006-13009.
7. G. Chen, L. N. Zakharov, M. E. Bowden, A. J. Karkamkar, S. M. Whittemore, E. B. Garner, III, T. C. Mikulas, D. A. Dixon, T. Autrey and S.-Y. Liu, *J. Am. Chem. Soc.*, 2015, **137**, 134-137.
8. P. G. Campbell, L. N. Zakharov, D. J. Grant, D. A. Dixon and S.-Y. Liu, *J. Am. Chem. Soc.*, 2010, **132**, 3289-3291.
9. H. Wille and J. Goubeau, *J. Chem. Ber.*, 1972, **105**, 2156-2168.
10. M. Shimoi, S. Nagai, M. Ichikawa, Y. Kawano, K. Katoh, M. Uruichi and H. Ogino, *J. Am. Chem. Soc.*, 1999, **121**, 11704-11712.
11. G. J. Kubas, *Metal Dihydrogen and σ-bond complexes*, Kluwer, New York, 2001.
12. G. Alcaraz and S. Sabo-Etienne, *Angew. Chem. Int. Ed.*, 2010, **49**, 7170-7179.

13. C. J. Stevens, R. Dallanegra, A. B. Chaplin, A. S. Weller, S. A. Macgregor, B. Ward, D. Mckay, G. Alcaraz and S. Sabo-Etienne, *Chem. Eur. J.*, 2011, **17**, 3011-3020.

14. H. C. Johnson, A. P. M. Robertson, A. B. Chaplin, L. J. Sewell, A. L. Thompson, M. F. Haddow, I. Manners and A. S. Weller, *J. Am. Chem. Soc.*, 2011, **133**, 11076-11079.

15. A. Kumar, H. C. Johnson, T. N. Hooper, A. S. Weller, A. G. Algarra and S. A. Macgregor, *Chem. Sci.*, 2014, **5**, 2546-2553.

16. A. E. W. Ledger, C. E. Ellul, M. F. Mahon, J. M. J. Williams and M. K. Whittlesey, *Chem. Eur. J.*, 2011, **17**, 8704-8713.

17. R. Dallanegra, A. B. Chaplin and A. S. Weller, *Angew. Chem. Int. Ed.*, 2009, **48**, 6875-6878.

18. A. B. Chaplin and A. S. Weller, *Angew. Chem. Int. Ed.*, 2010, **49**, 581-584.

19. O. N. Michael, A. A. David, R. Ian, K. Michael, P. Nicholas and A. Simon, *J. Am. Chem. Soc.*, 2011, **133**, 11500-11503.

20. G. Alcaraz and S. Sabo-Etienne, *Coord. Chem. Rev.*, 2008, **252**, 2395-2409.

21. N. Merle, G. Koicok-Köhn, M. F. Mahon, C. G. Frost, G. D. Ruggerio, A. S. Weller and M. C. Willis, *Dalton Trans.*, 2004, 3883-3892.

22. A. G. Algarra, L. J. Sewell, H. C. Johnson, S. A. Macgregor and A. S. Weller, *Dalton Trans.*, 2014, **43**, 11118-11128.

23. W. Luo, L. N. Zakharov and S.-Y. Liu, *J. Am. Chem. Soc.*, 2011, **133**, 13006-13009.

24. C. J. Stevens, R. Dallanegra, A. B. Chaplin, A. S. Weller, S. A. Macgregor, B. Ward, D. McKay, G. Alcaraz and S. Sabo-Etienne, *Chem. Eur. J.*, 2011, **17**, 3011-3020.

25. T. M. Douglas, A. B. Chaplin, A. S. Weller, X. Yang and M. B. Hall, *J. Am. Chem. Soc.*, 2009, **131**, 15440-15456.

26. T. D. Forster, H. M. Tuononen, M. Parvez and R. Roesler, *J. Am. Chem. Soc.*, 2009, **131**, 6689-6691.

27. H. Helten, B. Dutta, J. R. Vance, M. E. Sloan, M. F. Haddow, S. Sproules, D. Collison, G. R. Whittell, G. C. Lloyd-Jones and I. Manners, *Angew. Chem. Int. Ed.*, 2012, **52**, 437-440.

28. L. J. Sewell, M. A. Huertos, M. E. Dickinson, A. S. Weller and G. C. Lloyd-Jones, *Inorg. Chem.*, 2013, **52**, 4509-4516.

29. K. Gruet, E. Clot, O. Eisenstein, D. H. Lee, B. Patel, A. Macchioni and R. H. Crabtree, *N. J. Chem.*, 2003, **27**, 80-87.

30. H. Wille and J. Goubeau, *Chem. Ber.*, 1972, **105**, 2156-2168.

31. H. C. Johnson and A. S. Weller, *J. Organomet. Chem.*, 2012, **721-722**, 17-22.

32. O. J. Metters, A. M. Chapman, A. P. M. Robertson, C. H. Woodall, P. J. Gates, D. F. Wass and I. Manners, *Chem. Commun.*, 2014, **50**, 12146-12149.

33. N. E. Stubbs, A. Schaeger, A. P. M. Robertson, E. M. Leitao, T. Jurca, H. A. Sparkes, C. H. Woodall, M. F. Haddow and I. Manners, *Inorg. Chem.*, 2015, **54**, 10878-10889.

34. A. Kumar, J. S. A. Ishibashi, T. N. Hooper, T. C. Mikulas, D. A. Dixon, S.-Y. Liu and A. S. Weller, *Chem. Eur. J.*, 2016, **22**, 310-322.

35. C. A. Jaska, K. Temple, A. J. Lough and I. Manners, *J. Am. Chem. Soc.*, 2003, **125**, 9424-9434.

36. A. B. Chaplin and A. S. Weller, *Inorg. Chem.*, 2010, **49**, 1111-1121.

37. A. B. Chaplin and A. S. Weller, *Inorg. Chem.*, 2010, **49**, 1111-1121.

38. T. M. Douglas, A. B. Chaplin and A. S. Weller, *J. Am. Chem. Soc.*, 2008, **130**, 14432-14433.

39. R. Dallanegra, A. P. M. Robertson, A. B. Chaplin, I. Manners and A. S. Weller, *Chem. Commun.*, 2011, **47**, 3763-3765.

40. M. Brookhart, B. Grant and A. F. Volpe, *Organometallics*, 1992, **11**, 3920-3922.

41. F. H. Stephens, R. T. Baker, M. H. Matus, D. J. Grant and D. A. Dixon, *Angew. Chem. Int. Ed.*, 2007, **46**, 746-749.

42. M. D. Fryzuk, W. E. Piers, F. W. B. Einstein and T. Jones, *Can. J. Chem.*, 1989, **67**, 883-896.

43. C. Kohrt, W. Baumann, A. Spannenberg, H. J. Drexler, I. D. Gridnev and D. Heller, *Chem. Eur. J.*, 2013, **19**, 7443-7451.

44. I. R. Butler, W. R. Cullen, T.-J. Kim, F. W. B. Einstein and T. Jones, *J. Chem. Soc. Chem. Commun.*, 1984, 719-721.

45. C. Kohrt, W. Baumann, A. Spannenberg, H.-J. Drexler, I. D. Gridnev and D. Heller, *Chem. Eur. J.*, 2013, **19**, 7443-7451.

46. J. Wolf, O. Nürnberg, M. Schäfer and H. Werner, *Z. Anorg. Allg. Chem.*, 1994, **620**, 1157-1162.

47. M. J. Geier, S. J. Geier, N. R. Halcovitch, C. M. Vogels, A. Decken and S. A. Westcott, *Polyhedron*, 2013, **52**, 1181-1189.

48. A. S. Weller, F. M. Chadwick and N. Oliff, *J. Organomet. Chem.*, 2016, **in press http://dx.doi.org/10.1016/.**

49. G. J. Kubas, *J. Organomet. Chem.*, 2014, **751**, 33-49.

50. J. H. Espenson, *Chemical Kinetics and Reaction Mechanisms*, McGraw-Hill, Inc., 1995.

51. L. J. Sewell, M. A. Huertos, M. E. Dickinson, A. S. Weller and G. C. Lloyd-Jones, *Inorg. Chem.*, 2013, **52**, 4509-4516.

52. J. M. Brown and G. C. Lloyd-Jones, *J. Chem. Soc. Chem. Commun.*, 1992, 710.

53. G. P. Van Strijdonck, M. D. Boele, P. C. Kamer, J. G. De Vries and P. van Leeuwen, *Eur. J. Inorg. Chem.*, 1999.

54. J. F. Hooper, R. D. Young, I. Pernik, A. S. Weller and M. C. Willis, *Chem. Sci.*, 2013, **4**, 1568.

55. J. E. Marshall, J. B. Keister and S. T. Diver, *Organometallics*, 2011, **30**, 1319-1321.

6 Experimental

6.1 Experimental techniques

All manipulations, unless otherwise stated, were performed under an atmosphere of argon using standard Schlenk and glovebox techniques. Glassware was oven dried at 130°C overnight and flamed under vacuum prior to use. CH_2Cl_2, MeCN, Et_2O, toluene, pentane and hexane were dried using a Grubbs-type solvent purification system (MBraun SPS-800) and degassed by successive freeze-pump-thaw cycles.[1] THF was distilled from sodium benzophenone ketyl, degassed by successive freeze-pump-thaw cycles and stored over 3 Å molecular sieves. 1,2-$F_2C_6H_4$ (pretreated with alumina), C_6H_5F, d8-THF, CD_2Cl_2 were dried over CaH_2, vacuum distilled and stored over 3 Å molecular sieves.

6.1.1 Nuclear Magnetic Resonance Spectroscopy

NMR spectra were recorded on Bruker AVIII500 or Bruker DPX250 spectrometers at room temperature, unless otherwise stated. Residual protio solvent was used as a reference for ^{1}H and ^{13}C NMR spectra in deuterated solvent samples. In 1,2-$F_2C_6H_4$ or C_6H_5F, the spectrometer was pre-locked and shimmed to a sample containing 25% C_6D_6 and 75% 1,2- $F_2C_6H_4$ and referenced to the centre of the downfield solvent multiplet (δ 7.07 or 7.11, respectively). $^{31}P\{^{1}H\}$ and ^{11}B NMR spectra were referenced externally against 85% H_3PO_4 and $BF_3{\cdot}OEt_2$, respectively. Chemical shifts are quoted in ppm. Coupling constants are quoted in Hz.

6.1.2 Mass Spectrometry

Electrospray Ionisation Mass Spectrometry (ESI-MS) was recorded using a Bruker MicrOTOF instrument directly connected to a modified Innovative Technology glovebox.[2] The mass spectrometer was calibrated in positive ion mode using a 10 ng/mL mixture of tetraalkylammonium bromide salts $[N(C_nH_{2n+1})_4]Br$ (n = 2 - 8, 12, 16, 18) in CH_2Cl_2. Typical

acquisition parameters were: sample flow rate, 4 µL/min; nebuliser gas pressure, 0.4 bar; drying gas (argon) at 60 °C flowing at 4L/min; capillary voltage, 4.5 kV; funnel voltage, 200 Vpp. The solvents used were 1,2-$F_2C_6H_4$, C_6H_5F or THF. Samples were diluted to a concentration of approximately 1 x 10^{-6} M before running.

6.1.3 Elemental microanalysis

Elemental microanalyses were performed by Elemental Microanalysis Ltd or Stephen Boyer at London Meteropolitan University (UK).

6.1.4 Gel Permeation Chromatography

Gel Permeation Chromatography (GPC) was performed by Gemma Adams on Waters 1515 equipped with an isocratic HPLC Pump. Styragel HR5E THF (4.6 x 300 mm) columns were used. THF containing 0.1% w/w [$^nBu_4N$]Br was used as the eluent at a flow rate of 1.0 mL min^{-1}. Samples were dissolved in the eluent (2 mg mL^{-1}), left for 6 h at room temperature and filtered with an Acrodisc CR 13 mm syringe filter (with 0.2 µm PTFE membrane) before analysis. The calibration was conducted using Polystyrene Ready-Cal kit.

6.1.5 X-ray crystallography

Structure determinations were carried out by Dr. Sebastian D. Pike, Dr. Tom Hooper or myself, and relevant crystallographic data can be found in Tables in the Appendix. Data for **7**, **9**, **12**, **13**, **15**, **18**, **20**, **21**, **22** and **27** were collected on an Agilent Supernova diffractometer using graphite monochromated Cu Kα radiation (λ = 1.54180 Å) and a low temperature device; reduction and cell refinement was performed using CrysAlisPro.[3] Data for **4'**, **4b'**, **5a**, **6**, **8**, **23**, **24**, **25** and **26** were collected on a Enraf Nonious Kappa CCD difractometer using graphite monochromated Mo Kα radiation (λ = 0.71073 Å) and a low temperature device;[4] data were collected using COLLECT, reduction and cell

refinement was performed using DENZO/SCALEPACK.[5] All structures were solved using Sir92[6] or Superflip[7] or SHELXS-97.[8] All were refined using CRYSTALS[9] or SHELXL-97.[8]

6.1.6 General procedure for hydrogenation

The sample was freeze-pump-thaw degassed twice, backfilled with H_2 at 77 K (flask immersed in liquid N_2) and then flask was closed. The internal H_2 pressure on warming was *ca.* 4 atm.

6.2 Synthesis and characterisation

6.2.1 Starting materials

The starting materials $H_3B{\cdot}NMeH_2$,[10] $H_3B{\cdot}NH_2BH_2{\cdot}NH_3$,[11] $H_3B{\cdot}NH_2BH_2NH_2BH_2{\cdot}NH_3$,[12] $[IrHPCy_2(\eta^2\text{-}C_6H_9)PCy_2(\eta^3\text{-}C_6H_8)][BAr^F{}_4]$,[13] $[IrHPCy_2(\eta^2\text{-}C_6H_9)PCy_2(\eta^3\text{-}C_6H_8)][Bar^{Cl}{}_4]$[14], $[Rh(P^iPr_2(CH_2)_3P^iPr_2)(C_6H_5F)][BAr^F{}_4]$,[15] $[Rh(PPh_2(CH_2)_nPPh_2)(C_6H_5F)][BAr^F{}_4]$ (n = 3, 5),[16] $[Rh(P^iPr_2(CH_2)_3P^iPr_2)(\mu\text{-}H)]_2$,[17] $[H(OEt_2)_2][BAr^F{}_4]$,[18] and $[BH_2(OEt_2)NH_3][BAr^F{}_4]$[19] were prepared by literature methods or variations thereof. *Tert*-butylethylene (TBE) and cyclohexene were dried over sodium, vacuum distilled and stored over 3 Å molecular sieves. $H_3B{\cdot}NMe_3$ and $H_3B{\cdot}NMe_2H$ were purchased from Aldrich and sublimed once and twice prior to use (5 x 10^{-2} mbar, 298 K), respectively. $H_3B{\cdot}NH_3$ was purchased from Aldrich and used as it is for stoichiometric experiments. For kinetics studies, $H_3B{\cdot}NH_3$ was sublimed (7 x 10^{-3} mbar, 323 K) before use. Cyclic amine-boranes (**A**-**C**) were synthesised by Jacob S. A. Ishibashi (Liu group, Boston College, USA).[20]

6.2.2 Synthesis of new complexes

Complexes **14**, **15** and **16** were synthesised by Isobel Priest and **17** was synthesised by Dr. Tom Hooper by the methods described here.

$[Ir(H)_2(PCy_3)_2(\eta^2\text{-}H_3B{\cdot}NH_3)][BAr^F{}_4]$ (4)

In a high pressure NMR tube equipped with a J. Young's valve $[IrHPCy_2(\eta^2\text{-}C_6H_9)PCy_2(\eta^3\text{-}C_6H_8)][BAr^F{}_4]$ (23 mg, 1.4 x 10^{-2} mmol) in C_6H_5F was hydrogenated at 4 atm at 298 K. The tube was occasionally shaken over a period of 20 min to produce a colourless solution $[Ir(H)_2(PCy_3)_2(H_2)_2][BAr^F{}_4]$ (**II**). The solution of **II** was rapidly transferred under argon to another high pressure NMR tube containing $H_3B{\cdot}NH_3$ (0.5 mg, 1.6 x 10^{-2} mmol) and an immediate change from colourless to purple was observed. A gentle inversion of NMR tube for another 50 min made the solution again colourless. It was then degassed through freeze-pump-thaw method and gently inverted for 10 more min. Analysis by NMR spectroscopy at this point showed the formation of $[Ir(H)_2(PCy_3)_2(\eta^2\text{-}H_3B{\cdot}NH_3)][BAr^F{}_4]$ (**4**) in more than 95% yield. Attempt to isolate crystals of **4** by layering with pentane or hexane was not successful and resulted in an unidentified yellow oil and some white suspension.

^{1}H NMR (500 MHz, C_6H_5F): δ 8.35 (s, 8H, $[BAr^F{}_4]^-$), 7.66 (s, 4H, $[BAr^F{}_4]^-$), 3.63 (s, 3H, NH_3), 1.93-1.21 (m, 66H, Cy), −5.96 (br, 2H, σ-bound BH_2), −20.28 (t, $^2J_{HP}$ = 15, 2H, IrH_2), The remaining BH signal is not observed, presumably as too broad or obscured by solvent peak (In case of $[Ir(H)_2(PCy_3)_2(\eta^2\text{-}H_3B{\cdot}NH_2Me)][BAr^F{}_4]$, the unbound B−H signal comes at 6.09 in C_6H_5F at 250K).[14]

^{31}P{^{1}H} NMR (202 MHz, C_6H_5F): δ 38.2 (br, 1P), 33.4 (br, 1P).

^{31}P{^{1}H} NMR (202 MHz, C_6H_5F, 250 K): δ 38.6 (d, $^2J_{PP}$ = 273, 1P), 32.2 (d, $^2J_{PP}$ = 273, 1P).

^{11}B NMR (160 MHz, C_6H_5F): δ 10.5 (br, bound BH_3), −5.9 (s, $[BAr^F{}_4]^-$).

ESI-MS (C_6H_5F, 60°C) positive ion: m/z 786.50 [M+] (calc. 786.50).

$[Ir(H)_2(PCy_3)_2(\eta^2\text{-}H_3B{\cdot}NH_3)][BAr^{Cl}{}_4]$ (4')

In a Young's flask $[IrHPCy_2(\eta^2\text{-}C_6H_9)PCy_2(\eta^3\text{-}C_6H_8)][BAr^{Cl}{}_4]$ (30 mg, 2.2 x 10^{-2} mmol) in C_6H_5F (2 mL) was hydrogenated as described in the general procedures. It was stirred for 20 min to produce a colourless solution of $[Ir(H)_2(PCy_3)_2(H_2)_2][BAr^{Cl}{}_4]$. The solution, then, was rapidly transferred under argon to another Young's flask containing $H_3B{\cdot}NH_3$ (0.8 mg,

2.6 x 10^{-2} mmol). Stirring for another 50 min was followed by degassing by a freeze-pump-thaw cycle. Stirring the solution for 30 more min resulted in a white precipitate. The solvent was removed by cannula filtration and the white precipitate was dried to obtain the white solid of $[Ir(H)_2(PCy_3)_2(\eta^2\text{-}H_3B{\cdot}NH_3)][BAr^{Cl}{}_4]$ (**4'**) in 48% yield. Crystals suitable for X-ray diffraction were obtained by recrystallisation from 1,2-$F_2C_6H_4$/pentane at 5°C. **^{1}H NMR (500 MHz, 1,2-$F_2C_6H_4$)**: δ 7.37 (s, 8H, $[BAr^{Cl}{}_4]^-$), 4.22 (s, 3H, NH_3), 1.9-1.1 (m, 66H, Cy), −5.91 (br, 2H, σ-bound BH_2), −20.33 (br, t, $^2J_{HP}$ = 15, 2H, IrH_2). The remaining BH signal is not observed, presumably as too broad or obscured by solvent peak. Other $[BAr^{Cl}{}_4]^-$ peak is also obscured by the solvent.

^{1}H NMR (500 MHz, CD_2Cl_2, 250 K): δ 7.22 (br, m, 2H, $[BAr^{Cl}{}_4]^-$), 7.16 (br, m, 2H, $[BAr^{Cl}{}_4]^-$), 7.10 (s, 6H, $[BAr^{Cl}{}_4]^-$), 7.06 (s, 2H, $[BAr^{Cl}{}_4]^-$), 6.13 (br, 1H, BH), 3.95 (s, 3H, NH_3), 1.96-1.26 (m, 66H, Cy), −6.14 (br, 2H, σ-bound BH_2), −20.32 (br, t, $^2J_{HP}$ = 15, 2H, IrH_2).

^{31}P{^{1}H} NMR (202 MHz, 1,2-$F_2C_6H_4$): δ 38.1 (br, 1P), 32.9 (br, 1P).

^{31}P{^{1}H} NMR (202 MHz, CD_2Cl_2): δ 38.1 (br, 1P), 33.3 (br, 1P).

^{31}P{^{1}H} NMR (202 MHz, 1,2-$F_2C_6H_4$, 250K): δ 38.5 (d, $^2J_{PP}$ = 273, 1P), 31.9 (d, $^2J_{PP}$ = 273, 1P).

^{11}B NMR (160 MHz, 1,2-$F_2C_6H_4$): δ 10.8 (br, bound BH_3), −6.7 (s, $[BAr^{Cl}{}_4]^-$).

^{11}B NMR (160 MHz, CD_2Cl_2): δ 10.2 (br, bound BH_3), −6.9 (s, $[BAr^{Cl}{}_4]^-$).

Elemental Microanalysis: Calc. [$C_{60}H_{86}B_2Cl_8IrNP_2$ + $C_6H_4F_2$] (1494.83 gmol^{-1}): C, 53.03; H, 6.07; N, 0.94. Found: C, 53.22; H, 5.84; N, 1.22.

$[Ir(H)_2(PCy_3)_2(\eta^2\text{-}H_3B{\cdot}NH_2BH_2{\cdot}NH_3)][BAr^F{}_4]$ (4a)

In a high pressure NMR tube equipped with a J. Young's valve $[IrHPCy_2(\eta^2\text{-}C_6H_9)PCy_2(\eta^3\text{-}C_6H_8)][BAr^F{}_4]$ (32 mg, 2.0 x 10^{-2} mmol) in C_6H_5F was hydrogenated as described in the general procedures. The tube was occasionally shaken over a period of 20 min to produce a colourless solution $[Ir(H)_2(PCy_3)_2(H_2)_2][BAr^F{}_4]$ (**II**). The solution of **II** was rapidly transferred under argon to another high pressure NMR tube containing $H_3B{\cdot}NH_2BH_2{\cdot}NH_3$ (1.3 mg, 2.0 x 10^{-2} mmol). The NMR tube was sonicated for 5 min and then gently inverted

for 2 h. ESI-MS and NMR spectra showed the formation of $[Ir(H)_2(PCy_3)_2(\eta^2\text{-}H_3B{\cdot}NH_2BH_2{\cdot}NH_3)][BAr^F{}_4]$ (**4a**) in more than 95% yield as measured by the ^1H NMR spectroscopy. Attempt to isolate crystals of **4a** by layering with pentane or hexane was not successful and resulted in an unidentified yellow oil and some white suspension meaning that the elemental microanalysis was not possible.

^1H NMR (500 MHz, C_6H_5F): δ 8.35 (s, 8H, $[BAr^F{}_4]^-$), 7.66 (s, 4H, $[BAr^F{}_4]^-$), 3.35 (s, 3H, NH_3), 2.74 (s, 2H, NH_2), 2.35 (br, 2H, BH_2), 1.98-1.22 (m, 66H, Cy), −6.32 (br, 2H, σ-bound BH_2), −19.87 (apparent triplet, $^2J_{HP}$ = 15, 2H, IrH_2). The remaining BH signal is not observed, presumably as too broad or obscured by solvent peak.

$^1H\{^{11}B\}$ NMR (500 MHz, CD_2Cl_2): δ 7.78 (s, 8H, $[BAr^F{}_4]^-$), 7.62 (s, 4H, $[BAr^F{}_4]^-$), 6.23 (br, 1H, BH), 4.01 (s, 3H, NH_3), 3.00 (s, 2H, NH_2), 2.32 (br, 2H, BH_2), 1.98-1.30 (m, 66H, Cy), −6.33 (br, 2H, σ-bound BH_2), −20.09 (t, $^2J_{HP}$ = 15, 2H, IrH_2).

$^{31}P\{^1H\}$ NMR (202 MHz, C_6H_5F): δ 37.4 (d, $^2J_{PP}$ = 284, 1P), 32.2 (d, $^2J_{PP}$ = 284, 1P).

^{11}B NMR (160 MHz, C_6H_5F): δ 13.8 (br, bound BH_3), −6.1 (s, $[BAr^F{}_4]^-$), −11.5 (br, BH_2).

ESI-MS (C_6H_5F, 60°C) positive ion: m/z 815.55 [M+] (calc. 815.55).

$[Ir(H)_2(PCy_3)_2(\eta^2\text{-}H_3B{\cdot}NH_2BH_2{\cdot}NH_3)][BAr^{Cl}{}_4]$ (4a')

In a high pressure NMR tube equipped with a J. Young's valve $[IrHPCy_2(\eta^2\text{-}C_6H_9)PCy_2(\eta^3\text{-}C_6H_8)][BAr^{Cl}{}_4]$ (25 mg, 1.9 x 10^{-2} mmol) in 1,2-$F_2C_6H_4$ was hydrogenated as described in the general procedures. The tube was occasionally shaken over a period of 20 min to produce a colourless solution $[Ir(H)_2(PCy_3)_2(H_2)_2][BAr^{Cl}{}_4]$ **2**, which was rapidly transferred under argon to another high pressure NMR tube containing containing $H_3B{\cdot}NH_2BH_2{\cdot}NH_3$ (1.4 mg, 2.0 x 10^{-2} mmol). The resulting mixture was stirred at room temperature for 3.5 h under an argon atmosphere. The NMR tube was sonicated for 15 min and then gently inverted for 4 h. ESI-MS and NMR spectra at this stage showed the formation of $[Ir(H)_2(PCy_3)_2(\eta^2\text{-}H_3B{\cdot}NH_2BH_2{\cdot}NH_3)][BAr^{Cl}{}_4]$ (**4a'**), in more than 95% yield as measured by ^1H NMR spectroscopy. Solid or crystalline (**4a'**) could not be obtained through recrystallisation from 1,2-$F_2C_6H_4$/pentane at −30 °C.

$^{1}H\{^{11}B\}$ NMR (500 MHz, 1,2-$F_2C_6H_4$): δ 7.37 (s, 8H, $[BAr^{Cl}_4]^-$), 3.86 (s, 3H, NH_3), 3.03 (s, 2H, NH_2), 2.41 (s, 2H, BH_2), 1.94-1.20 (m, 66H, Cy), −6.36 (br, 2H, σ-bound BH_2), −19.87 (br, 2H, IrH_2). The remaining BH signal is not observed, presumably as too broad or obscured by solvent peak. Other $[BAr^{Cl}_4]^-$ peak is also obscured by the solvent. **$^{31}P\{^{1}H\}$ NMR (202 MHz, 1,2-$F_2C_6H_4$)**: δ 37.6 (d, $^{2}J_{PP}$ = 284, 1P), 32.2 (d, $^{2}J_{PP}$ = 284, 1P). **^{11}B NMR (160 MHz, 1,2-$F_2C_6H_4$)**: δ 13.9 (br, bound BH_3), −6.7 (s, $[BAr^{Cl}_4]^-$), −10.9 (br, BH_2).

$[Ir(H)_2(PCy_3)_2(\eta^2\text{-}H_3B{\cdot}NH_2BH_2NH_2BH_2{\cdot}NH_3)][BAr^F_4]$ (4b)

In a high pressure NMR tube equipped with a J. Young's valve $[IrHPCy_2(\eta^2\text{-}C_6H_9)PCy_2(\eta^3\text{-}C_6H_8)][BAr^F_4]$ (32 mg, 2.0 x 10^{-2} mmol) in C_6H_5F was hydrogenated as described in the general procedures. The tube was occasionally shaken over a period of 20 min to produce a colourless solution $[Ir(H)_2(PCy_3)_2(H_2)_2][BAr^F_4]$ (**II**). The solution of **II** was rapidly transferred under argon to another high pressure NMR tube containing $H_3B{\cdot}NH_2BH_2NH_2BH_2{\cdot}NH_3$ (1.8 mg, 2.0 x 10^{-2} mmol). The NMR tube was sonicated for 15 min and then gently inverted for 20 h. ESI-MS and NMR spectra showed the formation of $[Ir(H)_2(PCy_3)_2(\eta^2\text{-}H_3B{\cdot}NH_2BH_2NH_2BH_2{\cdot}NH_3)][BAr^F_4]$ (**4b**) in more than 95% yield (by NMR spectroscopy). Solids or crystals of **4b** could not be obtained through recrystallisation. **$^{1}H\{^{11}B\}$ NMR (500 MHz, C_6H_5F)**: δ 8.35 (s, 8H, $[BAr^F_4]^-$), 7.66 (s, 4H, $[BAr^F_4]^-$), 3.04 (br, 3H, NH_3), 2.79 (br, 2H, NH_2), 2.37 (br, 2H, NH_2), 2.27 (br, 2H, BH_2), 2.02-1.25 (m, 66H, Cy), −6.48 (br, 2H, σ-bound BH_2), −19.61 (apparent triplet, $^{2}J_{HP}$ = 15, 2H, IrH_2). The remaining BH signals are not observed; presumably the terminal unbound B−H signal is obscured by solvent and the remaining BH_2 signal by cyclohexyl peaks. **$^{1}H\{^{11}B\}$ NMR (500 MHz, CD_2Cl_2)**: δ 7.78 (s, 8H, $[BAr^F_4]^-$), 7.62 (s, 4H, $[BAr^F_4]^-$), 6.39 (br, 1H, BH), 3.94 (br, 3H, NH_3), 2.92 (br, 2H, NH_2), 2.72 (br, 2H, NH_2), 2.32 (br, 2H, BH_2), 1.96-1.30 (m, 66H, Cy), −6.58 (br, 2H, σ-bound BH_2), −19.84 (t, $^{2}J_{HP}$ = 15, 2H, IrH_2). The remaining BH signals are not observed, presumably as too broad or obscured by cyclohexyl peaks.

$^{31}P\{^{1}H\}$ NMR (202 MHz, C_6H_5F): δ 37.1 (d, $^{2}J_{PP}$ = 284, 1P), 32.2 (d, $^{2}J_{PP}$ = 284, 1P). **^{11}B NMR (160 MHz, C_6H_5F)**: δ 15.6 (br, bound BH_3), −6.1 (s, $[BAr^{F}_4]^-$), −11.7 (br, BH_2 and BH_3).

ESI-MS (C_6H_5F, 60°C) positive ion: m/z 844.59 [M+] (calc. 844.59).

$[Ir(H)_2(PCy_3)_2(\eta^2\text{-}H_3B{\cdot}NH_2BH_2NH_2BH_2{\cdot}NH_3)][BAr^{Cl}_4]$ (4b')

To a Young's flask $[IrHPCy_2(\eta^2\text{-}C_6H_9)PCy_2(\eta^3\text{-}C_6H_8)][BAr^{Cl}_4]$ (25 mg, 1.9 x 10^{-2} mmol) in 1,2-$F_2C_6H_4$ was hydrogenated as described in the general procedure. The solution was stirred over a period of 20 min to produce a colourless solution $[Ir(H)_2(PCy_3)_2(H_2)_2][BAr^{Cl}_4]$ which was rapidly transferred under argon to a Schlenk tube containing $H_3B{\cdot}NH_2BH_2NH_2BH_2{\cdot}NH_3$ (1.7 mg, 1.9 x 10^{-2} mmol). The resulting mixture was stirred at room temperature for 3.5 h under an argon atmosphere. The solution was then filtered to another Schlenk. Excess pentane was added to it while stirring which resulted in a white emulsion. Sonication for 15 min gave the mixture of a yellow oil stuck to the walls and a white emulsion. The white emulsion was cannula transferred to another Schlenk and dried in vacuum resulting in white solid. Crystals suitable for X-ray diffraction were obtained by recrystallisation from 1,2-$F_2C_6H_4$/pentane at −30 °C in 48% yield.

^{1}H NMR (500 MHz, 1,2-$F_2C_6H_4$): δ 7.37 (s, 8H, $[BAr^{Cl}_4]^-$), 3.64 (br, 3H, NH_3), 2.97 (br, 2H, NH_2), 2.65 (br, 2H, NH_2), 2.35 (br, 2H, BH_2), 1.95-1.16 (m, 66H, Cy), −6.58 (br, 2H, σ-bound BH_2), −19.62 (br, 2H, IrH_2), The remaining BH signals are not observed, presumably the terminal B−H (not σ-bound) signal is obscured by solvent and the remaining BH_2 signal by cyclohexyl peaks. Other $[BAr^{Cl}_4]^-$ peak is also obscured by the solvent.

$^{31}P\{^{1}H\}$ NMR (202 MHz, 1,2-$F_2C_6H_4$): δ 37.1 (d, $^{2}J_{PP}$ = 286, 1P), 32.1 (d, $^{2}J_{PP}$ = 286, 1P). **^{11}B NMR (160 MHz, 1,2-$F_2C_6H_4$)**: δ 15.8 (br, bound BH_3), −6.7 (s, $[BAr^{Cl}_4]^-$), −11.7 (br, BH_2 and BH_3).

ESI-MS (C_6H_5F, 60°C) positive ion: m/z 844.59 [M+] (calc. 844.59).

Elemental Microanalysis: Calc. [$C_{60}H_{94}B_4Cl_8IrN_3P_2$] (1435.44 gmol^{-1}): C, 50.10; H, 6.59; N, 2.92. Found: C, 50.81; H, 6.28; N, 2.90.

[Rh(PPh$_2$(CH$_2$)$_3$PPh$_2$)(THF)$_2$][BAr$^F{}_4$] (6)

THF (1 mL) was added to a Schlenk flask containing [Rh(PPh$_2$(CH$_2$)$_3$PPh$_2$)(C$_6$H$_5$F)][BAr$^F{}_4$] (50 mg, 3.4 x 10^{-2} mmol) and stirred for 15 min. Resulting orange solution was layered with pentane at –18ºC to yield [Rh(PPh$_2$(CH$_2$)$_3$PPh$_2$)(THF)$_2$][BAr$^F{}_4$] (**6**) as orange crystals. Yield: 30 mg, 60%.

^{1}H NMR (500 MHz, d8-THF): δ 7.82 (s, 8H, [BAr$^F{}_4$]$^-$), 7.62 (s, 4H, [BAr$^F{}_4$]$^-$), 7.61 (br, 8 H, Ph) 7.47 (br, 12H, Ph), 2.50 (br, 8H, OCH$_2$), 1.35-0.93 (m, 8H, CH2), 0.15 (br, 6H, CH$_2$CH$_2$CH$_2$).

^{31}P{^{1}H} NMR (202 MHz, d8-THF): δ 37.3 (d, $^1J_{RhP}$ = 192).

ESI-MS (THF, 60°C) positive ion: m/z 659.18 [M+] (calc. 659.17).

Elemental Microanalysis: Calc. [$C_{50}H_{58}B_2F_{24}NP_2Rh$] (1315.29 gmol^{-1}): C, 52.85; H, 3.57. Found: C, 52.95; H, 3.10.

[(Rh(PPh$_2$(CH$_2$)$_3$PPh$_2$))$_2$(μ-H)(μ-BH$_2$NH$_2$)][BAr$^F{}_4$] (7)

H$_3$B·NH$_3$ (0.7 mg, 2.2 x 10^{-2} mmol) was added to [Rh(PPh$_2$(CH$_2$)$_3$PPh$_2$)(C$_6$H$_5$F)][BAr$^F{}_4$] (30 mg, 2.0 x 10^{-2} mmol) in THF in a sealed NMR tube. NMR spectroscopy and ESI-MS after 2 min showed the formation of [(Rh(PPh$_2$(CH$_2$)$_3$PPh$_2$))$_2$(μ-H)(μ-BH$_2$NH$_2$)][BAr$^F{}_4$] (**7**) as major product (90% by ^{31}P{^{1}H} NMR spectroscopy). Layering with pentane (–18ºC) afforded only few crystals, rest being oily material. Due to very low yield of crystalline material, pure NMR spectra of **7** could not be obtained though single crystal X-ray diffraction was possible.

Spectral details after 2 min of reaction:

^{1}H NMR (500 MHz, d_8-THF): δ 7.79 (s, $[BAr^{F}_4]^-$), 7.57 (s, $[BAr^{F}_4]^-$), 7.49 - 7.24 (overlapping m, Ph), 5.67 (br, NH_2), 1.99 (br, CH_2), −7.45 (s, BH_2 and RhH). Signal at δ −7.45 showed integral of 3H relative to the phenyl resonance.

^{31}P{^{1}H} NMR (202 MHz, d_8-THF): δ 18.2 (d, $^{1}J_{RhP}$ = 142).

^{11}B NMR (160 MHz, d_8-THF): δ 51.5 (br, BH_2), −6.5 (s, $[BAr^{F}_4]^-$), 0.5 (t, $^{1}J_{BH}$ = 108, corresponding to $[BH_2(NH_3)(THF)][BAr^{F}_4]$).

ESI-MS (1,2-$F_2C_6H_4$, 60°C) positive ion: m/z 1060.16 [M+] (calc. 1060.16).

$[Rh(P^iPr_2(CH_2)_3P^iPr_2)(\eta^2\text{-}H_3B{\cdot}NMe_3)][BAr^{F}_4]$ (8)

$[Rh(P^iPr_2(CH_2)_3P^iPr_2)(C_6H_5F)][BAr^{F}_4]$ (32 mg, 2.4 x 10^{-2} mmol) and $H_3B{\cdot}NMe_3$ (1.8 mg, 2.4 x 10^{-2} mmol) were added to a Schlenk flask to which Et_2O (~1 mL) was added. Resulting solution was stirred for 2 h and then layered with pentane at –18ºC to yield $[Rh(P^iPr_2(CH_2)_3P^iPr_2)(\eta^2\text{-}H_3B{\cdot}NMe_3)][BAr^{F}_4]$ (**8**) as purple crystals. Yield: 20 mg, 64%. **^{1}H NMR (500 MHz, CD_2Cl_2)**: δ 7.76 (s, 8H, $[BAr^{F}_4]^-$), 7.60 (s, 4H, $[BAr^{F}_4]^-$), 2.89 (s, 9H, NMe_3), 1.94 (br, 6H, $CH_2CH_2CH_2$), 1.5 (br, 4H, CH), 1.23 (m, 24H, CH_3), −1.9 (br, 3H, BH_3).

^{31}P{^{1}H} NMR (202 MHz, CD_2Cl_2): δ 59.2 (d, $^{1}J_{RhP}$ = 163).

^{11}B NMR (160 MHz, CD_2Cl_2): δ 24.5 (br, BH_2), −6.6 (s, $[BAr^{F}_4]^-$).

ESI-MS (1,2-$C_6H_4F_2$, 60°C) positive ion: m/z 492.25 [M+] (calc. 492.25).

Elemental Microanalysis: Calc. $[C_{50}H_{58}B_2F_{24}NP2Rh]$ (1315.29 $gmol^{-1}$): C, 45.65; H, 4.44; N, 1.06. Found: C, 45.95; H, 4.10; N, 1.12.

$[(Rh(P^iPr_2(CH_2)_3P^iPr_2))_2(\mu\text{-}H)(\mu\text{-}BH_2NH_2)][BAr^{F}_4]$ (9)

$[Rh(P^iPr_2(CH_2)_3P^iPr_2)(\mu\text{-}H)]_2$ (47 mg, 6.2 x 10^{-2} mmol) and $[BH_2(NH_3)(OEt_2)][BAr^{F}_4]$ (62 mg, 6.2 x 10^{-2} mmol) were added to a Schlenk flask to which Et_2O (~3 mL) was added. Addition of Et_2O led to immediate bubbling and the resulting orange solution was stirred for 10 min. The orange solution was filtered, concentrated to ~1 mL and then layered with

pentane at –18 ºC to yield [(Rh(P^{i}Pr$_2$(CH$_2$)$_3$P^{i}Pr$_2$))$_2$(μ-H)(μ-BH$_2$NH$_2$)][BAr$^F{}_4$] (**9**) as orange crystals. Yield: 80 mg, 78%.

^{1}H NMR (500 MHz, d$_8$-THF): δ 7.79 (s, 8H, [BAr$^F{}_4$]$^-$), 7.57 (s, 4H, [BAr$^F{}_4$]$^-$), 4.55 (s, 2H, NH$_2$), 2.09 (br, 8H, CH), 1.17 (m, 48H, CH$_3$), 0.11 (br, 12H, CH$_2$CH$_2$CH$_2$), −8.64 (s, 3H, BH$_2$ and RhH).

^{1}H NMR (500 MHz, d$_8$-THF, 180 K): δ 7.90 (s, 8H, [BAr$^F{}_4$]$^-$), 7.75 (s, 4H, [BAr$^F{}_4$]$^-$), 5.05 (s, 2H, NH$_2$), 1.14 (m, 48H, CH$_3$), 0.11 (br, 12H, CH$_2$CH$_2$CH$_2$), −8.16 (br, 2H, BH$_2$), −9.02 (br, 1H, RhH), CH signals are obscured by THF signals.

^{31}P{^{1}H} NMR (202 MHz, d$_8$-THF): δ 40.8 (d, $^1J_{RhP}$ = 142).

^{31}P{^{1}H} NMR (202 MHz, d$_8$-THF, 180 K): δ 41.6 (br d, $^1J_{RhP}$ = 140), 36.1 (br d, $^1J_{RhP}$ = 140).

^{11}B NMR (160 MHz, d$_8$-THF): δ 51.1 (br, BH$_2$), −6.5 (s, [BAr$^F{}_4$]$^-$).

ESI-MS (1,2-C$_6$H$_4$F$_2$, 60°C) positive ion: m/z 788.29 [M+] (calc. 788.29). **Elemental Microanalysis**: Calc. [C$_{62}$H$_{85}$B$_2$F$_{24}$NP$_4$Rh$_2$] (1651.66 gmol^{-1}): C, 45.09; H, 5.19; N, 0.85. Found: C, 44.42; H, 5.12; N, 0.94.

[Rh(^{i}Pr$_2$P(CH$_2$)$_3$P^{i}Pr$_2$)(η^6-PhH$_2$B·NMe$_3$)][BAr$^F{}_4$] (12)

To a Schlenk flask charged with [Rh(^{i}Pr$_2$P(CH$_2$)$_3$P^{i}Pr$_2$)(C$_6$H$_5$F)][BAr$^F{}_4$] (25.0 mg, 1.9 x 10^{-2} mmol) and PhH$_2$B·NMe$_3$ (3.1 mg, 2.1 x 10^{-2} mmol) was added 1,2-F$_2$C$_6$H$_4$ (0.5 mL). Resulting orange solution was stirred for 30 min and layered with pentane at −25˚C to afford the product as orange crystals. Yield: 20.0 mg, 77%.

^{1}H NMR (500 MHz, CD$_2$Cl$_2$): δ 7.76 (s, 8H, [BAr$^F{}_4$]$^-$), 7.60 (s, 4H, [BAr$^F{}_4$]$^-$), 6.93 (broad m, 1H, PhH), 6.31 (broad m, 4H, PhH), 2.55 (s, 9H, NMe$_3$), 1.88 (br, 6H, CH$_2$), 1.30 (br, 4H, CH), 1.19 (broad m, 12 H, CH$_3$), 1.12 (broad m, 12 H, CH$_3$), B*H$_2$* signals not detected due to quadrupolar broadening. On ^{11}B decoupling the B*H$_2$* resonance appears at δ 2.38 (s).

^{31}P{^{1}H} NMR (202 MHz, CD$_2$Cl$_2$): δ 45.0 (d, $^1J_{RhP}$ = 195).

^{11}B NMR (160 MHz, CD$_2$Cl$_2$): δ −2.1 (br, BH$_2$), −6.6 (s, [BAr$^F{}_4$]$^-$).

ESI-MS (1,2-$F_2C_6H_4$, 60°C) positive ion: m/z 528.26 [M^+] (calc. 528.26).

Elemental Microanalysis: Calc. [$C_{56}H_{62}B_2F_{24}NP_2Rh$] (1391.32 $gmol^{-1}$): C, 48.32; H, 4.49; N, 1.01. Found: C, 48.19; H, 4.38; N, 0.92.

[Rh(P^iPr_3)$_2$(η^2-$H_2PhB{\cdot}NMe_3$)][BAr^F_4] (13)

To a Schlenk flask charged with [Rh(P^iPr_3)$_2$(C_6H_5F)][BAr^F_4] (25.0 mg, 1.8 x 10^{-2} mmol) and $PhH_2B{\cdot}NMe_3$ (4 mg, 2.7 x 10^{-2} mmol) was added 1,2-$F_2C_6H_4$ (0.5 mL). The resulting blue/purple solution was layered with pentane at −25˚C to afford the product as blue crystals. Yield: 18 mg, 69%.

^{1}H NMR (500 MHz, CD_2Cl_2): δ 7.76 (s, 8H, [BAr^F_4]$^-$), 7.60 (s, 4H, [BAr^F_4]$^-$), 7.37 (br, 3H, PhH), 7.25 (br, 2H, PhH), 2.83 (s, 9H, NMe_3), 2.07 (broad m, 6H, CH), 1.32 (apparent dd, J ~ 12, J ~ 7, 36H, CH_3), −6.36 (br, 2H, BH_2).

^{31}P{^{1}H} NMR (202 MHz, CD_2Cl_2): δ 69.6 (d, $^1J_{RhP}$ = 176).

^{11}B NMR (160 MHz, CD_2Cl_2): δ 34.8 (br, BH_2), −6.6 (s, [BAr^F_4]$^-$).

ESI-MS (1,2-$F_2C_6H_4$, 60°C) positive ion: m/z 572.32 [M^+] (calc. 572.32).

Elemental Microanalysis: Calc. [$C_{59}H_{70}B_2F_{24}NP_2Rh$] (1435.38 g mol^{-1}): C, 49.35; H, 4.91; N, 0.98. Found: C, 49.32; H, 4.82; N, 1.01.

[Rh(P^iBu_3)$_2$(η^6-$PhH_2B{\cdot}NMe_3$)][BAr^F_4] (14) and [Rh(P^iBu_3)$_2$(η^2-$H_2PhB{\cdot}NMe_3$)][BAr^F_4] (15) and

To a Young's NMR tube charged with [Rh(P^iBu_3)$_2$(C_6H_5F)][BAr^F_4] (10 mg, 6.82 x 10^{-3} mmol) and $PhH_2B{\cdot}NMe_3$ (1.0 mg, 6.82 x 10^{-3} mmol, 1.0 equivalent) was added 1,2-$F_2C_6H_4$ (0.4 mL). Mixing resulted in blue/purple solution and the NMR spectra were taken of this sample *in situ* to show products **14** and **15** in approximately equal ratio. The solvent from this sample was removed in vacuo and CD_2Cl_2 added and the NMR spectroscopy repeated to reveal virtually identical data in CD_2Cl_2 and this is reported below. Bulk isolation of either **14** or **15** was not possible due to formation of a mixture of purple crystals (determined by single crystal X-ray

diffraction to be **15**) and orange oil therefore microanalysis of the sample was not possible.

^{1}H NMR (500 MHz, CD_2Cl_2): δ 7.72 (s, 8H, $[BAr^F{}_4]^-$), 7.56 (s, 4H, $[BAr^F{}_4]^-$), 7.33 (broad m, ~1H, PhH, **15**), 7.18 (broad m, ~0.5H, PhH, **15**), 7.12 (broad m, ~1H, PhH, **15**), 6.95 (broad m, ~0.5H, PhH, **14**), 6.10 (broad m, ~1H, PhH, **14**), 5.94 (broad m, ~1H, PhH, **14**), 2.76 (s, ~4.5H, NMe_3, **15**), 2.50 (s, ~4.5H, NMe_3, **14**), 1.98 (broad m, 6H, CH), 1.63 (broad m, ~6H, CH_2), 1.55 (broad m, ~6H, CH_2), 1.06 (apparent broad d, J ~ 5 Hz, 36H, CH_3), –5.06 (br, ~1H, BH_2, **15**). The signal for BH_2 in **14** was not observed due to quadrupolar broadening and overlap with other resonances. A $^{1}H\{^{11}B\}$ NMR spectrum showed this peak at δ 2.41.

$^{31}P\{^{1}H\}$ NMR (202 MHz, CD_2Cl_2): δ 34.1 (d, $^{1}J_{RhP}$ = 177, **15**), 25.2 (d, $^{1}J_{RhP}$ = 202, **14**).

^{11}B NMR (160 MHz, CD_2Cl_2): δ 29.5 (br, BH_2, **15**), −2.1 (br, BH_2, **14**), −6.6 (s, $[BAr^F{}_4]^-$).

ESI-MS (1,2-$F_2C_6H_4$, 60°C) positive ion: m/z 656.41 [M^+] (calc. 656.42).

$[Rh(Ph_2P(CH_2)_3PPh_2)(\eta^6\text{-}PhH_2B{\cdot}NMe_3)][BAr^F{}_4]$ (16)

To a Schlenk flask charged with $[Rh(Ph_2P(CH_2)_3PPh_2)(C_6H_5F)][BAr^F{}_4]$ (30.0 mg, 2.04 x 10^{-2} mmol) and $PhH_2B{\cdot}NMe_3$ (3.0 mg, 2.0 x 10^{-2} mmol) was added 1,2-$F_2C_6H_4$ (1.0 mL). The resulting orange solution was stirred for 30 min and layered with pentane at −25˚C to afford the product as orange crystals. Yield: 15.0 mg, 48%.

^{1}H NMR (500 MHz, CD_2Cl_2): δ 7.72 (s, 8H, $[BAr^F{}_4]^-$), 7.56 (s, 4H, $[BAr^F{}_4]^-$), 7.46 (broad m, 10H, PhH), 7.41-7.36 (broad m, 10H, PhH), 6.82 (apparent t, $^{3}J_{HH}$ = 6.1 Hz, 1H, PhH), 5.55 (apparent d, $^{3}J_{HH}$ = 6.1 Hz, 2H, PhH), 4.94 (apparent t, $^{3}J_{HH}$ = 6.1 Hz, 2H, PhH), 2.48 (s, 9H, NMe_3), 2.45 (broad m, overlap with the signal δ 2.48, 4H, CH_2), 1.85 (broad m, 2H, CH_2). The signal for BH_2 in **5** was not observed due to

quadrupolar broadening and overlap with other resonances. A $^{1}H\{^{11}B\}$ NMR spectrum showed this peak at δ 2.59.

$^{31}P\{^{1}H\}$ NMR (202 MHz, CD_2Cl_2): δ 25.5 (d, $^{1}J_{RhP}$ = 192).

^{11}B NMR (160 MHz, CD_2Cl_2): δ −2.0 (br, BH_2), −6.6 (s, $[BAr^F{}_4]^-$).

ESI-MS (1,2-$F_2C_6H_4$, 60°C) positive ion: m/z 664.19 [M^+] (calc. 664.19).

Elemental Microanalysis: Calc. [$C_{68}H_{54}B_2F_{24}NP_2Rh$] (1527.99 $gmol^{-1}$): C, 53.45; H, 3.56; N, 0.92. Found: C, 53.38; H, 3.43; N, 0.97.

[$Rh(Ph_2P(CH_2)_5PPh_2)(\eta^6\text{-}PhH_2B{\cdot}NMe_3)$][$BAr^F{}_4$] (17)

To a Schlenk flask charged with [$Rh(Ph_2P(CH_2)_5PPh_2)(C_6H_5F)$][$BAr^F{}_4$] (15.0 mg, 10.0 x 10^{-3} mmol) and $PhH_2B{\cdot}NMe_3$ (1.5 mg, 10.0 x 10^{-3} mmol) was added 1,2-$F_2C_6H_4$ (1.0 mL). The resulting orange solution was stirred for 30 min. The solvent was removed in vacuo and the orange oily solid redissolved in CH_2Cl_2 (1 mL). This solution was layered with pentane at −25˚C to afford the product as dark orange crystals. Yield: 5.0 mg, 32%.

^{1}H NMR (500 MHz, CD_2Cl_2): δ 7.72 (s, 8H, $[BAr^F{}_4]^-$), 7.56 (s, 4H, $[BAr^F{}_4]^-$), 7.41-7.31 (broad overlapping m, 20H, PhH), 7.12 (apparent broad t, $^{1}J_{HH}$ ~ 5.5 Hz, 1H, PhH), 5.21-5.17 (broad overlapping m, 4H, PhH), 2.47 (broad m, overlap with 2.45 signal, 2H, CH_2), 2.45 (s, 9H, NMe_3), 2.30 (broad m, 4H, CH_2), 1.91 (broad m, 4H, CH_2). The signal for BH_2 in **17** was not observed due to quadrupolar broadening and overlap with other resonances. A $^{1}H\{^{11}B\}$ NMR spectrum showed this peak at δ 2.51.

$^{31}P\{^{1}H\}$ NMR (202 MHz, CD_2Cl_2): δ 26.3 (d, $^{1}J_{RhP}$ = 204).

^{11}B NMR (160 MHz, CD_2Cl_2): δ −2.2 (br, BH_2), −6.6 (s, $[BAr^F{}_4]^-$).

ESI-MS (1,2-$F_2C_6H_4$, 60°C) positive ion: m/z 692.22 [M^+] (calc. 692.23).

Elemental Microanalysis: Calc. [$C_{70}H_{58}B_2F_{24}NP_2Rh$] (1556.04 $gmol^{-1}$): C, 54.03; H, 3.76; N, 0.90. Found: C, 53.92; H, 3.67; N, 1.00.

[Rh(^{i}Pr$_2$P(CH$_2$)$_3$P^{i}Pr$_2$)(η^6-PhH$_2$B·NMe$_2$H)][BAr$^F_4$] (18)

To a Schlenk flask charged with [Rh(^{i}Pr$_2$P(CH$_2$)$_3$P^{i}Pr$_2$)(C$_6$H$_5$F)][BAr$^F_4$] (25.0 mg, 1.9 x 10^{-2} mmol) and PhH$_2$B·NMe$_2$H (2.8 mg, 2.1 x 10^{-2} mmol) was added 1,2-F$_2$C$_6$H$_4$ (0.5 mL). Resulting orange solution was stirred for 24 h and layered with pentane at −25˚C to afford the product as orange crystals. Yield: 16 mg, 62%.

^{1}H NMR (500 MHz, CD$_2$Cl$_2$): δ 7.76 (s, 8H, [BAr$^F_4$]$^-$), 7.60 (s, 4H, [BAr$^F_4$]$^-$), 6.88 (broad m, 1H, PhH), 6.31 (broad m, 2H, PhH), 6.26 (broad m, 2H, PhH), 3.55 (br, 1H, NH), 2.52 (s, 6H, NMe$_2$), 1.86 (br, 6H, CH$_2$), 1.30 (br, 4H, CH), 1.18 (broad m, 12, CH$_3$), 1.11 (broad m, 12, CH$_3$). BH$_2$ signals not detected due to quadrupolar broadening.

^{31}P{^{1}H} NMR (202 MHz, CD$_2$Cl$_2$): δ 45.3 (d, $^1J_{RhP}$ = 196).

^{11}B NMR (160 MHz, CD$_2$Cl$_2$): δ −6.0 (br, BH$_2$), −6.6 (s, [BAr$^F_4$]$^-$).

ESI-MS (1,2-F$_2$C$_6$H$_4$, 60°C) positive ion: m/z 514.24 [M$^+$] (calc. 514.25).

Elemental Microanalysis: Calc. [C$_{55}$H$_{60}$B$_2$F$_{24}$NP$_2$Rh] (1377.31 gmol^{-1}): C, 47.96; H, 4.39; N, 1.02. Found: C, 47.60; H, 4.29; N, 1.13.

[Rh(P^{i}Pr$_3$)$_2$(H)$_2$(η^2-H$_2$PhB·NMe$_2$H)][BAr$^F_4$] (20)

To a sealed NMR tube charged with [Rh(P^{i}Pr$_3$)$_2$(C$_6$H$_5$F)][BAr$^F_4$] (25.0 mg, 1.8 x 10^{-2} mmol) and PhH$_2$B·NMe$_2$H (7.2 mg, 5.4 x 10^{-2} mmol) was added 1,2-F$_2$C$_6$H$_4$ (0.5 mL). Resulting colourless solution was mixed by inversion for 15 min and then transferred to a crystallisation tube. The 1,2-F$_2$C$_6$H$_4$ solution was layered with pentane and kept −25˚C for two days to afford the product as colourless crystals. Yield: 15 mg, 57%.

^{1}H NMR (500 MHz, CD$_2$Cl$_2$): δ 7.76 (s, 8H, [BAr$^F_4$]$^-$), 7.60 (s, 4H, [BAr$^F_4$]$^-$), 7.44 (br m, 2H, PhH), 7.39 (br m, 3H, PhH), 3.92 (s, 1H, NH), 2.64 (s, 6H, NMe$_2$), 1.90 (br, 6H, CH), 1.22 (apparent dd, J ~ 13, J ~ 6, 36H, CH$_3$), –2.08 (br, 2H, BH$_2$), –19.05 (broad m, 2H, RhH$_2$).

$^{1}H\{^{31}P\}$ NMR (500 MHz, CD_2Cl_2): δ 7.76 (s, 8H, $[BAr^F{}_4]^-$), 7.60 (s, 4H, $[BAr^F{}_4]^-$), 7.44 (br m, 2H, PhH), 7.39 (br m, 3H, PhH), 3.92 (s, 1H, NH), 2.64 (s, 6H, NMe_2), 1.90 (br, 6H, CH), 1.22 (br d, J ~ 6, 36H, CH_3), –2.08 (br, 2H, BH_2), –19.05 (br d, $^{1}J_{RhH}$ = 17, 2H, RhH_2).

$^{31}P\{^{1}H\}$ NMR (202 MHz, CD_2Cl_2): δ 64.7 (d, $^{1}J_{RhP}$ = 108).

^{11}B NMR (160 MHz, CD_2Cl_2): δ 8.0 (br, BH_2), −6.6 (s, $[BAr^F{}_4]^-$).

ESI-MS (1,2-$F_2C_6H_4$, 60°C) positive ion: m/z 560.32 [M^+] (calc. 560.32).

Elemental Microanalysis: Calc. [$C_{58}H_{70}B_2F_{24}NP_2Rh$] (1435.38 $gmol^{-1}$): C, 48.93; H, 4.96; N, 0.98. Found: C, 48.96; H, 4.62; N, 0.98.

$[Rh(P^iPr_3)_2(H)(BPhNMe_2)][BAr^F{}_4]$ (21)

To a sealed NMR tube charged with $[Rh(P^iPr_3)_2(C_6H_5F)][BAr^F{}_4]$ (25.0 mg, 1.8 x 10^{-2} mmol) and $PhH_2B{\cdot}NMe_2H$ (2.4 mg, 1.8 x 10^{-2} mmol) was added 1,2-$F_2C_6H_4$ (0.5 mL). Addition of 1,2-$F_2C_6H_4$ immediately resulted in a purple solution which turned to colourless in 5 min. Resulting colourless solution was mixed by inversion for 24 h which turned the colourless solution to yellow. The yellow solution was transferred to a crystallisation tube, layered with pentane and kept at −25˚C for 2 days which resulted in the formation of majority of pale yellow crystals and some colourless crystals. Pale yellow crystals were mechanically separated from the mixture for characterisation. Yield: 10 mg, 38%.

^{1}H NMR (500 MHz, CD_2Cl_2): δ 7.76 (s, 8H, $[BAr^F{}_4]^-$), 7.67 (m, 1H, Ph), 7.60 (s, 4H, $[BAr^F{}_4]^-$), 7.55 (broad d, 2H, Ph), 7.54 (br, 2H, PhH), 3.07 (s, 3H, NMe), 2.95 (s, 3H, NMe), 2.23 (br, 6H, CH), 1.26 (apparent dd, J ~ 13, J ~ 6, 18H, CH_3), 1.18 (apparent dd, J ~ 13, J ~ 6, 18H, CH_3), –21.71 (doublet of triplets, $^{1}J_{RhH}$ = 64, $^{1}J_{PH}$ = 12, 1H, RhH). The pale yellow solution of (**21**) in CD_2Cl_2 was not stable and decomposed in 6 h to form dark yellow solution of uncharacterized complexes.

$^{1}H\{^{31}P\}$ NMR (500 MHz, CD_2Cl_2, hydride region): –21.71 (d, $^{1}J_{RhH}$ = 64, 1H, RhH).

$^{31}P\{^{1}H\}$ NMR (202 MHz, CD_2Cl_2): δ 48.8 (d, $^{1}J_{RhP}$ = 120).

^{11}B NMR (160 MHz, CD_2Cl_2): δ 50.1 (br, RhB), –6.6 (s, $[BAr^F{}_4]^-$).

^{13}C{^{1}H} NMR (100.62 MHz, CD_2Cl_2): Shifts due to $[BAr^F{}_4]^-$ anion: δ 161.7 (q, $^1J_{BC}$ = 50), 134.8 (s), 128.8 (quartet of quartet, $^2J_{FC}$ = 26, $^3J_{BC}$ = 3), 124.6 (q, $^1J_{FC}$ = 272), 117.4 (apparent septet, $^3J_{FC}$ = 4); Shifts due to cation: δ 132.2 (s, Ph), 130.7 (s, Ph), 127.8 (s, Ph), 43.33 (s, NMe), 40.41 (s, NMe), 24.6 (overlapping doublets, $^1J_{PC}$ = 12, CH_{iPr}), 19.9 (s, CH_{3iPr}), 19.1 (s, CH_{3iPr}).

ESI-MS (1,2-$F_2C_6H_4$, 60°C) positive ion: m/z 556.29 [M^+] (calc. 556.29).

Elemental Microanalysis: Calc. [$C_{58}H_{66}B_2F_{24}NP_2Rh$] (1419.35 gmol^{-1}): C, 49.07; H, 4.69; N, 0.99. Found: C, 49.45; H, 4.20; N, 0.75.

$[Ir(H)_2(PCy_3)_2(\eta^2\text{-}H_2BNH_2(CH_2)_4)][BAr^F{}_4]$ (22)

In a Young's flask, $[IrHPCy_2(\eta^2\text{-}C_6H_9)PCy_2(\eta^3\text{-}C_6H_8)][BAr^F{}_4]$ (44 mg, 2.7 x 10^{-2} mmol) in C_6H_5F was hydrogenated at 4 atm as described in the general procedures. It was stirred for 20 min to produce a colourless solution of $[Ir(H)_2(PCy_3)_2(H_2)_2][BAr^F{}_4]$ which was rapidly transferred under argon to a Schlenk flask containing (**A**) (2.3 mg, 2.7 x 10^{-2} mmol). The resulting colourless solution was stirred for 2 min at 25˚C, then layered with pentane and held at −30˚C for 72 h to afford the product as colourless crystal. Yield: 20 mg, 43%. **^{1}H NMR (500 MHz, CD_2Cl_2)**: δ 7.76 (s, 8H, $[BAr^F{}_4]^-$), 7.60 (s, 4H, $[BAr^F{}_4]^-$), 4.07 (br, 2H, NH_2), 3.23 (br, 2H, CH_2 next to NH_2), 1.93-1.4 [m, 35H, PCy_3 (33H) and CH_2 (2H)], 1.36-1.29 (m, 33H, PCy_3), 0.92 (m, 4H, CH_2), −6.23 (br, 2H, BH_2), −20.53 (t, $^2J_{HP}$ = 16, IrH_2). The NH_2/CH_2 resonances were identified on the basis of the number of cross-peaks in the ^{1}H/^{1}H COSY spectrum. Furthermore the HSQC spectrum shows no cross peak between the signal at δ 4.07, while the signal at δ 3.23 is coupled to a ^{13}C NMR signal at 48.0 ppm. **^{31}P{^{1}H} NMR (202 MHz, CD_2Cl_2)**: δ 37.1 (d, $^2J_{PP}$ = 268, 1P), 35.3 (d, $^2J_{PP}$ = 268, 1P). **^{11}B NMR (160 MHz, CD_2Cl_2)**: δ 19.8 (br, bound BH_2), −6.6 (s, $[BAr^F{}_4]^-$).

ESI-MS (1,2-$F_2C_6H_4$, 60°C) positive ion: m/z 840.54 [M+] (calc. 840.55).

Elemental Microanalysis: Calc. [$C_{72}H_{92}B_2F_{24}IrNP_2$] (1703. 28 $gmol^{-1}$): C, 50.77; H, 5.44; N, 0.82. Found: C, 50.32; H, 5.33; N, 1.03.

[$Ir(H)_2(PCy_3)_2(\eta^2\text{-}H_2BNMeH(CH_2)_4)$][$BAr^F{}_4$] (23)

In a high pressure NMR tube equipped with a J. Young's valve, [$IrHPCy_2(\eta^2\text{-}C_6H_9)PCy_2(\eta^3\text{-}C_6H_8)$][$BAr^F{}_4$] (16 mg, 1 x 10^{-2} mmol) in C_6H_5F was hydrogenated at 4 atm as described in the general procedures. It was stirred for 20 min to produce a colourless solution of [$Ir(H)_2(PCy_3)_2(H_2)_2$][$BAr^F{}_4$] which was rapidly transferred under argon to another high pressure NMR tube containing **B** (1 mg, 1 x 10^{-2} mmol). Gentle rotation of NMR tube for 1.5 h resulted in the colourless solution of **23** and [$Ir(H_5)(PCy_3)_2$][21] in 20:1 ratio. **23** was characterized *in situ* by NMR spectroscopy and ESI-MS. A few single crystals suitable for X-ray diffraction studies were obtained by diffusion of pentane at −35°C which was sufficient for the single crystal X-ray diffraction but not for the elemental microanalysis. **^{1}H NMR (500 MHz, C_6H_5F)**: δ 8.34 (s, 8H, [$BAr^F{}_4$]$^-$), 7.67 (s, 4H, [$BAr^F{}_4$]$^-$), 4.01 (br, 1H, NH), 3.13 (m, 1H, CH_2), 2.69 (m, 1H, CH_2), 2.46 (s, 3H, NMe), 1.93-1.56 (m, 37H, PCy_3 (33H) and CH_2 (4H)), 1.39-1.21 (m, 33H, PCy_3), 0.87 (m, 1H, CH_2), 0.67 (br, 1H, CH_2), −6.24 (br, 1H, BH_2), −6.35 (br, 1H, BH_2), −20.58 (br, 1H, IrH_2), −20.82 (br, 1H, IrH_2).

^{31}P{^{1}H} NMR (202 MHz, C_6H_5F): δ 36.5 (d, $^2J_{PP}$ = 276, 1P), 33.2 (d, $^2J_{PP}$ = 276, 1P).

^{11}B NMR (160 MHz, C_6H_5F): δ 22.4 (br, bound BH_2), −6.1 (s, [$BAr^F{}_4$]$^-$).

ESI-MS (1,2-$F_2C_6H_4$, 60°C) positive ion: m/z 854.55 [M+] (calc. 854.56).

[$Rh(P^iPr_2(CH_2)_3P^iPr_2)(\eta^2\text{-}H_2BNH_2C_4H_8)$][$BAr^F{}_4$] (24)

1,2-$F_2C_6H_4$ (0.5 mL) was added to a high pressure NMR tube equipped with a J. Young's valve and charged with the compound **A** (1.2 mg, 1.4 x 10^{-2} mmol) and [$Rh(P^iPr_2(CH_2)_3P^iPr_2)(C_6H_5F)$][$BAr^F{}_4$] (16 mg, 1.2 x 10^{-2} mmol). Gentle rotation of NMR tube for 30 min resulted in a reddish orange solution consisting of [$Rh(P^iPr_2(CH_2)_3P^iPr_2)(\eta^2\text{-}H_2BNH_2C_4H_8)$][$BAr^F{}_4$] (**24**), amino-borane **E** and [$Rh(P^iPr_2(CH_2)_3P^iPr_2)(C_6H_5F)$][$BAr^F{}_4$] as measured by NMR spectroscopy. **24** was

characterized *in situ* by NMR spectroscopy and ESI-MS. Diffusion of pentane at –35 °C gave mixture of crystals corresponding to **24** (red) and [Rh($P^iPr_2(CH_2)_3P^iPr_2$)(C_6H_5F)] [BAr^F_4] (orange). Red crystals were mechanically separated from orange crystals for single crystal X-ray diffraction studies but due to its very low yield the elemental microanalysis was not possible.

^{1}H NMR (500 MHz, 1,2-$F_2C_6H_4$): δ 8.33 (s, 8H [BAr^F_4]$^-$), 7.69 (s, 4H, [BAr^F_4]$^-$), 4.54 (m, NH_2), 3.28 (br, CH_2), 3.18 (br, CH_2), 2.99 (br, CH_2) 1.76 (m, CH), 1.23-1.16 (br m, CH_3), 1.06 (br, $CH_2CH_2CH_2$), −4.83 (br, BH_2).

^{31}P{^{1}H} NMR (202 MHz, 1,2-$F_2C_6H_4$): δ 57.1 (d, $^1J_{RhP}$ = 160).

^{11}B NMR (160 MHz, 1,2-$F_2C_6H_4$): δ 29.3 (br, BH_2), −6.2 (s, [BAr^F_4]$^-$).

ESI-MS (1,2-$F_2C_6H_4$, 60°C) positive ion: m/z 464.23 [M+] (calc. 464.23).

[Rh(^{i}Pr$_2$P(CH$_2$)$_3$P^{i}Pr$_2$)(η^2-H$_2$BNHMeC$_4$H$_8$)][BAr$^F_4$] (25)

1,2-$F_2C_6H_4$ (0.5 mL) was added to a Young's flask charged with **B** (4.5 mg, 4.5 x 10^{-2}, 2.5 equivalents) and [Rh($P^iPr_2(CH_2)_3P^iPr_2$)(C_6H_5F)][BAr^F_4] (25 mg, 1.8 x 10^{-2} mmol). The resulting orange solution was stirred for 30 min to obtain a red solution. Diffusion of pentane into this solution at –35°C for 72 h afforded **25** as red crystals. Yield: 10 mg, 41%.

^{1}H NMR (500 MHz, CD_2Cl_2): δ 7.76 (s, 8H, [BAr^F_4]$^-$), 7.60 (s, 4H, [BAr^F_4]$^-$), 3.94 (br, 1H, NH), 3.33 (br d, 1H, CH_2), 2.91 (d, $^3J_{HH}$ = 5, 3H, NMe), 2.76 (m, 1H, CH_2), 2.37 (br, 1H, CH_2), 1.99-1.92 (br, 6H, CH (4H) and CH_2 (2H)), 1.65 (m, 1H, CH_2), 1.5-1.0 (br m, 26H, CH_3 (24H) and CH_2 (2H)), 0.52 (br, $CH_2CH_2CH_2$),−4.90 (br, 1H, BH_2), −5.38 (br, 1H, BH_2).

^{31}P{^{1}H} NMR (202 MHz, CD_2Cl_2): δ 57.9 (d, $^1J_{RhP}$ = 162).

^{31}P{^{1}H} NMR (202 MHz, CD_2Cl_2 , 190 K): δ 57.8 (overlapping dd, 1P, $^1J_{RhP}$ = 160, $^2J_{PP}$ = 56), 56.9 (overlapping dd, 1P, $^1J_{RhP}$ = 160, $^2J_{PP}$ = 56).

^{11}B NMR (160 MHz, CD_2Cl_2): δ 32.1 (br, BH_2), −6.6 (s, [BAr^F_4]$^-$).

ESI-MS (1,2-$F_2C_6H_4$, 60°C) positive ion: m/z 478.24 [M+] (calc. 478.24). **Elemental Microanalysis**: Calc. [$C_{52}H_{60}B_2F_{24}NP_2Rh$] (1341.49 gmol^{-1}): C, 46.56; H, 4.51; N, 1.04. Found: C, 46.17; H, 4.16; N, 0.68.

[Rh(^{i}Pr$_2$P(CH$_2$)$_3$P^{i}Pr$_2$)(η^2-H$_2$BNMe$_2$C$_4$H$_8$)][BAr$^F{}_4$] (26)

To a high pressure NMR tube equipped with a J. Young's valve and charged with **C** (0.69 M in 1,2-$F_2C_6H_4$, 0.04 mL, 2.6 x 10^{-2} mmol) and [Rh(P^{i}Pr$_2$(CH$_2$)$_3$P^{i}Pr$_2$)(C$_6$H$_5$F)][BAr$^F{}_4$] (18 mg, 1.3 x 10^{-2} mmol) was added 1,2-$F_2C_6H_4$ (0.4 mL). The NMR tube was rotated at 25ºC and the reaction was followed by NMR spectroscopy. After 24 h the reaction was complete and the resulting red solution was layered with pentane and kept at 25ºC for 72 h to afford the product as red crystals. Yield: 8 mg, 45%.

^{1}H NMR (500 MHz, CD$_2$Cl$_2$): δ 7.76 (s, 8H, [BAr$^F{}_4$]$^-$), 7.60 (s, 4H, [BAr$^F{}_4$]$^-$), 2.99 (br, 2H, CH$_2$), 2.85 (s, 6H, NMe$_2$), 1.92 (m, 4H, CH), 1.79 (br, 2H, CH$_2$), 1.65 (br, 2H, CH$_2$), 1.50 (br, 2H, CH$_2$), ~1.23 (br, 24H, CH$_3$), 0.5 (br, 6H, CH$_2$CH$_2$CH$_2$), −5.17 (br, 2H, BH$_2$).

^{31}P{^{1}H} NMR (202 MHz, CD$_2$Cl$_2$): δ 58.0 (d, $^1J_{RhP}$ = 163).

^{11}B NMR (160 MHz, CD$_2$Cl$_2$): δ 34.4 (br, BH$_2$), −6.6 (s, [BAr$^F{}_4$]$^-$).

ESI-MS (1,2-$C_6H_4F_2$, 60°C) positive ion: m/z 492.25 [M+] (calc. 492.25).

Elemental Microanalysis: Calc. [$C_{53}H_{62}B_2F_{24}NP_2Rh$] (1355.52 gmol^{-1}): C, 46.96; H, 4.61; N, 1.03. Found: C, 46.65; H, 4.10; N, 0.62.

[{Rh(P^{i}Pr$_2$(CH$_2$)$_3$P^{i}Pr$_2$)}$_2$(H)$_2$(*μ*-H)$_3$][BAr$^F{}_4$] (27)

[Rh(P^{i}Pr$_2$(CH$_2$)$_3$P^{i}Pr$_2$)]$_2$(*μ*-H)$_2$ (23 mg, 3.0 x 10^{-2} mmol) and [H(OEt$_2$)$_2$][BAr$^F{}_4$] (30 mg, 3.0 x 10^{-2} mmol) were added to a Young's flask. Addition of 1.0 mL of 1,2-$F_2C_6H_4$ led to the formation of a dark red solution which was immediately hydrogenated at 4 atm as described in the general procedures. The resulting solution was stirred for 1 h to obtain a dark orange solution. The solution was filtered into a crystallisation tube, layered with pentane and kept at –18ºC for 24 h from which dark red crystals were obtained in 70% yield (34 mg). This complex decomposes in CH_2Cl_2 solution (12 h) to give unidentified products, but shows greater stability in 1,2-$F_2C_6H_4$ (no decomposition after 24 h).

^{1}H NMR (400 MHz, CD$_2$Cl$_2$): δ 7.76 (s, 8H, [BAr$^F{}_4$]$^-$), 7.60 (s, 4H, [BAr$^F{}_4$]$^-$), 1.96 (m, 8H, CH), 1.56-1.1 [overlapping m, 60H, CH$_3$ (48 H) and CH$_2$ (12H)], −8.85 (br, 3H), −18.87 (br, 2H).

^{1}H NMR (500 MHz, 1,2-$F_2C_6H_4$): δ 8.34 (s, 8H, $[BAr^F{}_4]^-$), 7.70 (s, 4H, $[BAr^F{}_4]^-$), 1.96 (m, 8H, CH), 1.55-1.11 [overlapping m, 60H, CH_3 (48 H) and CH_2 (12H)], −8.25 (br, 3H), −18.90 (br, 2H).

^{1}H NMR (500 MHz, 1,2-$C_6H_4F_2$, 250 K): δ 8.34 (s, 8H, $[BAr^F{}_4]^-$), 1.93 (m, 8H, CH), 1.40-0.91 [overlapping m, 60H, CH_3 (48 H) and CH_2 (12H)], −7.91 (br, 2H), −9.52 (br, 1H), −18.71 (br, 2H).

^{31}P{^{1}H} NMR (162 MHz, CD_2Cl_2): δ 65.7 (br), 62.7 (br).

^{31}P{^{1}H} NMR (202 MHz, 1,2-$C_6H_4F_2$): δ 66.5 (br), 62.2 (br).

^{31}P{^{1}H} NMR (202 MHz, 1,2-$C_6H_4F_2$, 250 K): δ 66.4 (br d, $^{1}J_{RhP}$ = 100), 60.0 (br d, $^{1}J_{RhP}$ = 100).

Elemental Microanalysis: Calc. [$C_{62}H_{85}BF_{24}P_4Rh_2$] (1626.34 gmol^{-1}): C, 45.77; H, 5.27; Found: C, 45.33; H, 4.84.

[Rh(^{i}Pr$_2$P(CH$_2$)$_3$P^{i}Pr$_2$)(NCMe)$_2$][BAr$^F{}_4$] (28)

[Rh(P^{i}Pr$_2$(CH$_2$)$_3$P^{i}Pr$_2$)(C_6H_5F)][$BAr^F{}_4$] (20 mg, 1.4 x 10^{-2} mmol) was dissolved in 1,2-$F_2C_6H_4$ (1 mL) in a Schlenk flask to which CH_3CN (16 µL, 0.28 mmol) was added. Addition of CH_3CN immediately changed the color of solution from orange to pale yellow. Resulting solution was stirred for 10 min. 1,2-$F_2C_6H_4$ and unreacted CH_3CN were removed in vacuo to obtain pale yellow solid of **16** Yield: 14 mg, 70%.

^{1}H NMR (500 MHz, CD_2Cl_2): δ 7.76 (s, 8H, $[BAr^F{}_4]^-$), 7.61 (s, 4H, $[BAr^F{}_4]^-$), 2.25 (s, 6H, $NCCH_3$), 1.97 (br, 6H, CH_2), 1.33 [overlapping m, 16H, CH_3 (12 H) and CH (4H)], 1.19 (m, 12H, CH_3).

^{31}P{^{1}H} NMR (202 MHz, CD_2Cl_2): δ 42.5 (d, $^{1}J_{RhP}$ = 167).

ESI-MS (1,2-$F_2C_6H_4$, 60°C) positive ion: m/z 461.17 [M+] (calc. 461.17).

Elemental Microanalysis: Calc. [$C_{51}H_{52}BF_{24}N_2P_2Rh$] (1324.62 gmol^{-1}): C, 46.24; H, 3.96; N, 2.11. Found: C, 46.13; H, 3.95; N, 1.98.

6.3 Catalytic procedures

6.3.1 General procedure for the dehydrocoupling of amine-boranes in an open system − hydrogen evolution experiment

In a typical experiment amine-borane and the catalyst (*e.g.* 0.41 M $H_3B{\cdot}NMeH_2$, 0.5 mol% **III**) were added to a 3-necked Schlenk flask with a magnetic stirrer bar. A thin teflon tube was attached to the Schlenk, the other end of the tube was placed under an upturned 50 mL burette filled with water as shown in the Figure below. Reaction was started when the solvent (*e.g.* 0.7 mL 1,2-$F_2C_6H_4$) was injected to the Schlenk flask. The volume of hydrogen gas collected was recorded periodically until the reaction was complete.

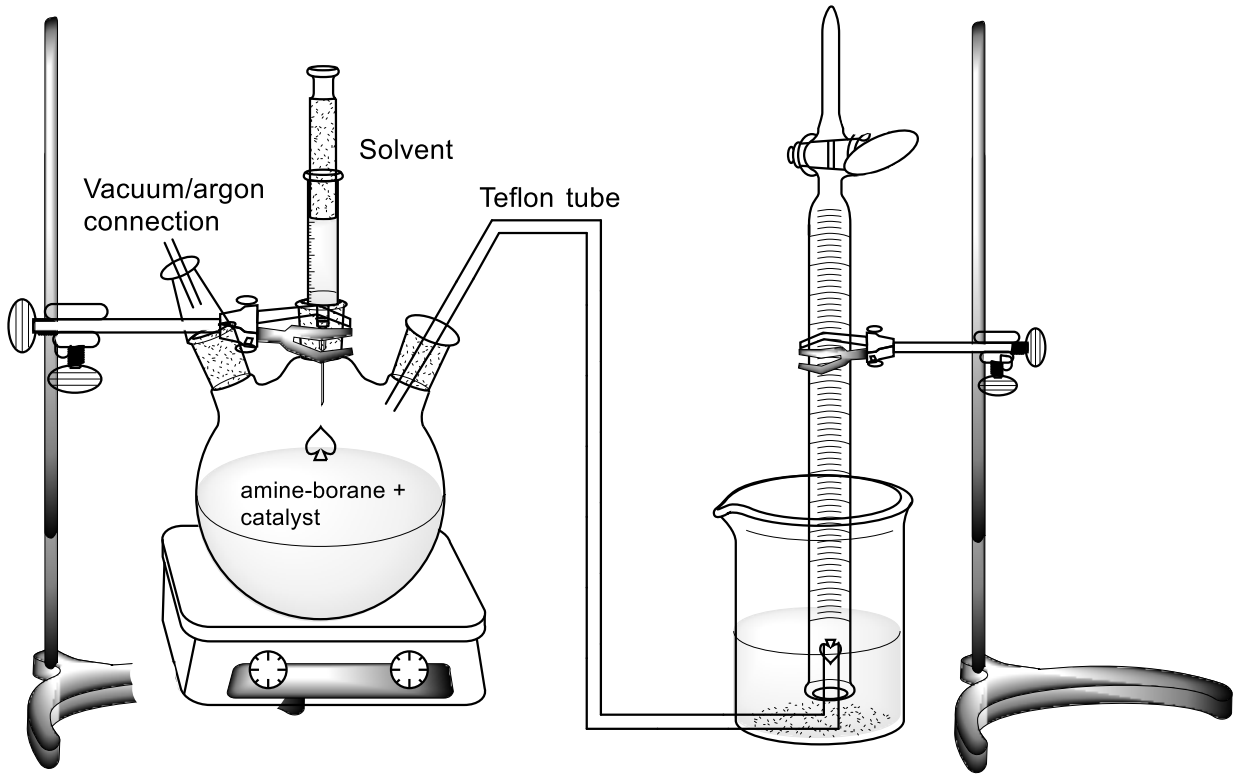


Figure 6.1 Schematic diagram for the hydrogen evolution experiment.

6.3.2 General procedure for the dehydropolymerisation of $H_3B{\cdot}NMeH_2$

In a typical experiment $H_3B{\cdot}NMeH_2$ and the catalyst (*e.g.* 0.41 M $H_3B{\cdot}NMeH_2$, 0.5 mol% **III**) were added to a 3-necked Schlenk flask with a magnetic stirrer bar. Under a flow of argon, an external mineral oil bubbler was connected and the argon flow adjusted to bubble at a rate of approximately two bubbles per second. Reaction was started when the solvent (*e.g.* 0.7 mL THF) was injected to the Schlenk. The mixture was stirred under argon, for the allotted time period (*e.g* ~100 min), then filtered to another Schlenk containing 15 mL of hexane and then sonicated for 15 min. This resulted in an off-white precipitate of $[H_2BNMeH]_n/H_3B{\cdot}NMeH_2$. This was filtered and washed with hexane twice (10 mL each). The resulting solid was dried *in vacuo* for at least 12 h before GPC analysis. Isolated yields ~ 40%.

6.3.3 General procedure for the dehydrocoupling of amine-boranes in a closed system

In a typical experiment amine-borane [*e.g.* 2,2-H,Me-1,2-B,N-C_4H_{10} (**B**), 3 mg, 3 x 10^{-2} mmol], catalyst [*e.g.* $[Rh(^iPr_2P(CH_2)_3P^iPr_2)(\eta^2\text{-}H_2BNHMeC_4H_8)][BAr^F{}_4]$ (**25**), 4 mg, 3 x 10^{-3} mmol, 10 mol%] and an internal standard ($[NBu_4][BAr^F{}_4]$, 10 mg) were added to a high pressure Young's NMR tube. Solvent [*e.g.* 1,2-$F_2C_6H_4$, 0.35 mL] was cannula transferred under argon to the NMR tube and the reaction progress was monitored using ^{11}B NMR spectroscopy at 298 K. Concentrations of boron containing species were calculated by the integrals relative to $[BAr^F{}_4]^-$ from the ^{11}B NMR spectra.

6.4 Computational details

Computational investigations described in Chapter 2 and 3 were carried out by Professor S. A. Macgregor, Dr. Andrés G. Algarra and Nicholas A. Beattie at the Heriot-Watt University. Calculations were run with Gaussian 03 Revision D.01[22] with PCM solvent corrections run with Gaussian 09, Revision A.02.[23] Geometry optimisations were performed using the BP86 functional[24] with Ir, Rh and P centres described with the

Stuttgart RECPs and associated basis sets[25] (with added d-orbital polarisation on P (ζ = 0.387)[26] and 6-31G** basis sets for all other atoms.[27] All stationary points were fully characterized via analytical frequency calculations as either minima (all positive eigenvalues) or transition states (one negative eigenvalue) and IRC calculations and subsequent geometry optimisations were used to confirm the minima linked by each transition state. Frequency calculations also provided a free energy in the gas-phase, computed at 298.15 K and 1 atm. Energies reported in the text are based on the gas-phase free energies and incorporate a correction for dispersion effects using Grimme's D3 parameter set[28] (i.e. BP86-D3) as well as solvation (PCM approach) in C_6H_5F and THF.

Atoms in Molecules[29] analyses were performed with the AIMALL program[30] and employed partially optimised structures based on the experimental heavy atom positions with fully optimised H atoms positions. NMR chemical shifts were calculated with the B3LYP functional[31] with Stuttgart RECPs and basis sets on Rh and P (with d-orbital polarisation on the latter, as above) and 6-311g++** basis sets[32] on C, H, O, B and N (BS2) and were based on the BP86-optimised geometries. Computed chemical shifts are quoted relative to $BF_3{\cdot}OEt_2$. All geometries are provided as sets of Cartesian coordinates as well as the separate file amino-borane.xyz readable by Chemcraft[33] and Mercury.[34] Pipek-Mezey localised orbitals were computed with ORCA Version 3.0.3[35] using def2-TZVP basis sets[36] on the atoms of the {Rh(μ-H)(μ-amino-borane)Rh} unit with a [SD(28,MHF)] ECP for Rh[37] and def2-SV(P) on other atoms.[38] ^{11}B NMR chemical shifts of the cyclic amine-borane dehydrocoupling intermediates (Chapter 5) were calculated by Tanya Mikulas and David Dixon (The University of Alabama) using DFT geometry optimisation coupled with GIAO.

6.5 References

1. A. B. Pangborn, M. A. Giardello, R. H. Grubbs, R. K. Rosen and F. J. Timmers, *Organometallics*, 1996, **15**, 1518-1520.

2. A. T. Lubben, J. S. McIndoe and A. S. Weller, *Organometallics*, 2008, **27**, 3303-3306.

3. *CrysAlisPro (Agilent Technologies, Oxford)*, 2011.

4. J. Cosier and A. M. Glazer, *J. Appl. Crystallogr.*, 1986, **19**, 105-107.

5. Z. Otwinowski and W. Minor, in *Methods Enzymol.*, ed. Charles W. Carter, Jr., Academic Press, 1997, vol. Volume 276, pp. 307-326.

6. A. Altomare, G. Cascarano, C. Giacovazzo, A. Guagliardi, M. C. Burla, G. Polidori and M. Camalli, *J. Appl. Crystallogr.*, 1994, **27**, 435.

7. L. Palatinus and G. Chapuis, *J. Appl. Crystallogr.*, 2007, **40**, 786-790.

8. G. M. Sheldrick, *Acta Crystallographica Section A*, 2008, **64**, 112-122.

9. P. W. Betteridge, J. R. Carruthers, R. I. Cooper, K. Prout and D. J. Watkin, *J. Appl. Crystallogr.*, 2003, **36**, 1487.

10. N. Blaquiere, S. Diallo-Garcia, S. I. Gorelsky, D. A. Black and K. Fagnou, *J. Am. Chem. Soc.*, 2008, **130**, 14034-14035.

11. X. Chen, J.-C. Zhao and S. G. Shore, *J. Am. Chem. Soc.*, 2010, **132**, 10658-10659.

12. W. C. Ewing, P. J. Carroll and L. G. Sneddon, *Inorg. Chem.*, 2013, **52**, 10690-10697.

13. G. Alcaraz, A. B. Chaplin, C. J. Stevens, E. Clot, L. Vendier, A. S. Weller and S. Sabo-Etienne, *Organometallics*, 2010, **29**, 5591-5595.

14. H. C. Johnson, A. P. M. Robertson, A. B. Chaplin, L. J. Sewell, A. L. Thompson, M. F. Haddow, I. Manners and A. S. Weller, *J. Am. Chem. Soc.*, 2011, **133**, 11076-11079.

15. I. Pernik, J. F. Hooper, A. B. Chaplin, A. S. Weller and M. C. Willis, *ACS Catal.*, 2012, **2**, 2779-2786.

16. R. Dallanegra, A. P. M. Robertson, A. B. Chaplin, I. Manners and A. S. Weller, *Chem. Commun.*, 2011, **47**, 3763-3765.

17. M. D. Fryzuk, W. E. Piers, F. W. B. Einstein and T. Jones, *Canadian Journal of Chemistry-Revue Canadienne De Chimie*, 1989, **67**, 883-896.

18. M. Brookhart, B. Grant and A. F. Volpe, *Organometallics*, 1992, **11**, 3920-3922.

19. F. H. Stephens, R. T. Baker, M. H. Matus, D. J. Grant and D. A. Dixon, *Angew. Chem. Int. Ed.*, 2007, **46**, 746-749.

20. A. Kumar, J. S. A. Ishibashi, T. N. Hooper, T. C. Mikulas, D. A. Dixon, S.-Y. Liu and A. S. Weller, *Chem. Eur. J.*, 2016, **22**, 310-322.

21. C. J. Stevens, R. Dallanegra, A. B. Chaplin, A. S. Weller, S. A. Macgregor, B. Ward, D. McKay, G. Alcaraz and S. Sabo-Etienne, *Chem. Eur. J.*, 2011, **17**, 3011-3020.

22. Gaussian 03, Revision C.02, M. J. Frisch, G. W. Trucks, H. B. Schlegel, G. E. Scuseria, M. A. Robb, J. R. Cheeseman, J. A. Montgomery, Jr., T. Vreven, K. N. Kudin, J. C. Burant, J. M. Millam, S. S. Iyengar, J. Tomasi, V. Barone, B. Mennucci, M. Cossi, G. Scalmani, N. Rega, G. A. Petersson, H. Nakatsuji, M. Hada, M. Ehara, K. Toyota, R. Fukuda, J. Hasegawa, M. Ishida, T. Nakajima, Y. Honda, O. Kitao, H. Nakai, M. Klene, X. Li, J. E. Knox, H. P. Hratchian, J. B. Cross, C. Adamo, J. Jaramillo, R. Gomperts, R. E. Stratmann, O. Yazyev, A. J. Austin, R. Cammi, C. Pomelli, J. W. Ochterski, P. Y. Ayala, K. Morokuma, G. A. Voth, P. Salvador, J. J. Dannenberg, V. G. Zakrzewski, S. Dapprich, A. D. Daniels, M. C. Strain, O. Farkas, D. K. Malick, A. D. Rabuck, K. Raghavachari, J. B. Foresman, J. V.

Ortiz, Q. Cui, A. G. Baboul, S. Clifford, J. Cioslowski, B. B. Stefanov, G. Liu, A. Liashenko, P. Piskorz, I. Komaromi, R. L. Martin, D. J. Fox, T. Keith, M. A. Al-Laham, C. Y. Peng, A. Nanayakkara, M. Challacombe, P. M. W. Gill, B. Johnson, W. Chen, M. W. Wong, C. Gonzalez, and J. A. Pople, Gaussian, Inc., Wallingford CT, 2004.

23. Gaussian 09, Revision A.02, M. J. Frisch, G. W. Trucks, H. B. Schlegel, G. E. Scuseria, M. A. Robb, J. R. Cheeseman, G. Scalmani, V. Barone, B. Mennucci, G. A. Petersson, H. Nakatsuji, M. Caricato, X. Li, H. P. Hratchian, A. F. Izmaylov, J. Bloino, G. Zheng, J. L. Sonnenberg, M. Hada, M. Ehara, K. Toyota, R. Fukuda, J. Hasegawa, M. Ishida, T. Nakajima, Y. Honda, O. Kitao, H. Nakai, T. Vreven, J. A. Montgomery, Jr., J. E. Peralta, F. Ogliaro, M. Bearpark, J. J. Heyd, E. Brothers, K. N. Kudin, V. N. Staroverov, R. Kobayashi, J. Normand, K. Raghavachari, A. Rendell, J. C. Burant, S. S. Iyengar, J. Tomasi, M. Cossi, N. Rega, J. M. Millam, M. Klene, J. E. Knox, J. B. Cross, V. Bakken, C. Adamo, J. Jaramillo, R. Gomperts, R. E. Stratmann, O. Yazyev, A. J. Austin, R. Cammi, C. Pomelli, J. W. Ochterski, R. L. Martin, K. Morokuma, V. G. Zakrzewski, G. A. Voth, P. Salvador, J. J. Dannenberg, S. Dapprich, A. D. Daniels, O. Farkas, J. B. Foresman, J. V. Ortiz, J. Cioslowski, and D. J. Fox, Gaussian, Inc., Wallingford CT, 2009.

24. A. D. Becke, Phys. Rev. A 1988, 38, 3098.

25. D. Andrae, U. Häußermann, M. Dolg, H. Stoll and H. Preuß, Theor. Chim. Acta 1990, 77, 123.

26. A. Hollwarth, M. Bohme, S. Dapprich, A. W. Ehlers, A. Gobbi, V. Jonas, K. F. Kohler, R. Stegmann, A. Veldkamp and G. Frenking, Chem. Phys. Lett. 1993, 208, 237.

27. W. J. Hehre, R. Ditchfield and J. A. Pople, J. Chem. Phys. 1972, 56, 2257.

28. S. Grimme, J. Antony, S. Ehrlich and H. Krieg, J. Chem. Phys. 2010, 132, 154104.

29. Atoms in Molecules - A Quantum Theory R.F.W. Bader, Oxford University Press, Oxford, 1990.

30. AIMAll (Version 13.02.26, Professional), Keith, T. A.; Gristmill, T. K. Software, Overland Park KS, USA, 2015 (aim.tkgristmill.com).

31. (i) A. D. Becke, J. Chem. Phys., 1993, 98, 5648-52; (ii) C. Lee, W. Yang, and R. G. Parr, Phys. Rev. B, 1988, 37, 785; (iii) S. H. Vosko, L. Wilk, and M. Nusair, Can. J. Phys., 1980, 58,1200-11.

32. A. D. McLean and G. S. Chandler, J. Chem. Phys., 1980, 72, 5639.

33. Chemcraft version 1.7 see http://www.chemcraftprog.com

34. Mercury CSD 2.0 C. F. Macrae, I. J. Bruno, J. A. Chisholm, P. R. Edgington, P. McCabe, E. Pidcock, L. Rodriguez-Monge, R. Taylor, J. van de Streek and P. A. Wood, J. Appl. Cryst., 41, 466-470, 2008

35. Frank Neese, Wiley Interdisciplinary Reviews: Computational Molecular Science 2012, 2, 73.

36. F. Weigend, R. Ahlrichs, Phys. Chem. Chem. Phys. 2005, 7, 3297.

37. Dirk Andrae, Diplomarbeit (1989) (unpublished).Your calculation utilizes the basis: Ahlrichs-VDZ

38. A. Schaefer, H. Horn and R. Ahlrichs, J. Chem. Phys. 1992, 97, 2571; (ii) A. Schaefer, C. Huber and R. Ahlrichs, J. Chem. Phys. 1994, 100, 5829.

7 Appendices

7.1 Crystallographic data

Table 7.1 Crystallographic data for **4'**, **5a** and **4b'**.

	4'	**5a**	**4b'**
CCDC number	971346	971347	988696
Formula	$IrP_2C_{69.80}H_{92.54}B_2Cl_8F_{3.27}N$	$Ir_2P_4C_{112.5}H_{163}B_2F_{25}$	$Ir_1P_2N_3C_{70}H_{118}B_4Cl_8$
M	1567.19	2484.26	1582.76
Crystal System	Monoclinic	Orthorhombic	Triclinic
Space group	$P2_1/c$	$P2_122_1$	*P*-1
T [K]	150(2)	150(2)	150(2)
a [Å]	13.2199 (1)	16.435 (3)	12.7377(1)
b [Å]	34.9437 (2)	17.300 (4)	12.8491(1)
c [Å]	18.4595 (1)	20.951 (4)	25.1406(2)
α [deg]	90	90	99.5231(4)
β [deg]	105.9144 (2)	90	98.2550(3)
γ [deg]	90	90	95.4001(3)
V [Å^3]	8200.57 (9)	5957 (2)	3986.57(5)
Z	4	2	2
Density [g cm^{-3}]	1.269	1.385	1.318
μ [mm^{-1}]	1.97	2.37	2.022
θ range [deg]	5.097 ≤ θ ≤ 27.469	5.10 ≤ θ ≤ 27.49	5.11 ≤ θ ≤ 27.515
Reflns collected	118540	13594	58065
R_{int}	0.041	0.048	0.030
Completeness	99.00%	99.10%	98.6%
Data/restr/param	18580/1027/820	13594/13/654	18071/140/1075
R_1 [I > 2σ(I)]	0.0553	0.034	0.0353
wR_2 [all data]	0.1376	0.0927	0.0763
GoF	1.0845	0.935	1.0098
Largest diff. pk and hole [eÅ^{-3}]	1.82, -1.21	1.14, −1.69	1.12, -1.01

Table 7.2 Crystallographic data for **6**, **7** and **8**.

	6	**7**	**8**
CCDC number	1438002	1438000	1438003
Formula	$C_{67}H_{54}O_2P_6Zn_4$	$C_{86}H_{69}B_2F_{24}N_1P_4Rh_2$	$C_{50}H_{58}B_1F_{24}N_1P_2Rh_1$
M	2125.23	1923.78	1315.44
Crystal System	Triclinic	Triclinic	Monoclinic
Space group	*P* -1	*P* -1	*P* 2_1/c
T [K]	150	150	150
a [Å]	12.81750(10)	12.9810(2)	13.01020(10)
b [Å]	14.3695(2)	17.1942(3)	18.4069(2)
c [Å]	19.6829(3)	21.5379(4)	24.2512(2)
α [deg]	71.2073(5)	68.0529(17)	90
β [deg]	76.2971(5)	84.7135(15)	92.6115(4)
γ [deg]	88.5829(6)	83.5328(15)	90
V [Å^3]	3329.03(5)	4423.92(14)	5801.58(5)
Z	2	2	4
μ [mm^{-1}]	1.149	4.526	0.461
θ range [deg]	5.133 ≤ *θ* ≤ 27.513	2.849 ≤ *θ* ≤ 76.410	5.099 ≤ *θ* ≤ 27.485
Reflns collected	61277	51685	73207
R_{int}	0.024	0.023	0.022
Data/restr/param	15170 / 852 / 985	18267 / 912 / 1180	13193 / 684 / 833
R_1 [I > 2σ(I)]	0.0454	0.0432	0.0736
wR_2 [all data]	0.1154	0.1118	0.1670
GoF	0.9240	0.9781	0.9672
Largest diff. pk and hole [eÅ^{-3}]	0.88, -0.65	1.94, -1.45	2.52, -4.45

Table 7.3 Crystallographic data for **9**, **12** and **13**.

	9	**12**	**13**
CCDC number	1438001	1445276	1445275
Formula	$C_{62}H_{85}B_2F_{24}N_1P_4Rh_2$	$C_{56}H_{62}B_2F_{24}NP_2Rh$	$C_{59}H_{70}B_2F_{24}NP_2Rh$
M	1651.64	1391.53	1435.63
Crystal System	Monoclinic	Orthorhombic	Monoclinic
Space group	*P* 2_1/c	*P b c a*	*P* 21/c
T [K]	150	150(2)	150(2)
a [Å]	18.5806(4)	25.1599(2)	36.8146(6)
b [Å]	15.9539(3)	18.78740(10)	14.0680(2)
c [Å]	25.1637(4)	26.2494(2)	26.0748(4)
α [deg]	90	90	90
β [deg]	97.5683(19)	90	103.843(2)
γ [deg]	90	90	90
V [Å^3]	7394.37(13)	12407.81(15)	13112.1(4)
Z	4	8	8
μ [mm^{-1}]	5.299	3.697	3.515
θ range [deg]	3.288 ≤ *θ* ≤ 74.469	3.367 ≤ θ ≤ 75.020	3.376 ≤ θ ≤ 76.415
Reflns collected	31990	31463	78635
R_{int}	0.025	0.0214	0.0295
Data/restr/param	14608 / 2729 / 1045	12403/608/1037	27168/1194/1869
R_1 [I > 2σ(I)]	0.0453	0.0393	0.0423
wR_2 [all data]	0.1196	0.1216	0.1206
GoF	0.9941	0.787	0.956
Largest diff. pk and hole [eÅ^{-3}]	0.88, −0.65	0.583, −0.680	0.891, −0.908

Table 7.4 Crystallographic data for **15**, **18** and **20**.

	15	**18**	**20**
CCDC number	1445277	1445280	1445281
Formula	$C_{65}H_{82}B_2F_{24}NP_2Rh$	$C_{55}H_{60}B_2F_{24}NP_2Rh$	$C_{58}H_{68}B_2F_{24}NP_2Rh$
M	1519.78	1377.51	1421.60
Crystal System	Orthorhombic	Orthorhombic	Monoclinic
Space group	*P n a* 21	*P b c a*	*C* 2/*c*
T [K]	150(2)	150(2)	150(2)
a [Å]	51.6071(4)	25.3462(3)	39.5210(18)
b [Å]	19.7098(2)	18.3643(2)	12.9114(4)
c [Å]	14.21100(10)	25.7382(3)	53.766(2)
α [deg]	90	90	90
β [deg]	90	90	110.023(5)
γ [deg]	90	90	90
V [Å^3]	14454.9(2)	11980.2(2)	25776.7(19)
Z	8	8	16
Density [g cm^{-3}]	1.397	1.527	1.465
μ [mm^{-1}]	3.219	3.823	3.571
θ range [deg]	$3.410 \leq \theta \leq 76.478$	$3.432 \leq \theta \leq 73.256$	$3.403 \leq \theta \leq 73.193$
Reflns collected	166541	85542	49960
R_{int}	0.0559	0.0351	0.0874
Completeness	98.0%	99.5%	96.3%
Data/restr/param	29727/2598/2360	11953/243/860	24884/1008/1984
R_1 [I > 2σ(I)]	0.0517	0.0549	0.0890
wR_2 [all data]	0.1318	0.1666	0.2482
GoF	0.867	0.841	0.994
Largest diff. pk and hole [eÅ^{-3}]	0.579, −1.076	3.169, −1.150	1.666, −1.725

Table 7.5 Crystallographic data for **21**.

	21
CCDC number	1445282
Formula	$C_{58}H_{66}B_2F_{24}NP_2Rh$
M	1419.58
Crystal System	Triclinic
Space group	*P*-1
T [K]	150(2)
a [Å]	12.3669(8)
b [Å]	14.4784(13)
c [Å]	18.9906(11)
α [deg]	103.872(6)
β [deg]	103.598(5)
γ [deg]	91.524(6)
V [Å^3]	3196.2(4)
Z	2
Density [g cm^{-3}]	1.475
μ [mm^{-1}]	3.600
θ range [deg]	$3.156 \leq \theta \leq 75.137$
Reflns collected	23146
R_{int}	0.0785
Completeness	95.8%
Data/restr/param	12646/553/1000
R_1 [I > 2σ(I)]	0.0834
wR_2 [all data]	0.2658
GoF	0.999
Largest diff. pk and hole [eÅ^{-3}]	0.845, −1.555

7.2 Publications

1. Kumar, A.; Beattie, N. A.; Pike, S. D.; Macgregor S. A.; Weller A. S. The Simplest Amino-borane $H_2B{=}NH_2$ Trapped on a Rh_2 Dimer *Angew. Chem. Int. Ed.*, **2016**, *accepted.*
2. Kumar, A.; Priest, I. K.; Hooper T.N.; Weller A. S. Variable Coordination Modes and Catalytic Dehydrogenation of B-Phenyl Amine-Boranes, *Dalton Trans* **2016**, *in press,* DOI: 10.1039/c6dt00197a.
3. Kumar, A.; Ishibashi, J. S. A.; Hooper T.N.; Mikulas, T. C; Dixon, D. A.; Liu, S.–Y.; Weller A. S. The Synthesis, Characterization and Dehydrogenation of Sigma–Complexes of BN–Cyclohexanes *Chem. Eur. J.* **2016***, 22*, 310.
4. Kumar, A.; Johnson, H. C.; Hooper T.N.; Weller A. S.; Algarra A.G.; Macgregor S. A. Multiple metal-bound oligomers from Ir-catalysed dehydropolymerisation of $H_3B{\cdot}NH_3$ as probed by experiment and computation *Chem. Sci.* **2014**, *5*, 2546*.*